



**pennsylvania**

DEPARTMENT OF TRANSPORTATION

# Data Management, Mining, and Inference for Bridge Monitoring

FINAL REPORT

Date 10/04/2023

By (PI) Piervincenzo Rizzo, Ph.D.  
and Alireza Enshaeian

University of Pittsburgh

COMMONWEALTH OF PENNSYLVANIA  
DEPARTMENT OF TRANSPORTATION

CONTRACT # 4400018535  
WORK ORDER # PIT WO 003





<b>1. Report No.</b> FHWA-PA-2023-003- PITT WO 003		<b>2. Government Accession No.</b>		<b>3. Recipient's Catalog No.</b>	
<b>4. Title and Subtitle</b>  Data Management, Mining, and Inference for Bridge Monitoring				<b>5. Report Date</b> 08/03/2023	
				<b>6. Performing Organization Code</b>	
<b>7. Author(s)</b>  Piervincenzo Rizzo, Ph.D. (PI) and Alireza Enshaeian (Graduate Student Researcher)				<b>8. Performing Organization Report No.</b>	
<b>9. Performing Organization Name and Address</b>  University of Pittsburgh, Dept. of Civil & Environmental Engineering 123 University Place Pittsburgh, PA, 15261				<b>10. Work Unit No. (TR AIS)</b>	
				<b>11. Contract or Grant No.</b> 4400018535, PIT WO 003	
<b>12. Sponsoring Agency Name and Address</b> The Pennsylvania Department of Transportation Bureau of Planning and Research 400 North Street, Keystone Building, 6th Floor, Harrisburg, PA 17120				<b>13. Type of Report and Period Covered</b>  Final Report 12/04/2019 – 10/03/2023	
				<b>14. Sponsoring Agency Code</b>	
<b>15. Supplementary Notes</b> <b>Technical Advisor</b> Patricia Kiehl, P.E. The Pennsylvania Department of Transportation, 400 North Street, Keystone Building, 7th Floor, Harrisburg, PA 17120. <a href="mailto:pkiehl@pa.gov">pkiehl@pa.gov</a> Phone: 717.772.0568					
<b>16. Abstract</b> According to the Federal Highway Administration (FHWA), there are over 600,000 highway bridges in the United States. Nationwide, the performance evaluation of bridges starts with the inspection of the bridge to determine the current condition. Inspections are conducted in accordance with the National Bridge Inspection Standards (NBIS). With more than 25,000 state-owned bridges, Pennsylvania has the third-largest number of bridges in the United States. As the average age is over 50 years old, the maintenance and management of this large inventory is critical to optimize repair and rehabilitation costs and to minimize the risk of structural failures. Over the past two decades there has been an escalating interest worldwide for cost-effective structural health monitoring (SHM) strategies to monitor bridges 24/7. SHM is the scientific process of identifying damage in a given structure of interest using a non-invasive network of sensors embedded or bonded to that structure. SHM evolves the inspection paradigm from "time-based" NDE in which a structure is inspected periodically, to permanent-based where the sensors monitor the structure in real-time in order to flag, locate, and quantify damage as it happens. The sensors measure physical characteristics like strain, acceleration, temperature, just to mention a few, while dedicated hardware/software elaborates the set of time series streamed from the sensors. In year 2017, the Pennsylvania Department of Transportation (PennDOT) started the pilot bridge instrumentation program. The program consisted of instrumenting ten bridges during the period 2017-2019 with a commercial system (hardware and software). Part of the hardware consisted of wireless sensors that provided real-time information about structural static and dynamic responses. Within that program, PennDOT intended to determine an assessment of the cost of components/equipment, system software, and labor to monitor the identified bridges and/or any or all bridges throughout the Commonwealth, versus the savings to PennDOT for a reduction in man hours and/or a reduction in spending to effectively manage and maintain the bridges. This document presents the main findings of a project that investigated advanced data management, analysis, mining and inference approaches for bridge health monitoring, safety evaluation, reliability and resilience assessment of instrumented bridges in Pennsylvania. This report provides a roadmap to guide the implementation on the broader use of the results of this project. The work consisted on the analysis of the data streamed by the sensors and the comparison of some specific readings to the numerical predictions obtained with the implementation of finite element models.					
<b>17. Key Words</b>  Bridge health monitoring, wireless sensing, finite element modeling, damage detection, bridge management.				<b>18. Distribution Statement</b> No restrictions. This document is available from the National Technical Information Service, Springfield, VA 22161	
<b>19. Security Classif. (of this report)</b>  Unclassified		<b>20. Security Classif. (of this page)</b>  Unclassified		<b>21. No. of Pages</b>  203	<b>22. Price</b>  N/A



University of Pittsburgh  
Department of Civil and Environmental Engineering

**DATA MANAGEMENT, MINING, and INFERENCE for BRIDGE MONITORING**

**FINAL REPORT**

By

**Piervincenzo Rizzo, Ph.D.**

*Professor*

**Mr. Alireza Enshaeian**

*Graduate Student Researcher*

Final Report

Contract No. 4400018535 - Work Order 003

Department of Civil and Environmental Engineering

University of Pittsburgh

Pittsburgh, Pennsylvania, 15261

October 2023



## **DISCLAIMER**

The content of this report reflects the views of the authors who are responsible for the facts and the accuracy of the data presented herein. The contents do not necessarily reflect the official views of policies of the U.S. Department of Transportation, Federal Highway Administration, or the Commonwealth of Pennsylvania at the time of publication. This report does not constitute a standard specification or regulation.

## **ACKNOWLEDGEMENTS**

This work was sponsored by the Pennsylvania Department of Transportation and the U.S. Department of Transportation Federal Highway Administration. The work about the finite element modeling was conducted by Mr. Behzad Ghahremani. His contribution to the project is highly appreciated.



# TABLE OF CONTENTS

<b>TABLE OF CONTENTS</b> .....	<b>iii</b>
<b>LIST OF FIGURES</b> .....	<b>vii</b>
<b>LIST OF TABLES</b> .....	<b>xiii</b>
<b>PROJECT HIGHLIGHTS</b> .....	<b>1</b>
<b>EXECUTIVE SUMMARY</b> .....	<b>2</b>
<b>CHAPTER 1: INTRODUCTION</b> .....	<b>3</b>
<b>CHAPTER 2: BRIDGE HEALTH MONITORING IN THE U.S.: A REVIEW</b> .....	<b>5</b>
<b>2.1. Sensing and a Few Notable Examples.</b> .....	<b>5</b>
<b>2.2. Data Inference Methods</b> .....	<b>10</b>
<b>2.3 Wireless Sensors Technologies and Sensors Drift</b> .....	<b>13</b>
<b>2.4 Conclusions</b> .....	<b>15</b>
<b>CHAPTER 3: THE PENNDOT PILOT BRIDGE PROGRAM</b> .....	<b>17</b>
<b>3.1. The Sensors</b> .....	<b>17</b>
<b>3.2. The Bridges</b> .....	<b>18</b>
3.2.1 <i>The Elizabeth Bridge</i> .....	18
3.2.2 <i>The Neville Island Bridge</i> .....	18
3.2.3 <i>The Birmingham Bridge</i> .....	18
3.2.4 <i>The Smithfield Street Bridge</i> .....	19
3.2.5 <i>The Clairton-Glassport Bridge</i> .....	19
3.2.6 <i>The Cooks Mill Bridge</i> .....	19
3.2.7 <i>The Somerset Bridge</i> .....	20
3.2.8 <i>The Tonolaway Bridge</i> .....	20
3.2.9 <i>The Chester County Bridge</i> .....	20
3.2.10 <i>The Sanatoga Bridge</i> .....	20
<b>CHAPTER 4: INFERENCE METHODS</b> .....	<b>21</b>
<b>4.1. Terminology</b> .....	<b>21</b>
<b>4.2. Data Processing</b> .....	<b>22</b>
<b>4.3 Finite Element Analysis</b> .....	<b>24</b>

<b>CHAPTER 5: THE SMITHFIELD STREET BRIDGE .....</b>	<b>27</b>
5.1. Setup .....	27
5.2. Numerical vs Experimental Results .....	28
5.3. Structural Health Monitoring Algorithms .....	29
5.3.1 Truck Test Monitoring and Interpretation .....	29
5.3.2 Long-Term Monitoring .....	30
5.4. Conclusions .....	34
<b>CHAPTER 6: THE CONCRETE BOX BEAMS: SMITHFIELD, COOKS MILL, AND TONOLAWAY BRIDGES .....</b>	<b>35</b>
6.1. Setup .....	35
6.2. Numerical vs Experimental Results .....	36
6.3. Long Term Monitoring .....	37
6.4. Conclusions .....	38
<b>CHAPTER 7: THE BIRMINGHAM, CLAIRTON, AND CHESTER BRIDGES .....</b>	<b>39</b>
7.1. Truck Test Results and Comparison to the Numerical Analyses .....	39
7.2. Long-Term Monitoring .....	41
7.3. Conclusions .....	43
<b>CHAPTER 8: THE ELIZABETH BRIDGE .....</b>	<b>45</b>
<b>CHAPTER 9: THE NEVILLE ISLAND BRIDGE .....</b>	<b>47</b>
<b>CHAPTER 10: THE SANATOGA BRIDGE .....</b>	<b>51</b>
10.1. Introduction .....	51
10.2. Long-term monitoring .....	51
10.3. Conclusions .....	52
<b>CHAPTER 11: FINDINGS/RECOMMENDATIONS .....</b>	<b>53</b>
11.1. Proprietary Software .....	53
11.2. Recorded Data .....	54
11.3. Drift .....	56
11.4. Damage Estimation Methodologies Using Recorded Data .....	57

11.5 Retrofit/repair Evaluation Using Recorded Data .....	58
11.6. Long-Term Bridge Instrumentation Objectives .....	58
11.7 Temperature Effects on Sensor Data .....	59
<b>CHAPTER 12: PUB 238 UPDATES .....</b>	<b>61</b>
12.1. Bridge Instrumentation .....	61
12.2. Contracting Procedures .....	62
12.3 Instrumentation .....	62
12.4. Diagnostic Test Program .....	62
12.5 Evaluation of instrumentation Results .....	63
12.6. Reporting .....	63
12.7. Instrumentation Systems .....	63
<b>CHAPTER 13: CONCLUSIONS .....</b>	<b>65</b>
13.1. Instrumentation Programs .....	65
13.2. PennDOT Pilot Instrumentation Program.....	66
13.3 Finite Element Modeling .....	69
<b>REFERENCES: .....</b>	<b>71</b>
<b>APPENDIX A: FUTURE STUDIES .....</b>	<b>75</b>



## LIST OF FIGURES

<b>Fig. 1.1</b> - Pennsylvania map and location of the bridges under the P2BIP program.	1
<b>Fig. 3.1</b> - Location of the sensing system on the Elizabeth bridge (Elevation looking downstream). From left to right, piers 10, 11, 12, and 13 are visible.	2
<b>Fig.3.2</b> - The Neville Island bridge. Source: <a href="https://www.penndot.gov/RegionalOffices/district11/PublicMeetings/Documents/SR0079%20A61%20Detour%20Slides%201-21-2020.pdf">https://www.penndot.gov/RegionalOffices/district11/PublicMeetings/Documents/SR0079%20A61%20Detour%20Slides%201-21-2020.pdf</a>	3
<b>Fig. 3.3</b> - Photos of the Birmingham Bridge. (a) <a href="https://www.flickr.com/photos/jag9889/10148146816">https://www.flickr.com/photos/jag9889/10148146816</a> ; (b) <a href="http://pghbridges.com/pittsburghE/0587-4476/birmingham.htm">http://pghbridges.com/pittsburghE/0587-4476/birmingham.htm</a>	3
<b>Fig. 3.4</b> - The Smithfield bridge with directions and nomenclature. Span 3 is in the far end (North side).	4
<b>Fig. 3.5</b> - Photo of the Clairton-Glassport Bridge	4
<b>Fig. 3.6</b> - Photo of the Cooks Mill Bridge	5
<b>Fig. 3.7</b> - Photos of the 55-3014-0050-0509 bridge (Somerset Bridge). Figure adapted from PennDOT bridge inspection 2014. Upstream view.	5
<b>Fig. 3.8</b> - Photo of the single span ID 29-2004-0040-0000 bridge over little Tonoloway Creek in Fulton County	5
<b>Fig. 3.9</b> - Photos of the BMS ID 15-0082-0592-0385 BRIDGE in Chester County. (Top left) Upstream elevation looking downstream. (Top right): Downstream elevation looking upstream. (Bottom left): Deck underside and superstructure, Span 1, Span 2 similar. Figures adapted from the 2015 bridge inspection report.	6
<b>Fig. 3.10</b> - Photos of the BMS ID 46-4031-0314-1676 in the Montgomery County. (Figures adapted from a 2015 bridge inspection report).	6
<b>Fig. 4.1</b> - Example of raw strain downloaded from the Vendor repository and associated with a strain gage.	7
<b>Fig. 4.2</b> - Example of the raw temperature downloaded from the Vendor repository. The temperature gage shown here belong to two strain gages installed in the Somerset Bridge. Plots like these may show anomalous spikes, likely due to electromagnetic interference, extreme hot or cold temperature (see second week of January 2018). Last but not least may confirm the termination of a given sensor.	7
<b>Fig. 4.3</b> - Example of the raw strain overlapped to the corresponding 15-minutes average. The data are from the same gages shown in Fig. 2.3, i.e. from the Somerset Bridge.	8
<b>Fig. 4.4</b> - Example of the raw strain vs raw temperature. For plots like these, the equation of the linear regression and the corresponding $R^2$ value are computed for further analysis.	8
<b>Fig. 4.5</b> - True strain computed for the time interval 11:30 – 12:30 of the graph of <b>Fig. 4.2</b> .	9
<b>Fig. 4.6</b> - Example of counting the number of occurrences by computing how many times a certain strain was observed. The vertical red line represents the maximum value recorded by the given strain sensor during the truck load test. The dashed vertical lines bound the $\pm 4s$ interval. The strain in question was measured from one of the strain gages mounted on the Smithfield Bridge and the monitoring period in question spanned for 12 months, from 08/01/2019 to 07/31/2020.	9
<b>Fig. 4.7</b> - Example of outlier analysis applied to true strain data collected from the 30 gages of the Somerset Bridge.	10
<b>Fig. 5.1</b> - The Smithfield bridge with directions and nomenclature.	11
<b>Fig. 5.2</b> - Close-up view of the center truss, with the top, diagonal, and bottom member. The west truss and some strain gages are also visible. Photos by Piervincenzo Rizzo	12
<b>Fig. 5.3</b> - Drawings of the East, Center and West trusses. The members instrumented with a wireless strain gage are labeled according to the gage number.	13
<b>Fig. 5.4</b> - Maximum strain increase during the truck test recorded at each of the instrumented members. Note that the sensors on the East truss face west, whereas the gages on the Center and West truss face east. The values are expressed in microstrains.	13
<b>Fig. 5.5</b> - Finite element model of the Smithfield Street Bridge.	14
<b>Fig. 5.6</b> - Schematics of the AASHTO trucks and of the truck used by the Vendor for the test on the bridge.	15

<b>Fig. 5.7</b> - Numerical setup relative to the analysis of the ML-80 AASHTO truck. The pink dots locate the position of the truck wheels.	<b>16</b>
<b>Fig. 5.8</b> - Numerical strains due to a simulated symmetric load. The values are expressed in microstrains.	<b>17</b>
<b>Fig. 5.9</b> - Strain measured during the truck test performed by Vendor.	<b>18</b>
<b>Fig. 5.10</b> - True strains from gages S07 – S18 extracted from the raw strains stored during the controlled load truck test. (The values on the vertical axes indicate strains and are expressed in microstrains).	<b>19</b>
<b>Fig. 5.11</b> - (a) Top. Raw and 15-minutes moving average of the temperature data. (b) Center. Raw and 15-minutes moving average of the strain data. (c) Bottom. Live load strain.	<b>20</b>
<b>Fig. 5.12</b> - Raw strain and corresponding moving average recorded by each sensor over the 12 month period.	<b>21</b>
<b>Fig. 5.13</b> - Raw strain vs raw temperature for all the strain gages.	<b>22</b>
<b>Fig. 5.14</b> - Analysis of the strain gages bonded to the truss. (a) Slope of linear interpolation of the strain vs temperature graphs. The values are expressed in $\mu\epsilon/^{\circ}F$ . (b) Residual R2 of the linear interpolation strain vs temperature.	<b>23</b>
<b>Fig. 5.15</b> - Drawings of the east, center and west truss with the members instrumented and the corresponding strain rate expressed in $\mu\epsilon/^{\circ}C$ .	<b>24</b>
<b>Fig. 5.16</b> - Live load strain for computed for all 18 strain gages. The $4\sigma$ interval is overlapped.	<b>25</b>
<b>Fig. 5.17</b> - Value of the $4\sigma$ interval in $\mu\epsilon$ calculated for each strain gages on the truss.	<b>26</b>
<b>Fig. 5.18</b> - Mahalanobis squared distance applied to the strain gage data on the individual trusses.	<b>27</b>
<b>Fig. 6.1</b> - Photos of the three bridges considered in this study. (a) Upstream view of the BMS 55-3014-0050-0509 bridge, for convenience referred here as the Somerset bridge. (b) Cooks Mill Bridge (BMS ID 05-3001-0080-0000). (c) Single span ID 29-2004-0040-0000 bridge over little Tonoloway Creek in Fulton County.	<b>28</b>
<b>Fig. 6.2</b> - Cross section of the (a) Somerset Bridge, (b) Cooks Mill Bridge, and (c) of the Tonoloway Creek Bridge. Units expressed in inches following the shop drawings provided to the authors.	<b>29</b>
<b>Fig. 6.3</b> - Schematics of the location of the strain sensors at the (a) Somerset Bridge, (b) Cooks Mill Bridge, and (c) of the Tonoloway Creek Bridge. The box beams have a skew angle of $30^{\circ}$ .	<b>30</b>
<b>Fig. 6.4</b> - Somerset Bridge. Snapshots from the high-fidelity finite element model (a) overall look; (b) cross section.	<b>31</b>
<b>Fig. 6.5</b> - Cooks Mill Bridge. Snapshots of the low-fidelity model.	<b>31</b>
<b>Fig. 6.6</b> - Details of the configuration and dimension of the test truck (a) Side view; (b) Top view.	<b>32</b>
<b>Fig. 6.7</b> - Truck load test of the Cooks Mill Bridge. (a) Raw strains and (b) corresponding true strains measured by gage 06.	<b>32</b>
<b>Fig. 6.8</b> - Somerset Bridge. Predicted and numerical (under pristine and damage scenario 1) strains when the truck was 1.52 m (5 ft.) away from the north parapet.	<b>33</b>
<b>Fig. 6.9</b> - Somerset Bridge. Predicted and numerical (under pristine and damage scenario 6) strains when the truck was 1.52 m (5 ft.) away from the north parapet.	<b>34</b>
<b>Fig. 6.10</b> The shear keys at the Somerset Bridge that their contacts with the adjacent beams were changed to “No separation”.	<b>34</b>
<b>Fig. 6.11</b> - Somerset Bridge. Predicted and numerical (under pristine and damage scenario 6) strains when the truck was 4.57 m (15 ft.) away from the north parapet.	<b>35</b>
<b>Fig. 6.12</b> - Cooks Mill Bridge analysis. Comparison of the experimental and numerical data. (a) Use of low-fidelity finite element models with the truck 1.52 m (5 ft.) away from the north parapet. (b) Same load scenario as in (a) but using EFEM. (c) Same as (b) but the truck at truck 4.57 m (15 ft.) away from the north parapet.	<b>36</b>
<b>Fig. 6.13</b> - (a) The shear keys that their contacts with the adjacent beams were changed to “No separation”.	<b>37</b>
<b>Fig. 6.14</b> - Raw strain and corresponding 15-minutes average recorded by sensor 05 mounted on the (a)	<b>38</b>

Somerset Bridge, (b) Cooks Mill Bridge, and (c) Tonolaway Bridge.	
<b>Fig. 6.15</b> - Cooks Mill Bridge. Raw strain vs raw temperature measured by gage 05..	<b>39</b>
<b>Fig. 6.16</b> - Cooks Mill Bridge. Slope of linear regression of the strain vs temperature graphs (the values are expressed in $\mu\epsilon/^\circ\text{F}$ ) and Residual R2 of the linear interpolation strain vs temperature. S01-S10 were bolted to the first span and S21-S30 were bolted to the second span.	<b>39</b>
<b>Fig. 6.17</b> - Somerset Bridge. Slope of linear regression of the strain vs temperature graphs (the values are expressed in $\mu\epsilon/^\circ\text{F}$ ) and Residual R2 of the linear interpolation strain vs temperature. S01-S10 were bolted to the first span and S21-S30 were bolted to the second span.	<b>40</b>
<b>Fig. 6.18</b> - Cooks Mill Bridge. True strain calculated as the difference between the raw strain and the moving averaged strain.	<b>41</b>
<b>Fig. 6.19</b> - Cooks Mill Bridge. Histogram chart relative to the true cleaned strain of gage S05.	<b>41</b>
<b>Fig. 6.20</b> - Values of the $\pm 4$ standard deviation range of the true clean strain calculated for (a, b) – the Somerset Bridge and (c) - the Cooks Mill Bridge.	<b>42</b>
<b>Fig. 6.21</b> - Mahalanobis squared distance applied to the live strains from gages (a)-1 to 10 and (b)- 21 to 30.	<b>43</b>
<b>Fig. 6.22</b> - Mahalanobis squared distance applied to the live strains from all ten strain gages on the Cooks Mill bridge.	<b>44</b>
<b>Fig. 7.1</b> - Photos of the (a) Birmingham Bridge. (Figures adapted from <a href="https://www.flickr.com/photos/jag9889/10148146816">https://www.flickr.com/photos/jag9889/10148146816</a> ) (b) Glassport-Clairton Bridge. (c) Chester Bridge. (Upstream elevation looking downstream and deck underside and superstructure. Figure adapted from the 2015 bridge inspection report).	<b>45</b>
<b>Fig. 7.2</b> - Instrumentation plan of the Birmingham Bridge.	<b>46</b>
<b>Fig. 7.3</b> - Instrumentation plan of the Clairton Bridge.	<b>47</b>
<b>Fig. 7.4</b> - Instrumentation plan and meaning of the Chester Bridge.	<b>48</b>
<b>Fig. 7.5</b> - Snapshots of the digital replicas of the three bridges considered in this study.	<b>49</b>
<b>Fig. 7.6</b> - Clairton Bridge analysis. Load Case 2: A truck load was applied in the middle of Span 13 in South bound direction.	<b>49</b>
<b>Fig. 7.7</b> - Representative result of the truck load test on the Birmingham Bridge. Values recorded by gage FB01-WEST-IN.	<b>50</b>
<b>Fig. 7.8</b> - The changed contacts of the third stringers for damage scenario 3.	<b>50</b>
<b>Fig. 7.9</b> - Load transfer mechanism between stringer 3 and FB19 under pristine and damage scenario 3.	<b>51</b>
<b>Fig. 7.10</b> - Clairton Bridge modeling. Damage scenario 5: side view and 3D view from the end of the West girder.	<b>51</b>
<b>Fig. 7.11</b> - The added rectangular plate to the location of the fifth damage scenario.	<b>51</b>
<b>Fig. 7.12</b> - Chester Bridge truck testing. Raw strains recorded by the sensors bonded to girder 3 (left column), girder 4 (middle column), and girder 5 (right column). From top to bottom the sensors were those bonded to the top flange, web, and the bottom flange.	<b>52</b>
<b>Fig. 7.13</b> - Representative result of the truck load test on the Chester Bridge. True strains.	<b>53</b>
<b>Fig. 7.14</b> - The predicted strains at certain locations of the bridge for the sixth damage scenario. (a) to (d) refer to Experiment 1, and (e) to (h) to Experiment 2. In Exp. 1 and 2, the truck travelled over the bridge northbound and southbound, respectively. For (a), (b), (e), and (f), the truck is at the middle of the first span and for (c), (d), (g) and (h) is at the middle of the second span. The field data were extracted from the graphs published by the Company executing the test in the report provided to the authors by the project sponsor.	<b>54</b>
<b>Fig. 7.15</b> - Raw and moving averaged strain recorded through January 31st 2021, Birmingham Bridge.	<b>55</b>
<b>Fig. 7.16</b> - Raw and moving averaged strain recorded through February 28th 2021, Clairton Bridge.	<b>55</b>
<b>Fig. 7.17</b> - Birmingham Bridge. Raw strain vs raw temperature recorded by gage FB00-WEST-IN along the	<b>56</b>

yy direction. The period observation lasted until January 31st 2021.	
<b>Fig. 7.18</b> - Birmingham Bridge. Slope of linear regression of the strain vs temperature graphs (the values are expressed in $\mu\epsilon/^\circ\text{F}$ ) and residual $R^2$ of the linear interpolation strain vs temperature.	<b>57</b>
<b>Fig. 7.19</b> - Clairton Bridge. Slope of linear regression of the strain vs temperature graphs (the values are expressed in $\mu\epsilon/^\circ\text{F}$ ) and residual $R^2$ of the linear strain vs temperature.	<b>58</b>
<b>Fig. 7.20</b> - (a) Slope of linear interpolation of the strain vs temperature graphs. The values are expressed in $\mu\epsilon/^\circ\text{F}$ . (b) Residual $R^2$ of the linear interpolation strain vs temperature.	<b>59</b>
<b>Fig. 7.21</b> - Birmingham Bridge. Time – histories of the calculated true strains from the rosette FB01- EAST-OUT.	<b>60</b>
<b>Fig. 7.22</b> - Birmingham Bridge. $4\pm s$ interval associated with the cleansed true strains.	<b>61</b>
<b>Fig. 7.23</b> - Value of the $\pm 4\sigma$ interval in $\mu\epsilon$ calculated for each strain gages. Chester Bridge.	<b>62</b>
<b>Fig. 7.24</b> - Outlier Analysis: XX-direction strains. Mahalanobis Squared Distance calculated during the whole monitoring period and during the truck test.	<b>63</b>
<b>Fig. 7.25</b> - Mahalanobis squared distance applied to the whole monitoring period. Top row: top flange. Middle row: web. Bottom row: Bottom flange. The threshold was computed by considering the data from the first month of operation without the truck test.	<b>64</b>
<b>Fig. 8.1</b> - Cable gauges used for data comparison.	<b>65</b>
<b>Fig. 8.2</b> - The location of the removed cable for damage scenario 3.	<b>65</b>
<b>Fig. 8.3</b> - The location of the removed diagonal members for damage scenario 4.	<b>66</b>
<b>Fig. 8.4</b> - The location of the damaged floorbeam in damage scenario 5.	<b>66</b>
<b>Fig. 9.1</b> - Location of the structural members and some of the installed sensors on the bridge. The letter S means strain gage, the letters RR indicates resistance strain gage, FB means floorbeam, W indicates web, LT stands for left truss, and TP for top.	<b>67</b>
<b>Fig. 9.2</b> - Removed cables from the East and West arches of the bridge (highlighted in pink)..	<b>68</b>
<b>Fig. 9.3</b> - The factors affecting the predicted strain values under damage scenario 3 condition.	<b>68</b>
<b>Fig. 9.4</b> - Simulation of the 0.1 in corrosion in the East tie-girder.	<b>69</b>
<b>Fig. 9.5</b> - The justification of the predicted strains under damage scenario 4 condition.	<b>69</b>
<b>Fig. 9.6</b> - Scheme of the damage scenario 5.	<b>70</b>
<b>Fig. 9.7</b> - The justification of the predicted strains under damage scenario 6.	<b>70</b>
<b>Fig. 10.1</b> - PITCH. Raw values and corresponding moving average associated with all 8 inclinometers.	<b>71</b>
<b>Fig. 10.2</b> - ROLL. Raw values and corresponding moving average associated with all 8 inclinometers.	<b>72</b>
<b>Fig. 10.3</b> - TILT X. Raw values and corresponding moving average associated with all 8 inclinometers.	<b>73</b>
<b>Fig. 10.4</b> - TILT Y. Raw values and corresponding moving average associated with all 8 inclinometers.	<b>74</b>
<b>Fig. 10.5</b> - TILT Z. Raw values and corresponding moving average associated with all 8 inclinometers.	<b>75</b>
<b>Fig. 10.6</b> - Raw temperature from the 42 strain gages.	<b>76</b>
<b>Fig. 10.7</b> - PITCH. Raw pitch vs temperature.	<b>77</b>
<b>Fig. 10.8</b> - PITCH. True pitch during the monitoring period.	<b>78</b>
<b>Fig. 10.9</b> - TILT-Y. True tilt-Y during the monitoring period.	<b>79</b>
<b>Fig. 10.10</b> - Mahalanobis squared distance applied to the pitch and the roll data.	<b>80</b>
<b>Fig. 10.11</b> - Mahalanobis squared distance applied to the Tilt data.	<b>81</b>
<b>Fig. 11.1</b> - Readings from the low-resolution tiltmeters installed on the Smithfield Street Bridge. The plots on	<b>82</b>

the left column refer to the gages installed on the north portal of Span 3 (closer to downtown). The plots on the right column refer to the gages installed on the south portal of Span 4 (closer to Southside / Station square).

**Fig. 11.2** - Readings from the hi-res tiltmeters installed on the Smithfield Street Bridge. The plots on the left column refer to the gages installed on the north portal of Span 3 (closer to downtown). The plots on the right column refer to the gages installed on the south portal of Span 4 (closer to Southside / Station square).

**83**



## LIST OF TABLES

<b>Table 1.1</b> - Bridges under the PennDOT pilot bridge instrumentation program (P2BIP) and typology.	1
<b>Table 2.1</b> - Bridges in the United States instrumented with sensing systems prior to 2011 according to Table 1.1 of Xu and Xia (2011).	2
<b>Table 2.2</b> - Bridges in the United States instrumented with sensing systems prior/after 2011 and not included in Table 2.1.	3
<b>Table 3.1</b> - Planned performance of the SHM system.	8
<b>Table 3.2</b> - Expected and actual duration of the sensing system.	9
<b>Table 3.3</b> - Expected and effective number of gages of the SHM system installed on each bridge.	9
<b>Table 5.1</b> - Total cross-section area of each element of the three trusses.	10
<b>Table 5.2</b> - Position of the rear axle of the truck from Pier 3 and corresponding strain on the diagonal member. The distances are expressed in m. (in.). Forces are expressed in kN (kip).	10
<b>Table 5.3</b> - Position of the rear axle of the truck from Pier 4 and corresponding strain on the diagonal member. The distances are expressed in m. (in.). Forces are expressed in kN (kip).	10
<b>Table 5.4</b> - Numerical maximum strain at the two control diagonal members of the Span 4 center truss as a result of the presence of a single truck. Values expressed in $\mu\epsilon$ .	11
<b>Table 5.5</b> - Predicted numerical response of the bridge element close to the south portal of Span 4 under the action of two simulated extreme load events. Values expressed in $\mu\epsilon$ . The colored cells cluster the top chords, the bottom chords, and the diagonal members	11
<b>Table 6.1</b> - Properties of the concrete and steel components used in the finite element models.	12
<b>Table 6.2a</b> - Damage Scenarios simulated in the study presented in this paper. (Somerset Bridge).	13
<b>Table 6.2b</b> - Damage Scenarios simulated in the study presented in this paper. (Cooks Mill Bridge).	13
<b>Table 6.2c</b> - Damage Scenarios simulated in the study presented in this paper. (Tonoloway Bridge).	13
<b>Table 7.1</b> - Properties of the concrete and steel components used in the finite element models.	14
<b>Table 7.2a</b> - Damage scenarios simulated for the Birmingham Bridge.	14
<b>Table 7.2b</b> - Damage scenarios simulated for the Clairton Bridge.	14
<b>Table 7.2c</b> - Damage scenarios simulated for the Chester Bridge.	14
<b>Table 7.3a</b> - Birmingham Bridge. The predicted strains at certain locations of the bridge for the <u>third damage scenario</u> . The measured data refers to the <u>north bound</u> crossing of the truck along the bike lane. (Two crossings were completed).	15
<b>Table 7.3b</b> - Birmingham Bridge. The predicted strains at certain locations of the bridge for the <u>third damage scenario</u> . The measured data refers to the <u>south bound</u> crossing of the truck along the right lane. (Two crossings were completed).	15
<b>Table 7.4</b> - Clairton Bridge. The predicted strains at certain locations of the bridge under damage scenario 5 and Load Case 2.	15
<b>Table 7.5</b> - Chester Bridge. Predicted strains at certain locations under damage scenario 4. (Test 5)	16
<b>Table 7.6</b> - Chester Bridge. Predicted strains at certain locations under damage scenario 5. (Test 5)	17

<b>Table 8.1</b> - The experimental and numerical tension (axial) forces (kips) at specific locations of the bridge for damage scenario 1. The “Diff.” column quantifies the difference between the numerical tension forces under pristine and damaged conditions.	<b>18</b>
<b>Table 8.2</b> - The experimental and numerical tension (axial) forces (kips) at specific locations of the bridge for damage scenario 2.	<b>18</b>
<b>Table 8.3</b> - The experimental and numerical tension (axial) forces (kips) at specific locations of the bridge for damage scenario 3.	<b>18</b>
<b>Table 8.4</b> - The experimental and numerical tension (axial) forces (kips) at specific locations of the bridge for damage scenario 4.	<b>19</b>
<b>Table 8.5</b> - The experimental and numerical tension (axial) forces (kips) at specific locations of the bridge for damage scenario 5.	<b>19</b>
<b>Table 9.1</b> - The experimental and numerical strains ( $\mu\epsilon$ ) at specific locations of the bridge for damage scenario 1 (Tests 5 and 6).	<b>20</b>
<b>Table 9.2</b> - The experimental and numerical strains ( $\mu\epsilon$ ) at specific locations of the bridge for damage scenario 1 (Tests 9 and 10)	<b>20</b>
<b>Table 9.3</b> - The experimental and numerical strains ( $\mu\epsilon$ ) at specific locations of the bridge for damage scenario 2 (Tests 5 and 6)	<b>21</b>
<b>Table 9.4</b> - The experimental and numerical strains ( $\mu\epsilon$ ) at specific locations of the bridge for damage scenario 2 (Tests 9 and 10)	<b>21</b>
<b>Table 9.5</b> - The experimental and numerical strains ( $\mu\epsilon$ ) at specific locations of the bridge for damage scenario 3 (Tests 5 and 6)	<b>22</b>
<b>Table 9.6</b> - The experimental and numerical strains ( $\mu\epsilon$ ) at specific locations of the bridge for damage scenario 3 (Tests 9 and 10)	<b>22</b>
<b>Table 9.7</b> - The experimental and numerical strains ( $\mu\epsilon$ ) at specific locations of the bridge for damage scenario 4 (Tests 5 and 6)	<b>23</b>
<b>Table 9.8</b> - The experimental and numerical strains ( $\mu\epsilon$ ) at specific locations of the bridge for damage scenario 4 (Tests 9 and 10)	<b>23</b>
<b>Table 9.9</b> - The experimental and numerical strains ( $\mu\epsilon$ ) at specific locations of the bridge for damage scenario 5 (Tests 5 and 6)	<b>24</b>
<b>Table 9.10</b> - The experimental and numerical strains ( $\mu\epsilon$ ) at specific locations of the bridge for damage scenario 5 (Tests 9 and 10)	<b>24</b>
<b>Table 9.11</b> - The experimental and numerical strains ( $\mu\epsilon$ ) at specific locations of the bridge for damage scenario 6 (Tests 5 and 6)	<b>25</b>
<b>Table 9.12</b> - The experimental and numerical strains ( $\mu\epsilon$ ) at specific locations of the bridge for damage scenario 6 (Tests 9 and 10)	<b>25</b>
<b>Table 10.1</b> - Data analysis of the raw data as a function of the corresponding raw temperature	<b>26</b>
<b>Table 11.1</b> - Details about which and when some sensors failed.	<b>27</b>
<b>Table 13.1</b> - Summary of the bridge ratings according to inspections reports dated not later than 2020.	<b>30</b>

## PROJECT HIGHLIGHTS

1. Structural health monitoring (SHM) for bridges is on the rise in many Countries worldwide.
2. There are not many peer-reviewed scientific publications about long-term (2+ years) bridge health monitoring programs in the United States.
3. The most common parameter considered in bridge health monitoring is strain.
4. The PennDOT Pilot Bridge Instrumentation Program consisted of the instrumentation of a SHM system based on wireless sensors on ten bridges.
5. The most numerous sensors used in this PennDOT Program were strain gages, followed by displacement gages, and tiltmeters.
6. The installed SHM systems were active longer than planned.
7. Only a small number of sensors stopped working earlier than expected.
8. In at least three bridges, the readings of most low-resolution tiltmeters were not reliable.
9. Only a very few strain gages drifted.
10. Adhesive-type strain gages did not work well when bonded directly to concrete.
11. The password-protected repository software was easy to navigate and use.
12. The software allows any authorized user to download the data in order to develop own processing strategies. This is pivotal to implement smart strategies that separate the effect of thermal stress to the effect of transient loads and damage, and identify structural anomalies.
13. High-fidelity finite element models of the superstructures were created using a commercial finite element software and then validated with the experimental data extracted from controlled truck load test.
14. For some bridges, low-fidelity finite element models were created.
15. The high-fidelity models were used to identify the cause of anomalous data readings in some bridges.
16. The high-fidelity models were used and can be used to predict the response of the structures under any mechanical loading and under any damage scenario.
17. The low-fidelity models provided approximate results in most cases.
18. Thermal-related strain and displacement dominate the long-term performance of the monitored structures. Effective processing strategies were developed to isolate and separate thermal-related effects from other factors.
19. The interpretation of data anomalies or discrepancies between the numerical predictions and the experimental observation was not corroborated by field visits by the Investigators.
20. When validated by adequate sensing data, the high-fidelity finite element models may be used to compare the numerical loads to the analyses conducted for bridge posting.
21. A few amendments to Ch. 8 of Pub 238 are warranted, based on the experience gained through this project.
22. Future studies related to bridge health monitoring shall survey the current state-of-the-art technology commercially available, and include thermal effect in the modeling.

## EXECUTIVE SUMMARY

A few years ago, the Pennsylvania Department of Transportation implemented a bridge monitoring program for ten bridges.

The present document summarizes the key finding of a research project related to that program. The scope of the project was to investigate advanced data management, analysis, mining and inference approaches for bridge health monitoring, safety evaluation, reliability, and resilience assessment of those ten bridges. The project tasks included:

- (1) a systematic review of other bridge health monitoring programs in the United States over the last 25 years;
- (2) the creation of a finite element model of nine of the ten bridges;
- (3) the use of these models to predict the static response of original and simulated damaged bridges to concentrated loads that mimic the presence of trucks;
- (4) the comparison of these calculate responses to the field measurements retrieved by the Investigators from a password-protected repository or from documents made available to them;
- (5) the development of a long-term monitoring strategy for bridges;
- (6) an evaluation of the ability and reliability of the wireless sensing systems installed in the ten bridges at providing relevant data to fully characterize the in-service behavior of the structures.

The findings presented in this report indicate that the structural health monitoring (SHM) systems installed on those bridges operated reliably and accurately with little data losses and with a very few sensor failures. The data, while not identifying any critical occurrence that compromise the safety of the bridge, did reveal some unexpected behavior for some bridges that could not be possibly identified with conventional visual inspection. This includes the crossing of heavy trucks beyond posted limits. Another relevant finding of the project is that the numerical predictions obtained with the high-fidelity finite element models created for most bridges match well with the field data outputs from the sensor array under truckload conditions. These models were also instrumental for the diagnosis of some of the structural anomalies identified with the sensor arrays. The simplified models, which included the extensive use of line elements instead of solid body elements, yielded to discrepancy between numerical predictions and experimental measurements. Among all the sensing systems evaluated in the project the low resolution tiltmeters did not perform as expected showing significant signs of drift. Adhesive tape strain gages bonded to concrete materials were also a source of concern in terms of reliability.

Finally, the findings of the project were used to update a specific section of the PennDOT Bridge Inspection Policy and Procedures Manual, Publication 238, and to provide some recommendations for future applications/programs.

## 1. INTRODUCTION

According to the Federal Highway Administration (FHWA) (Federal Highway Administration 2019a), there are over 600,000 (616,096) highway bridges<sup>1</sup> in the United States. Of these, about 46% is rated in good condition, 46.4% is rated as fair, and the remaining is rated as poor<sup>2</sup> (Federal Highway Administration, 2019b). With more than 25,000 state-owned bridges, Pennsylvania has the third-largest number of bridges in the U.S., with an average age of 50+ years. Nationwide, the performance evaluation of bridges starts with the inspection of the bridge to determine the current condition. Inspections are conducted in a variety of ways, but they are all completed in accordance with the National Bridge Inspection Standards (NBIS). According to NBIS, bridges must be inspected at least every two years while some bridges that have shown problematic areas may be inspected more frequently at the discretion of the owner. Any structure with a span equal to 20' (6 m) and greater needs to be rated on a scale 0 to 9 for National Bridge Inventory (NBI), where 9 is for a new bridge and 0 is for bridges being out of service.

As conventional non-destructive evaluation (NDE) can do little when flaws become critical between two consecutive inspections, there is an interest for cost-effective structural health monitoring (SHM) for bridges. SHM is the scientific process of identifying damage in a given structure of interest using a non-invasive network of sensors embedded or bonded to that structure. SHM evolves the inspection paradigm from “time-based” NDE in which a structure is inspected periodically, to permanent-based where the sensors monitor the structure in real-time in order to flag, locate, and quantify damage as it happens.

A few years ago, the Pennsylvania Department of Transportation (PennDOT) started the pilot bridge instrumentation program. The program consisted of instrumenting ten bridges during the period 2017-2019 with a commercial system (hardware and software) from a Company, hereinafter referred to with the term Vendor. The ten bridges are listed in **Table 1.1** and localized in the map of **Fig. 1.1**. Part of the hardware consisted of wireless sensors that provided real-time information about structural static and dynamic responses. Within that program, PennDOT intended to determine an assessment of the cost of components/equipment, system software, and labor to monitor the identified bridges and/or any or all bridges throughout the Commonwealth, versus the savings to PennDOT for a reduction in man hours and/or a reduction in spending to effectively manage and maintain the bridges. The bridges were monitored during various timeframes and some of them are still being monitored with the purpose of effectively assessing the benefit of the instrumentation and monitoring of the bridges and the cost to monitor the bridges.

This document presents the main findings of a project that investigated advanced data management, analysis, mining and inference approaches for bridge health monitoring, safety evaluation, reliability and resilience assessment of the ten instrumented bridges. The project consisted of the following eight tasks.

Task 1: Literature Review – Conduct a literature review of current practice in using bridge instrumentation for structural health monitoring, reliability and resilience assessment.

Task 2: Review of Structures – Examine the ten structures in the PennDOT pilot bridge instrumentation program using as-built drawings, instrumentation plans, inspection reports, approved instrumentation reports and load test report. The documents were provided by PennDOT.

---

<sup>1</sup> **Highway Bridge:** A public vehicular structure more than 6.1 meters (20 feet) in length that spans an obstruction or depression. In data terms, all of the following apply: Item 5a=1; Item 49>=6.1 meters; Item 112=Y; and Item 42a=1 or 4 or 5 or 6 or 7 or 8 (Federal Highway Administration, (2019b)).

<sup>2</sup> **Good (G), Fair (F), Poor(P):** These terms are defined in accordance with the [Pavement and Bridge Condition Performance Measures final rule](#), published in January of 2017. Bridge Condition is determined by the lowest rating of National Bridge Inventory (NBI) condition ratings for Item 58 (Deck), Item 59 (Superstructure), Item 60 (Substructure), or Item 62 (Culvert). If the lowest rating is greater than or equal to 7, the bridge is classified as Good; if it is less than or equal to 4, the classification is Poor. Bridges rated 5 or 6 are classified as Fair (Federal Highway Administration 2019b).

Task 3: Evaluation of Recorded Data – Extract the data recorded during test-load events, representative service load events and, if available, extreme load events. The data were extracted from a password-protected repository.

Task 4: Model Development – Develop numerical models to assist in validation of the recorded data.

Task 5: Comparison of Recorded Data and Numerical Analyses – Compare the recorded structural responses (e.g. strains, displacements and rotations, and etc.) to the numerically generated results.

Task 6: Damage/Deterioration and Repair Scenarios - Evaluate damage, deterioration and subsequent repair scenarios using either high-fidelity models or lower-fidelity line-element models.

Task 7: Findings/Recommendations – Provides findings and recommendations relative to the PennDOT bridge instrumentation program.

Task 8: Update of Pub 238 – Propose updates for the PennDOT Publication 238, chapter on Non-destructive Load Testing.

For each task, a report was submitted, and the interested readers are referred to those reports for a comprehensive knowledge of Task-specific outcomes.

For the sake of brevity, this final report presents the main findings and is organized as follows:

**Chapter 2** summarizes the outcomes of Task 1 and provides very few examples of bridge health monitoring in the United States. Note that besides the Task report, the review resulted in two scientific publications (Rizzo and Enshaeian 2021)

**Chapter 3** lists the Bridges that were included in the bridge pilot program and the characteristics of the proprietary sensing system installed on those bridges.

**Chapter 4** describes the data inference method implemented in this study by the Pitt team.

**Chapter 5** summarizes the results of Tasks 3 thru 6 and relative to the Smithfield Street Bridge, perhaps the most iconic bridge among the ten bridges of the program. It is disclosed here that this chapter is largely extracted from a paper submitted for possible publication.

**Chapter 6** clusters the results relative to the three prestressed concrete box beams bridges of the program. It is disclosed here that this chapter is largely extracted from a paper submitted for possible publication.

**Chapter 7** summarizes the results of Tasks 3 thru 6 and relative to the Birmingham Bridge, the Clairton-Glassport Bridge, and the Chester Bridge. These bridges have in common the fact that they were modeled using high-fidelity models. It is disclosed here that this chapter is largely extracted from a paper submitted for possible publication.

**Chapters 8 – 10** summarize the results of Tasks 3 thru 6 relative to the Elizabeth, Neville Island, and the Sanatoga Bridge, respectively, which were instead modeled with a low-fidelity finite element model.

**Chapter 11** provides an overall evaluation of the sensing system installed on the bridges based on what observed in the empirical values and based on the comparative analysis with the numerical models.

**Chapter 12** represents the suggested amended section of Pub 238.

**Chapter 13** ends the reports with some concluding remarks and a list of suggestions for possible future research studies or future bridge health monitoring programs.

An **Appendix** provides some suggestions for future studies.

## 2. BRIDGE HEALTH MONITORING IN THE U.S.: A REVIEW

The main goals of the review were:

- (1) listing State and Federal bridge instrumentation programs;
- (2) identifying and classifying the different data inference methods developed to evaluate short-term damages and long-term degradations associated with specific anomalies such as fatigue cracks and scour;
- (3) evaluating and recommending generic technical requirements for future bridge HM;
- (4) assessing the data validation techniques in terms of accuracy of recorded data and sensors drift.

The information considered for inclusion was based on peer-reviewed documents and/or technical reports available in the scientific literature and accessible to the public. Whenever possible and compatible to the amount of information found in the literature, Task 1 included a discussion on data management, analysis, mining and inference approaches to access reliable safety evaluation, resilience assessment and future life prediction of bridges. In bridge SHM, sensors are used to monitor external loading (wind, seismic, and traffic), structural responses (strain, displacement, and acceleration), environmental parameters (temperature, humidity, and rain), and chemical attacks (corrosion). The array of sensors is connected to dedicated hardware/software that elaborates the set of time series streamed from the sensors, in order to infer properly the health of the component being monitored, and the response of the structure to given loads.

One of the challenges associated with the SHM of bridges is related with the fact that these structures have very little in common with each other and almost any new bridge is unique. This implies that a uniform SHM paradigm valid for a bridge may not be adequate for another (Sharyatpanahi 2015). This complication also arises when structures are to be modeled and damage is simulated numerically but cannot be validated experimentally. Material wise, bridges are mainly designed using concrete, steel or timber. Each of these materials has special characteristic that determine which types of defects inspectors or SHM systems have to monitor. According to Alhborn et al. (2010), 64.3% of the bridges are made of concrete, 30.9% are steel bridges, about 4.2% are timber bridges, and 0.3% are masonry bridges.

This chapter is organized in the following sub-sections.

- Chapter 2.1 provides a list of active and past instrumentation programs devoted to bridge HM, and describes some of these programs. For each bridge a brief synopsis of the implemented instrumentation is given along with the scope and (where available) the monitoring period.
- Chapter 2.2 reviews the work conducted in terms of data inference method.
- Chapter 2.3 discusses the advantages and the challenges associated with the wireless sensing systems used for SHM applications.
- Chapter 2.4 ends this Chapter with some concluding remarks.

### 2.1 SENSING AND A FEW NOTABLE EXAMPLES

**Table 2.1** (excerpted from Xu and Xia 2011) and **Table 2.2** (stemmed from the literature review conducted as part of Task 1) list the U.S. bridges monitored with one or more sensors types. The sensors listed in the note below **Table 2.1** is nearly comprehensive. For the sake of completeness, a brief review of the major sensors is given here and excerpted from (Sharyatpanahi 2015). A more comprehensive discussion of the sensing technologies used in SHM can be found in several review articles, including (Moreno-Gomez et al. 2018).

**Strain** is perhaps the most common parameter measured in a SHM system. Strain sensing technologies have the potential to be very effective for crack detection since crack opening leads to abrupt strain change in the localized area (Li et al. 2019). There are several ways to measure strain in a bridge. They include conventional electrical resistant strain gauges (ERSGs), fiber optics, and vibrating wires.

Ambient temperature and the temperature of structural components, measured for example with **thermocouples** or **thermistors**, are used to evaluate thermal effect on the overall deflection and deformation of bridges. Additionally, excessive thermal stresses can damage bridges (Xu and Xia 2011). It is noted the temperature is usually non-uniformly distributed over the entire structure and is different from the ambient temperature, due to heat transfer. As such, engineers calibrate their models in order to take into account possible temperature gradients.

**Tiltmeters** are sensitive inclinometers designed to measure very small changes from the vertical level, either on the ground or in structures. In bridge SHM, tiltmeters are typically used to indirectly infer the presence of scour, which is the engineering term for the erosion of soil surrounding a bridge foundation (piers and abutments). Bridge scour occurs when fast-moving water around a bridge removes sediment from around the bridge foundation, leaving behind scour holes. These holes, in turn, can greatly compromise the bridge's integrity (Orsak 2019).

**Accelerometers** are used to quantify the dynamic response of a given structure to ambient or forced excitations. Vibration-based SHM uses dynamic response measurements under the premise that they contain information about the dynamic properties of a system, which can be subsequently mapped to structural damage and integrity measures.

The measurement of the displacement can be acquired using directly linear variable differential transducers (LVDTs), or indirectly by double integration of accelerometer time-series data. If accelerometer-based systems are used, the accelerometers must be strategically deployed at specific locations to facilitate real-time measurement of the actual structural response and eventually to determine the mode-shapes of the vibrations. Each approach has advantages and limitations. LVDTs are perhaps the most common **displacement sensor**; they consist of a hollow metallic casing in which a shaft, called the core, moves freely back and forth along the axis of measurement. The core is made of a magnetically conductive material, and a coil assembly surrounds the metallic shaft (Dong et al. 2010). For structures with long-period responses ( $T > 1$  sec.), such as tall buildings and bridges, direct displacement measurements can be obtained using GPS, for instance by placing GPS receivers at the roof.

**Seismometers** measure ground motions including those generated by earthquakes. For short-period seismometers, the inertial force produced by a seismic ground motion deflects the mass from its equilibrium position, and the displacement or velocity of the mass is then converted into an electric signal as the output proportional to the seismic ground motion. Broadband seismometers are built according to the force-balanced principle, in which the inertial force is compensated with an electrically generated force so that the mass moves as little as possible.

**Table 2.2** was compiled to our best knowledge and contained information found up to Spring 2020. The exclusion of any relevant monitoring programs was not intentional. Owing to the scope of this document, the description of the over 60 monitoring programs listed in **Tables 2.1** and **2.2** cannot be reported here. The interested readers may request a copy of Task 1 report to the Authors or to PennDOT, or are referred to Rizzo and Enshaeian (2021). In what follows, just a few cases are presented.



Owing to its location, the **Sunshine Skyway Bridge** is vulnerable to high open channel winds. The bridge was instrumented with multiple sensor types, including five (5) global positioning systems (GPS), distributed throughout the structure providing real-time measurements on wind velocity and direction, concrete temperature, and overall bridge position. Weather stations were installed at the mid-span and

South locations and additional automatic total stations were deployed on select concrete impact barriers (Agdas et al. 2015). Periodic vibration measurements were performed on stay cables to provide cable tension estimates. Some sensor data were also used to calibrate an interactive finite element model (FEM) predicting the movement of the bridge as a function of temperature and wind variances. According to Agdas et al. (2015), the objective of the FEM was to obtain “*predictions that can be used to determine bridge response thresholds allowing for sensor alarm systems to be adjusted accordingly*”. This can be said of any finite element analysis applied on any bridge.

An article by Schenewerk et al. (2006) described the use of the GPS on the **Sunshine Skyway Bridge**. GPS receivers were placed at the top of the two (2) bridge towers and at the midpoint of the center span; a fixed GPS reference site was established on the shore several miles away. Data from all four sites were collected at 1 Hz rate. The findings from six (6) months of data indicated that the positions of autonomous sites located on a bridge can be measured automatically using GPS in near real-time, with centimeter-level accuracies. Fifteen-minute measurements provide sufficient accuracy to reveal a complex variety of motions at each point monitored on the bridge. The GPS data were used to refine a simple numerical model aimed at predicting the motion of the bridge under a variety of environmental conditions. Another remote sensing, more NDE-like kind of approach, for the Bridge is based on laser sensing in which a laser is used to detect the vibration of the cables and infer the force and the damping of the cables. Damping measurements are used to evaluate the contribution of external damping devices and to ensure proper functioning of the dampers and adequacy of the overall damping for suppression of wind-induced vibration (Mehrabi and Farhangdoust 2018).



The I-35W **St. Anthony Falls Bridge** is a concrete post-tensioned box girder bridge located in Minneapolis and opened to traffic in September 2008. It was constructed as two (2) separate post-tensioned concrete box girder bridges built adjacent to each other. Each bridge consists of four (4) spans numbered in ascending order from south to north. Spans 1 through 3 are continuous, and Span 4 is separated from the rest of the structure by an expansion joint at Pier 4 (French et al. 2014).

The bridge was instrumented with more than 500 sensors of different types in order to conduct a long-term monitoring of the bridge structural behavior (French et al. 2012, 2014, Hedegaard et al. 2013). Parameters such as deformations, temperature, vibrations, expansion, and corrosion were monitored. Structural deformations were measured by a number of different instruments, including 198 vibrating-wire strain gauges, 24 resistive strain gauges, and 12 fiber-optic strain gauges. Temperatures in the bridge were measured by 246 thermistors some of which integrated into the vibrating-wire strain gauges. Twenty-six (26) accelerometers were deployed to measure vibrations while 12 linear potentiometers were located at the expansion joints to measure the overall expansion and contraction of the bridge. Electrochemical activity and concrete resistivity was also monitored to identify corrosion. For a detailed account of the location of the sensors, the interested readers are referred to Tables 2.1 and 2.2 of (French et al. 2014).

Along with the installation of the sensors, linear elastic FEM models in ABAQUS were constructed and validated using truck-load tests (Hedegaard et al. 2013). Local bending in the top flange had a large effect on how measured data compared with the computed results. Computed results revealed that the strain profile at the centerline of the boxes was nonlinear for loadings directly above and also slightly offset from the instrumentation. Overall, the numerical results model compared well with respect to the truck test data. One of the recommendations following the study was the use of additional instrumentation such as inclinometers, near the bearings in order to quantifying restraint caused by the bearings. The data were used to validate a FEM model to assist further bridge behaviors evaluation.

French et al. (2014) investigated the time-dependent and temperature-dependent behavior of the bridge. This time-dependency involves creep, which is the continued deformation of concrete under

sustained load, and shrinkage, which is the reduction in volume due to moisture loss. Both may cause excessive loss of post-tensioning leading to possible concrete cracking or large deflections that can impair the serviceability of the structure. They used a combination of laboratory creep and shrinkage tests, in situ monitoring of longitudinal deflections and strains using the first five (5) years of bridge operation, and finite element modeling.

It is noted here that the monitoring programs conducted on this bridge has been perhaps one of the most comprehensive SHM programs in the U.S. The interested readers are referred to (Dalia et al. 2018; Inaudi et al. 2009; French et al. 2012, 2014; Hedeegard et al. 2013, 2017a, 2017b; Gaebler et al. 2018).



The 1056 m long **New Carquinez Bridge**, officially named the **Alfred Zampa Memorial Bridge** is a suspension bridge with a main span of 730 m. A permanent seismic monitoring system was installed on the New Carquinez Bridge by the California Strong Motion Instrumentation Program in 2004. The system includes 76 sensors on the suspension bridge, 27 sensors on the approach (Nagarajaiah and Erazo 2016), and 1 anemometer. The 76 force balance accelerometers were distributed along the main span, towers, and foundations and the anemometer and all wired to a central data-acquisition system (Zhang et al. 2017). The wired monitoring system is operated based on triggering from ground motions but manual data collection is possible.

A separate wireless structural monitoring system was installed in 2010 with iterations to the monitoring system configuration occurring between 2010 and 2011 (Kurata et al. 2013). The wireless monitoring system is designed to collect data on a regular basis (e.g., schedule-based) but is not designed to be triggered based on motion. The wireless monitoring system was designed based on the Narada wireless sensor platform developed at the University of Michigan (Swartz et al. 2010). Narada supports data acquisition on four (4) sensing channels with a 16-bit analog-to-digital conversion resolution. The long-term wireless structural monitoring system was designed to record bridge responses (i.e., strains, displacements, and accelerations) and environmental conditions (i.e., temperature, wind speed, and wind direction). For the **Alfred Zampa Memorial Bridge**, 35 sensor nodes collecting data from 76 sensing channels were installed. To measure the vertical and transverse motion of the orthotropic steel deck, 19 triaxial accelerometers were installed along the length of the deck. At the top of each tower, two tri-axial accelerometers measuring one vertical, one transverse, and two longitudinal degrees-of-freedom were also installed. To measure strain of the orthotropic steel deck, metal foil strain gauges were mounted to the interior surface of the box girder at three locations along the span: over the north and south towers and approximately at midspan. At each location, three strain gauges were installed to measure longitudinal strain on the top and bottom girder surfaces and transverse strain on the top surface. For thermal compensation, three thermistors measured the top and bottom girder surface temperatures and ambient internal air temperature of the girder. To capture the longitudinal displacement of the steel orthotropic deck relative to the concrete towers, three string potentiometers were installed: two at the south tower and one at the north tower. In addition, three weather stations were installed each consisting of one anemometer, additional environmental sensors (either a wind vane, thermistor, or humidity sensor). In total, 46 channels of acceleration, 10 channels of strain, 3 channels of displacement, and 17 channels of environmental parameters (wind speed and direction, temperature, and humidity) were installed.

A comprehensive system identification study was carried out under ambient and forced vibration (Conte et al. 2008, He et al. 2009). A set of dynamic field tests was performed just before the bridge opened in November 2003. The tests included ambient vibration tests, mainly wind induced, and forced vibration tests based on controlled traffic loads and vehicle induced impact loads. Four different controlled traffic load patterns and seven (7) different vehicle-induced impact load configurations were used in the forced vibration tests. The dynamic response of the bridge was measured through an array of 34 uniaxial and 10 triaxial force-balanced accelerometers deployed along the whole length of the bridge. In order to extract the modal characteristics of the pristine bridge, namely natural frequencies, damping

ratios, and mode shapes, a few approaches were used: the natural excitation technique - eigensystem realization algorithm (MNEXT-ERA), the stochastic subspace approach (SSI) and the enhanced frequency domain decomposition (EFDD) algorithm. Although the study conducted by Conte et al. (2008) was not about a permanent bridge health monitoring system, its outcomes may be used in the future as baseline for future SHM of this bridge.

Zhang et al. (2017) used the permanent wireless monitoring system and the data generated since 2010 to propose an automated stochastic identification approach for the extraction of bridge modal properties. The study fits logistic distributions to the extracted modal frequencies and modal damping ratios to provide statistical models for these important bridge properties. Low levels of modal damping well below 0.8% are reported for the majority of structural modes. Bridge modal properties exhibit sensitivity to the environmental and operational conditions of the bridge. Ridge regression and Gaussian process regression (GPR) were used to model the dependency of modal frequency on bridge environmental and operational conditions. The analysis conducted by Zhang et al. (2017) using data collected between 01/01/2013 and 12/21/2014, about bridge responses, wind speed and direction, and bridge temperature (daily for 8 min at 20 Hz every 1 or 4 h, depending on energy availability), determined the long-term modal properties of the bridge. A total of 27 operational modes were identified, of which 15 were confirmed to correspond to previously reported structural modes. With accurate estimation of modal frequencies, the median modal frequency and damping ratio of each mode was reported for each data set analyzed. The empirically derived distributions for modal damping revealed that the mode of the distributions for most structural modes were well below 0.8% with many low-order modes less than 0.3%, such as the first, third, and fourth vertical structural modes. These low modal damping ratios confirm that the 0.3% damping ratio used in the design of the Bridge was a reasonable value.



The movable **Sunrise Boulevard Bridge** in the city of Fort Lauderdale in Florida was selected to prove a correlation-based SHM methodology as an effective approach for detecting and localizing structural changes using strain data under operational loading conditions (Catbas et al. 2010, 2012). The methodology is based on tracking correlation coefficients between strain time histories at different locations. The bridge was monitored before, during, and after damage was induced. The algorithm was calibrated first in laboratory tests and then validated in the field. It is shown that structural changes can be detected and located for both the laboratory test structure and the real-life bridge using the variations in the correlation matrices. As the bridge was monitored under different conditions, the effectiveness of the bridge repair was also presented in comparative fashion with respect to undamaged conditions. The selected portion (movable span) of the bridge was the westbound span of two parallel spans on SR-838, crossing a canal in Ft. Lauderdale. This span was constructed in 1989. It has double bascule leaves, with a total length of 35.7 m and a width of 16.3 m, carrying three (3) traffic lanes. The sensor installation consisted of an array of 160 sensors to monitor main girders, floor beams, stringers, live load shoes (LLSs), and span locks (SLs). On a movable bridge, LLSs are the support locations of the main girders in closed position and are one of the critical structural components. Main operational concern of LLS is the loss of contact that makes the shims crucial at these locations. Small gaps due to deterioration of the shims lead the girders to pound on the LLSs, which results in further misalignment, additional stresses, stress redistributions, fatigue damage, and excessive wear (Catbas et al. 2012). Data from the dynamic strain gages (Hitec weldable) at the bottom flanges of the main girders (a total of 12 sensors) were used and sampled at 250 Hz. Three (3) prescheduled time slots (morning and early and late afternoons), corresponding to peak hours of operation, were selected for 5 min. data collection.

Damage was simulated by removing both LLS and SL shims. This approach was selected because some of the most common structural maintenance problems are identified as LLS shim removal and SL shim removal. First, the West South LLS (WS3) shims were removed (Case 1), then the West South SL

(WS1) shims (Case 2), and finally, the shims from LLS and SL of West South side were removed for the combined damage scenario (Case 3).

The analysis proposed for the bridge was based on the premise that the correlations between two sensor signals ideally should be “constant” or “stationary” until a change or damage occurs. The dynamic data from the strain sensor associated with the pristine and the damaged structure are collected (Catbas et al. 2012). The dynamic components for each channel are filtered out for the correlation analysis, and the correlation coefficient of each channel is calculated against all the channels to form the correlation matrix for each data set. The procedure is repeated to obtain the correlation matrices throughout the monitoring period and to create a population of matrices from each data set. Finally, set of matrices are averaged for both undamaged and damaged scenarios and their difference matrix is calculated. Quoting Catbas et al. (2012): “*This difference matrix will show whether there is a change in the correlation coefficients in each cell. After observing the changes in the cells, the whole matrix is used to detect the damage location easily by identifying sensors that have the significant changes*”. As it stands, the method requires the collection of baseline data.

The above concept was applied to the bridge data under pristine conditions, when the three damage cases were induced (Cases 1–3), and after damage was repaired. Then, the difference matrices were obtained for each case. Ten different data sets were collected for the baseline case (pristine conditions). Five data sets were collected for each damage case (Cases 1–3). Afterward, the shims were replaced on the structure, and ten new data sets were collected. All the collections occurred during normal operating traffic, and no special trucks or lane closures were required. Catbas et al. (2012) demonstrated that the correlation of the strain time histories from different sensor locations was effective at detecting anomalies for damaged conditions. The cross-correlations of the strain indicated a level of correlation among different sensor pairs. The correlation analysis reduced the data size to provide useful information from large amounts of data, thus offering an efficient data handling capability. According to the authors of the research, the proposed approach eliminates the need for loading information (magnitude and placement) for strain monitoring applications because the strain time histories were obtained from arbitrary operating traffic conditions. If the correlation was not employed, raw strain data may have led to false negatives/positives since the strain levels depend on the traffic.

## 2.2 DATA INFERENCE METHODS.

This section reviews the data inference methods used to detect time-dependent (creep and shrinkage) and temperature-dependent deformations, fatigue, corrosion, scour, and accidental impacts. They are all considered major factors that contribute to long-term degradation of bridges.

**Time-dependent and temperature-dependent deformations** have been a concern for decades, and a number of models were proposed to make predictions. For concrete structures, time-dependent factors include creep and shrinkage. For the **Streckner Bridge** for example, a model was developed to predict creep and shrinkage. The model was periodically updated using field measurements taken from fiber optics sensors. The accuracy of those existing models are improving as research progresses.

Robertson (2005) presented the results of nine years vertical deflection monitoring data of the **North Halawa Valley Viaduct**. The author found a disagreement between the theoretical design predictions and measured vertical deflections, and proposed an improved creep and shrinkage model, as it was believed that the sensors data were reliable. In support of the improved creep and shrinkage models, numerous laboratory tests were conducted and four existing predictive models were considered: the ACI 209 model, the CEB-90 model, the short-form of Bazant B3, and the Gardner model. A conclusion of the study was that the Bazant B3 model predicts long-term creep best, whereas the Gardner model predicts the long-term shrinkage best. The combination of these two models achieved the agreement of prediction deflection and measured data.

Ghali et al. (2000) investigated both short-term and long-term behavior and performance of the **Confederation Bridge** in Canada. The bridge connects Prince Edward Island to New Brunswick, has 45 main spans; each is 250 m long. The cross section of the bridge is a single box; the width of the deck is 11 m. The depth of the cross section varies from 14.0 m over the piers to 4.5 m at mid-span (Ghali et al. 2000). The study analyzed the time-dependent properties of concrete and compared field measured deflections to predicted deflections. The estimated creep was obtained with the equations from the CEB–FIP MC90 and ACI 209. Ten cylinder creep tests were conducted, by using least square fitting of the measured creep coefficients, a best-fit predictive creep equation was developed. For shrinkage, six (6) cylinders were taken to measure the free shrinkage. Measured shrinkage strain were used to obtain the predictive shrinkage equations. With other material parameters, creep and shrinkage equations were employed to analyze the deflections. After the analyses of long-term deflection, all the analyses were conducted again to induce the variation of temperature during the same time intervals. The result showed that with consideration of temperature effects, the predicted results became closer to the measured ones.

Omenzetter and Brownjohn (2006) processed the data from an active SHM system installed in the Singapore–Malaysia Second Link, also referred to as the Tuas Link. Strain data were modelled using two autoregressive integrated moving average models. The first one is a univariate model that described the signal recorded by a single strain sensor. The other model was a multivariate model, which enabled simultaneous analysis of signals from multiple channels and took into account the correlation among the signals. The method was successfully applied to strains recorded during bridge construction, when structural changes corresponded to known significant events such as tensioning of tendons. Then, the method was used to analyze signals recorded when the bridge was in service. Some significant changes in strain time series and associated models were also revealed and attributed to false positives. As the proposed approach did not use temperature data, the authors argued that some of the observed changes may in fact be caused by abnormal temperature variations and not structural changes.

Understanding and predicting the **fatigue behavior** of bridges are important factors for bridge safety evaluation especially in lieu of aging infrastructures. Any initial fatigue crack may propagate due to increase in traffic tonnage, harsh environment, design errors, and age. Several researchers have proposed different mathematical tools to assess and evaluate bridge fatigue reliability.

Kwon and Frangopol (2010) applied concepts related with fatigue reliability to the **Neville Island Bridge** and the **Birmingham Bridge** in Pennsylvania. Probability density functions were used to estimate equivalent stress ranges based on field monitoring data. In addition, AASHTO S-N curve was used to provide relevant information about structural details. Lognormal, Weibull and Gamma distributions were considered. Rain-flow counting method was used to obtain the stress-range bin histogram from the monitoring data. There were seven steps in total to conduct the assessment of the two Bridges.

Li et al. (2001) developed a methodology for fatigue damage assessment and life prediction of bridge-deck sections of existing bridges using SHM data. A fatigue damage model based on the continuum damage mechanics was developed for evaluating accumulative fatigue damage of existing bridges. A structural model for the fatigue stress analysis of bridge-deck structures was proposed, in which structures were modeled by elastic members and welded connections with possible accumulative damage. The methodology uses strain history data. In order to compare results of fatigue damage and service life prediction evaluated by the continuum damage mechanics, a modified Palmgren–Miner rule is developed for the same fatigue problem.

The **Tsing Ma Bridge** in Hong Kong, the world's 14<sup>th</sup>-longest span suspension bridge and the 2<sup>nd</sup> longest at time of completion was the subject of several studies related with the estimation of fatigue life. The bridge has two decks and carries both road and rail traffic, which also makes it the largest suspension bridge of this type. Chen et al. (2011) proposed a fatigue analysis framework for long-span suspension bridges under multiple loading and applied the framework to the **Tsing Ma Bridge**, using data from the SHM systems instrumented there. Dynamics stress analysis was conducted and maximum stress range was

selected as the index to identify the fatigue-critical locations of bridge components. Database of wind-induced, railway-induced and highway-induced dynamic stress response were established based on the site measurements. A rain-flow counting method was used in the fatigue analysis.

For the same Bridge, Ye et al. (2012) developed a fatigue life assessment method based on strain data and then stress time histories obtained by converting strain data. The rain-flow counting algorithm and statistical analysis were used to identify the standard stress spectrum. Fatigue life was calculated by using S-N curve method and Miner's rule. Ni et al. (2010) proposed a fatigue assessment method to integrate the hot spot stress range, which was based on Miner's damage cumulative rule with continuous probabilistic formulation. In this study, field measured data and stress concentration factors were considered as random variables to develop a probabilistic model for fatigue life evaluation. The stress range from monitoring data was created by using the finite mixture distribution and a hybrid parameter estimation method.

Guo et al. (2012) proposed an approach to evaluate the time-dependent fatigue reliability of steel bridges with traffic load model and probabilistic finite element analysis. In this study, equivalent stress range was obtained by integrating collected weigh-in-motion data and finite element analyzing under uncertainties. By regression analysis, the most appropriate probabilistic distribution of equivalent stress range was determined.

The **corrosion of metallic parts** such as cables, reinforcements, connections, or girders is almost unavoidable and may cause significant degradation. The monitoring of corrosion is therefore necessary for identifying critical degradation need to be repaired and maintained. Corrosion monitoring can provide more complete information of changing condition of a structure. In past years, many researchers have investigated this topic. Morris et al. (2002) investigated the effects of local variables on rebar corrosion process and proposed a criterion for rebar corrosion evaluation based on measurements of concrete electrical resistivity. Seashore environment and partially immersed in a saline solution were selected as two exposure conditions. Two water to cement ratios and various initial chloride ion additions were selected for experiment. The results showed that the electrical resistivity can be used to evaluate the potential of steel corrosion. Additionally, concrete mix design, environmental exposure conditions and initial chloride concentration have effect on rebar corrosion process. Deeble Sloane et al. (2013) proposed a monitoring corrosion strategy for the high-strength steel wires of suspension bridges by developing a sensor network to indirectly assess the environmental conditions and the deterioration of the interior of bridge main cables. The functionality of both the individual sensors and the monitoring system was tested on a full-scale mock-up cable. Temperature, relative humidity (RH), and corrosion rate levels were recorded by all sensors. The proposed network system was able to provide an understanding of the interior environment of a suspension bridge's main cable. Although they did not follow consistent trends across the cable's cross section, the RH values were strong indicators of corrosion rate levels.

**Scour** is the erosion or removal of stream bed or bank material around bridge foundations due to flowing water. Although bridges rest on normally stable foundations of piers, abutments, and caissons, scour at a dangerous level can cause bridges to become unstable and unsafe for traffic (Dong et al. 2010). Various studies in bridge safety evaluation revealed that foundation scour is the major cause for bridge failure. Specifically, Lagasse et al. (1997) reported that scour-related issues account for 60% of bridge failures in the United States, i.e. scour is the primary cause of bridge failure in the United States where more than 20,000 highway bridges are rated "scour critical" (Hunt 2009). Thus, the understanding of damages and degradation caused by scour is important to make decisions for bridge maintenance and repair. Bridge failure caused by scour has been investigated by many researchers worldwide.

Hunt (2009) presented a report about the current state of practice for fixed scour bridge monitoring by performing a literature review, surveying the state transportation agencies, and conducting a few interviews. Thirty-seven state DOTs responded to the survey. Information about the other thirteen states was obtained from the literature review. Thirty-two of the 50 states use, or have employed, fixed scour monitoring

instrumentation on their highway bridges. Following the completion of NCHRP Project 21-03, *Instrumentation for Measuring Scour at Bridge Piers and Abutments*, Hunt (2009) identified a total of 120 bridge sites that are using or have employed fixed scour monitors. The monitoring systems used by the states, with the exception of time domain reflectometry, are described in the current FHWA guidelines on scour countermeasures and monitoring, Hydraulic Engineering Circular 23.

Three types of scour monitoring exist: fixed, portable, and visual monitoring instrumentation. The first type include sonars, magnetic sliding collars, float-out devices, sounding rods, tilt sensors and time domain reflectometers (TDRs). Tables 2, 3, and 4 of (Hunt 2009) list the bridges with active or past fixed scour systems. Portable devices includes sounding rods, sonars on floating boards, scour boats, and scour trucks. They are manually carried, and transported from one bridge to another; as such, they are more cost-effective than fixed instruments because they can be used in multiple bridges. However, portable devices have the same limitations of any device used periodically and cannot be used during a storm event. Visual inspection monitoring can be performed at standard regular intervals and can include increased monitoring during high flow events (flood watch), land monitoring, and/or underwater inspections. Similar to portable monitoring, there are limitations on when inspectors can visit the bridges during storms. The scour hole that forms during a high-flow event is often filled in during the receding stage as the stream flow returns to normal (Hunt 2009). The problems reported by the states in response to the survey promoted by Hunt (2009) were very similar. The difficulties with maintenance and repairs to the scour monitoring systems were the most common theme throughout the survey responses. The leading cause of damage to the systems was debris flows and accumulation. Other common problems were vandalism and corrosion.

### **2.3 WIRELESS SENSORS TECHNOLOGIES AND SENSORS DRIFT**

The cost of traditional wired SHM systems, due in part to cabling networks, is detrimental for the deployment of high-density sensor systems or for usage in long-span bridges. SHM using wireless sensors can overcome the limitations of traditional wired methods with many attractive features such as wireless communication, on-board computation, battery power, ease of installation, and so on. Many groups worldwide, including researchers at the University of Illinois at Urbana Champaign (Jo et al. 2012, 2013; Moreu et al. 2015, 2016) have successfully implemented wireless sensors technologies for SHM and demonstrated the efficacy of such technologies in measuring structural acceleration, strain, and displacement responses over full-scale applications (Jang et al., 2010).

Platforms for SHM containing wireless smart sensing (WSS) have been developed during the past years. WSSs are devices that have sensor, microprocessor, radio frequency transceiver, memory, and power source integrated into one small size unit and are characterized by their capabilities of sensing, computation, data transmission, and storage, all achieved by a single device. They represent an attractive alternative to their wired counterparts because of the lower cost achieved by removing the need for cables (including cost for labor), and by the widespread production of micro-electro-mechanical sensors (MEMS). The wireless communication capability allows flexible network topology and hence enables a decentralized monitoring scheme, which adds robustness to the SHM system compared with the centralized approach in wired systems (Li et al. 2016).

Smart sensing platforms are generally featured by several characteristics: (1) on-board central processing unit (CPU); (2) small size; (3) wireless communication and data transmission; and (4) low-cost. Many WSS platforms have been developed and applied in SHM. They include the Mica series, iMote series, and Xnode. The Xnode is an advanced wireless sensing platform with several critical features such as reliable wireless communication, high-fidelity analog-to-digital converter, expandable data storage, high-precision synchronized sensing, user-configurable middleware software library, automated long-term operation of wireless network, and so on (Spencer et al. 2017). Based on advanced

wireless sensing platforms, many kinds of accompanying sensor boards have been developed to interact with the wireless sensing platforms for achieving diverse sensing capabilities.

Noel et al. (2017) presented a comprehensive review of wireless sensor network (WSN) for SHM applications, outlining the: (1) algorithms used in damage detection and localization, (2) network design challenges, and (3) future research directions. Solutions to network design problems such as scalability, time synchronization, sensor placement, and data processing were compared and discussed. The work by Noel et al. (2017) is one of the most recent papers on the subject, and follows the other excellent reviews from Lynch and Loh (2006) and Aygün and Gungor (2011).

More recently, Abdulkarem et al. (2019) presented a contemporary review of collective experience researchers about WSN for SHM. Technologies of wired and wireless sensor systems were investigated along with wireless sensor node architecture, functionality, communication technologies, and popular operating systems. Then, comprehensive summaries of the state-of-the-art academic and commercial wireless platform technologies used in laboratory testbeds and field tests for SHM applications were reviewed and tabulated. This review provided a classification of the key challenges associated with WSN for SHM to assist researchers and practitioners in understanding the obstacles and the suitability of implementing wireless sensing for SHM.

This report has emphasized the advantage of using SHM systems to evaluate structural conditions remotely using noninvasive methods. However, the reliability of the sensors is crucial to have a reliable SHM implementation and a trustworthy complement to annual inspections. As sensors age along with the structure they aim to monitor, sensors may experience a drift phenomenon. Drift is a slow, often linear or exponential decrease in accuracy that can at times go unnoticed if not appropriately monitored. If a sensor becomes too inaccurate, it can trigger false positive or (in the worst case scenario) false negatives. False positives would cause human resources to be employed to verify the alarms triggered by the SHM system. False negatives would leave critical damage to go unnoticed until the next cycle of bridge inspection.

Engineers and SHM specialists are therefore challenged with the development of methods and strategies to alleviate or eliminate drift due to sensors age without becoming a costly practice that nulls the economic advantages of wireless sensors with respect to wired technology. As a matter of fact, despite wireless sensors have become relatively inexpensive, the cost in labor to replace them can be very high, and in some cases is an incredibly high safety risk. Various methods have been investigated to correct drift. One of these methods is to cluster sensors in regions, rather than have a single sensor, and to evaluate the detections of all sensors in the cluster. By determining a uniform baseline from this data, sensors are calibrated back to a determined “zero-line” and establish the detectable threshold from there. This can be done either manually using remote computers, or by utilizing auto-calibrating sensors. The approach also relies on the ability to recognize data that are skewed and reject them from the results in order to prevent errors (Takruri et al. 2011).

Other challenges in wireless-based SHM systems include but are not limited to power the system and therefore harvest energy, limited communication bandwidth and range, data loss, time synchronization (TS), and signal length (Li et al. 2016, Noel et al. 2017).

Issues related with synchronization were reviewed and addressed by Li et al. (2016). Synchronization errors may occur because each smart sensor in the network has an independent processor, with its own local clock, which is not necessarily synchronized with the clocks of other sensors. Moreover, even with clocks perfectly synchronized, the data may lack synchronization because: (1) the sensors start sensing at different times due to random variations in the processing time in the sensor board driver; (2) the low quality of crystals may cause differences in the sampling frequencies among the nodes; and (3) the sampling frequency for each individual sensor node can fluctuate over time because of jitter (Li et al. 2016). When data are not synchronized, there is a shift in the phase information, which some algorithms consider as damage indicators. When modal analysis is used and high frequency vibrations are used to

detect damage because such vibrations are more sensitive to local defects, the accuracy of time synchronization at high frequency is pivotal. For example, a 1 *millisec* synchronization error between two measured accelerations will result in  $3.6^\circ$  error in phase angle at 10 Hz and  $36^\circ$  error at 100 Hz. So, if the damage detection algorithm linked to the SHM system is based on mode shapes, the mode shape error due to phase angle errors can lead to false positives.

The scientific literature contains several time synchronization protocols for WSNs and the interested readers are referred to Li et al. (2016) for a brief overview and for a few solutions experimented on a Korean bridge and on the **Arsenal Bridge** in the U.S. The monitoring of the latter added extra challenges, related to the extended sensing duration required to fully capture a transient event. For example, the monitoring of an entire vibration response during a swing event requires 10 min of data at 50 Hz (30,000 data points).

Clock drift is also caused by temperature variation to which a sensor may be exposed during the day due to exposure to direct sunlight or other weather related factors, or because heat generated by the processor itself. It has been shown that temperature change can cause nonlinear clock drift, which poses an additional challenge for synchronized sensing in SHM.

Sensing for SHM is characterized by much more sampled data points than, for example, temperature measurements. For example, under a given frequency bandwidth, more data points provide higher resolution once the data is converted into the frequency domain, and therefore, higher accuracy of estimated modal frequencies can be achieved. The requirement for longer sensing duration needed to extract meaningful information of structural characteristics poses challenges related with power, board memory, and data transmission. Longer recordings are instead required to capture the complete record of the forced vibration caused by a train crossing the bridge, which takes about 10 min. Extended sensing duration may exacerbate the problem of clock drift (skew), which is a phenomenon that two clocks drift away from each other because of differential clock speed. Even though the clocks were accurately synchronized when sensing started, they can drift away from each other during sensing and cause errors in timestamps, which in turn leads to synchronization error in the sampled data. Researchers address this problem by implementing clock skew compensation.

## 2.4 CONCLUSIONS

The review of the SHM programs for U.S. bridges focused primarily on: (1) Methodologies and objectives of the bridge instrumentation programs; (2) Data inference methods to evaluate structural parameters and detect structural irregularities using data from varying instrument types; (3) Validation techniques to assess the accuracy of the recorded data including from wireless sensors. Nearly seventy bridges across the U.S. in almost every state of the Union were reported. According to the information collected during this review, the following conclusions are drawn:

1. Most of the bridge instrumentation programs included at least three (3) different sensors types: one to collect ambient conditions (e.g. temperature and wind); one to collect static performance (e.g. strain gages); one to collect dynamic responses (e.g. accelerometers).
2. The vast majority of the monitored bridges were less than 30 years old at the time the monitoring began. A few bridges were instrumented during construction.
3. The most common sensors type is strain gages, with conventional foil strain gages widely adopted and recent surge in fiber optic technology.
4. Many publications were about a few controlled load truck tests.
5. Most documents referring to long-term monitoring programs were observations that lasted a few months, and not years.

6. Time-series associated with the dynamic response of bridge are almost always converted into the frequency domain in order to extract the frequency of vibration of as many modes as possible and use them as indicator of potential damage.
7. There is a general well-established consensus that temperature plays a detrimental role in the modal analysis of bridges and any robust SHM strategy cannot disregard the effect of temperature on mode shapes and vibration frequencies in order to avoid false positives/negatives.
8. Factors such as snow or water seems to have been persistently neglected as potential factors influencing the field data.
9. Wireless sensors are gaining momentum in bridge health monitoring. However, there are still technical challenges that prevent their exclusive use in lieu of conventional wired systems.
10. Owing to the size of the structures being involved and owing to the nature of the degradation processes, robust finite element modeling seems to be the preferred way to validate any SHM protocol installed in a given bridge. For some of the bridges discussed in this review, 3D FEM were implemented using commercial software such as ABAQUS or SAP2000.
11. Whenever finite element modeling has supplemented the SHM protocols, the latter ones are deemed the ones providing the accurate results and therefore the models are calibrated to “match” field data.
12. Based on what reported on bullet 11, researchers have come to the conclusion that field measurements are reliable and initial models are not accurate enough to portray the effective response the structure to real loads and traffic. So, calibration is always warranted.
13. Only a few studies have reported inaccuracies of sensors data. Most of the issues reported was related to vandalism, power supplies, and maintenance. It is believe by the authors of this review that any issue associated with the sensors that invalidated data would not be reported in the published documents. As such, it is difficult to gage the success rate and the durability of the instrumentation programs presented here.
14. As bridges have very little in common with each other and almost any new bridge is unique, it is difficult to design a uniform SHM paradigm valid for any bridge. What is adequate for some may not be adequate for another. This complication increases when structures are modeled but damage can only be simulated numerically but not (logically) induced experimentally.
15. Because of 14, it is not guaranteed that a damage identification method developed for a certain bridge is applicable to another bridge. As demonstrated in a few studies (e.g. Talebinejad et al. 2011) some methods work and some methods do not even work for a given bridge using the same data set.
16. To follow-up on item 15, only one study reported the use of a SHM strategy for two bridges, which are considered “sisters”: the Neville Island Bridge and the Birmingham Bridge.
17. In only one study, the bridge under consideration was “physically damaged” and repaired to consent the observation of the system prior, during, and after a structural flaw.

### 3. THE PENNDOT PILOT BRIDGE PROGRAM

This Chapter describes the instrumentation and the ten bridges involved in the program. **Table 3.1** lists the condition to be assessed for every bridge of the PennDOT program. **Table 3.2** shows the expected and the effective duration of the monitoring system, whereas **Table 3.3** compares the planned and the effective number of sensors for each bridge.

#### 3.1 THE SENSORS

Strain was the parameter measured in every bridge. Other parameters measured in some bridges were displacement, rotation, and acceleration. The information provided in this section is based on the Vendor's documentation.

The **Wireless Strain Gauge Sensors** use Vendor's proprietary sensing, scheduling and ultra-low power synchronization technology designed to operate maintenance-free. The self-adhesive types do not require drilling and have an accuracy of 1  $\mu\epsilon$ . The working temperature is comprised between -40 and +65°C (-40 °F to +150°F) and a 1.0 km communication range in free space. The wireless transmitter is 50mm (1.96") x 50mm (1.96") x 34mm (1.34") and each strain gauge sensor is 76.2mm (3") x 33.4mm (1.30") x 10mm (0.4"). Each sensor has an adjustable trigger from 16  $\mu\epsilon$  to 512  $\mu\epsilon$  and the sampling rate can be changed from 10 ms to 200 ms. The gages have a resolution of 1.6  $\mu\epsilon$  for steel and 3.6  $\mu\epsilon$  for concrete and a full range:  $\pm 4000 \mu\epsilon$ . While strain gages are bonded to the steel structure using adhesives, the installation on concrete surface requires drilling a flange-mount. The adhesive type gages are temperature compensated and contain the following additional sensing: temperature, battery voltage, wireless signal strength (RSSI). The sampling interval is set to 8 seconds once the transmission interval is set to 6 minutes. The strain sensors measure the strain every 20 to 25 milliseconds, equivalent to 50 Hz and 40 Hz, respectively. If strain variation exceeds a preset threshold (minimum of about 30-40  $\mu\epsilon$ ) in a short period of time (~ 100 msec) and the strain level remains high or low for about 200 msec a strain event (or Strain-triggered burst) packet will be generated and sent with the same rate (20 to 25 msec). If gage does not detect any event, strain readings will be captured on fixed intervals (ex. 8 sec.), and transmitted on the next transmission interval (ex. 6 minutes).

The **Wireless Tilt/Inclination Sensors** measure movement, settling, deformation and abnormal tilting of bridge piers. They operate along the three axis with a resolution of 0.1 degree angle. If the high-precision version is used, the sensor has a resolution of 0.00016 degrees (0.5 arc seconds) with full range options of  $\pm 1$  degrees and  $\pm 10$  degrees. Tilt sensors also provide additional sensing: temperature, battery voltage, and RSSI. Hi-resolution sensors are sampled once per each transmission interval, whereas high-rate tilt sensors are sampled 64 times per each transmission interval.

The **Wireless Displacement/Crack Meter displacement meters** have a sliding element which moves with displacement of structure or growth of a crack. The sensor has a resolution of 0.1mil (2.5 micrometers), repeatability of 0.4mil (10 micrometer), and comes with different full range options: .5in, 10in, 2.0in, 3.0in, 4.0in, 5.0in, 6.0in, 12.0in. The displacement is sampled once per transmission interval.

The **Wireless Vibration/Acceleration sensors** monitor vibration. For steel applications, the sensor itself is self-adhesive. For concrete, it is mounted on a flange and drilling is required. The working temperature is -40 to +65°C (-40 °F to +150°F) and a 1 km long communication range in free space. Complementary sensing include temperature, battery voltage, and RSSI. The resolution is 0.1mg or 1.0mg with full range options:  $\pm 2g$ ,  $\pm 4g$ ,  $\pm 8g$ , user selectable. For the acceleration sensors, the sampling frequency could be set to 100 samples per second. In those bridges in which cameras were installed as

well, the cameras take picture when a vibration event has been detected by their built in accelerometer. In other words cameras are enabled by a vibration sensor.

## 3.2 THE BRIDGES

### 3.2.1 *The Elizabeth Bridge*

The Regis R. Malady Bridge, commonly known as the **Elizabeth Bridge (Fig. 3.1)** is a steel thru-truss arch bridge that carries vehicular traffic across the Monongahela River between Elizabeth and West Elizabeth. The bridge is 1,500 ft (457 m) long and features freeway ramps at either end, with an exit to Third Street in Elizabeth (signed as Elizabeth/Glassport) on the south bank and exits for Route 837 North to Clairton and Route 837 South to West Elizabeth on the north bank. The deck is supported by wire rope hangers. For the narration, the left truss is the truss located upstream with respect to the river's water flow direction, i.e. the truss visible from the Elizabeth riverfront park where **Fig. 3.1** was taken. The right truss is instead the truss that is the downstream with respect to the water flow. In Spring 2018, the bridge was instrumented with 40 strain sensors, 16 high-resolution tilt sensors, 8 displacement (4") sensors, 4 three-dimensional accelerometers, 16 cable gauges, 2 wireless cameras, 3 signal repeaters, and 3 data logger and remote communication gateways. The main scope of the monitoring was to identify broken wires, redistribution of axial loads along the cables, and notification of barge collisions and other impacts. Displacement gauges D07 thru D14 were at the truss expansion connections to record relative longitudinal movement between the members. Rotation gauges R09, R12, R13 and R16 were oriented to record pier column rotation in the transverse direction with respect to the bridge centerline. The rotation gauges R10, R11, R14 and R15 were oriented to record pier column rotation in the longitudinal direction with respect to the bridge centerline. The truck test had the scope to measure the axial load on the cable to unfold the mismatch between structurally similar members.

### 3.2.2 *The Neville Island Bridge*

The **Neville Island Bridge** carries Interstate 79 and the Yellow Belt over Neville Island, west of Pittsburgh (PA). The bridge was opened in 1976. The whole structure consists of 27 spans for a total length of 4,544 ft (1,385 m). The main span, Span 21, over the Ohio River consists of a 750 foot (229 m.) tied arch span (**Fig. 3.2**) while other spans consist of both straight and curved plate girders. This span 21 is a thru steel tie-arch with steel hangers and welded plate girder-floorbeam-rolled stringer systems. The deck of the steel arch truss is supported by suspender cables. The arch was instrumented in August 2018 with 4 data logger and remote communication gateway Data Acquisition, 64 strain, 22 displacement sensors, 4 Hi-Res tiltmeters, 2 tiltmeters (3D Lo-Res), 7 wireless accelerometers, and 2 cellular cameras. On August 10, 2018 a live load test was performed with a truck crossing at low speed ( $\leq 5$  mph) from 9:00 PM until 1:00 AM. The certified total weight of the truck was 58,320 lb. Due to the size and configuration of the bridge high speed tests were deemed unnecessary. The truck traveled over the bridge at crawl speeds twelve times in total. It crossed twice the right, middle, and left lane of both directions.

### 3.2.3 *The Birmingham Bridge*

The 12 span **Birmingham Bridge (Fig. 3.3)** is a bowstring arch bridge located in Pittsburgh crossing over the Monongahela River. The total length of the structure is 1,662 feet (507 m), while the arch is 620 ft. (189 m.) long. The bridge is considered the sister of the Neville Island bridge. The structure is a steel thru-tied arch with steel welded plate floorbeam and rolled steel wide flange stringers. It is designated as Span 11. It stands on Piers 10 and 11 (River Piers 1 and 2). The bridge was instrumented during the period April 16-20, 2018 with 18 displacement gages (4"); 17 tiltmeters, and 16 strain sensors. The

displacement gages were positioned at the bearing locations to record relative longitudinal movement between the superstructure and substructure. The rotation gages were positioned to record angular changes between the floorbeam and tension tie. A controlled truckload test was performed on 04/23/2018. The weight of the truck was 69,960 lb. The test began at 08:00 PM. Truck first travelled on the North bound. Truck travelled on the bike lane, right lane, middle lane and left lane. Truck stopped on right lane close to floor beams FB00, FB01, FB19 and FB20 on the east side. The travel was repeated on four lanes and truck then changed its location to the southbound of the bridge. Travelling on four lanes in north bound, truck then stopped at the right lane close to each of four monitored floor beams on the west side. Truck repeated travelling on four lanes again.

### ***3.2.4 The Smithfield Street Bridge***

The **Smithfield Street Bridge** (**Fig. 3.4**) is a riveted built-up lenticular through-trusses with rolled steel floorbeam-stringer floor system crossing the Monongahela River in Pittsburgh (PA). The bridge was built between 1881 and 1883, widened in 1889 and widened again in 1911. The whole structure is 1,777 ft (542 m) long and consists of seven spans. The lenticular through-trusses represent Span 3 (close to downtown) and Span 4 (close to the south side). **Fig. 3.4** shows the west, east, and center trusses as well as the top, bottom, and diagonal elements of the bridge. The span closer to the south side of the bridge is Span 4 while the span close to the North side of the bridge is Span 3. The inspection report dated July 2019 rated the bridge as follows: deck: 5 (Fair); superstructure: 5 (Fair); substructure: 5 (Fair). In July 2019, an array of sensors was instrumented on Span 4. The live load test was performed with a 57,920 lb (26,272 kg) truck. During the test, truck first travelled over the bridge in the Northbound. First, truck travelled on the left lane, at the crawl speed (~5mph). Then, the truck stopped at beginning and end of span while it was on the left lane (Test 1). This test was repeated for another time (Test 2). Then, Tests 1 and 2 were performed in the Northbound while truck was on the right lane (Tests 3 and 4). After that truck changed its location to the Southbound of the bridge and Tests 1 to 4 were conducted again as Tests 5 and 6 (right lane) and Tests 7 and 8 (left lane).

### ***3.2.5 The Clairton-Glassport Bridge***

The BMS ID 02-2038-0010-0140 Clairton-Glassport Bridge (**Fig. 3.5**) carries the traffic across the Monongahela River between Glassport and Clairton Counties in southwestern PA, south of Pittsburgh. The bridge was completed in 1987 and rehabilitated in 2011. It consists of steel girders and prestressed concrete I beams. Overall, the structure has 17 spans, for a total length of 2,190 ft (668 m). The superstructure consists of: Spans 1 and 2, two-span continuous, welded steel multi-girder; Spans 3-11 and 15-17, Prestressed Concrete I-beams. Spans 5-8 are continuous, all other spans are simple; Spans 12-14, three-span continuous, welded steel multi-girder. The SHM system installed on the bridge consisted of 20 strain sensors, 24 displacement sensors, 4 two-dimensional high resolution tiltmeters, 4 accelerometers, 4 cellular cameras, and 2 data logger and remote communication gateways. No live load truck test was performed as the main scope of the SHM was detecting large collisions.

### ***3.2.6 The Cooks Mill Bridge***

The BMS ID 05-3001-0080-0000 Cooks Mill Bridge (**Fig. 3.6**) in Bedford County (PA) carries traffic over the Wills Creek River in the Londonderry Township. This three-span pretensioned concrete adjacent box beam bridge was built in 1961 for a total length of 195 ft (59.4 m). The gages were attached at midspan on the bottom flange of every beam and on the outside web of the fascia beams. Six month later, bolted type strain-gages were installed to replace the old one because moisture inside the concrete interfered with the performance of some of the adhesive-type strain gages. On July 25, 2018, a live load

truck test was performed between 9:00 am and 11:00 am. The certified total weight of the truck was 58,460 lb. Two types of tests were conducted on the bridge. In a first group of tests (20 tests), the truck traveled slowly (speed not exceeding 5 mph) over the bridge at known lateral distance from the south parapet. In the second group of tests (4 tests) the truck traveled at high speed of close to 40 mph over the bridge. Owing to the relatively narrow time window of the live load test and the subject material was concrete, the effect of built-in thermal stress/strain was considered negligible.

### ***3.2.7 The Somerset Bridge***

The two spans BMS ID 55-3014-0050-0509 bridge (**Fig. 3.7**), located over Laurel Hill Creek in Barronvale, Somerset County, in the borough of Middlecreek, was built in 1959 and consists of pretensioned adjacent concrete box beams. The total length is 166 ft (51 m). This bridge is structurally similar to the Cooks Mill Bridge. As a matter of fact, the curb-to-curb width (28 ft) and the out-to-out width (33 ft 6 in) of this and of the Cooks Mill Bridge are identical. The SHM system installed on the bridge consists of one Gateway box, one repeater, and 30 bolted-type strain gages, which collect data at four samples per second. Twenty sensors are located in Span 1 and ten sensors on span 2. A live load test was performed on July 2018 from 3:00 pm until 5:00 pm using a 58,460 lb truck. Twenty low speed tests (5 mph) were conducted at known lateral distance from the south parapet. The distances were 1 ft through 19 ft at 2 ft steps. Two passes per distance were performed.

### ***3.2.8 The Tonolaway Bridge***

The 1987 single span BMS ID 29-2004-0040-0000 bridge (**Fig. 3.8**) over little Tonolaway Creek in Fulton County carries the traffic of Manor Road. It consists of eight (8) pretensioned adjacent concrete box beams supported by reinforced abutments for a total length of 87 ft (27 m) and curb-to-curb width of 30.2 feet (9.2 m). This bridge is structurally very similar to the Cooks Mill Bridge. The instrumentation plan included 10 strain gages instrumented at the midspan of each box beam. In November 2017 ten strain sensors were installed along with one data logger and remote communication gateway. A few days later, a live load truck was conducted using a 57,120 lb truck. Three types of tests were completed. In the first group of tests, the truck traveled over the bridge at known lateral distance from the south parapet. In the second group of tests, the truck stayed stationary at the middle of the span for about 30-50 seconds. In the third group of tests the truck traveled close to 50 mph over the bridge.

### ***3.2.9 The Chester County Bridge***

The three spans BMS ID 15-0082-0592-0385 bridge (**Fig. 3.9**) carries the traffic of Manor Road over East Branch Brandywine Creek in Chester County. This rolled steel I-Beams bridge was built in 1937 and its total length is 105 ft (32 m). The instrumentation comprised 42 strain gages. A truck test was performed in July 2018, using a 58,460 lb. Both low and high speed tests were completed.

### ***3.2.10 The Sanatoga Bridge***

The two-spans closed spandrel stone masonry arch BMS ID 46-4031-0314-1676 in the Montgomery County is 60 ft. (18 m) long (**Fig. 3.10**). The installation consisted of 8 two-dimensional high resolution tilt sensors, 1 ultrasonic level meter sensors, 1 cellular Camera, and a data logger and remote communication gateway.

## 4. INFERENCE METHODS

This section is organized in three parts. The first part defines the most common terms used in the remaining part of the report. The second part describes the inference methods implemented by the research team to analyze the test-load and the representative service load data downloaded from the password-protected repository. The last part of the chapter provides an overall account of the finite element model implemented in ANSYS.

### 4.1 TERMINOLOGY

The terms *old repository* and *new repository* indicate two password-protected websites that provide access to the proprietary software system where the user can visualize the time-series associated with a given sensor, can perform some analyses, and can extract the data. During this project, Pitt investigators have had access to both the old and the new repository. The old repository was the first gateway created by the Vendor to access the data and was the portal from which we downloaded the data that we post-processed. We preferred to use the old repository to download the data because it was accompanied by a user manual and because, contrary to the new repository, we could easily download and save the data easily. Noteworthy, the new portal underwent some significant and interesting enhancements over the past 24 months. These improvements will be discussed later in this report.

The term *extraction* identifies the process of downloading the sensors data into Pitt-owned PC/laptop and saving those data in *.txt* files for post-processing. For each bridge, these *.txt* files were clustered according to the sensor types.

The term *analysis* identifies the processing of those *.txt* data using algorithms created and implemented in Matlab<sup>®</sup> by the investigators and based, in part, on the outcomes of the literature review conducted under Task 1 and in part based on the experience and knowledge of the principal investigator. This initial step enabled the investigators to interface with the Vendor website and gage the capabilities of the website.

The term *recorded data* identifies the values of the physical properties, e.g. strains and displacements, measured by the sensors installed on the bridges, streamed to the Website, and from there downloaded to Pitt hard-drives. Sometimes, these data are also referred as the *raw data* to emphasize the fact that they were not subjected yet to any post-processing.

*Drift* is a slow decrease in accuracy that can at times go unnoticed if not appropriately monitored. If a sensor becomes too inaccurate, it can trigger false positives or (in the worst-case scenario) false negatives. In this study, we considered drift any long-term monotonic trend observed over time in any given physical property. We labeled *drift* any long-term monotonic trend that is not deemed compatible with the environmental (temperature) and structural (traffic) conditions.

In SHM, the term *damage* may have several significances. Perhaps the most popular significance is that damage is defined as “*changes to the material and/or geometric properties [...], including changes to the boundary conditions and system connectivity, which adversely affect the current or future performance of these systems*” (Worden et al. 2007). In the context of this report, damage is any anomaly that differs from the design values or from the expected material properties. The presence of damage detected through the processing of the data did not necessarily imply that the structural integrity of the whole structure is compromised or that there is a need for immediate repair.

In this project, the parameter of the *temperature* and the *temperature changes* were considered in two manners. First, we looked at the temperature as any other physical parameter measured by each gage of the SHM system. The time-histories associated with this parameter were plotted and evaluated to look for

possible signs of anomalies in the sensor itself or in the communication system. Second, the temperature was linked to the other physical parameter measured by the same gage to quantify the effect of the temperature on the structural response of the bridges.

## 4.2 DATA PROCESSING

The sensors data were analyzed with the scope of: (1) evaluating the capabilities of the software system in terms of data extraction and analysis; (2) assessing the quality of the recorded data; (3) quantifying drift; (4) measuring temperature effects.

The raw data stored in a password-secured repository were post-processed using a general framework that was designed, implemented, and then finalized by the Authors using Matlab software. This framework should not be considered fully comprehensive as the scientific literature presents dozens of different strategies for the SHM of bridges. Overall, our analyses considered three distinct time phases.

**The first phase** consisted of the analysis of the first few days immediately after installation. This phase contributed to establish the origin (time zero) of the monitoring period and to observe any offset that may have been carried out ever since. It was noted that some sensors were not re-set to zero once they became operative. Strain gages installed at different moments, i.e. at different temperature of the monitored element, contribute to a possible misleading interpretation of the data because the reference temperature is not the same within the same array. Nonetheless, the SHM and the data provided are to be considered reliable, secure, and durable.

**The second phase** analyzed the controlled load truck tests. An example is shown in **Fig. 4.1**, where the strain associated with a gage is plotted as a function of time. The time interval refers to the day of the truck test. The time-series as the one shown in **Fig. 4.1** were processed in order to calibrate our data processing. Our findings were compared and matched well with those reported by the Vendor.

**The third phase** considered the data between the day (or a few days) after the truck test and the present. With the term “present” we indicate the day (or the few days) prior to the moment we downloaded all the data from the Vendor repository. Owing to the volume of the data and owing to the number of bridges we analyzed, the “present day” is different for different bridges. Once the raw data were saved into the Pitt computers, the following strategies were implemented.

- 1) **UPSAMPLING.** Each sensor has an embedded temperature gage. However, the number of data samples relative to the temperature are not the same and are not necessarily synchronized to the data samples relative to the parameter (e.g. strain) being observed. As such, an up-sampling procedure was developed, in order to associate a temperature to any given parameter sample.
- 2) **RAW PARAMETER vs TIME.** The raw parameters were plotted as a function of time, where the time was provided by the internal clock of the SHM system. These plots provide a quick look and detect any offset in the parameter value. In addition, any sensor malfunctioning, service interruption, data shortage becomes visible, or value drift, can be seen. An example of such raw parameter, namely raw strain, over time was shown in **Fig. 4.1**.
- 3) **RAW TEMPERATURE vs TIME.** The raw temperatures were plotted as a function of time. These plots allow for a rapid assessment of the system functioning and serve to identify spikes in the hot or cold temperature that may have had an effect on the other physical parameter measured by the same gage. Additional information that may be extracted from the time-histories of the temperature is about the reliability of the gage itself. For example, in a few instances it was noted that the readings of the temperature were consistent with the rest of the array but the readings of the physical parameter, e.g. strain, was not. Such types of observations may lead to the conclusions that the structural element

under which the gage is bonded/bolted may experience anomalous loadings. A close-up view of the temperature distribution across the sensors of the same bridge may also help (in future studies) to understand the structural response of the bridge to loadings and other normal operation activities. An example of raw temperature data is presented in **Fig. 4.2**.

- 4) **15-MINUTES MOVING AVERAGE vs TIME.** Parameters such as strain and displacement are heavily biased by the temperature. To mitigate/eliminate such effect, a 2-steps procedure was implemented. The first step consisted of synchronizing the raw strain gage data and the raw temperature data. Then, a 15-minutes moving average for both parameters was calculated. The second step consisted of calculating the difference between the raw strain data and the moving averaged strain. The difference represents the true strain associated with the transient event, such as traffic. The hypothesis behind the selection of the 15-minutes moving average is that any sudden event caused by traffic impact, traffic overload, or barge collision last much shorter than 15 minutes and therefore its effect on the moving average of the strain is negligible. This procedure was deemed effective because it is based on the assumption that the effect of the temperature is not instantaneous and it manifests slowly. The diagrams of the raw data and of the 15-minutes moving average data over time enable to identify anomalous spikes of the parameter and to identify long-term trends that could be associated to the deterioration of the structural element or to a drift of the sensor itself. An example of raw temperature data is presented in **Fig. 4.3**.
- 5) **SCATTER PLOT: RAW PARAMETER vs RAW TEMPERATURE.** The raw parameter, for example the raw strain was plotted as a function of the corresponding raw temperature. An example of raw strain vs raw temperature is presented in **Fig. 4.4**. This analysis may identify:
  - a. anomalous structural response to thermal loading, e.g. bearings that are “locked” but instead were expected to expand/contract freely;
  - b. outlier behavior at the extreme temperatures (hot/cold);
  - c. different response to thermal loading across structural members that instead should exhibit similar (if not identical) behavior.
- 6) **TRUE PARAMETER.** The difference between the raw parameter and its corresponding 15-minute average was computed and plotted as a function of time. We called this difference true strain, true displacement, etc... These “true” values are believed to be triggered by rapid transient events such as heavy truck crossings, barge collisions, traffic collisions, etc. After the analysis of a few bridges, the computation of the true parameters was polished further as we discovered that the shortage of data for periods longer than 30 minutes would create “artificial” spikes that may mislead the interpretation of the plots. These plots were complemented with a few additional statistical analysis, in order to identify:
  - a. anomalous values of the parameter of interest that may be associated to illegal crossing, sudden collisions, or other unexpected/unwanted transient events;
  - b. benchmark values that could be used in future tasks (or future studies) to model the bridge;
  - c. different response to transient loading across structural members that instead should exhibit similar (if not identical) behavior.

An example of the true strain applied to the data presented in **Fig. 4.1** are presented in **Fig. 4.5**. The advantage of the proposed algorithm is evident and will be discussed in detail for each given bridge.
- 7) **COUNTING OCCURRENCES.** To have a more quantitative account of the live loads, i.e. events that are considered to be transient, we counted the number of observations per given bin of strains. This number of occurrences is not equal to the number of original data samples downloaded from the

Vendor repository. As a matter of fact, the data were oversampled in order to assign a strain value to each timestamp from each sensor, as different strain gages (even from the same bridge) had different number of data samples. The occurrences were presented as histograms with respect to a certain strain bin (**Fig. 4.6**). The scope of such analysis was to quantify:

- a) how much any given sensor is skewed toward positive or negative strains and the outcome can be compared in future tasks to a finite element model prediction;
- b) how many occurrences exceeded the maximum strain increase recorded during the truck test;
- c) the responsiveness, of each sensor to live load events. This in turn can help better identify those members that seem "locked" and those that seem free to expand/contract.

This analysis was dismissed after being applied to a few bridges. While still deemed valuable, the analysis may overestimate the number of real occurrences owing to the need of equalize the number of readings from all the sensors involved. For future studies, it is recommended that the analysis is carried out for each sensor at the individual level. By combining information with other monitoring systems, e.g. weigh-in motion devices, this analysis can be used to count and classify vehicles.

- 8) **OUTLIER ANALYSIS (OA)**. OA is a novelty detection method that establishes whether a new configuration of the system is discordant or inconsistent from the baseline configuration, which consists of an existing set of data (or patterns) that describe the normal operative conditions. The novelty detection approach belongs to the unsupervised learning class of pattern recognition algorithms, and it offers the fundamental advantage that information about damage do not need to be known a priori, contrarily to the supervised learning class. The unsupervised learning approach is particularly useful when it is difficult to simulate damage prior to the use of the monitoring system, as in the case of many structures in service. Ideally, if the OA is used for detecting damaged states, the baseline should include normal variations in environmental or operative conditions of the structure (e.g. temperature, humidity, loads). However, it is generally difficult to account for all of the environmental variables that may affect a damage-sensitive set of features. In this study, the Mahalanobis squared distance (MSD),  $D_\zeta$ , which is a scalar defined as:

$$D_\zeta = \left( \{x_\zeta\} - \{\bar{x}\} \right)^T \cdot [K]^{-1} \cdot \left( \{x_\zeta\} - \{\bar{x}\} \right) \quad (4.1)$$

is used. In Eq. (4.1),  $\{x_\zeta\}$  is the potential outlier vector,  $\{\bar{x}\}$  is the mean vector of the baseline,  $[K]$  is the covariance matrix of the baseline and  $T$  is the transpose symbol. In order to determine whether a new datum (uni- or multi-dimensional) is an outlier, the corresponding value of  $D_\zeta$  has to be compared to a threshold computed from the baseline. Usually, the baseline data set consists of a large number of samples that can be obtained from a large number of experimental acquisitions of more realistically can be constructed by corrupting a certain number of experimental measurements with digital random noise. Once the values of  $D_\zeta$  of the baseline distribution are determined, the threshold value is typically taken as the upper value of  $3\sigma$ , equal to 99.73% of the Gaussian confidence limit. Thus if a new datum was classified as an outlier, theoretically there is only a 0.27% chance of a "false positive" reading. This approach assumes that samples sufficiently represent the statistical distribution as a Gaussian curve. However, in this study we considered the threshold as the upper value of  $4\sigma$ . An example of outlier analysis applied to the whole monitoring period of the Somerset Bridge is presented in **Fig. 4.7**.

### 4.3 FINITE ELEMENT ANALYSIS

The finite element models were created to calculate the deformation of bridges under certain loads and under certain health conditions. The models were developed to assist in validation of the recorded data. A

high-fidelity model (HFM) was developed for one bridge of each structural type (e.g. concrete box girder, steel plate girder, etc.). The remaining bridges were modeled with a low-fidelity line-element models (LFM). The Sanatoga Bridge was excluded from the analysis. Both models were used to compare numerical and experimental strain in order to validate the data streamed from the bridges. In addition, the models were used to perform a sensitivity analysis during which the effect of simulated damage on strains was quantified. The number of structural elements and components of the HFM were as close as possible to the real bridge. The LFM were instead simplified by ignoring or simplifying some elements of the bridge structures. It is emphasized here that the numerical models may have varied slightly from bridge to bridge due to the characteristics of the bridge itself. The HFM and LFM models can be also used to estimate displacement and rotation of the bridges at any discrete location identified with the mesh nodes.

First, a few preliminary static analyses were conducted to validate the models. Where applicable, a dynamic analysis was performed to extract the modal characteristics (mode shapes and corresponding frequencies) of those bridges instrumented with accelerometers. Long-term phenomena such as concrete creep, shrinkage, and steel relaxation to compute long-term deformations and stresses were not modeled. The HFM provides a very accurate account of the real bridge and includes as many details as possible. The only challenge would be the computational cost associated with the implementation of the model and the computational cost associated with the subsequent static analysis. The LFM is a simplified representation of the bridge with a lower number of bridge details and, where possible, the structural elements were modeled using line bodies as much as possible.

Results from those two models relative to the analyzed bridges will be presented in future chapters. The time independent finite element models, as constructed and analyzed using the procedures detailed in each chapter, are compared to some of the strains recorded by the Vendor' SHM system during the controlled load truck testing. It is **emphasized here**, that the numerical predictions are obtained under the placement of a static concentrated load at a certain location on the deck. Results from the time independent and temperature constant HFM and LFM were compared to measured data that may have been obtained under varying temperature. However, the tables presented by the Vendor were adjusted by considering strain increase due to the crossing of the truck. It must be said that since the truck was a moving vehicle, we did not determine the exact location of the truck at which a given strain gage experienced its largest (positive or negative) deformation. Nonetheless, the position of the concentrated loads in the models was considered to be reasonably close to the point where a certain set of sensors would experience maximum deformation. In addition, as the longitudinal strain is dependent on the internal moment, the exact location of the strain gage along the span of any given bridge is critical to perform a reliable comparison. As such, a discrepancy from the planned position of the sensor may lead to a discrepancy between the numerical and the empirical data.

The comparisons include test-load events and representative service load events. A parametric sensitivity analysis was also conducted to evaluate which numerical parameters can be adjusted to correlate numerical results with recorded data. Parameters evaluated in these studies included but were not limited to the modulus of elasticity of the bridge deck. In the last part of the analyses, we estimated the level of structural deterioration and/or damage resulting from long-term factors including corrosion and fatigue as well as short-term damage resulting from extreme load events. In these evaluations, damage/deterioration and repairs were to be introduced in the analytical models, and numerical results were to be extracted at the location of the physical instruments. To achieve these objectives, each structure was subjected to a range of damage and/or deterioration scenarios, including: (1) simulated corrosion; (2) broken or missing element that could be the effect of long-term deterioration resulting from fatigue or from vehicle impact.



## 5. THE SMITHFIELD STREET BRIDGE

### 5.1 SETUP

The Smithfield Street Bridge is a riveted built-up lenticular through-trusses with rolled steel floorbeam-stringer floor system (**Fig. 5.1**). Span 4 is the subject of this chapter. It is pinned north and has an expansion joint on its south end. For convenience, each truss is labeled as the west, center, and east (**Fig. 5.1**), and several close-up photos are presented in **Fig. 5.2**. Each truss is composed of three main parts: the top chord, the bottom chord, and the diagonal element. The top chord is formed by four I-shape steel members riveted together. The bottom chord is formed by eight bars pinned together. The diagonal element consists of a single bar. **Table 5.1** lists the areas of the cross-section of the truss elements.

In July 2019, the Vendor instrumented Span 4 with 30 strain gages, 7 displacement sensors, 3 high-resolution tilt sensors. Each sensor embeds a temperature detector that collects and periodically transmits the value of the temperature of the steel member. **Figure 5.3** shows the location of the 18 strain gages bonded to the trusses. Although the top chord is likely carrying bending stress as well, i.e. it does not act as a pure truss member carrying axial loading only, it may be argued that the location of sensors S01, S07, and S13 is at the neutral axis and therefore subjected to the stress associated with axial force. Strain gages 19 through 30 were bonded to the south portal, four on each of the three columns of the portal, one on each face of each column. These 12 gages, the displacement sensors, and the tiltmeters are not part of the study presented here and are ignored hereinafter.

Shortly after installation, a truckload test was performed using a 26,272 kg (57,920 lb) truck. The steer axle was 7992 kg (17,620 lb) and the drive ‘tandem’ axles were 18280 kg (40,300 lb). First, the truck travelled northbound twice (Tests 1 and 2) crawling at about 8 km/h on the left lane. Then, the truck stopped at both ends of span 4. Tests 1 and 2 were repeated with the truck crawling northbound on the right lane (Tests 3 and 4). After that, the truck was directed southbound, and Tests 1 to 4 were replicated and are labeled as Tests 5 and 6 (right lane) and Tests 7 and 8 (left lane). The largest difference between the strain with and without the truck at each gage during each test run was calculated and reported by the Vendor. **Figure 5.4** portrays the largest strain difference calculated for each gage in the Vendor’s tests. It shows that the top chords being monitored are in compression, whereas the other elements are in tension. With the exception of the south diagonal member and bottom chord on the east truss, the deformations on west truss are smaller than on the east.

The high-fidelity model of Span 4 was created. The digital twin of the superstructure and the deck would contain more than 17,000 structural components, most of which are connector members. To make the analysis computationally manageable, the following few simplifications were made: (1) the diaphragm members and the stiffeners of the floorbeams were not modeled; (2) the splice plates and a few other connection members were neglected; (3) the rebar of the concrete deck were replaced by a steel plate under the deck; (4) the gateways were approximated; (5) the bottom chord was modeled as a single 8” × 10” steel bar instead of the actual ten 8”×1” bars; (6) the top chord was replaced by a rectangular element having the cross-section area equal to the total cross-sectional area of the true element. The model used in the analyses consisted of 880 structural components, more than 244,700 finite elements, and over 698,700 nodes. Some screenshots of the finite element model are presented in **Fig. 5.5**.

Three AASHTO (American Association of State Highway and Transportation) trucks, namely the ML-80, the H20, and the HS20 were considered. A fourth truck, having the same characteristics of the truck used by the Vendor to perform the load test, was considered. The weight and the relative axles distance of the four trucks are schematized in **Fig. 5.6**. The static analyses conducted in ANSYS calculated the deformation generated by each individual truck on the two diagonal members hereinafter labelled as  $L_1U_2$  and  $L'_1U'_2$ . These members are located at the center truss and are monitored with strain

gages S09 and S10, respectively. These two bars are considered control members because they allegedly sustain the largest stress among the components being monitored. Each truck was placed on the northbound left lane of the bridge. A few positions were considered to identify the location that maximizes the strain of these control members. **Figure 5.7** provides a close-up view of the setup relative to the AASHTO ML-80 truck, near to member  $L_1U_2$ , i.e. close to the north end of the span. Seven distances of the rear axle from the end were considered, and they are listed in **Table 5.2** along with the calculated corresponding axial force and strain. The largest numerical load and strain resulted to be equal to 76.15 kN (17.12 kips) and 114.1  $\mu\epsilon$ , respectively when the rear axle of the truck is 10.16 m (400 in.) away from the north end of the span. Based on the information available to the authors, the steel used for the control members has a nominal yield stress  $\sigma_Y$  equal to 228 MPa (33 ksi) and Young's modulus equal to the 200 GPa (29,000 ksi), which implies that the yield strain is equal to 1138  $\mu\epsilon$ . If a safety limit equivalent to 55% of the yield stress is chosen, the corresponding safety deformation is equal to 626  $\mu\epsilon$ . If the distribution factor to center truss is assumed to be equal to 1.965 and the impact factor is assumed to be equal to 1.28, the calculated strain increase of 114.1  $\mu\epsilon$  caused by the ML-80 truck on the element  $L_1U_2$  is equal to 288  $\mu\epsilon$  ( $= 114.3 \mu\epsilon \times 1.965 \times 1.28$ ). The value of 288  $\mu\epsilon$  was obtained with a longitudinal distance resolution of 1.27 meters and with the left wheels located 0.89 m. (35 in.) away from the centerline of the bridge. It cannot be excluded that the calculated numerical deformation would be slightly larger if small adjustments to the lateral and longitudinal position of the truck are made. It must be emphasized that the model and therefore this value do not take into account the dead load of the bridge.

The same approach was applied to calculate the largest values on the diagonal member close to the south side of the bridge. **Table 5.3** summarizes the positions of the truck and the corresponding load and strain. As expected, the calculated values are nearly identical to those relative to the north side of the same span. The small difference (<1%) is likely due to the resolution (1.27 m.) of the longitudinal position of the truck. The same procedure was then applied to the other three trucks and the results are summarized in **Table 5.4**, where the maximum calculated strains in the two diagonal members of the center truss are listed. The results confirm the symmetry of the truss and are consistent with the weight of each truck. It must be noted though that the points of application of the forces, i.e. the position of the wheels differ from truck to truck along the longitudinal direction but are at the same lateral distance from the parapet.

## 5.2 NUMERICAL VS EXPERIMENTAL RESULTS

The numerical results relative to the truck used in the field on the left northbound lane were compared to the experimental results reported by the Vendor. The strains measured by sensor S09 during the two crossings of the truck were equal to 67.0 and 66.9  $\mu\epsilon$ . These values are about 17% lower than the calculated numerical deformation of 80.9  $\mu\epsilon$  listed in **Table 5.3**. The experimental values recorded by S10 were equal to 71.5 and 71.2  $\mu\epsilon$ , i.e. only 12.3% lower than the numerical prediction of 80.9  $\mu\epsilon$ . The difference is likely due to a discrepancy between numerical and the real (but unknown) lateral distance of the truck from the parapet. As a matter of fact, if the applied numerical load is 1.91 m (75 in.) away from the centerline instead of the 0.89 m (35 in.) location, the numerical strain on member  $L_1U_2$  would be equal to 69.2  $\mu\epsilon$ , just 3.3% higher than the experimental values recorded by S09. Similarly, if the numerical truck is 1.27 m (50 in.) from the center truss, the numerical strain on member  $L_1U_2$  is equal to 77.09  $\mu\epsilon$ , just 7.8% higher than the recorded values from gage S10. The outcome of this analysis is that a direct comparison between the finite element estimation and the experimental measurements suffers from the lack of knowledge about the exact lateral position of the truck. Nonetheless, the agreement between the numerical and the experimental results is quite good and prove the reliability of the finite element model.

According to the drawings, each truss is symmetric with respect to the midspan, but the west-to-center truss distance is about 300 mm (11.8 in.) shorter than the east-to-center truss distance. In addition, as said

above, the cross-sectional area of the chords are not the same for each truss. To quantify the effects of these differences on the deformation of the members instrumented with the wireless sensors, a symmetric load was applied at the midspan. Four concentrated forces were applied at the midspan and equidistant to the centerline of the bridge, as if two wheels were on the northbound lane and two wheels were on the southbound lane. Each force was 44.5 kN (10 kips), and the relative longitudinal and lateral distance were equal to 2.54 m (100 in.). The results are visualized in **Fig. 5.8**, where the axial strain along the 18 members instrumented with the sensors is displayed. The results prove the symmetry of the bridge with respect to the midspan. However, the strains at the east truss are higher than at the corresponding elements of the west truss. The deformation at the northeast top chord is  $-4.26 \mu\epsilon$  whereas the deformation of the north west top chord is  $-2.42 \mu\epsilon$ . Another example, the diagonal members have a deformation of  $-9.31 \mu\epsilon$  vs  $-7.61 \mu\epsilon$ . These numerical findings are consistent with the fact that the total cross-sectional area of the top and bottom east chord was smaller than at the west chords. The outcome of this analysis may explain why the overall deformation on the east truss were lower than the corresponding strains in the west truss.

Finally, two extreme load events were simulated. The first event was a truck, 30% heavier than the one used for the bridge test, traveling northbound on the right lane. The deck was assumed to be covered by 50.8 mm (2 in.) of snow that applies 160 Pa (0.02315 *psi*) of distributed load. The second extreme load event consisted of two identical test trucks traveling in opposite directions on the left lanes. This scenario simulated the simultaneous occurrence of Tests 1&2 and Tests 7&8. In both events, the effect on the deformation close to the south portal of span 4 was investigated. **Table 5.5** summarizes the results and shows that the largest strain, equal to 133  $\mu\epsilon$ , is expected to be recorded by the diagonal member on the center truss by the control member. It should be noted that the principle of superposition can be used because of the linearity of the finite element model and the fact that the deformation are below yielding. Not shown here, we found that the predicted strains for S10, S11, and S12 during the second extreme load event are approximately equal to the sum of the predicted values during Tests 1&2 and Tests 7&8, considered individually.

## 5.3 STRUCTURAL HEALTH MONITORING ALGORITHMS

### 5.3.1 Truck test Monitoring and Interpretation

The results from the 18 strain gages are presented here. For the Smithfield Street Bridge, the framework was validated first by processing the data relative to the truckload test. Then, three years (August 1<sup>st</sup>, 2019 through July 31<sup>st</sup> 2022) worth of data were examined.

**Figure 5.9** shows the raw strains recorded during the truck test, which lasted about 90 minutes during which the steel cooled about 3°C (5.5°F). From top to bottom, the values relative to the east, center, and west trusses are displayed. To ease comparison, the range of the vertical axes is the same for the three subplots. Some symmetric elements exhibit significant difference. This is because the sensors were installed at different moments on a summer day, when the temperature of the steel may have differed by more than 10°C. The consequence is that the strains are offset with respect to each other because the “reference temperature”, i.e. the temperature at which the gages read zero deformation, is different for each sensor.

To minimize or eliminate any bias attributable to the temperature, the following 3-steps procedure was implemented. First, the raw strain data and the raw temperature data were synchronized and this required some up-sampling and interpolation of the temperature data. Then, the 15-minutes moving average for both parameters was calculated. Finally, the difference between the raw and the moving averaged strain was calculated to obtain what hereinafter is referred to as the “true strain”. The hypothesis behind such procedure is that the effect of any transient event, e.g. vehicle overload, vehicle crashes, or barge collisions, last much less than 15 minutes and therefore its effect on the moving average of the strain is

negligible. In addition, the temperature effects on the structural steel are not instantaneous. The reliability of this procedure was applied to the data shown in **Fig. 5.9** and the results relative to twelve sensors are presented in **Fig. 5.10**, where the true strains relative to the sensors bonded to the center and the west trusses are presented. Here, the vertical axes are between  $-40 \mu\epsilon$  and  $+100 \mu\epsilon$ . In the absence of any live load, each gage value is centered to zero. Consistent with what observed with **Fig. 5.3b**, the highest deformation was recorded by S09 and S10 bonded to the two control members. As the strains are mostly negative, **Figure 5.10** confirms that the top chords monitored with sensors 07, 12, 13 and 18 are under compression. The qualitative and quantitative comparison between **Fig. 5.10** and **Fig. 5.4** demonstrates the reliability of the data processing.

The reliability of the 3-steps procedure described above is demonstrated further with **Fig. 5.11**, which shows the data recorded by S16 on July 19 – 23 of year 2020. The sensor is bonded to the single diagonal member of the west truss on the south side of the bridge. The steel temperature and the corresponding moving average are presented in **Fig. 5.11a** and they overlap because metal heating or cooling takes longer than 15 minutes to significantly change the temperature of the element being monitored. As such, the values of the real-time temperature and the moving average temperature are very close. The raw strains and the corresponding moving average are presented instead in **Fig. 5.11b**. The moving average is clearly tied to the temperature trend. The decrease in temperature increases the strain and vice versa. The raw strains are instead a combination of traffic and thermal load. The difference between the two is presented in **Fig. 5.11c** which represents the true strain. Besides the fact that the least activity is seen in the early hours of each day, **Fig. 5.11c** shows an anomalous spike in the early morning of 07/21/2020. The value of this spike ( $152 \mu\epsilon$ ) is nearly twice any strain seen in **Fig. 5.10** and is associated with the crossing of a truck weighting more than the posted 23 tons weigh limit. It is noted here that the predicted numerical static strain associated with a ML-80 type truck standing close to the south portal on the right southbound lane is equal to  $102.1 \mu\epsilon$ . If the impact factor of 1.28 is used to take into account the dynamic impact of the truck traveling southbound, the resulting value of  $131 \mu\epsilon$  ( $=102.1 \times 1.28$ ) is close to the deformation of  $152 \mu\epsilon$ , seen in **Fig. 5.11c**.

From graphs like **Fig. 5.10** and **Fig. 5.11c**, the average value (typically  $\sim 0 \mu\epsilon$ ) and the standard deviation  $\sigma$  can be extracted. Choosing an interval equal to  $4\sigma$ , we can label as bridge overloads all those events that occur 0.0063% of the cases, i.e. one case over 15,787 events. The selection of  $4\sigma$  as threshold is arbitrary and based on statistical considerations. It can be replaced by a threshold based on engineering judgement such as traffic tonnage or numerical calculations. For example, for the specific case of sensor 16, the threshold could be set equal to  $72 \times 1.28$  ( $= 92.16$ )  $\mu\epsilon$ , which is the static strain increase recorded in the diagonal member 16 when the 26308 kg (58 kip) truck crawled over the southbound lane close to the parapet multiplied moving effects.

### 5.3.2 Long-term Monitoring

This section discusses the outcome of the analyses of three years (01 – August – 2019 to 31 – July - 2022) of active monitoring of the Smithfield Street Bridge. The SHM system was installed a few weeks earlier (July 2019) and the sensors are still active.

**Figure 5.12** shows the raw strain and the corresponding 15-minutes moving average of gages S13 through S18. The two horizontal lines identify the  $\pm 4\sigma$  range. To facilitate data comparison, the vertical scale is identical and comprised between  $-150 \mu\epsilon$  and  $200 \mu\epsilon$ . If the modulus of the steel is assumed to be equal to  $E = 200 \text{ GPa}$  ( $E = 29,000 \text{ ksi}$ ), the selected range goes from 30 MPa (4.35 ksi) in compression to 40 MPa (5.8 ksi) in tension. For the sake of space, the graphs relative to the other 12 gages are not reported here, and can be found in the report of Task 3. The following overall considerations can be made by observing **Fig. 5.12**:

- As expected, most deformations follow the seasonal changes of the temperature. This is particularly evident for the diagonal member monitored by gage S16.
- Sensors S14 and S15 do not exhibit significant periodicity.
- The width of the  $\pm 4\sigma$  range is not the same for all sensors. While some ranges among those not shown here (S02, S05) are below  $50 \mu\epsilon$ , other gages (S01, S07, S13, S16) have  $\pm 4\sigma$  range wider than  $150 \mu\epsilon$ . This is another indication that some members are less prone to thermal expansion/contraction.
- Only one isolated spike exceeded the  $\pm 4\sigma$  range and it was caused by the truck crossing discussed earlier. Not shown here, another spike was for instance seen in gage S04 on 02/14/2020 at 9:15:48 AM. S10 also showed a spike on 07/22/2021 at 15:21:02.
- Among the less thermally prone members, thousands of deformations were outside the  $\pm 4\sigma$  interval. They are false positives, suggesting that the width of this interval is too conservative for certain structural elements and therefore ineffective at identifying overloads or other transient events.

Graphs like **Fig. 5.12** can enable the identification of permanent deformation, and sensor drift. To date, nothing significant has emerged from the raw strains measured by the 18 sensors.

The raw strains and the corresponding raw temperatures from each sensor were synchronized to create a matrix with three columns: strain, temperature, and corresponding timestamp. The strain vs temperature data are plotted in **Fig. 5.13** for the same gages considered in **Fig. 5.12**. With the exception of sensor 17 bonded to the bottom chord on the south side of the west truss, the strain decreases with the increase of the temperature, i.e. as the bridge becomes warmer its structural members tend to compress. The response of S17 is believed to be caused by an error during the installation, which however does not compromise the reliability of the information.

Each graph contains the lines bounding the  $\pm 4\sigma$  interval and a thick red line that represents the linear regression. The equation of this line and the corresponding  $R^2$  are provided as well. If any given member of the trusses is free to expand/contract, the slope of the equation would represent the coefficients of linear thermal expansion of the steel. The heavy truck crossing discussed earlier emerges with the dot close to  $200 \mu\epsilon$  and  $21^\circ\text{C}$  (gage S16). Other scatters are visible in some of the graphs not shown here for the sake of space. However, none of them is as discordant as the one just mentioned.

The slope and the corresponding  $R^2$  for each sensor are presented in **Fig. 5.14a** and **Fig. 5.14b**, respectively. The slope is also visualized on the bridge schematics presented in **Fig. 5.15**. Consistent with the circumstance that the south portal of Span 4 is on an expansion joint, eight of the nine slopes calculated for the sensors bonded on the south end of the bridge are higher than the corresponding slopes for the north end. The only exception is gage S12, whose slope ( $-0.34 \mu\epsilon/^\circ\text{C}$ ) is smaller than the slope calculated for gage S07 ( $-0.53 \mu\epsilon/^\circ\text{C}$ ). The nine monitored members located on the north end have nearly the same slope. The only relevant exception is the diagonal member of the center truss, i.e. gage S09, for which the value of  $-0.17 \mu\epsilon/^\circ\text{C}$  is 34% the gradient calculated for the diagonal member on the east truss. Owing that the control members on the south side are expected to be the most prone to thermal expansion, it is interesting to note that the slope relative to sensor S04 is 51% the value of S16 ( $-1.32 \mu\epsilon/^\circ\text{C}$  vs  $-2.59 \mu\epsilon/^\circ\text{C}$ ), and 40% the value of S10 ( $-1.32 \mu\epsilon/^\circ\text{C}$  vs  $-3.32 \mu\epsilon/^\circ\text{C}$ ). It cannot be excluded that such difference is attributable to the fact that the cross-sections of those elements are not the same. Notably, the slope associated with S10 ( $-3.32 \mu\epsilon/^\circ\text{C}$ ) is nearly twenty-fold the value calculated for S09 ( $-0.17 \mu\epsilon/^\circ\text{C}$ ). Such difference is not seen in any other sensors pair. Finally, the readings from the south end of the west truss seem to suggest that this part of the bridge responds to thermal variations more than its east counterpart, although the top chord does not corroborate such interpretation. **Figure 5.14b** proves that the three single diagonal elements on the south side of the bridge, which is free to expand, respond linearly to the

temperature variation as can be concluded by observing that the corresponding  $R^2$  are close to 0.9. Similarly, all the sensors bonded to the north side of Span 4, which cannot expand, exhibit the lowest  $R^2$ .

The cross-comparison of graphs like **Figs. 5.13-5.15** can reveal anomalous response to thermal load and this can lead to the detection of structural anomalies, as discussed in what follows. Based on what observed through **Figs. 5.12-5.15**, it may be argued that the bridge does not respond symmetrically with respect to the median line and does not respond symmetrically with respect to the mid-span. The bottom chord on the south side of the west truss (S17) stands out from the other chords. The diagonal member on the south side of the East truss monitored with gage S04 seems to be partially locked as it does not exhibit the same gradient of the other two counterparts.

An example of live load for a subset of strain gages is presented in **Fig. 5.16** along with two horizontal lines that bound the  $\pm 4\sigma$  range. To ease data comparison, the vertical scale is identical to all 6 graphs and comprised between  $-50 \mu\epsilon$  and  $100 \mu\epsilon$ . Under the assumption that  $E= 200 \text{ GPa}$ , the selected range goes from 10 MPa in compression to 20 MPa in tension. The live strains are consistent with what seen with the truck load test (**Fig. 5.10**): the gages that exhibited small deformations ( $<20 \mu\epsilon$ ) still showed small deformation over the last three years; the sensors (03, 04, 09, 10, 15, and 16) that exhibited an increase in strain above  $50 \mu\epsilon$  instead showed high values of strains. On a few occasions, the sensors exceeded the maximum strain increase recorded during the truck test. Sensor S13 was subjected to an isolated event in November 2021 when the true strain was nearly  $50 \mu\epsilon$ , significantly higher than the values typically recorded by this sensor. Gage S15 displays several isolated events, the most notable ones in December 2019, October 2020, and April 2022. Gage S16 displays a single spike much higher than  $100 \mu\epsilon$  ( $151 \mu\epsilon$ ), on July 21<sup>st</sup>, 2020, which is relative to the heavy truck crossing discussed previously. As observed for the raw strains, the selection of the  $\pm 4\sigma$  range may be too conservative to identify relevant transient events..

The values of the  $\pm 4\sigma$  range for all 18 gages are presented in **Fig. 5.17**. The graphs corroborate what found during the controlled truck test. The members that exhibited very small strain increase (see **Fig. 5.10**) are the same that have the smallest range. This is a further proof of the reliability of the algorithm developed to extract the information about live loads. The analysis of the live strains shall not ignore the traffic pattern. The south portal of the bridge is located on an expansion joint but is also at a short distance from a traffic light. Traffic traveling northbound are approaching the bridge after a right or left turn and are therefore accelerating and reach constant full speed when approaching the north portal of Span 4. The vehicles traveling southbound likely start decelerating and breaking as they approach the south portal and the traffic light and the 90-degrees right or left turn become more visible. This implies that members instrumented with sensors S16-S18 are likely to be subjected to the dynamic impact of traffic heading southbound. Conversely, the members instrumented with sensors S04-S06 (East truss) are subjected to smaller dynamic loads because the vehicles heading northbound are slower and may begin accelerating. This may be the reason why the live strain graphs associated with some sensors may result noisier than other. Note that the controlled truck test was conducted at constant speed 8 km/h (5 mph) regardless of the traveling direction.

The analysis of **Figs. 5.16 and 5.17**, including the graphs of the 12 sensors not displayed here, led to the following considerations:

- The live strain relative to sensors 02, 06, 08, 12, 14, and 18 does not reveal anything significant. Owing to its geometry, it is reasonable to believe that the strains at the top chord are in between the bottom and the diagonal members.
- Sensor S17 (west truss) was significantly “noisier” than sensors S05 and S11 located on the other bottom chords on the south side. This could be caused by traffic decelerations or by inclination to expand/contract more than the other two.

- The sensor on the diagonal member of the East truss (S04) is the least noisy than S10 and S16 bonded to the other two diagonal members of the south side. This evidence aligns with the hypothesis the northbound lane close to south side is where vehicles accelerate and therefore they are expected to be at lower speed than the vehicles on the opposite side (southbound). An isolated event was detected around mid-February 2020 with a value close to the maximum strain of  $51.9 \mu\epsilon$  recorded during the truck test. Sensor S10 at the center truss is mostly skewed to tensile stress with some events close to the value of  $79.5 \mu\epsilon$  recorded during the truck test. This sensor recorded a significant negative strain ( $-395 \mu\epsilon$ ) on July 22<sup>nd</sup> 2022 at 15:21:02. Since it was only a single data point, not seen by any other gage, it is attributed to an electromagnetic interference. Sensor S16 detected a major event on July 21<sup>st</sup> 2020 with a peak that is twice the value of  $72.1 \mu\epsilon$  recorded during the truck test.
- Looking at the elements that are allegedly symmetric with respect to the center of Span 4, it is noted that the comparison of S01 with S06, S02 with S05, and sensor S03 with S04, all located on the East Truss, show that the sensors on the north side are noisier than the corresponding ones on the south side. This supports the hypothesis that the vehicles heading to northbound travel faster when they approach the north end of span 4.
- The comparison of the sensors located on the Center truss did not reveal any specific trend. Owing to their location, any peak may be the result of the simultaneous crossing of two vehicles along the two directions.

The value of the  $\pm 4\sigma$  interval displayed in **Fig. 5.17** may also provide a qualitative estimate of the responsiveness of each sensor and of the proper elongation/contraction of the relative bridge element. **Figure 5.17** shows that the individual diagonal members experienced the largest strain variation. The exception is the top member located on the north side of the east truss (S01). Conversely, the bottom chords seem to be the most rigid with least strain variation. Overall, the behavior observed with **Fig. 5.16** is compatible to the geometry of the 18 members being monitored: the slender elements exhibit the largest interval, whereas the bulkiest part (the bottom chords) exhibit the smallest interval. The outlier represented by the information collected with S01 may be related to the installation of the sensor far from the neutral axis, i.e. the sensor may read bending strain besides axial strain.

For the OA, each truss was considered individually. As such, the input vector contains the true strains from six sensors. The baseline consisted of all the data collected during the month of August 2019. This relatively short interval was deemed to be effective to be representative of the baseline because the OA was applied to the live strains, and the live strains are unbiased by thermal effect. The threshold was instead set as the upper value of  $4\sigma$ . The results of the OA are presented in **Fig. 5.18**. About twenty relevant outliers emerge and are indicated with date and times. The largest MSD (close to 10,000) was found at the center truss on 07/22/2021 and was caused by what is believed to be an electromagnetic interference. The second largest MSD ( $\sim 2,000$ ) was seen at the West truss on 07/21/2020 and is relative to the heavy truck crossings discussed previously. By looking at the date and hours, it was determined that these outliers were caused by the sensors bonded to the single elements of the bridge, i.e. to the diagonal members.

**Fig. 5.18** shows the reliability of the analysis at identifying outliers of a certain significance. To this end, while the investigation of the outlier on 07/22/2021 in the Center truss identified a false positive occasion, the outlier on 07/21/2020 in the West truss revealed the passing of an overweight unauthorized truck over the bridge. In addition, the classification of the sensors into three groups (East, Center, and West) may help the localization of any potential issues recorded by the sensors. For example, the outlier relative to the overweight truck is identified in the West truss analysis, which implies that the truck was travelling southbound, close to the parapet. It must be noted that the application of the OA presented here required some data prepping. As a matter of fact, due to sensors synchronization, the time stamp for each recording may not have been identical to each of the sensors included in a given cluster, i.e. in a given

truss. To overcome the lack of data synchronization, the pre-processing included the insertion of strain data that represented the linear interpolation between two consecutive recordings.

The OA was also run for the time interval corresponding to the evening of the controlled truck load test. For the sake of space, the results are not shown here. However, it was found that most of the truck crossings resulted in several outliers slightly above the corresponding threshold of each truss.

## 5.4 CONCLUSIONS

The analysis of the Smithfield Street Bridge determined that the west truss shows slightly larger thermal expansion/contraction with respect to the east truss. The same truss shows slightly higher and “noisier” live strains. The motivation may be structural, but it may be also associated with differences in the number and speed of the vehicles traveling southbound or northbound. The live load graphs may reveal isolated peaks that can be attributed to heavy traffic or a sudden transient event of different kind. These graphs enable the comparison with the value of the maximum strain recorded during controlled truck tests because the graphs are not adversely affected by the offset induced by the installation. However, live load graphs cannot reveal neither sensors drift nor permanent deterioration of the structure because the live load is obtained by subtracting the raw strain to the 15-minutes moving average.

Owing to the geometry of the monitored components, a direct comparison between the diagonal member and the top chord, and the diagonal member and the bottom chord can only be approximate. As a matter of fact, the diagonal member is a single element carrying axial stress; the instrumented bottom chord is one of the ten bars designed to carry axial stress; the cross-section of the top chord is different than the other two. As a matter of fact, the strain gage sensors installed on the bridge are still active and over the three years considered in this chapter, they did not show any relevant issues except one occasion in which one of them was subjected to an electromagnetic interference that we were not able to confirm.

## 6. THE CONCRETE BOX BEAMS: SOMERSET, COOKS MILL, AND TONOLAWAY BRIDGES

### 6.1 SETUP

**Figure 6.1** shows the photos of the three bridges clustered in this Chapter because they are nearly identical and analyzed using the same processing and numerical approach. The first one (**Fig. 6.1a**), hereinafter referred to as the Somerset Bridge. The second bridge (**Fig. 6.1b**) is the Cooks Mill Bridge in Bedford County. The last structure (**Fig. 6.1c**) is a single span bridge, hereinafter referred to as the Tonoloway Bridge in Fulton County. The cross-section of each bridge is shown in **Fig. 6.2**.

The Somerset Bridge was instrumented with 30 bolted-type proprietary wireless strain gages. Each gage embeds a thermocouple. Both spans were instrumented with one sensor bolted to bottom of each box beam, as shown in **Fig. 6.3a**. Four gages, namely S01, S10, S21, and S30, were bolted to the outer face of the side girders. **Figure 6.3a** also shows the presence of ten more sensors. The bridge was tested with a truck. The steer axle was 18,400 lb and the drive tandem axles were 40,060 lb. The test consisted of crossings the bridge slowly at known lateral distance from the north parapet. The distances were 0.305 m (1 ft) through 5.8 m (19 ft) at 0.61 m (2 ft) steps. Two crossings per distance were completed. The Cooks Mill Bridge was instrumented with ten bolted type strain gages at the bottom of the midspan of each beam, and on the outside web of the fascia beams (**Fig. 6.3b**). The sensors bolted to both bridges were not temperature-compensated. The tests was conducted with the same truck using the same protocol adopted for the Somerset Bridge. Finally, the Tonoloway Bridge was instrumented with ten adhesive type strain gages at the locations schematized in **Fig. 6.3c**. The test was conducted using a 57,120 lb truck: steer axle: 16,940 lb; drive ‘tandem’ axles: 40,180 lb. Three types of tests were completed. In the first group of tests, the truck traveled over the bridge at known lateral distance from the south parapet. In the second group, the truck stayed stationary at the middle of the span for about 30-50 seconds. In the third group of tests the truck traveled close to 80 kmh (50 mph) over the bridge.

The finite element replica of the Somerset Bridge was created (**Fig. 6.4**) using 3-D 20-node solid body elements were used for the parapets, the beams, and the deck. REINF264 elements were used to analyze the strands, rebars, and stirrups that were considered line bodies. The final model consisted of 83,891 elements. The material properties are summarized in **Table 6.1**, and are representative of the properties selected for the other two bridges as well. For the other two structures, a low-fidelity model (LFM) was created. The box beams and the parapets were “Line Bodies” and analyzed using “Beam Elements”. The rebars inside the slabs were replaced by a 0.75 in steel plate. An enhanced finite element model (EFEM) was also built by considering the box beams and the parapets as “Solid Bodies” to be analyzed using “Solid Elements”. The LFM of the Tonoloway bridge included 178,774 nodes whereas the modified models included 314,522 nodes and 3128 structural components, most of which were the rebars and the strands of the concrete box beams. The EFEM of the Cooks Mill Bridge had 7300 structural components that a major part of them are the rebars and strands. For illustrative purposes, the LFM Cooks Mill Bridge is shown in **Fig. 6.5**.

For each bridge, a static analysis was conducted by applying a six point-load on the deck (**Fig. 6.6**). The relative position of the forces was compatible to the relative distance of the wheels of the truck. Pristine conditions were simulated by considering the drawings. Then, the six damage scenarios summarized in **Tables 6.2a-6.2c** were implemented individually and subjected to same load conditions. The scenarios #5 and #6 represented loss of composite behavior by changing the contact type of the girders from “Bounded” to “No Separation”. In ANSYS software, “Bounded” contact type between two objects means that the objects are perfectly bounded to each other and they cannot slide or be separated. “No separation” contact type between two components means that the objects can slide along the contact surface but they cannot be separated.

## 6.2 NUMERICAL VS EXPERIMENTAL RESULTS

The value of the raw data were subtracted from their 15-minutes moving average in order to obtain the so-called true strain to target the detection of transient events and filters out long-term factors such as thermal effect and drift. The term true strain shall not be considered the actual strain as pre-stress level and the reference temperature at the time of sensor installation is not known.

For illustrative purposes, **Fig. 6.7** shows the raw (**Fig. 6.7a**) and the corresponding true strains (**Fig. 6.7b**) associated with sensor S06 during the test of the Cooks Mill Bridge. The number of spikes (twenty) is consistent with the number of truck crossings. The earlier peaks are likely linked to the arrival of the crew and preparation. **Figure 6.7a** shows that the strain without the truck, changed about  $25 \mu\epsilon$  due to temperature. Such variation is almost larger than the strain induced by the truck. **Figure 6.7b** demonstrates that the 15-minutes average removes the thermal-related bias and the increase in strain due to the truck can be easily quantified. As expected, the values of these peaks are not constant because the truck crossed the bridge at different lateral distances from the parapets, i.e. at different distances from the strain gages. As gage six was closer to the south part of the bridge, the highest strains occurred around the second half of the test. Similar outcomes were seen for the other sensors and the other bridges.

**Figure 6.8** compares the experimental maximum strains recorded by each sensor at a given crossing to the numerical strains calculated under pristine and damage scenario 1. The case of the Somerset Bridge with the truck 1.52 m (5 ft.) away from the north parapet, and at the middle of span 1 (**Fig. 6.8a**) and span 2 (**Fig. 6.8b**) is presented. The static calculations are consistent with the fact that the centroid of the wheels is closest to gages S04 and S25, and farthest from S09 and S29. The excellent agreement between the numerical and the experimental values is evident with the exception of S05, S06, and S25. The discordant response of these three gages is explained with **Fig. 6.9**, which shows the results under damage scenario 6 that simulated the absence of shear keys at the locations shown in **Fig. 6.10** and the loss of composite behavior of the shown girders. The lack of proper load transfer across adjacent boxes causes uneven distribution of the strains. The outcomes of **Figs. 6.8** and **6.9** demonstrate the quality of the high-fidelity model developed in this study but also the importance of accurate modeling for the explanation of issues revealed with the use of the sensing system.

The interpretation of **Fig. 6.9** is confined with **Fig. 6.11**, which shows the experimental and the calculated strains induced by the truck 4.57 m (15 ft.) away from the north parapet. Similar analyses were conducted for the other two bridges. The results relative to the Cooks Mill Bridge when the truck was 1.52 m (5 ft.) away from the north parapet are presented in **Fig. 6.12a**, which shows the outcomes of both the LFM and the EFEM. Clearly, the LFM did not capture adequately the response of the strain gages located far away from the point of application of the forces. Beam elements are 1D elements while solid elements are 3D elements with more nodes and degrees of freedom. Owing the poor accuracy of the LFM, the EFEM was used to calculate the stresses under damaged conditions shown in **Fig. 6.12b**. **Figure 6.12b** present the results relative to damage scenario 6, where girders G4 and G6 lost composite behavior and their contact with adjacent beams using shear keys was changed to “No separation” as shown in **Fig. 6.13**. **Figure 6.12b** shows that the strains were not distributed uniformly. As the contacts of G4 and G6 with the deck and the adjacent shear keys were changed, the stress at those girders is underestimated. Also, the model overestimates the strain for the other beams because the other beams compensate the defect of G4 and G6 due to the load redistribution. Finally, **Fig. 6.12c** shows the result of the same damage scenario but for a different truck distance from the parapet.

The application of the LFM to the Tonolaway Bridge yields to the same considerations in terms of accuracy and its outcome is not presented here for the sake of space. The static analyses conducted for all three bridges led to the following additional considerations. The linearity of the models was such that the 10% reduction of the concrete stiffness led to about 10% increase in the overall strains. Under damage scenario 2, the beams adjacent to girders G3 and G6 bear some effects whereas the beams far away from the damage experience lesser strain increase. The reduction of the strands cross-section did not lead to

significant change in strain. Because prestress was not included in any of the models, it is believed that the reason behind the results is that the concrete and strand bear the force caused by the truck together. As the cross-section area of concrete is more than the cross-section area of strands, the stress is mainly transferred to the concrete. Some manual calculations were done for the Somerset Bridge considering 20% reduction in strands' cross section. The calculations verify the obtained results from the ANSYS model. Finally, the models predict that the presence of localized cracks at the bottom of some concrete beams cause such small variations undetectable with the installed sensors.

### 6.3 LONG-TERM MONITORING

The historical data downloaded from the password-protected repository of each bridge were analyzed in order to formulate a general SHM paradigm. For representative purposes, **Fig. 6.14** shows the raw strain and the 15-minutes average of the gages labeled as S05 in **Fig. 6.3**. The  $\pm 4\sigma$  interval is overlapped. As the SHM systems were installed months apart, the monitoring windows were different. The history of the Somerset Bridge (**Fig. 6.14a**) and the Cooks Mill Bridge (**Fig. 6.14b**) show the seasonal trend with peak-to-peak values of about 400  $\mu\epsilon$ , which is one order of magnitude larger than the strain increase experienced during the truck test. This is because the sensors were not temperature-compensated. The spike seen in **Fig. 6.14a** was likely due to an electromagnetic interference as it was observed across all the sensors. Not shown in **Fig. 6.14**, the strains from the sensors bolted to the outer walls exhibited wider ranges because they were more exposed to solar radiations. The extreme strains recorded in January 2019 (**Fig. 6.14a and 14b**) were caused by exceptionally cold ambient temperatures. **Fig. 6.14c** presents the results relative to the Tonolaway Bridge. A few isolated spikes occurred throughout the monitored period, likely caused by electromagnetic interference because the associated strains were 1-2 order of magnitude higher than what recorded during the truck tests and were seen also in the other gages. Some of those spikes seem to have shifted the value of the raw strain permanently. Owing to the vertical scale of the plot, the daily trends associated with the temperature cannot be seen. In addition, the sensor S05 drifted significantly for several months, and a similar behavior was seen in other gages. It was concluded that these adhesive-type gages drifted because concrete moisture degraded the bondline. Owing to this behavior, the long-term analysis of the Tonolaway Bridge is not considered further.

The raw strain and the corresponding temperature are presented in **Fig. 6.15** for sensor S05 bolted to the Cooks Mill Bridge. The linear regression and the  $\pm 4\sigma$  interval are overlapped. The few scattered dots around 10 °C (50 °F) are likely due to maintenance activities of the sensing systems. This hypothesis was not discussed with the Vendor, and is based on observations from the other sensors.

The slope of the regression and the residual  $R^2$  computed for every sensor of the Cooks Mill Bridge are plotted in **Fig. 6.16**. It is reminded here that S01 and S10 were bolted to the north and south exterior box, respectively. Most of the residual values were around 0.96 - 0.99 because the sensors were not temperature compensated. Nonetheless, the slopes can be used to identify uneven responsiveness of each box to thermal load. Despite S01 and S10 are exposed to different solar illumination, their slope is nearly identical. However, the slopes associated with gages S02 and S09 that are symmetrical opposite with respect to the bridge centerline vary by about 12%. In addition, the beams instrumented with gages S03 and S08 expand much less than their adjacent beams. In numbers, the slope of gage S07 is 25% higher than the slope of gage S08. Sensors S04 through sensors S17 have nearly the same values.

Similar considerations can be extrapolated from **Fig. 6.17**, which shows the same quantitative strain-temperature information extracted from the Somerset Bridge. Some boxes do not expand as much as the adjacent one and this align with the truck load test results discussed in the previous section. For example, the gradient (-7.66  $\mu\epsilon/^\circ\text{F}$ ) of gage S03 is 27% higher than the adjacent member S02 (-6.05  $\mu\epsilon/^\circ\text{F}$ ) and 13% higher than the adjacent beam S04 (-6.8  $\mu\epsilon/^\circ\text{F}$ ). These number reveal uneven expansion/contraction. Similar considerations can be extrapolated for sensors S22-S24. Overall, Span 1 and Span 2 have

different gradients. For example, the slope of S23 ( $-5.16 \mu\epsilon/^\circ\text{F}$ ) is 30% smaller than its counterpart S03 ( $-7.66 \mu\epsilon/^\circ\text{F}$ ). These responses are in part aligned with what discussed about the truck test, and a numerical study that takes into account the effect of thermal load is warranted.

**Figure 6.18** shows the true strain for sensors S05 bolted to the Cooks Mill Bridge. Values above  $20 \mu\epsilon$  can be considered equivalent to the crossing of a 58,460 lb truck. Owing to the availability of the model, plots like **Fig. 6.18** can identify unexpected transient events, including unauthorized heavy crossings, but cannot reveal sensors drift or concrete creep. Still, these graphs have the advantages of not being bias by any kind of offset. The use of threshold, like the one overlapped in the figure, may help setting an upper limit to set an alert. The large negative true strains are likely due to the vibrations caused by a heavy truck crossing at high-speed. As a matter of fact, it was shown that the same algorithm applied to the case of a slow-crossing truck does not cause significant negative strains. It is emphasized here that negative strains do not imply that the beam was under compression because the reference temperature and the prestress level of the box beams at the time of installation were not known.

From **Fig. 6.18**, the number of occurrences at a given strain value bin was plotted in semi-log scale as shown in **Fig. 6.19**. For convenience, the value of the largest strain increase recorded by the same gage during the truck testing is overlapped. This graph shows one or two occurrences above  $+100 \mu\epsilon$ . These are single episodes that may be likely ignored especially if they were also recorded by the other sensors as they may result of false positives or electromagnetic interference. In this figure, negative and positive values correspond to transient strains below and above the 15-minute average raw strains respectively.

**Figure 6.20** presents the value of the  $\pm 4\sigma$  interval overlapped to the true strain data as in **Fig. 6.18**. The results relative to the sensors bolted to the Somerset Bridge (**Fig. 6.19a**) and the Cooks Mill Bridge (**Fig. 6.19b**) are presented and they may serve as additional indicators of the loading resistance capacity of the individual girders and the ability to transfer loadings evenly across adjacent girders. The data relative to the first span of the Somerset Bridge show that sensors S05 and S06 bore the largest strain. This is consistent with the fact that most traffic is likely to occur close to the centerline of the bridge in the absence of incoming vehicles from the opposite direction. Interestingly, the same response was not seen for the second span of the bridge for which the width of the  $\pm 4\sigma$  interval associated with sensors S24 (equal to  $29 \mu\epsilon$ ) is double the value of the adjacent sensors. As there is a road intersection close to the east abutment, it is hypothesized that the traffic is slower when traveling above Span 2.

The OA applied to sensors S01-S10 and to sensors S21-S30 of the Somerset Bridge is presented in **Figs. 6.21a and 21b**, respectively. The measurements collected in May 2018 constituted the baseline. A few outliers are visible in June 2018, and February, March, and April of year 2019. As expected, the electromagnetic interference discussed in previous figures stands out clearly in **Fig. 6.21**. The same OA was applied to the ten strain gages on the Cooks Mills Bridge. The result is shown in **Fig. 6.22**. The largest MSD is visible on November 16<sup>th</sup> of 2020 caused by the same event discussed in **Fig. 6.15**. Specifically, a high true strain was seen in S03, S04, S08 and S09, likely due to maintenance of the hardware. As a matter of fact these four sensors were not streaming data for a few months when they became active again on that day.

## 6.4. CONCLUSIONS

This Chapter presented some representative project's outcomes relative to the three concrete box bridges instrumented under the PennDOT pilot program. Based on what observed, it is believed that none of the three bridges experienced new critical damage or growth of existing issues. The analysis of the truck test on the Somerset Bridge revealed some uneven distribution of the load. The use of the 15-minutes moving average may cause false-positives when two consecutive samples of the raw data are collected 30 minutes apart or more and, at the same time, the thermal effect changed the baseline strain significantly. As such, the true strains computed from such samples should be discarded.

## 7. THE BIRMINGHAM, CLAIRTON-GLASSPORT, AND CHESTER BRIDGES

A photo of the bridges discussed in this Chapter are shown in **Fig. 7.1**. **Figures 7.2-7.4** present instead the locations of the strain gages that were analyzed. The finite element replica of the Birmingham Bridge (**Fig. 7.5**) consisted of 8124 structural components, 452,000 finite elements, and about 1,310,000 nodes. Most components were considered solid bodies, whereas line bodies were used for the cables and for the rebar. The material properties are summarized in **Table 7.1**, and are representative of the properties selected for the other two bridges as well. For the Clairton Bridge, class AAA cement concrete was used for the slabs, whereas ASTM A36, A572, and A588 were used for the steel elements. The model included 5242 structural components, and about 285,800 finite elements and 835,300 nodes. The replica of the Chester Bridge consisted of 441 structural components, more than 90,900 finite elements, and over 400,700 nodes. It is noted here that for every bridge the largest number of structural components was represented by the steel reinforcement of the concrete deck.

The original (pristine) conditions were simulated by considering the drawings provided to the authors by PennDOT. Then, the six damage scenarios summarized in **Tables 7.2a-7.2c** were implemented individually. To mimic any loss of composite behavior on the Chester Bridge, the contact type of the girders was changed from “Bounded” to “No Separation”. In ANSYS software, “Bounded” contact between two objects means that the objects are perfectly bounded to each other and they cannot slide or be separated. “No separation” contact type between two components means that the objects can slide along the contact surface, but they cannot be separated.

For the Birmingham and the Chester Bridge, a static analysis was conducted by applying a six point-load on the deck to reproduce the action of the truck’s steering wheels and tandem axles. Owing to the lack of truck test, the static analysis of the Clairton Bridge consisted of applying the weight of a 58,460 truck (steer axle and drive tandem axle equal to 18,400 lb and 40,060 lb, respectively) at the center of the north bound direction of span 12, and at the center of the south bound direction of Span 13 (**Fig. 7.6**).

### 7.1 TRUCK TEST RESULTS AND COMPARISON TO THE NUMERICAL ANALYSES

For illustrative purposes, **Fig. 7.7** shows the raw strains recorded by the rosette FB01-West-IN relative to the Birmingham Bridge. The label indicates that the sensor was on the west side of floorbeam 1, farther from the tension tie. The number of twin-spikes between 20:00 and 22:15 is consistent with the 18 truck crossings. The baseline strain, i.e., the measurement without the truck, remained nearly constant, as the temperature of the steel did not change much during the experiment.

The empirical results of the truck test were compared to the numerical calculations obtained with the ANSYS model. An example of such analysis is presented in **Table 7.3**, which lists the results associated with two specific crossings, and the computed strains results relative to the original bridge design and to the bridge under one simulated damage scenario. This damage consisted of locking the contact of stringer No. 3 with floorbeam 19, as seen in **Fig. 7.8**.

**Tables 7.3a** lists the maximum XX and YY strains recorded by the four rosettes located on the east side of the bridge while the truck crossed (twice) the northbound bike lane. Note that if  $E=29,000$  ksi, the value of  $100 \mu\epsilon$  corresponds to 2.9 ksi of stress. The sensors did not peak simultaneously. For example, the maximum YY strain at FB19-EAST-IN (equal to  $-79.4 \mu\epsilon$ ) did not occur when sensor FB19-EAST-OUT experienced its maximum value of  $-12.7 \mu\epsilon$ . When this was the case, an asterisk on **Table 7.3** indicates the strains recorded at the same instant. This choice enables the comparison of the numerical

calculations computed with a truck at a specific bridge location and the consequent deformation across the neighbor sensors. **Tables 7.3b** lists the results associated with the rosettes located on the west side of the bridge, when the truck crossed (twice) the southbound right lane. The experimental values listed on the table were extracted from the Tables reported by the Company and made available to the authors of this study by the project sponsor. The asterisk shown on the table means that the values were instead extrapolated from the strain waveforms presented in the mentioned report. Table 7.3 shows that the experimental strains recorded by the sensors that are equidistant from the centerline of the bridge did not deform evenly. For example, the FB01-East-IN rosette responded differently during two identical crossings ( $-73.40 \mu\epsilon$  vs  $-57.5 \mu\epsilon$ ). Similar considerations can be made for FB19-West-Out along the YY direction ( $22.00 \mu\epsilon$  vs  $28.00 \mu\epsilon$ ). This mismatch may be attributed to experimental uncertainties, including the fact that the sensors are bonded to areas of stress concentration. Despite the complexity of the structure, the numerical results under pristine conditions agreed overall well to the experimental values. The right most column of each graph quantifies the percentage difference between the original design and the numerical damaged scenario. For the inner gages, the variation of the predicted strains may be significant. The origin of such variation is illustrated with **Fig. 7.9** that explains the difference between the load transferring from the stringers to the floorbeams under pristine and under damage scenario 3. The third stringer contributes to the load transfer to the floor beams and therefore, some of the truckload is shifted toward the tie girder. Thus, the damage will cause more compression at the locations of inner sensors. Similarly, according to FE model's results presented in Tables 3, the inner sensors in YY direction show more compression.

For illustrative purpose, **Fig. 7.10** shows the location of damage 5 of the Clairton Bridge. The web thickness of the west girder was reduced from 0.5 inches to 0.15 inches due to triangle-shaped corrosion at the south end of the bridge (span 12). **Table 7.4** presents the results. As the damage was just above S01, its larger effect is detected by that sensor whereas is negligible elsewhere. The S01 strain was 31% lower, which seems to be counterintuitive as thinner web should induce larger localized stress and strain. As a matter of fact, the effect of the same damage at other locations of the west girder increases the strain at the middle of the west girder. As such, the 31% strain reduction reported in Table 4 may be the effect of local instances that are not well captured by the model given that the values are quite small.

The analyses associated with the other damages showed the following. The reduction of the modulus of elasticity of the steel (case scenario 1) increases the overall strains by about 5%, consistent with the linearity of the model and the fact that most members of the bridge are made of steel. When the modulus of the concrete deck was reduced by 15% (case scenario 2), the strains resulted 1.5% higher than the original design. This modest increase is driven by the dominance of the steel elements. The removal of the diaphragms and diagonal bracings from the middle of the span 12 (west side) and span 13 (east side) do not affect the overall strains at the sensors' locations. This is compatible with the fact that the simulated damage was too far away from the sensors. This was proven by evaluating the strains at the middle of span 13. Under load case 2, strain difference is in the order of 4-6%, proving that sensors location are a key factor in the success of any health monitoring program. When the modulus of elasticity of the middle girder was reduced by 10% (damage 4), the girders experienced about 2-3% higher strain. Since the damage changes the stiffness of the middle girder, load distribution between the girder changes. The last simulation on the Clairton Bridge consisted of adding a 0.5 inches rectangular plate to the location of the previous damage scenario in order to mimic a repair (**Fig. 7.11**). The subsequent analysis demonstrated that the repair reinstated the pristine condition of the girder.

The Chester Bridge is a steel-concrete composite bridge. The neutral axis is localized close to the top flange. **Figure 7.12** shows the raw strains recorded by the gages bonded to girders 3, 4, and 5 during the truck test. While the response at the web is quite similar, the measurements at the top and bottom flanges across the three girders is uneven. After reviewing the technical report submitted by the Company performing the truck test, it was determined that the repository mislabels the time-series. As such, the time-series labeled as G04B is to be intended as G04T and viceversa. With that clarification, the subplots

in **Fig. 7.12** demonstrate that girders 3-5 work as composite bridge. Under the effect of the truck load, the top flange undergoes compression and the bottom flanges experience larger tensile stress than the web.

The graphs of the true strains (**Fig. 7.13**) prove that the thermal-related bias is removed while the information relative to the strain increase caused by the truck is kept. As a matter of fact, the values of the peaks are not uniform, consistent with the fact that the truck crossed the bridge at different lateral distances, i.e. above different girder.

The empirical values of the Chester Bridge were compared to the computed strains. Specifically, **Figs. 7.14a-d** present the case of the truck standing above the center of span 1 and span 2 of the northbound lane, whereas **Fig. 7.14e-h** refer to the truck standing at the southbound lane. The experimental and numerical strain under pristine and damage scenario 6 are presented. The measured strains agreed extremely well to the FE results. The few exceptions of S4, S5, and S19 are attributed to uneven transfer across adjacent members as proven by looking at the difference between pristine and damaged scenario. Regarding the other scenarios, it was found that the corrosion of the bottom flanges (damage 1), which represented about 15% thickness reduction, increases the strain by 6% - 7%, as the neutral axis shifts. Under damage scenario 2, where the thickness of the web decreased 10% from 0.564 in to 0.504 in, the strains increased about 3% - 4%. Owing to the linearity of the model, a 5% decrease of the Young's modulus of the steel (damage #3) increase the strain by about 5%. The localized damage at girder 3 and 12 (damage #4) induced some local change in the predicted strain as can be seen in **Table 7.5**. In this damage scenario, the modulus of elasticity reduction is applied only for two beams. The results show that all the beams experience an increase in strains. Since the beams are connected to each other through the deck, the adjacent beams bear some of the effect of G3 and G12 deterioration. The absence of seven diaphragms (steel bracing) that mimic the localized rupture of some welded connection between the girders and diaphragms yielded to very modest differences in strains with a few exceptions visible in **Table 7.6**. As the diaphragms connect two adjacent beams in three single points, they do not contribute in load distribution significantly, and the deck is mainly responsible for load distribution. Therefore, the simulated damage did not alter the strain values at the web and bottom flange of the girders.

## 7.2. LONG-TERM MONITORING

Representative historical raw strains and the corresponding 15-minutes average for the Birmingham Bridge is given in **Fig. 7.15**. While the rosette bonded to the floorbeam labelled as 00 has a seasonal cyclic trend, the gage bonded on its symmetric counterpart (FB20) drifted. Noteworthy a few other sensors mounted on the Birmingham Bridge experienced drift. **Figure 7.16** presents a representative time waveform of the Clairton Bridge strain. With respect to the Birmingham Bridge, the temperature-related variations are lower likely because of the element being monitored. The repository lacked data around October 2019 for reasons unknown to the authors.

The Chester Bridge was monitored for 2 ½ years from June 2018 to January 2021. For the sake of space, no time histories are presented here. It was observed that most of the gages displayed a clear cyclic trend associated with the seasons. The sensors bonded to girders #1 and #8 exhibited larger daily variations than any other girders because they were exposed west. Five sensors stopped working earlier than the others.

The deformation of the structures caused by the ambient temperatures was investigated as a possible marker for structural anomalies. To describe the procedure, **Fig. 7.17** presents the raw strains and the associated temperature from the Birmingham Bridge. The equation of the linear regression and the corresponding  $R^2$  values are overlapped. The strain gradient, namely the slope of the regression and the  $R^2$  from all the rosettes bonded to the Birmingham Bridge are displayed in **Fig. 7.18**. Most of the gradients are positive, which means that the structural member expanded with the increase of the

temperature. The two evident exceptions were the two rosette bonded on the east side of FB20. As those sensors drifted, their reliability is questionable. Looking at the residuals, those associated with the direction perpendicular to traffic (YY) are lower than the vertical and diagonal directions. Most of the gages with the lowest  $R^2$  ( $< 0.1$ ) exhibited also the slope closest to zero, which implies that the corresponding structural member was not prone to significant thermal effects. The behavior of the gages bonded to symmetric members is not necessarily similar. For example, the slope associated with FB00-EAST-IN and FB00-WEST-IN are equal to  $-0.46 \mu\epsilon/^\circ\text{F}$  and  $2.58 \mu\epsilon/^\circ\text{F}$  (along XX), respectively, and  $-0.64 \mu\epsilon/^\circ\text{F}$  and  $1.68 \mu\epsilon/^\circ\text{F}$  (along XY), respectively.

A similar analysis was carried for the other two bridges. The results are in **Fig. 7.19** (Clairton Bridge) and **Fig. 7.20** (Chester Bridge), respectively. Gages S04, S07, S12, and S14 bonded to the Clairton Bridge have the largest negative gradients. These sensors are bonded to the web of the lower beam of diaphragms (see Fig. 3b), which are therefore highly responsive to temperature changes. Additionally, it is evident that even within a single diaphragm, the sensitivity to temperature is not consistent. For instance, although sensors S07 and S09 are both installed on the web at Pier 12, the slope relative to S07 is more than twice that of S09. Moreover, their  $R^2$  values differ significantly. This inconsistency between these two sensors can be partially attributed to the asymmetric geometry of the diaphragm (**Fig. 7.3b**). In contrast, S04 and S19, located at the southern and northern piers (Piers 11 and 14), respectively, appear to provide consistent strain data. The  $R^2$  values are nearly the same (around 0.6). Besides, the strain-temperature slopes for these two gages indicate that they are not highly responsive to temperature changes.

The results of the Chester Bridge are clustered according to the girders number. Girders 1 through 7 belong to span 1, and girders 8 thru 14 belong to span 2. Some data are not included because the corresponding sensors stopped working too early. The gradients calculated from the sensors bonded to the top flange are not uniform with an obvious discordancy noted at girder 5. Notably, the two girders facing west have the lowest residual. The thermal response at the webs was uniform and clearly linear. The only exceptions were the external girders (1, 7, 8, and 14). Being located close to the neutral axis, the web sensors were less prone to bending stress. Finally, regarding the bottom flange, the slopes associated with the inner girders, i.e. 2 thru 6 (span 1) and 8 thru 13 (span 2) are overall uniform and comprised between  $-0.93$  and  $-0.60 \mu\epsilon/^\circ\text{F}$ . The negative sign implies that the increase of the temperature compresses the bottom flange, i.e. negative bending. Despite located on the same west side of the bridge, the deformation of girder 1 is nearly half than girder 8. As noted in **Fig. 7.20**, the residual seen for the bottom flange is quite low when compared to the others.

A representation of the true strain computed from FB01 of the Birmingham Bridge is provided in **Fig. 7.21**. Each time series is completed with the superposition of two horizontal lines that represent the strain range  $\pm 4\sigma$ . A few abnormal peaks are seen in Spring 2019 and their origin could not be determined although may be the effect of the crossing of heavy trucks. Besides the identification of spikes attributable to severe transient events, graphs like those shown in **Fig. 7.22** can be used to ascertain the responsiveness of the bridge to traffic loadings. A quantitative measure could be the estimation of the  $\pm 4\sigma$  interval. This analysis is presented in **Fig. 7.22**. When comparing the graphs from the other strain gage, the north side of the bridge seems to experience more traffic load than the south side. Overall, the rosette bonded on the outer side of the cope are less subjected to the effect of traffic. Interestingly, the sensing system on the south side of the bridge denotes intervals that are 10-20% higher than the south side. One possible reason could be the fact that there are two ramps close to the north side (pier 11) whereas vehicles travels at full speed when close to the south pier (pier 10).

The values of the  $\pm 4\sigma$  interval computed from the rosettes are presented in **Fig. 7.22**. The comparison of the  $\pm 4\sigma$  across symmetric elements or across adjacent members may be interpreted as a marker of the structural response to traffic load, the responsiveness of each sensor, and the deformation of the monitored structural member. Figure 7.22 shows that the  $\pm 4\sigma$  intervals relative to the YY direction are

twice as the corresponding XX direction. The sensor bonded on the north and east side of the bridge on the floorbeam #19 shows the highest interval. It is worth noting that any  $\pm 4\sigma$  interval below  $8 \mu\epsilon$  is compatible with readings that fluctuates between + and  $- 1 \mu\epsilon$ , which is the claimed resolution of the gages.

The same analysis was carried for the other two structures. For the Clairton Bridge the analysis did not reveal anything significant. Most of the gages resulted below  $\pm 4\sigma < 10 \mu\epsilon$ , i.e. within the resolution of the sensors. The results relative to the Chester Bridge (**Fig. 7.23**) shows that the largest  $\pm 4\sigma$  intervals are associated with the sensors bonded to the web of girders 1, 8, and 14. Interestingly, these three girders are located on the outer side of the bridge (east side or west side). **Figure 7.23** shows also that most of the sensors bonded to the top flange have values below  $8 \mu\epsilon$ . None of the forty values reported stood out from the others.

The results of the OA are presented in **Figs. 7.24** and **7.25**. The first month of monitoring constituted the baseline to calculate the threshold. **Figure 7.24** refers to the Birmingham Bridge and shows the MSD calculated to the truck test data and to the whole monitoring. To ease comparison, the vertical axes are the same. The case of the XX-direction strain data is presented. The crossing of the truck did induced a very few outliers, the first of which likely related with the arrival of the crew at the bridge. The investigation of the datapoints with the highest MSD values, it was found that the first four highest ones correspond to the data recorded by FB19-EAST-OUT, FB20-EAST-OUT, and FB01-EAST-OUT. It is believed, but it is not proved with any experimental evidence, that the larger sparse MSD are related to the simultaneous crossing of more than one truck on this six lanes bridge.

The MSD relative to the truck load test performed on the Chester Bridge did show only one outlier from the web. The analysis applied to the whole dataset is presented in **Fig. 7.25**. As the sensors bonded to the top flange were close to the neutral axis, the MSD threshold is about one order of magnitude smaller than the threshold associated with the sensors at the bottom flange. Overall, the strain gages bonded to the top flange and the web identify some outliers including those discussed in previous section. There were no outliers from strain gage data from the bottom flange although some are very close to the threshold and of similar values to the truck test.

### 7.3 CONCLUSIONS

This Chapter presented the numerical formulation and the empirical application of a SHM strategy for three bridges instrumented with strain gages adhesively bonded to different locations. The strain measurements relative to a truckload test, and the measurements collected during more than two years of structural monitoring were downloaded from a password-protected repository and processed. The interpretation of the experimental data was supported with a high-fidelity finite element model implemented with a commercial software. The results showed the excellent agreement between the numerical and the field data. Such agreement validated the accuracy of the model. The comparison also revealed the presence of a few non-critical anomalies in one of the structures being monitored. Finally, while most of the sensors operated well throughout the monitoring period considered in this study, some gages showed signs of drift, a few other stopped working earlier than expected, and the repository had two gages mislabeled.



## 8. THE ELIZABETH BRIDGE

This bridge was chosen to see if the loads in the cables were being distributed in accordance with the number of broken wires. A LFM was created for this bridge and the static analysis was performed by applying the weight of the truck close to those cables. The results of experimental and numerical data comparison showed that the predicted axial forces of the cables of the bridge are reasonable and acceptable. Even though the predicted axial forces of the cables are reasonable, they are not well aligned with the experimental data and some mismatches were observed. It is noted here that the Elizabeth Bridge was extensively rehabilitated and therefore the field data are obsolete with respect to the current rehabilitated bridge.

The bridge was also instrumented with strain gages on some truss arch members. In the LFM, the truss arch members were modeled as line bodies and analyzed using link/truss (only tension and compression) elements. Large mismatches between the experimental and numerical strains are observed at the location of the installed strain sensors. The large mismatch between the experimental and the numerical values suggest that the members were not behaving as truss members. This hypothesis is corroborated by the differences in strain between the two sides of any given member. In Task 5, it was concluded that the LFM of the Elizabeth Bridge may not be sufficient for predicting the true strain of the truss members because the contact of line bodies (truss arch members) with solid bodies (floor beams) cannot be modeled well in ANSYS, especially when there is a connection in the middle of the line bodies with the solid bodies.

The LFM was applied in order to quantify the effect of five damage scenarios at the two instrumented cables shown in **Fig. 8.1**. Specifically, namely the axial tension forces caused by the truck load at cables L8 Right, L8 Left, L9' Right, and L9' Left in pristine condition were compared to the simulated scenarios. **Tables 8.1** through **8.5** present the experimental and the numerical axial (tension) forces under the pristine and damaged conditions at certain locations of the bridge.

**Damage Scenario 1:** The modulus of elasticity of steel was reduced by 5%.

**Table 8.1** presents the axial forces under damage scenario 1 condition. The “Diff.” column of **Table 8.1** indicates that the tension forces decrease slightly when the Young’s modulus of the steel is 5% smaller. Except concrete deck, the structural members are made of steel. Therefore, changing the stiffness of all steel members does not change the load distribution significantly. Note that the presented values in the table are the axial forces, not strains. For example, strain in cable L8 Right in pristine condition can be expressed as  $\epsilon_{pristine}=F/(EA)$  and in damage scenario 1 condition is  $\epsilon_{damaged}=[(1-0.006)F]/(0.95EA)=1.046\epsilon_{pristine}$ . It means that the strain in cable L8 increased by 4.6% due to the damage but the axial force did not change considerably.

**Damage Scenario 2:** The modulus of elasticity of the concrete deck was reduced by 15%.

**Table 8.2** presents the tension forces at specific locations of the bridge under this second damage scenario. About 2% increase in axial forces is predicted due to the damage. This small effect is due to the fact that the bridge mainly consists of steel material. Therefore, the change in concrete stiffness does not change much the deformation at the gages’ location because the stiffness of the steel governs the overall stiffness of the bridge.

**Damage Scenario 3:** L10' cable was removed from the Left (upstream) truss.

The removed cable is highlighted in red in **Fig. 8.2**. **Table 8.3** present the tension forces associated with damage scenario 3. L10' Left cable removal changed the load distribution between the cables and therefore, the adjacent cables bear more load in comparison to the pristine condition. Gauge L9' Left is installed on the adjacent cable of the removed cable but the other three gauges are not close to the damage location. Accordingly, the tension force increased significantly at the location of gauge L9' Left.

**Damage Scenario 4:** Two diagonal members were removed from the Left and Right trusses.

**Fig. 8.3** shows the position of the removed diagonal members from the trusses. The axial forces under this damage scenario are listed in **Table 8.4**. The "Diff." column of the table demonstrates that the removal of the diagonal members did not change the tension force at the location of the installed gauges. This damage scenario may not be detected by the gauges.

**Damage Scenario 5:** The modulus of elasticity was reduced by 20% for the floorbeam which is under L8 left and L8 right cables.

The damaged floorbeam is shown in **Fig. 8.4**. **Table 8.5** presents the tension forces under damage scenario 5 condition. The installed gauges on L9' Right and L9' Left cables are not close to the damage location. Thus, for these gauges the tension force did not change. For the gauges installed on L8 Right and L8 Left cables, a 2% reduction in axial forces is observed. It is believed that the change in the stiffness of the floorbeam caused load redistribution between the adjacent floorbeams. Since the damaged floorbeam has less stiffness in comparison to the pristine condition, less load is transferred to it and more load is transferred to the adjacent floorbeams. Accordingly, the tension force in the L8 right and L8 Left cables is lower than the pristine condition.

Overall, it was found that the low-fidelity FE model is not adequate at matching the experimental data. Although the predicted axial (tension) forces of the cables were acceptable and reasonable, they were not well aligned with the experimental data. The analysis of the simulated damage demonstrated the importance of the sensors' location in accurate damage detection.

## 9. THE NEVILLE ISLAND BRIDGE

As a reminder, the bridge was instrumented with 64 wireless strain gages, 22 wireless displacement sensors, 6 wireless tilt sensors, 7 wireless accelerometers, and 2 cameras. The locations of the sensors are shown in **Fig. 9.1**. For this bridge, a LFM was developed using the geometric and material properties found in reference S-9424. The arches were modeled as line bodies and analyzed using beam elements. The diagonal members connecting the two arches were modeled as line bodies and analyzed using truss elements. The four 2.875 in. strands serving as hangers connecting the arches to the deck were replaced by a single 5.75 in. strand. The longitudinal and the vertical stiffeners of the floorbeams were neglected. The diagonal members at the bottom of the bridge were modeled as line bodies and analyzed using truss elements. Tie girders, floorbeams, and stringers were modeled as solid bodies and they were analyzed using solid elements. The rebar and diaphragms in the concrete deck were replaced by a steel plate located under the concrete deck. The LFM contained 320 structural components, about 327,600 finite elements, and about 1,174,500 nodes.

The LFM was used to predict the strains at some sensor locations under the same truck load used by the vendor and the numerical strains were compared to the empirical maximum measured strains listed in the tables of the Vendor's report. To compare the strain values at a certain time step, the provided time-strain graphs in Vendor's report were used. It was observed that most of the strain predictions in pristine condition of the bridge match the experimental data and there is a 100% agreement between experiment and model about the sign of the strain. However, some significant mismatch was observed for two sensors, namely S51 (installed on the West side of FB14) and S54 (installed on the East side of FB14).

In what follows, the strains under pristine and six simulated damage caused by a truck traveling north bound on the left lane (Tests 5&6) and southbound on the middle lane (Tests 9&10) are presented in **Tables 9.1** through **9.12**. The strains refer to the XY direction (see **Fig. 9.1**) for sensors installed on FB01 and FB14; and refer to the longitudinal direction for the sensors installed on the tie-girders. Each table contains a "Diff." column which quantifies the difference between the numerical strains under pristine and damaged conditions.

### 1- **Damage Scenario 1:** The modulus of elasticity of steel was reduced by 5%.

**Tables 9.1** and **9.2** present the strains under damage scenario 1 condition. The "Diff." column indicates that the strains increase about 5% when the when the Young's modulus of the steel is 5% smaller. Owing to the linearity of the model, the results were changed 5% and this observation confirms the reliability of the model since it replicates the real behavior of the linear material and the model can be considered as the digital twin of the structure.

### 2- **Damage Scenario 2:** The modulus of elasticity of the concrete deck was reduced by 15%.

**Tables 9.3** and **9.4** present the strains under this second damage scenario. A 0.8% - 1% increase in strains are predicted due to the damage. This small effect is due to the fact that the bridge mainly consists of steel material. Therefore, the 15% stiffness reduction of the 8 inches concrete does not change much the deformation at the sensors' location because the stiffness of the steel governs the overall rigidity of the bridge. The outcome of this damage scenario suggests that defects on the concrete deck may go undetected with the strain gauges installed on the floorbeams and tie-girder due to the sensors' sensitivity.

### 3- **Damage Scenario 3:** Cable 12 from the East arch (right side of the Northbound) and Cable 14 from the West arch (right side of the Southbound) were removed.

The removed cables are highlighted in pink in **Fig. 9.2** and the effects on the strains are presented in **Tables 9.5** and **9.6**. During Tests 5&6, the truck crossed the northbound left lane. **Table 9.5** shows that sensors installed on FB01 (S46 and S47) and FB14 (S54 and S55) are not impacted by the missing cables because the sensors are not close to the damage location. Instead, gauges S13 and S15 installed at the East tie-girder close to FB12 experience 4% increase in strain. The increment is due to the combination of two factors schematized in **Fig. 9.3**. The left drawing of **Fig. 9.3** displays the deformation of the tie-girder before and after the cable removal. Cable removal causes change in the deformation of the tie-girder and the strains increase at the location of the installed sensors on the tie-girder. On the other hand, cable removal reduces the stiffness of the boundary condition of FB12 (see the right drawing of **Fig. 9.3**). Therefore, the load distribution changes and less load is transferred to the East tie-girder and thus, the strains decrease at the location of the installed sensors on the tie-girder. Combination of these two factors caused about 4% strain increment for S13 and S15.

The same simulation was conducted with the truck travelling the southbound center lane (Test 9&10). Cable 14 was removed from the west arch. **Table 9.6** shows that the sensors on FB01 and on the tie-girder close to FB12 do not show any change compatible with the fact that they are not close to the missing cables. For the sensors installed on FB14, slightly less strains were observed, caused by load redistribution between the west and east side of the FB14 since a boundary condition changed (see the right drawing of **Fig. 9.3**).

#### 4- **Damage Scenario 4:** 0.1 in corrosion in the East tie-girder (right side of the northbound)

Corrosion was simulated by reducing the thickness of the flange and web of the tie girder as shown in **Fig. 9.4**. The results are presented in **Tables 9.7** and **9.8**. Similar to damage scenario 3, the corrosion reduces the stiffness of the boundary condition of the floorbeams at the East side. Therefore, less load is transferred to the East side of the floorbeams in comparison to the pristine condition as shown in **Fig. 9.5**. Since during Tests 5&6, the truck is in the northbound and the corrosion is modeled in the East tie-girder that is in the right side of the northbound, the FE model predicts less strains at the location of the installed sensors on the FB01 and FB14 according to **Table 9.7**. For the installed sensors on the tie-girder close to FB12, there is another factor that affects the results as well as the aforementioned factor. The other factor is that the section loss of the East tie-girder in this damage scenario, causes strain increment at S13 and S15. Combination of these two factors (i.e. load redistribution and section loss) resulted in strain increase for the installed sensors on the East tie-girder close to FB12.

According to **Table 9.8**, the sensors on the west side of the bridge show more strains because more load is transferred to the West tie-girder due to the simulated damage.

#### 5- **Damage Scenario 5:** Bolt loosening at the West side of FB01 and at the East side of FB12.

Bolt loosening mimics the effect of fatigue. To simulate this scenario, a part of the connection of FB01 and FB12 with their respective tie-girders was removed as shown in **Fig. 9.6**. **Tables 9.9** and **9.10** present the strains under damage scenario 5 condition. The damage reduces the local stiffness, which in turn causes a new load distribution pattern. Sensors S42 and S43 experience lower strains because less load is transferred to the West side of FB01 whereas, more deformation occurs at S46 and S47 bounded to the East side of the FB01 because more load is transferred to the East side of the floorbeam. The same explanation can be used for the installed sensors on the tie-girders close to FB12 considering the fact that the stiffness of the boundary condition of the East side of FB12 reduced due to the damage. The installed gages on FB14 do not change since they are not close to the damage locations.

**6- Damage Scenario 6:** The modulus of elasticity of the FB01 steel is 15% lower.

**Tables 9.11 and 9.12** presents the strains associated with the simulation of this damage scenario. The installed sensors on FB14 and on the tie-girders close to FB12 are not close to the damage location. Therefore, for these sensors the strains did not change. For the sensors installed on FB01, the change in the stiffness of FB01 caused load redistribution between the adjacent floorbeams. Since FB01 has less stiffness in this damage scenario, less load will be transferred to FB01 in comparison to the pristine condition causing lower deformation of FB01 (see **Fig. 9.7**).

The LFM applied to the Neville Island Bridge indicated that most of the strain predictions in the pristine condition matches the experimental data. However, the mismatches between the numerical and experimental strains were relatively significant for S51 and S54. The six damage scenarios were simulated to determine the plausible defects which can cause the mismatches for S51 and S54. However, the mismatches could not be justified by the damage scenarios simulated in this chapter. Strain experimental readings, position of the load truck, and variabilities associated with the finite element mesh are plausible source of the differences.



## 10. THE SANATOGA BRIDGE

### 10.1 INTRODUCTION

On July 23-24, 2018, the Vendor installed eight 2-D high resolution tilt sensors, 1 ultrasonic level meter sensors, 1 cellular Camera, and a data logger and remote communication gateway. The scope of the instrumentation was to observe any movement of the stone masonry arch ring or wall and to observe any scour. The duration of the instrumentation was originally planned for three years. The sensors were installed as follows. Four sensors facing north, i.e. upstream (**US-NF**). Two on the west arch (sensors label **US-NF-WW** and **US-NF-WW**), two located on the east arch (sensors label **US-NF-EW** and **US-NF-EW**). For each arch, one sensor was located on the east side, one on the west side. Four sensors were distributed on the south side, i.e. downstream (**DS-SF**). The distribution across the south side followed the same scheme of the sensors on the north side. They are labeled as follows: **DS-SF-WW**, **DS-SF-WW**, **DS-SF-EW**, and **DS-SF-EW**. There was no controlled live truck test performed on the bridge.

Pitt's investigators were informed about the occurrence of a flood. The flood occurred on July 11, 2019 in Sanatoga and the water level sensor showed at least 7 *ft* of water level increase. With 7 *ft* water level increase, the water passed the crown point of the arches, causing submersion of the instrument gateway and most of the tilt meters on the Bridge. As the figures of this section will demonstrate, the monitoring system were not affected by the flood.

On August 4<sup>th</sup> 2020, a storm increased the water level by approximately 7 *ft*, with a maximum depth of 9 *ft* from the bedrock. The average water level was about 2 *ft* from the bedrock. It was determined by the Vendor that the tilt meters showed no permanent change in the structure caused by the flood.

### 10.2 LONG-TERM MONITORING

**Figure 10.1** shows some representative the **raw pitches** and the corresponding 15-minutes averages. The two shown refers to sensors bolted downstream, i.e. south face (**DS-SF**). One tiltmeter, not shown here (the gage **DS-SF-EE**) survived 6 months and then became inactive. All other readings had a positive negative variation lower than 1 degree. A few sensors have shown a permanent pitch that have reached as much as +0.4 degrees. Some steps-up or -down are visible. The tiltmeter **US-NF-WW** (not shown here) underwent a significant abrupt step down and then step-up in Fall 2018. All long-term figures are presented in Task 3 report.

Alike **Fig. 10.1**, **Fig. 10.2** shows the **raw roll** and the corresponding 15-minutes averages of two tiltmeters. The roll data confirmed that tiltmeter **DS-SF-EE** survived 6 months and then became inactive. All other readings have a positive negative variation lower than 2 degrees. A few sensors drifted as much as 0.3 degrees with respect to the original zero value. Some steps-up or -down are visible. Alike for the pitch data, the roll recorded by the tiltmeter **US-NF-WW** underwent a significant abrupt step down and then step-up in Fall 2018.

**Figures 10.3-10.5** show the **raw values** and the corresponding 15-minutes averages of Tilt X, Tilt Y, and Tilt Z. It was also noted that none of these three parameters was zeroed at the time of installation and that all the values display significant drift as much as 4 degrees. These sensors exhibited the same behavior of a similar sensors installed on the Smithfield Bridge and at least one sensor installed on the Clairton Bridge. It is concluded that this low-resolution tiltmeters may not be fully reliable.

The analysis of the raw temperature recorded by the gage embedded in the tiltmeters revealed that all tiltmeters were off in January 2019 and summer 2019. This is seen in the representative graph of **Fig. 10.6**. Overall, it was observed that the temperature readings were consistent with the seasons with the extreme cold temperature recorded at the end of January of 2019 (as observed in other bridges).

**Figure 10.7** shows three graphs where the raw pitch is plotted against its corresponding raw temperature. The graphs are representative of three different responses observed in the data. The equation of the linear regression and the corresponding  $R^2$  value are provided as well. The summary of the quantitative values of the equations associated with the linear regression is provided in **Table 10.1**. Some pitch values have a positive gradient while others have a negative gradient. Several scatters are also visible. The same consideration were drawn for the raw roll vs the raw temperature data. Both the pitch and the roll data seem not to be strongly linearly related to the temperature as the  $R^2$  values for each gage is small. It is noted here that data associated with unrealistic temperatures below  $-20$  °F were not included in the analysis.

Some representative analyses of the parameters unbiased by any thermal effects is shown in **Figs. 10.8** (true pitch) and **10.9** (true tilt around the Y axis). These figures as well as the other not presented here for the sake of space, show a few short periods with no data that are preceded and followed by spikes. This suggest that the spikes were related to the sensors and not to bridge overload or arch movements. Most of the “true values” relative to the pitch and roll are within the resolution of the corresponding sensors.

The MSD applied to the true data recorded from the eight sensors are presented in **Figs. 10.10** for the pitch and the roll data, and **Fig. 10.11** for the Tilt data. The baseline consisted of values detected during the first month of monitoring. The graphs are presented in semi-log scale and the baseline (horizontal continuous line) was the four time the standard deviation of the baseline MSD. **Figure 10.10** reveals the presence of three significant outliers. Two of them occurred immediately after an interval with no data and may be attributed to issues related with the software/hardware. The third significant outlier was recorded on October 2018 and it may deserve further attention. The MSD relative to the Tilt data (**Fig. 10.11**) are similar to the pitch and roll data.

### 10.3 CONCLUSIONS

The visual observation of the raw data and the corresponding moving averages revealed that most of the sensors have drifted although not significantly (within 1 degree or so). A few significant spikes were detected most of which are believed to be related to software/hardware. The analysis of this bridge was challenging because the physical meaning of the Tilt data was unclear. Nonetheless, 7 out of 8 sensors were still active after 30 months. The data from the Sanatoga Bridge experience some of the issues seen elsewhere:

- Different sensors also have different time stamps even for the same quantity. For example, temperature readings from different sensors have different time-stamps.
- Some sensors in some occasions were not working (or data were not recorded) for several consecutive hours.
- One sensor became inactive after a few months.

## 11. FINDINGS / RECOMMENDATIONS

This Chapter reviews the findings/recommendations relative to the PennDOT bridge instrumentation program in the following areas:

1. *Evaluation of the proprietary software system for data extraction, presentation and analysis.*
2. *Evaluation of recorded data.*
3. *Long-term wireless sensor drift.*
4. *Damage estimation methodologies using recorded data.*
5. *Retrofit/repair evaluation using recorded data.*
6. *Analytical tools to achieve long-term bridge instrumentation objectives.*
7. *Temperature effects on sensor data”*

The evaluations presented here are based on the outcomes of the analyses of the installed systems, the recorded data, and the finite element modeling of the bridges.

### 11.1 PROPRIETARY SOFTWARE

Both the old and the new repositories are relatively easy to navigate and therefore no specific training was deemed necessary. For the old repository, we occasionally read the accompanying manual. Over the last 36 months, the old repository remained identical. Its functionality consists of plotting the time history for each given parameter, let say strain, across any interval of time that can be selected by the user. The strain vs time charts can provide some insights and an initial clue about possible anomalies. The website shows also links to photographs (in .jpg format) taken from the cameras mounted on the superstructure or the substructure of some bridges.

With respect to the old repository, the new repository has the following improvements and functionalities.

- 1) Each time history is accompanied with a histogram that reports the number of counts observed on that time interval with a specific value-bin.
- 2) The same time history is also accompanied by a box plot, which shows the distribution of the data with respect to the number of data points. Moving the cursor on the box plot allows the user to read some quantitative statistics of the plotted time waveforms.
- 3) The quantitative information attained via the box plot are also presented in a table form, which includes the standard deviation and the number of points (“N Values”).
- 4) The Fast Fourier Transform (FFT) of any given time waveform can also be added. This mathematical tool would be particularly useful for the identification of periodic trends.
- 5) Images from the cameras are readily available without the need to click on a link

For both repositories, the user can select which sensor visualize and which time-interval observe and has the option to export the corresponding data into .xls or .csv file. Both repositories allow to display the time histories relative to two or more sensors on the same graph. This is important to compare the performance of two or more sensors, or to observe the structural response of similar structural members.

The software has embedded thresholds that cannot be modified by the user but could (perhaps) be modified by authorized users. Any time, the value from a given sensor exceeds the set threshold, an alarm

is sent. Based on the Vendor Web Portal Manual: “*There are two different thresholds that need to be taken into consideration. Event detection threshold and Alert generation threshold. The event detection threshold is used by the sensor on its electronics to detect a variation of measurement that exceeds a preconfigured level. If an event detection threshold is triggered, an event will be detected and captured with higher sampling rate. The second type of the threshold is Alert generation threshold. This threshold is not applied on the sensors directly. The threshold will be triggered after sensor transmits its data into the database servers.*”

When working with the old software, we were not able to reproduce the same time-series seen in the truck tests Vendor reports, e.g. strain vs time. To our understanding, the graphs generated in the Vendor software cluster the data at regular time intervals, e.g. every 6 minutes. Data points were often stored at packets with the same timestamp. This makes it difficult to establish the duration of a transient event and does not allow to measure the speed of a truck, if an event is believed to be caused by the crossing of a heavy vehicle. The new repository does not have the same limitation as were able to plot the time series in a format that allows to time lapse of the same event recorded by two distant sensors.

During the execution of Task 3, we noted minor differences in the data extracted from the new and the old repository. One example was the accelerations collected from the Neville Island Bridge. We did not investigate the possible source of this mismatch because it did not seem to adversely affect the analysis. We believe that the difference may be relative to the timestamp associated with the individual data points.

**FINAL DETERMINATION.** Overall, we believe that the capabilities of the software system in terms of data visualization and extraction is good. We did not find any major issues of concerns or any major issues that could not be solved in the future. The scientific literature about bridge health monitoring (Task 1) shows the existence of dozens signal processing algorithms aimed at extracting sensitive features symptomatic of structural damage or unexpected structural response. Some of the functionalities seen in the new repository seem to go towards that direction. The fact that the data can be exported to *.xls or .csv* files for post-processing is relevant to allow future developers at coding *ad hoc* signal processing strategies. These ad hoc strategies can be aligned to finite element simulations as done in Tasks 5 and 6.

## 11.2 RECORDED DATA

To full potential of the recorded data can be achieved with some prepping that consisted in downloading, upsampling, and synchronization.

1) **Download.** The download of the data from the old repository was quite smooth. However, we had some technical issues in downloading data from the new repository.

2) **Upsampling.** The number of data points for a given parameter (strain, displacement, rotation, and acceleration) measured by a given sensor and the number of data points relative to the temperature measured by the same sensor are not the same. As such, in order to perform some of the analyses proposed in Task 3, we had to “align” the time domain of both series (the parameter and the temperature). This process required to up-sample, via linear interpolation, the raw temperature data in order to have the same timestamps for both the raw parameter and the raw temperature.

It is emphasized here that the difference in the number of data samples is not a flaw of the proprietary software, but it is common to SHM applications based on wireless sensing. As a matter of fact, the review presented in Ch. 3 has shown that sensing for SHM is characterized by much more sampled data points than, for example, temperature measurements. In addition, the manual of the old repository explains that the number of data points relative to the temperature may be different than the physical parameters recorded by the sensors.

3) **Synchronization.** The sensors installed on the bridges measured and transmitted the values of physical quantities such as displacement, acceleration, etc... in an independent and unsynchronized fashion from each other. In other words, the timestamps associated with these recorded quantities are not the same across different sensors on the same bridge. For instance, a strain gage bonded to location 1 on a certain bridge measures strain at that location. Another gage located at a different position measures strain as well, but the measurements from these two sensors may not be synchronized. This is because all the sensors work independently and are triggered independently. This requires some pre-processing, referred here as synchronization, in order to “align” the data samples in the time domain. The synchronization was a step necessary to apply some of the algorithms implemented in this project. As for the up-sampling, synchronization is another process that would have been likely performed even if another SHM system and another proprietary software had been used. As a matter of fact, wireless SHM sensors typically operate “independently” and are triggered by local events.

Synchronization errors may occur because each sensor in the network has an independent processor, with its own local clock, which is not necessarily synchronized with the clocks of other sensors. Moreover, even with clocks perfectly synchronized, the data may lack synchronization because: (1) the sensors start sensing at different times due to random variations in the processing time in the sensor board driver; (2) the low quality of crystals may cause differences in the sampling frequencies among the nodes; and (3) the sampling frequency for each individual sensor node can fluctuate over time because of jitter<sup>3</sup>. The scientific literature contains several time-synchronization protocols for wireless sensor network.

The possibility to transfer the data and to save them as a *.xls* or *.csv* file was excellent and offer the opportunity to develop user-designed algorithms, to analyze the data and generate outcomes that can be used in maintenance and planning. We encourage PennDOT to consider the opportunity to analyze the data in the future, and expand the possibilities offered by the availability of the data.

Some gages measure physical quantities along orthogonal directions, namely X, Y and Z. Although Pitt researchers could interpret the meaning behind each direction the sensor-manuals found on the Vendor’s webpage, these directions may need to be specified more clearly to avoid any potential misinterpretation by future users.

Based on the information collected during this project, the Vendor’s has set one or more threshold values that trigger an alarm when these values are exceeded. A similar approach can be established when post-processing the data and applied for any given parameter (strain, displacement, or acceleration). The quantification of this threshold was not studied as not part of the scope of work. There are several approaches to set such a critical value, some of which based on simple empirical evidence while other based on heavy statistics. For example, it can be labeled as critical any value reached by any given structural element being monitored by a given sensor in response to a controlled truck test. As investigated during execution of Task 3, this “critical” value may represent a reliable approach to identify any unauthorized overload crossing but not necessarily symptomatic of structural problems. Another possible approach may rely on the computation of the average value  $V_{avg}$  and the standard deviation  $\sigma$  of an extensive set of data collected under normal regular operation and then set as “critical” any value above or below  $V_{avg} \pm 4\sigma$ . It is believed this approach might be too conservative especially if rarely detected or barely exceeded. For the strain data, a critical value could be set if the yielding stress (for steel) or ultimate strength (for concrete) is approached beyond the safety factor.

**FINAL DETERMINATION.** Owing to the total number of sensors installed on the ten bridges, and owing to the length of the monitoring period, we believe that the overall quality of the recorded data and the overall quality of the sensors was quite good and for some bridges excellent. Only in a very few

---

<sup>3</sup> In the context of this report, jitter is the deviation from true periodicity of a presumably [periodic signal](https://en.wikipedia.org/wiki/periodic_signal), often in relation to a reference [clock signal](https://en.wikipedia.org/wiki/clock_signal) (<https://en.wikipedia.org/wiki/Jitter>).

circumstances, the values of the recorded data had raised some concerns that warrant either a site visit to inspect the structural element of the bridge to which the sensor was bonded to, or a discussion with the Vendor. An example is the strain gage readings at the North Side of the Birmingham Bridge and the low-resolution rotation gages on the portals of the Smithfield Street Bridge. As noted by the Vendor in two of the reports we studied during task 2, the adhesive type strain gage shall not be bonded directly to concrete materials because moisture may degrade the bondline.

The acceleration data collected from the old website are sampled in a way that prevents the joint time-frequency analysis, which is necessary to identify the modal characteristics of the bridge. To this end, it is necessary to use the new portal to analyze the accelerometers' data appropriately.

The state-of-the-art review completed in Task 1 revealed that the scientific literature is scarce about long-term (> 3 years) continuous data monitoring. The fact that the sensors installed in some bridges are providing uninterrupted information till these days is noteworthy. To offer a holistic view of the sensor activities, **Table 11.1** specifies, for each bridge, which sensors are inactive or active. The Table demonstrates that a notable portion of the sensors, especially on the Smithfield Street and Clairton-Glassport bridges, are still working and the data stream continues. For other bridges the SHM system was terminated because the bridges were subjected to extensive rehabilitation (Elizabeth Bridge, Neville Island Bridge), not maintained because beyond the planned period of performance, or because in Spring 2022 the carrier upgraded the service to 4G and without modems being upgraded, data could not be transmitted. The only modems that were ungraded were those for the Smithfield Street Bridge and The Clairton-Glassport Bridge in April 2022.

### 11.3 DRIFT

One remarkable aspect of the SHM systems used in this PennDOT pilot program is the use of wireless sensors. The increased use of wireless sensing technology in SHM responds to the evidence that traditional wired SHM systems, due in part to cabling networks, are detrimental for the deployment of high-density sensor systems. SHM using wireless sensors can overcome the limitations of traditional wired methods with many attractive features such as wireless communication, on-board computation, battery power, ease of installation, and so on. As such, platforms for SHM containing wireless smart sensing (WSS) represents an attractive alternative to their wired counterparts because of the lower cost achieved by removing the need for cables (including cost for labor). One of the challenges is associated with drift. In wireless-based SHM systems, drift is a slow decrease in accuracy that can at times go unnoticed if not appropriately monitored. If a sensor becomes too inaccurate, it can trigger false positives or (in the worst-case scenario) false negatives. False positives would force crews to the field to verify the alarms triggered by the system. False negatives would leave critical damage to go unnoticed until the next cycle of bridge inspection. Engineers and SHM specialists are therefore challenged with the development of methods and strategies to alleviate or eliminate drift due to sensors age without becoming a costly practice that nulls the economic advantages of wireless sensors with respect to wired technology.

Overall, we believe that the tiltmeters were the only sensors that exhibited signs of drift. Long-term observations showed that drifts involved the low-resolution tiltmeters. This is shown in **Fig. 11.1**, which presents the data from the North and the South Portal of the Smithfield Street Bridge. The left column refers to the gages installed on the north portal of Span 3 (closer to downtown). The right column presents the measurements from the gages installed on the south portal of Span 4 (closer to Southside / Station square). The data cover the time between installation and mid-September 2022. The angle measured by all five tiltmeters steadily increased and positive rotation means counterclockwise rotation. As the tiltmeters are about 4 meters from the ground, a rotation of 1 degree from the base, implies a horizontal shift of the tiltmeter of about ~70 mm, (2 ¾ in.). The rotations observed in **Fig. 11.1** were not confirmed by the high-resolution tiltmeters data presented in **Fig. 11.2**, which shows that each element of the bridges

rotated seasonally much less than 1 degree. In addition, PennDOT personnel went to the bridge and noted no abnormalities with the portal. As such, it can be concluded that the sensors whose data are shown in **Fig. 11.1** were drifting.

Significant high strain (in the order of millistrains) was recorded by a few gages bonded to the Birmingham Bridge, PennDOT crew was sent to the bridge and did not find anything anomalous.

**FINAL DETERMINATION.** Owing to the large number of wireless sensors involved in this study and the small number of sensors that have shown suspicious signs of drift, we can consider the performance of the sensors quite satisfactory in terms of drift. We would recommend the use of these sensors in the future, except for the low-res tiltmeters for which we recommended a discussion with the Vendor to identify the source (mechanical, electronic) of the observed drifts.

#### **11.4 DAMAGE ESTIMATION METHODOLOGIES USING RECORDED DATA**

The literature review conducted as part of Task 1, which included the state of practice in the United States, revealed the large number of methodologies in terms of sensors type, hardware, and signal processing. In addition, the challenges associated with environmental effects such as temperature and cost were discussed. In task 3, we proposed several methodologies to detect structural anomalies from the recorded data, due to service load and thermal load. We also proposed an effective strategy to separate traffic load (and other transient events) from thermal load.

The damage estimation methodologies were enhanced by comparing the experimental data to the numerical calculation obtained with the finite element models. In addition, the models provided a valid instrument to quantify the required sensitivity that each sensor should have and the area around the sensors that can be effectively monitored. The high-fidelity and low-fidelity (line-element) models were used to evaluate damage, deterioration and subsequent repair scenarios. Since the low and high-fidelity models were generated in ANSYS based on the structural drawing provided by PennDOT, the models represented the pristine condition of the bridges. Any degradation after construction was not initially included in the models. Having the analysis results from the numerical simulations and comparing the structural response of the models with the empirical sensors data helped identify any damage/degradation in the bridges.

We believe that the ability to detect damage using the current sensing system is strongly dependent on the bridge type and the location of the gages. During this project, we revealed that some bridges do not have a uniform response to thermal loading. In other bridges, we noted that some shear keys may not work as expected by the design. For some structures, the finite element models reveal that damage would have no effect or very minimal effect to the strain at areas instrumented with sensors.

In terms of bridge health monitoring, Tasks 3-6 have demonstrated the ability and the reliability of the proprietary hardware/software and of the algorithms we have developed at evaluating:

- 1) unsymmetrical responses to static load, i.e. unsymmetrical loading distribution between structurally symmetric elements.
- 2) the presence of heavy transient loads caused, for example, by the crossing of heavy trucks.
- 3) the growth of local deterioration by observing high strains at certain sensors.
- 4) the presence of existing damage.

**FINAL DETERMINATION.** Overall, we believe that the data analysis performed in this WO-003 project has proven the value of SHM in bridges. Owing to the nature of the structures being monitored, and owing to the relatively short span of the monitored period for some the bridges, it is unlikely that new

damage would have been developed and progressed to a level that would have been detectable and localized. The absence of baseline values associated with the pristine structure requires accurate modeling of the bridges to detect existing damages as carried out during the execution of Tasks 4 and 5. The drawings provided by PennDOT to Pitt investigators were sufficient to generate both low and high-fidelity models, which in turn were instrumental to determine the effectiveness of the SHM at detecting damage and more in general at evaluating the reliability of the sensing system.

### **11.5 RETROFIT/REPAIR EVALUATION USING RECORDED DATA**

To our knowledge, only the Neville Island Bridge and the Elizabeth Bridge were retrofitted after being instrumented. However, the SHM system was shut off before the work began. As such, the evaluation of the effect of the repair on the sensors data, i.e. on the structural response of the bridge could not be quantified.

To compensate for such lack of experimental data, we performed some finite element analyses that considered two different scenarios. For example, the prestressed concrete adjacent box girder bridges were considered with and without shear keys between the girders and the deck, i.e. with and without composite behavior. We proved that the strain gages could reveal the difference. However, the experimental proof could not be provided as the instrumented box girder bridges were retrofitted before instrumentation.

To evaluate the retrofit/repair using sensors' data, it is required to have the SHM system active on the same bridge before and after the repair or retrofit process. Otherwise, there is no ground to compare the structural behavior of the bridge prior and after of the rehabilitation.

**FINAL DETERMINATION.** Similar to what discussed for the ability to detect damage, the capability of the current SHM system at evaluating the effectiveness of rehabilitation/repair is strongly dependent on the location and the number of sensors used.

### **11.6 LONG-TERM BRIDGE INSTRUMENTATION OBJECTIVES.**

The fact that the sensing system in two bridges is still active and provided 3+ years' worth of recordings from four other bridges (**Table 3.4**) makes the pilot program successful in terms of long-term instrumentation. The storage and maintenance of large amount of data fall within big data management.

Within the scope of this pilot bridge instrumentation program, Pitt investigators developed strategies for the analysis of a massive amount of data that proved to be reliable and effective. Specifically, we:

- Demonstrated that the strain increase (as well as any other parameter) associated with the crossing of an individual truck of a given known load can be rapidly and easily determined by using some certain signal processing that removes the temperature bias from the raw data.
- Applied the same signal processing to the whole time-series (raw data) to identify potential occurrences that could be related with suspicious and potentially harmful (for the bridge) events.
- Implemented an unsupervised learning algorithm based on outlier analysis to identify anomalous readings from the whole set of data.
- Created the conditions to use principal component analyses, which is one of the most common strategies to separate temperature effects from other effects, to the pre-processed raw data.
- We proposed ways to analyze data that could be used in future studies.

**FINAL DETERMINATION.** We did not identify any concerning issues about the availability of long-term bridge instrumentation data using the current version of the hardware and software provided by the Vendor. Although some technical issues were observed about the new repository, we believe they can be solved.

### **11.7 TEMPERATURE EFFECTS ON SENSOR DATA.**

The (detrimental) effects of the temperature on many of the physical parameters measured by the SHM systems have been known to SHM specialists for at least two decades. The data collected from the ten bridges that are part of the PennDOT pilot program do not make any exception. Temperature-dependent deformations have been a concern for decades, and a number of techniques to remove such effect using signal processing were proposed. As summarized in the report of Task 1, temperature plays perhaps the most detrimental role in SHM because some parameters, such as strain, are affected by temperature more than live loads such as those associated with traffic. In Task 3, we developed some specific strategies to remove the effect of temperatures on the static properties of the bridges we analyzed. These strategies span from calculating the difference between raw and 15-minutes averaged data and further cleansing to a more sophisticated principal component analysis. Owing to the limited number of dynamic sensors, namely accelerometers, deployed on three bridges (Smithfield, Clairton-Glassport, and Elizabeth) the temperature-effects on the dynamic properties of bridges were ignored.

By comparing what we called the live (true) values to the corresponding values reported by the Vendor for the truck test, we believe that the proposed strategies to remove the effect of the temperature was effective.

**FINAL DETERMINATION.** Overall, the temperature sensors embedded in each gage performed well and were consistent across the whole array. This allowed establishing relevant relationship between a given parameter and the temperatures. These relationships can be used as markers to identify some type of problems within the structures.



## 12.PUB 238 UPDATES to 2022 EDITION: Part IE, Chapter 8 – Nondestructive Load Testing

This chapter presents the proposed updates to Chapter 8 Part IE of Pub 238. To facilitate the identification of the suggested amendments, the parts to be removed are highlighted in yellow with strikethrough, while the sentences to be added are highlighted in green.

### 12.1 BRIDGE INSTRUMENTATION

The purpose of instrumentation and monitoring of a bridge is to help diagnose a known deficiency and aid in the development of retrofit details to correct the deficiency.

The diagnostic testing shall include both the static and dynamic response of the bridge. The diagnostic testing must be implemented in accordance with a pre-defined test program including objectives and a detailed instrumentation plan. Typically, instrumentation and monitoring has been used to perform fatigue evaluation of steel bridges for the purpose of estimating remaining fatigue life and developing retrofit concepts. The instrumentation and monitoring of a bridge shall not be used to determine the load carrying capacity or load posting unless otherwise approved by the Chief Bridge Engineer. The bridge load carrying capacity predicted from field load testing is affected by several factors such as:

- unintended composite action
- unintended continuity or bearing fixity
- participation of secondary members
- participation of nonstructural members
- portion of load carried by deck

These factors tend to influence test results by indicating lower live load stresses than calculated stresses, and thus predict a higher load carrying capacity at service load levels. The enhanced behavior due to unintended participation may not be present at load levels higher than the test load. At the higher load levels, the loss of unintended participation will result in increased stresses in main members. Therefore, the extrapolation of test results to determine the load carrying capacity at load levels in excess of the tested live loads is not permitted.

The reliability and the accuracy of the sensing system may be determined using a detailed model of the bridge in combination with static and dynamic analysis. If accompanied by field load testing, the static and dynamic analysis may be able to quantify the effects of the five factors listed above. A detailed model may include all structural components of the bridge. If such a detailed model is available, it may be considered to determine the load carrying capacity or load posting of a bridge.

If the instrumentation and monitoring is designed to remain active for several months, the monitoring system may be utilized to potentially detect the growth of known deficiencies that may become critical between two consecutive routine bridge inspections. It would also be desirable to detect other potentially critical issues through instrumentation which may not be visually discernible. An example may be the detection of frozen bearings or high stress levels at a location of potential crack propagation.

## 12.2 CONTRACTING PROCEDURES

The instrumentation and monitoring of bridges is a professional service. Companies that intend to provide these services must be a registered business partner with a relationship type classification of consultant in the Department's Engineering and Construction Management System (ECMS). In addition to registering as a business partner, the company must have an active consultant qualification package, an approved overhead rate, and an employee roster in ECMS. Companies intending to provide testing services must have a demonstrated record of performing such work, including both the physical installation of monitoring systems as well as the interpretation of the data.

Typically, this service is one of many tasks within a contract, and therefore bridge testing service is performed by a sub-consultant on behalf of the consultant.

## 12.3 INSTRUMENTATION

The instrumentation used for diagnostic bridge testing may include:

- ~~Strain gages or other types of strain transducers~~
- Strain gages, preferable temperature-compensated, or other types of strain transducers
- Displacement transducers
- Rotation gages
- Accelerometers
- Cameras
- Weigh-in-motion sensors

Ideally, one or more of the sensors type listed above shall have the capability to record temperature. If the temperature is captured with the sensors being utilized in the instrumentation, the temperature shall be sampled at the same rate of the static parameters being stored (strain, displacement, rotation, etc.). If one or more cameras are to be used, they should be placed in a manner to be able to see the trucks that are going over the bridge and have the ability to read the license plate. Also, where applicable, one or more cameras should point downward at a pier to see barge collisions.

The instrumentation must be connected to a data acquisition system that is capable of capturing and storing response data for processing of the results to fulfill the objectives of the testing program. Specifically, data must be sampled at a rate high enough to ensure that the peak response of a given bridge element is captured. Moreover, the data acquisition system must have sufficiently high resolution to ensure that the complete response of a given bridge element is measured. For fatigue evaluations, the data acquisition must be capable of performing cycle counting using the rainflow cycle-counting algorithm. This algorithm is used to develop the measured stress-range histograms at strain gauge locations.

## 12.4 DIAGNOSTIC TEST PROGRAM

A diagnostic testing program shall be developed prior to the field instrumentation and monitoring of a bridge. The program shall include the test objectives, level of structural analysis to be performed prior to and after field testing, types and layout of instrumentation, the test load to be used, field testing procedures, expected duration and requirements for maintenance and protection of traffic, as well as evaluation methodology of test data and reporting. The test load may consist of controlled vehicles of known weight and/or the regular traffic on the bridge. Using controlled vehicles of known weight

traveling at known locations provides data to correlate the responses of all sensors with a known load. The controlled test, when running test vehicles along the same positions at crawl and full speeds, also allows assessing the effects of dynamic impact.

When the test load uses vehicles of a certified weight, it should be performed under closed-to-traffic conditions if logistics allow. If the bridge is instrumented at control members that are subjected to high-stress/high-strain, the stress and strain induced during the controlled truck test may be used to establish a conservative threshold to flag trigger events that may overstress control members or structural components prone to fatigue or prone to damage. Ideally, the time waveforms associated with the observed physical parameters (e.g. strain, displacement, etc.) recorded during the crossing of the truck testing should be made available for post-processing analyses. For strain sensing a strain resolution of 1  $\mu\epsilon$  is preferable. Dynamic effects and dynamic response of bridges may be better assessed if the time waveforms are sampled above 10 Hz.

Each bridge is unique and therefore, when compared to even similar bridge types, may respond differently to the same controlled truck load testing, leading to different readings even from identical monitoring systems. As such, the definition of a threshold for instrumentation frequency or for trigger events should be made case by case, by whoever performs the truck test and examines the results, and a bridge engineer.

## 12.5 EVALUATION OF INSTRUMENTATION RESULTS

The test results shall be evaluated in such a manner to satisfy the objectives set in the test program. The results of the instrumentation should be compared to analytical predictions to demonstrate the validity of the tests. A comparison of static and dynamic measurements shall be performed to assess the dynamic amplification effects. In addition, a determination of live load distribution factor shall be performed. The calculated live load distribution shall be compared to values predicted from the AASHTO LRFD Bridge Design Specifications. For fatigue testing results, measured stress range histograms shall be compared to the S-N fatigue curves in the AASHTO-LRFD Bridge Specifications.

## 12.6 REPORTING

A comprehensive report shall be prepared describing the general features of the bridge, the objectives of the testing program, description of the testing procedures, instrumentation plan, instrumentation results, interpretation of the instrumentation results (including but not limited to data management and data mining), and comparison of results with numerical analysis, as well as the evaluation of the results per Section 5.5I for dynamic amplification effects and live load distribution. The objective of the instrumentation and monitoring is to ~~correct a known deficiency~~ monitor over time a known deficiency between two inspection cycles, to evaluate the static and dynamic effects of a known deficiency, or to detect and monitor structural anomalies that cannot be inferred with conventional bridge inspections. ~~thus~~ The report may include repair recommendations and retrofit concepts if warranted based on the results of the static and dynamic evaluation. The report shall include an executive summary, photographs of the instrumentation, and graphical and tabular presentation of results. The report shall be signed and sealed by a Professional Engineer Registered in the Commonwealth of Pennsylvania.

## 12.7 INSTRUMENTATION SYSTEMS

~~The most common method of determining the behavior of a bridge is through instrumentation with strain gages/transducers and displacement measuring devices.~~ The most common method of determining the behavior of a bridge is through instrumentation with devices that measure strain, displacement,

**acceleration, and temperature.** The use of strain and displacement measuring devices has proven history of providing reliable results that fulfill the objective of most bridge testing programs.

As technology continues to evolve, additional types of sensors, instrumentation devices, or wireless or remote monitoring systems (both in terms of sensors and data acquisition systems) have been developed or are still being developed. New instrumentation systems that have not been used by the Department shall be evaluated for proof of concept. The proof-of-concept evaluation may occur by:

- Concerted research project conducted by the Department Success performance and favorable evaluation of the system by another Department of Transportation or governmental agency.

#### COMMENTARY:

IC5.7I Two different monitoring sensors have been tested through Research Project No.: 3900017209, titled “Remote Health Monitoring and Load Modeling of Cracked Fracture Critical Bridge Components”. LifeSpan Technologies’ Model LST Structural Health Sensor (LST) and Matech Material Technologies’ Electrochemical Fatigue Sensor (EFS) systems.

A third project, Contract No 4400017287, 3515R08 “Instrumentation & Monitoring of PA Bridges.” The contract duration is 2017 thru 2021 and the instrumentation that is being evaluated under this contract is by Resensys.

## 13. CONCLUSIONS

In the study presented in this report, advanced data management, analysis, mining and inference approaches for bridge health monitoring, safety evaluation, and reliability of instrumented bridges in Pennsylvania were investigated. The study included a review of the existing bridge health monitoring programs in the United States and the creation of finite element models for those bridges that are part of the PennDOT pilot bridge program, which began in year 2017.

The study demonstrated the potential benefit of the pilot bridge instrumentation program especially if it includes a comprehensive signal processing and statistical analysis, and is complemented with high-fidelity finite element modeling of the monitored bridges. The data provided real-time information about structural static responses. Although an official survey nationwide had not been conducted, it would not be a surprise to learn that this pilot program is one of the most long-lived bridge health monitoring programs in the U.S., given that the sensing system installed on two bridges are still active after more than two years.

While it is too premature to consider SHM as a replacement of bridge inspection, the study presented in this report has demonstrated that there are cost-effective values on the use of sensor systems in support of bridge management and maintenance. One of the keys for the success is to install the sensors at appropriate locations and possibly adding sensing redundancy. In what follows, a few concluding remarks are provided in terms of instrumentation, data inference, and finite element modeling.

### 13.1 INSTRUMENTATION PROGRAMS

The review of the instrumentation programs for the health monitoring of U.S. bridges was based on documents found in the scientific literature and available to the public. The review focused primarily on the three primary topics: (1) methodologies and objectives of the programs; (2) data inference methods to evaluate structural parameters and detect structural irregularities; and (3) validation techniques to assess the accuracy of the recorded data. The review included nearly seventy bridges. Most of the documents were authored by researchers from the academia and only a small fraction came directly from companies financially involved with the instrumentation being installed. The following conclusions were drawn:

1. Most of the bridge instrumentation programs included at least three different sensors types: one to collect ambient conditions (e.g. temperature and wind); one to collect static performance (e.g. strain gages); one to collect dynamic responses (e.g. accelerometers).
2. Most bridges were less than 30 years old at the time the monitoring began. A few bridges were instrumented during construction. Strain gages are, by far, the most common instrumentation used.
3. While conventional foil strain gages, i.e. ERSGs, were extensively used in old programs, in recent years there has been an increasing interest in fiber optic technology, which is also gaining momentum as fiber optics may integrate multiple sensing modalities using robust and rugged technology.
4. A good number of publications report short-term monitoring, which refers to a few controlled load truck tests.
5. Long-term monitoring programs are in most cases continuous observations conducted over a few months period and in a few cases a few years period.
6. Time-series associated with the dynamic response of bridge are almost always converted into the frequency domain in order to extract the frequency of vibration of as many modes as possible and use them as indicator of potential damage.

7. There is a general consensus that temperature plays a detrimental role in the modal analysis of bridges and any robust SHM strategy cannot disregard the effect of temperature on mode shapes and vibration frequencies in order to avoid false positives/negatives.
8. Wireless sensors are gaining momentum in bridge health monitoring. However, there are still technical challenges that prevent their exclusive use in lieu of conventional wired systems.
9. Owing to the size of the structures being involved and owing to the nature of the degradation processes, robust finite element modeling seems to be the preferred way to validate any SHM protocol installed in a given bridge.
10. Whenever finite element modeling has supplemented the SHM protocols, the latter ones are deemed the ones providing the accurate results and therefore the models are calibrated to “match” field data. As such, researchers have come to the conclusion that field measurements are reliable and initial models are not accurate enough to portray the effective response the structure to real loads and traffic. So, calibration is always warranted.
11. Only a few studies have reported inaccuracies of sensors data. Most of the issues reported was related to vandalism, power supplies, and maintenance. It is believe by the authors of this review that any issue associated with the sensors that invalidated data would not be reported in the published documents. As such, it is difficult to gage the success rate and the durability of the instrumentation programs presented here.
12. When bridges have very little in common with each other, it is difficult to design a uniform SHM paradigm valid for any bridge. What is adequate for some may not be adequate for another. This complication increases when structures are modeled but damage can only be simulated numerically but not induced experimentally. The consequence is that there is no guarantee that a damage identification method developed for a certain bridge is applicable to another bridge. As demonstrated in a few studies (e.g. Talebinejad et al. 2011) some methods work and some methods do not even work for a given bridge using the same data set.

### 13.2 PENNDOT PILOT INSTRUMENTATION PROGRAM

The review of the ten bridges involved in the PennDOT pilot bridge instrumentation program included the examination of drawings, SHM instrumentation plans, latest inspection reports, and live load test reports. All these documents were provided by PennDOT to the Pitt investigators. The bridge ratings according to inspection reports submitted not later than year 2020 are summarized in **Table 13.1**. The SHM systems were installed during the period 2017-2019. Only the systems on the Smithfield Bridge and the Clairton Bridge are still active (as of May 2023).

From the password-protected repositories, the data recorded during test-load events and representative service load events were recorded. While the “*data recorded during test-load events*” were easy to identify and isolate, the identification of “*representative service load events and, if available, extreme load events*” required some prepping and massive analyses. The time histories of the recorded parameters were split in three time-intervals.

- a. The first time-interval included the first few days around installation. This set of data may enable to identify and quantify offsets in the data recordings that are carried over throughout the lifespan of the sensor, quantify the daily variations induced by the temperature on the pristine sensors, determine whether the gages were reset to a zero value after installation, and to establish the temperature of the structural member at the moment of the installation. The latter information can aid in the exact determination of the true strain on any given structural member being monitored.

- b. The second time series was about the truck test and consisted either the whole day during which the test was performed or just a few hours. The analysis of the truck test enables to achieve one of the main goals of Task 3: quantifies the strain, displacement, etc... induced on a given structural member by a known concentrated load. Besides that, the quantification of the physical parameters establishes a benchmark against which all the other data can be compared to in order to identify overstresses that may be associated with illegal heavy truck crossings, and enables to validate the quality of some of the algorithms we have developed.
- c. The third time-interval spans from the day after the truck test until the day before download. In this report, we denoted this time-interval as the long-term monitoring period. The long-term analysis enables to identify structural anomalies, sensors anomalies, transient events, etc. For the analyses at bullets *b* and *c*, a series of data processing algorithms were created, developed, and finalized throughout the execution of the task. The data processing had multiple objectives that spanned from the removal of thermal bias to determine the value, e.g. strain, associated with transient event in order to identifying anomalous data without the need to consider every single sensor.

Overall, the following conclusions were drawn about capabilities, performance, drift, and temperature effects.

***(1) Evaluate the capabilities of the software system in terms of data extraction and analysis.***

- The accessibility to the software was relatively easy and straightforward. Pitt investigators found the software suitable to extract graphs of interests where a given parameter (strain, displacement, temperature, etc.) is displayed as a function of time for any given interval selected by the user. The strain vs time charts can provide some insights and an initial clue about possible anomalies. However, any further analysis requires download and post-processing.
- The old and the new repository are organized in a way that any user can access and visualize the data collected from sensors as time histories. The user can choose any arbitrary time interval and plot the values, let say strain, as a function of time directly on the website. The user has the option to export the same data relative to the same interval to *.xls* or *.csv* file. Because MS Excel cannot manage millions of lines, the *.xls* or *.csv* files were opened in Matlab.
- The portal offers the option to display in a single plot the time-history of the same parameter, e.g. strain, from different sensors. This is an important feature that may help compare the performance of two or more sensors, or to observe the structural response of similar structural members.
- Pitt investigators were not able to produce the same time-series seen in the Vendor's truck test reports. To our understanding, the graphs generated in the Vendor software cluster the data at regular time intervals, e.g. every 6 minutes. Data points are often stored at packets with the same timestamp. This makes it difficult to establish the duration of a transient event and does not allow to measure the speed of a truck, if an event is believed to be caused by a heavy truck crossing.
- It seems that the above problem has been solved with the new repository, where each single data point has a unique timestamp. Sometimes, however, we have encountered some technical problems when downloading the accelerometers data from the new webpage.
- The majority of the sensors are reporting temperature in addition to the main physical quantity they are set to record. The temperature readings from different sensors are very consistent and showed very good agreement between one sensor compared to another one. This implies that the thermometers embedded in the sensors are of high quality and durability.
- In a very few cases a given sensor is shown twice in the database while another sensor is missing. As an example, the rotation gage number 06 of the Smithfield Bridge is presented twice but data from

rotation gage number 05 seems absent in the repository. Some doubt is also cast about two sensors on the Chester Bridge; namely, the labels of sensors 04T and 04B are perhaps inverted.

- The general structure of the webpages is such that any authorized user can easily extract the data. Not only the sensors on a desired bridge can be selected, but the measured quantity (such as strain, temperature, ...) and the time window of the measurements can be set in a pretty straightforward way. In a few occasions, we noted minor differences in the data extracted from the new and the old webpages. The accelerations collected from the accelerometers of the Neville Island Bridge are an example. This means that these two webpages may not provide the same identical data. We did not investigate the possible source of this mismatch because it does not seem to affect critically the determination of the health of the bridge.

**FINAL DETERMINATION.** Overall, we believe that the capabilities of the software system in terms of data extraction and analysis is good, for we did not find any major issues of concerns or any major issues that could not be solved in the future. As notable events may occur sharply and briefly, the plots containing a few data points every hour may miss some relevant information (or events) that have occurred in between. The use of a trigger level to record and store dense data point immediately before and after a certain trigger (threshold) is exceeded represents a valuable solution. However, the trigger value should be determined on a case-by-case situation, given the unique geometric and structural characteristics of each bridge.

***(2) Perform an evaluation of the quality of the recorded data.***

- We believe that the overall quality of the recorded data and the sensors was good and for some bridges excellent. In two circumstances, the values of the recorded data raised concerns and a site visit was warranted. It was determined that the values were false positives due to drift.
- The acceleration data collected from the old website are sampled in a way that prevents the joint time-frequency analysis, which is necessary to identify the modal characteristics of the bridge.
- Based on the outcomes of the state-of-the-art review conducted under Task 1, there are not many cases reported in the scientific literature about long-term (> 2years) of continuous data monitoring. The fact that the sensors are providing uninterrupted information for a few years is noteworthy.

**FINAL DETERMINATION.** Owing to the total number of sensors installed on the ten bridges, and owing to the length of the monitoring period, we believe that the quality of the recorded data is satisfactory, and the reliability of the majority of the sensors is good.

***(3) Evaluate long-term wireless sensor drift.***

- One noteworthy feature of the SHM systems installed on the ten bridges is that all the sensors involved were wireless. One of the challenges associated with the network design and physical implementation and monitoring is drift, i.e. the slow decrease in accuracy that can at times go unnoticed. Many low-resolution tiltmeters and a few strain gages exhibited signs of drift.
- As stated by the Vendor in one of their reports, adhesively bonded strain gages did not work well when bonded to concrete. For concrete structural elements, bolted-based strain gages show longer durability and better reliability. However, the effect of the temperature is amplified because the bolted strain gages are not temperature compensated (as disclosed by Vendor in the operating manual).

**FINAL DETERMINATION.** Owing to the large number of wireless sensors involved in this study and the small number of sensors that have shown signs of drift, we can consider the performance of the sensors satisfactory. Doubts about the performance of low-resolution tiltmeters (rotation gages) are cast.

***(4) Assess temperature changes on recorded data.***

- The (detrimental) effects of the temperature on many of the physical parameters measured by the SHM systems have been known to SHM specialists for at least two decades. The data collected from the ten bridges that are part of the PennDOT pilot program did not make any exception.
- We have developed some specific strategies to remove the effect of temperatures on the static properties of the bridges we analyzed. These strategies span from calculating the difference between raw and 15-minutes averaged data to a more sophisticated principal component analysis.
- By comparing what we called the live (true) values to the corresponding values reported by the Vendor for the truck test, we believe that the proposed strategies to remove the effect of the temperature was effective.

**FINAL DETERMINATION.** Overall, the temperature sensors embedded in each gage performed well and were consistent across the whole array. This allowed to establish relevant relationship between a given parameter and the temperatures. Owing to the nature of the structures being monitored and owing to the relatively short span of the monitored period, it is unlike that new damage would have been developed and progressed to a level that would have been detectable and localized.

### **13.3 FINITE ELEMENT MODELING**

The research team at the University of Pittsburgh now possess very accurate models of six Pennsylvanian Bridges. The models contain nearly every single component of the bridge. For the remaining bridges, low-fidelity models were created. Both high- and low-fidelity models were validated with field-controlled tests performed. These validations demonstrated that the high-fidelity model matches well or extremely well with the field data whereas the low-fidelity models capture the overall trend but do not show good quantitative agreement. The models were also used to simulate damage and were useful to identify the cause of some of the anomalies seen in the experimental data.

The long-term advantage of these models is that they represent an excellent starting point to:

- Evaluate the cost-benefit of more sensors or of sensors of different types with respect to the current ones;
- Optimize sensor location for any type of bridge of any span length;
- Evaluate cost-benefit of rehabilitation projects and predict the structural benefits of such rehabilitations;
- Quantify the smallest critical defects a given installed SHM system or potential SHM system can detect;
- Create the HFM of other bridges of interests for PennDOT;
- Introduce environmental effects, namely extreme temperatures, on the models and quantify how the extreme temperature affect the structural response of bridges in terms of strain and displacement.
- Develop user-friendly interfaces to ease the use of the models by PennDOT engineers.



## REFERENCES

1. Abdulkarem, M., Samsudin, K., Rokhani, F. Z., and A Rasid, M. F. (2019). Wireless sensor network for structural health monitoring: A contemporary review of technologies, challenges, and future direction. *Structural Health Monitoring*, 1475921719854528.
2. Agdas, D., Rice, J. A., Martinez, J. R., and Lasa, I. R. (2015). Comparison of visual inspection and structural health monitoring as bridge condition assessment methods. *Journal of Performance of Constructed Facilities*, 30(3), 04015049.
3. Ahlborn, T. M., Shuchman, R., Sutter, L. L., Brooks, C. N., Harris, D. K., Burns, J. W., ... and Oats, R. C. (2010). The state-of-the-practice of modern structural health monitoring for bridges: A comprehensive review. Technical Report. <https://trid.trb.org/view/1101239>
4. Aygün, B., and Gungor, V.C. (2011). "Wireless sensor networks for structure health monitoring: Recent advances and future research directions," *Sensor Rev.*, 31(3), 261–276.
5. Catbas, F. N., Gul, M., Zaurin, R., Gokce, H. B., Terrell, T., Dumlupinar, T., and Maier, D. (2010). Long term bridge maintenance monitoring demonstration on a movable bridge: A framework for structural health monitoring of movable bridges. <https://trid.trb.org/view/927119>
6. Catbas, F. N., Gokce, H. B., and Gul, M. (2012). Nonparametric analysis of structural health monitoring data for identification and localization of changes: Concept, lab, and real-life studies. *Structural Health Monitoring*, 11(5), 613-626.
7. Chen, Z. W., Xu, Y.L., Xia, Y., Li, Q. and Wong, K.Y. (2011). Fatigue analysis of long-span suspension bridges under multiple loading: Case study. *Engineering Structures*, 33(12), 3246–3256.
8. Conte, J., Xianfei He, Babak Moaveni, Sami F. Masri, John P. Caffrey, Mazen Wahbeh, Farzad Tasbihgoo, Daniel H. Whang, and Ahmed Elgamal (2008). "Dynamic Testing of Alfred Zampa Memorial Bridge," *Journal of Structural Engineering*, 134(6):1006–1015.
9. Dalia, Z. M., Bagchi, S., Sabamehr, A., Bagchi, A., and Bhowmick, A. (2018). Life cycle cost-benefit analysis of SHM of I-35 W St. Anthony Falls bridge. *Strain*, 9(14), 15.
10. Deeble Sloane, M. J., Betti, R., Marconi, G., Hong, A. L., and Khazem, D. (2013). Experimental analysis of a nondestructive corrosion monitoring system for main cables of suspension bridges. *Journal of Bridge Engineering*, 18(7), 653-662.
11. Dong, Y., Song, R., and Liu, H. (2010). Bridges structural health monitoring and deterioration detection-synthesis of knowledge and technology. No. AUTC# 309036. Alaska. Dept. of Transportation and Public Facilities, 2010.
12. Federal Highway Administration, (2019a), <https://www.fhwa.dot.gov/bridge/nbi/ascii.cfm> (last date accessed October 31, 2019)
13. Federal Highway Administration, (2019b), <https://www.fhwa.dot.gov/bridge/fc.cfm> (last date accessed October 31, 2019)
14. French, C. E. W., Shield, C. K., Stolarski, H. K., Hedegaard, B. D., and Jilk, B. J. (2012). "Instrumentation, Monitoring, and Modeling of the I-35W Bridge." Rep. MN/RC 2012-24, Minnesota Dept. of Transportation, Minneapolis.
15. French, C., Shield, C.K. and Brock D. Hedegaard. (2014). "Modeling and monitoring the long-term behavior of post-tensioned concrete bridges." Research Project Final Report 2014-39
16. Gaebler, K. O., Hedegaard, B. D., Shield, C. K., and Linderman, L. E. (2018). Signal selection and analysis methodology of long-term vibration data from the I-35W St. Anthony Falls Bridge. *Structural Control and Health Monitoring*, 25(7), e2182.
17. Ghali, A., Elbadry, M., and Megally, S. (2000). Two-year deflections of the Confederation Bridge. *Canadian Journal of Civil Engineering*, 27(6), 1139-1149.
18. Guo, T., Frangopol, D. M., and Chen, Y. (2012). Fatigue reliability assessment of steel bridge details integrating weigh-in-motion data and probabilistic finite element analysis. *Computers and Structures*, 112, 245-257.

19. He, X., Moaveni, B., Conte, J., Elgamal, A. and Masri, S. (2009), "System identification of Alfred Zampa Memorial Bridge using dynamic field test data", *ASCE J. Struct. Eng.*, 135(1), 54-66.
20. Hedegaard, B. D., French, C. E., Shield, C. K., Stolarski, H. K., and Jilk, B. J. (2013). Instrumentation and modeling of I-35W St. Anthony Falls bridge. *Journal of Bridge Engineering*, 18(6), 476-485.
21. Hedegaard, B. D., French, C. E., and Shield, C. K. (2017a). Time-dependent monitoring and modeling of I-35W St. Anthony Falls Bridge. I: Analysis of monitoring data. *Journal of Bridge Engineering*, 22(7), 04017025.
22. Hedegaard, B. D., French, C. E., and Shield, C. K. (2017b). Long-Term Monitoring Strategy for Time-Dependent Deflections of Posttensioned Concrete Bridges. *Journal of Bridge Engineering*, 22(11), 04017095.
23. Hunt, B. E. (2009). *Monitoring scour critical bridges* (Vol. 396). Transportation Research Board.
24. Inaudi, D., Bolster, M., Deblois, R., French, C., Phipps, A., Sebasky, J., and Western, K. (2009). Structural health monitoring system for the new I-35W St Anthony Falls Bridge. In 4th International Conference on Structural Health Monitoring of Intelligent Infrastructure, SHMII 2009.
25. Kurata, M., Kim, J., Lynch, J. P., van der Linden, G. W., Sedarat, H., Thometz, E., Hipley, P., and Sheng, L.-H. (2013). "Internet-enabled wireless structural monitoring systems: Development and permanent deployment at the New Carquinez suspension bridge." *J. Struct. Eng.*, 10.1061/(ASCE)ST.1943-541X.0000609, 1688–1702.
26. Kwon, K. and Frangopol, D.M. (2010). Bridge fatigue reliability assessment using probability density functions of equivalent stress range based on field monitoring data. *International Journal of Fatigue*, 32(8):1221– 1232.
27. Jang, S., Jo, H., Cho, S., Mechitov, K., Rice, J. A., Sim, S. H., ... and Agha, G. (2010). Structural health monitoring of a cable-stayed bridge using smart sensor technology: deployment and evaluation. *Smart Structures and Systems*, 6(5-6), 439-459.
28. Jo, H., Sim, S.-H., Nagayama, T., and Spencer, B. F., Jr. (2012). Development and application of high-sensitivity wireless smart sensors for decentralized stochastic modal identification. *Journal of Engineering Mechanics*, 138(6), 683–694.
29. Jo, H., Park, J.-W., Spencer, B. F., Jr., and Jung, H.-J. (2013). Development of high-sensitivity wireless strain sensor for structural health monitoring. *Smart Structures and Systems*, 11(5), 477–496.
30. Lagasse, P.F., Richardson, E.V., Schall, J.D., and Price, G.R. (1997). Instrumentation for Measuring Scour at Bridge Piers and Abutments. NCHRP Report 396, Transportation Research Board, National Research Council, National Academy Press, Washington, D.C.
31. Li, Z. X., Tommy HT Chan, and Jan Ming Ko. "Fatigue analysis and life prediction of bridges with structural health monitoring data—Part I: methodology and strategy." *International Journal of Fatigue* 23.1 (2001): 45-53.
32. Li, J., Mechitov, K. A., Kim, R. E., and Spencer Jr, B. F. (2016). Efficient time synchronization for structural health monitoring using wireless smart sensor networks. *Structural Control and Health Monitoring*, 23(3), 470-486.
33. Li, J., Bennett, C., Collins, W., Laflamme, S., and Jo, H. (2019). *Strain-based Fatigue Crack Monitoring of Steel Bridges using Wireless Elastomeric Skin Sensors* (No. FHWA-KS-19-01).
34. Lynch, J. P., and Loh, K. J. (2006). "A summary review of wireless sensors and sensor networks for structural health monitoring," *Shock Vib. Dig.*, vol. 38, no. 2, pp. 91–130.
35. Mehrabi, A. B., and Farhangdoust, S. (2018). A laser-based noncontact vibration technique for health monitoring of structural cables: background, success, and new developments. *Advances in Acoustics and Vibration*, 2018.
36. Moreu, F., Jo, H., Li, J., Kim, R. E., Cho, S., Kimmle, A., ... LaFave, J. M. (2015). Dynamic assessment of timber railroad bridges using displacements. *Journal of Bridge Engineering*, 20(10), 04014114.
37. Moreu, F., Li, J., Jo, H., Kim, R. E., Scola, S., Spencer, B. F., and LaFave, J. M. (2016). Reference-free displacements for condition assessment of timber railroad bridges. *Journal of Bridge Engineering*, 21(2), 04015052.
38. Moreno-Gomez, A., Perez-Ramirez, C. A., Dominguez-Gonzalez, A., Valtierra-Rodriguez, M., Chavez-

- Alegria, O., and Amezcuita-Sanchez, J. P. (2018). Sensors used in structural health monitoring. *Archives of Computational Methods in Engineering*, 25(4), 901-918.
39. Morris, W., Vico, A., Vazquez, M and de Sanchez, S.R. (2002). Corrosion of reinforcing steel evaluated by means of concrete resistivity measurements. *Corrosion Science*, 44(1):81–99, January 2002.
  40. Nagarajaiah, S., and Erazo, K. (2016). Structural monitoring and identification of civil infrastructure in the United States. *Struct. Monit. Maint*, 3(1), 51-69.
  41. Ni, Y. Q., Ye, X. W. and Ko, J. M. (2010). Monitoring-Based Fatigue Reliability Assessment of Steel Bridges: Analytical Model and Application. *Journal of Structural Engineering*, 136(12):1563–1573.
  42. Noel, A. B., Abdaoui, A., Elfouly, T., Ahmed, M. H., Badawy, A., and Shehata, M. S. (2017). Structural health monitoring using wireless sensor networks: A comprehensive survey. *IEEE Communications Surveys and Tutorials*, 19(3), 1403-1423.
  43. Piotr Omenzetter and James Mark William Brownjohn (2006). Application of time series analysis for bridge monitoring. *Smart Materials and Structures*, 15(1):129–138.
  44. Orsak, John (2019). A New Method for Detecting the Onset of Scour and Managing Scour Critical Bridges. No. DOT/FRA/ORD-19/32. United States. Department of Transportation. Federal Railroad Administration.
  45. Rizzo, P. and Enshaiean, A. (2021). Challenges in Bridge Health Monitoring: A Review. *Sensors journal*, 21(13), 4336. <https://doi.org/10.3390/s21134336> .
  46. Robertson, I. N. (2005). Prediction of vertical deflections for a long-span prestressed concrete bridge structure. *Engineering Structures*, 27(12), 1820-1827.
  47. Schenewerk, M. S., Harris, R. S., and Stowell, J. (2006). Structural Health Monitoring Using GPS. *Bridges*, 9(2).
  48. Sharyatpanahi , S.B.G. (2015). “Structural health monitoring of bridges using wireless sensor networks” M.S. thesis, <https://digitalcommons.njit.edu/theses/231/>
  49. Spencer Jr, B. F., Park, J. W., Mechitov, K. A., Jo, H., & Agha, G. (2017). Next generation wireless smart sensors toward sustainable civil infrastructure. *Procedia Engineering*, 171, 5-13.
  50. Swartz, R., Lynch, J., Sweetman, B., and Rolfes, R. (2010). “Structural monitoring of wind turbines using wireless sensor networks.” *Smart Struct. Syst.*, 6(3), 183–196.
  51. Takruri, M., Rajasegarar, S., Challa, S., Leckie, C., and Palaniswami, M. (2011). Spatio-temporal modelling-based drift-aware wireless sensor networks. *IET wireless sensor systems*, 1(2), 110-122.
  52. Xu, Y., and Xia, Y. (2011). *Structural health monitoring of long-span suspension bridges*. CRC Press.
  53. X.W. Ye, Y.Q. Ni, K.Y. Wong, and J.M. Ko (2012). Statistical analysis of stress spectra for fatigue life assessment of steel bridges with structural health monitoring data. *Engineering Structures*, 45:166–176.
  54. Worden, K., Farrar, C. R., Manson, G., & Park, G. (2007). The fundamental axioms of structural health monitoring. *Proceedings of the Royal Society A: Mathematical, Physical and Engineering Sciences*, 463(2082), 1639-1664.
  55. Zhang, Y., Kurata, M., and Lynch, J. P. (2017). Long-term modal analysis of wireless structural monitoring data from a suspension bridge under varying environmental and operational conditions: System design and automated modal analysis. *Journal of Engineering Mechanics*, 143(4), 04016124.



## APPENDIX A - FUTURE STUDIES

This appendix provides some suggestions about possible future studies. These suggestions are based on the lessons learned in this project and represents the opinions of the Pitt investigators.

Any future review of the state-of-the-art in bridge health monitoring in the U.S. may include an online survey to be distributed across all the DOTs, railroad owners, and any agencies responsible of the management of this strategically important civil engineering structures.

The evaluation of the Vendor software is complete and comprehensive. The fact that the repositories contain historical data that, for some bridges, span longer than what considered in this study, warrant follow-up studies to consolidate what discussed here. As a matter of fact, the availability of large amount of data and the fact that the sensing systems in two bridges are still active offer unique opportunities to branch the project along multiple directions. The following list provides some suggestions with no particular order and therefore it should not considered from the highest to the lowest priority or vice-versa.

- **FURTHER ANALYSIS.** New analyses may help to understand further the response of the bridges to man-made events and to identify the response of the structure or sub-structure to transient sharp events. One of such analyses would be a close-up view of the outliers identified through the Mahalanobis squared distance. The time-stamps associated with those outliers would represent the starting point to isolate the data samples and to reconstruct the events around those time stamps. The reconstruction of the events implies the plots of the time-series of all the sensors to localize the source of the problem and eventually to characterize it.
- **ALGORITHM DEVELOPMENT 1.** The proper and complete installation of any large array of SHM sensors requires several hours if not a few days of labor-intensive activities. This means that the temperature of the structural element to which any given sensor is bonded or bolted cannot be identical for the whole array. The consequence is that the values read from the sensors, e.g. strain, may be biased by the lack of uniformity. For example, the recorded strain from two symmetric structural elements under the same loading may result significantly different because the reference temperature is different. Future studies may look at ways to remove such bias. This is possible by knowing the temperature of the structural element when a given sensor was installed.
- **SOFTWARE DEVELOPMENT.** The amount of data analyzed in this study was truly massive. In addition, data were prepped to be able to execute some of the processing algorithms. We believe that the development stage has demonstrated the effectiveness of bridge health monitoring at providing different types of information. Nonetheless, the algorithms we have developed were coded in Matlab using hundreds of code lines, specifically developed for each bridge individually. These lines may be difficult to be navigated by newcomers. In the future, a friendly user interface, i.e. a dedicated software, could be developed to enable any PennDOT engineer or any interested part, to observe daily, weekly, and/or monthly trends without the need to understand and modify the code.
- **NEW INSTALLATIONS.** For those bridges that underwent rehabilitation or are currently under rehabilitation, we recommend the installation of a new array of sensors, possibly at the same location in order to compare the effects of the renovation on certain static and (where possible) dynamic responses of the Bridge. The use of lower-end cameras pointing at the roadways would represent a redundant system to corroborate instances that are believed to be generated by the crossings of heavy trucks. For large bridges, the number of sensors should be increased in order to provide redundancy, prove/disprove drift, and large coverage in terms of structural monitoring. The new installation shall consider the use of more accelerometers. The investigators believe that the accelerometers used under this program were insufficient at determining the dynamic characteristics of the Bridges.

- **ADDITIONAL SHM METHODOLOGIES.** An interesting (and more advanced) alternative to the use of accelerometers and, as a matter of fact, displacement sensors is the use of one or a few high-resolution high-speed cameras. By using one or a few cameras, each pixel of a given video becomes a displacement sensor and by time derivation an accelerometer. By pointing the camera to a given bridge from a certain distance, short (a few seconds) videos at 100-200 frames per seconds could be taken to identify sub-mm displacement of the bridge and to extract its mode shapes. Other DOTs have explored such approaches for the contactless remote monitoring of real bridges.

The use of weigh-in-motion sensors (either commercial ones or newly developed through a specific research project) may be a viable and reliable source to validate those alerts received by the SHM system and associated with heavy weight truck crossings. The other (and more important) benefit is that the knowledge of a specific weight at discrete point(s) on a deck can be translated into a static or dynamic force input in a given high-fidelity or low-fidelity model of the given bridge.

- **TEST PROTOCOLS.** More truck tests are warranted to observe deterioration in the durability of the sensors and to observe structural changes in the load distribution across any given bridge. In the framework of this study, only one bridge (the Smithfield Street Bridge) was tested twice, several months apart. Unfortunately, the weight of the truck used in the two tests was different and therefore a direct comparison between the resulting strains could not be carried out in a straightforward way without including the high-fidelity finite element model. The Cooks Mills Bridge was also retested in 2020 but the associated data were not analyzed.
- **TRAINING.** Structural health monitoring is a relatively new engineering discipline. A future project may consider the training of engineering students through undergraduate research, “internships” or “co-op” opportunities. The training may help PennDOT hiring qualified personnel that can capitalize on the investments made through the pilot instrumentation program. The training may also help with the recruitment of students exposed to structural health monitoring and relative statistical analyses, which are relatively young engineering disciplines that are becoming complementary to more traditional bridge inspection.
- **COST-ANALYSIS.** Owing to the “young age” of structural health monitoring, the development of software and hardware for bridge monitoring is at its infancy and the market is expanding. A future study may quantify, through surveys and interviews, the current cost of turnkey products, and also may describe which commercial systems offer the opportunity to access the raw data to develop ad-hoc smart processing.
- **MODELING.** The finite element models shall include the effect of the temperature, in order to describe and quantify the mechanism that induce deformation due to cooling / heating.
- **SIGNAL PROCESSING.** The scientific literature about signal processing for bridge data is quite extensive. It is not excluded that strategies different than what used in this project may be even more effective. Future studies may consider a systematic review of those strategies.
- **LOAD RATING.** Look into ways to get the results from the sensors (strain) to match the strain for the controlling member in the load rating.

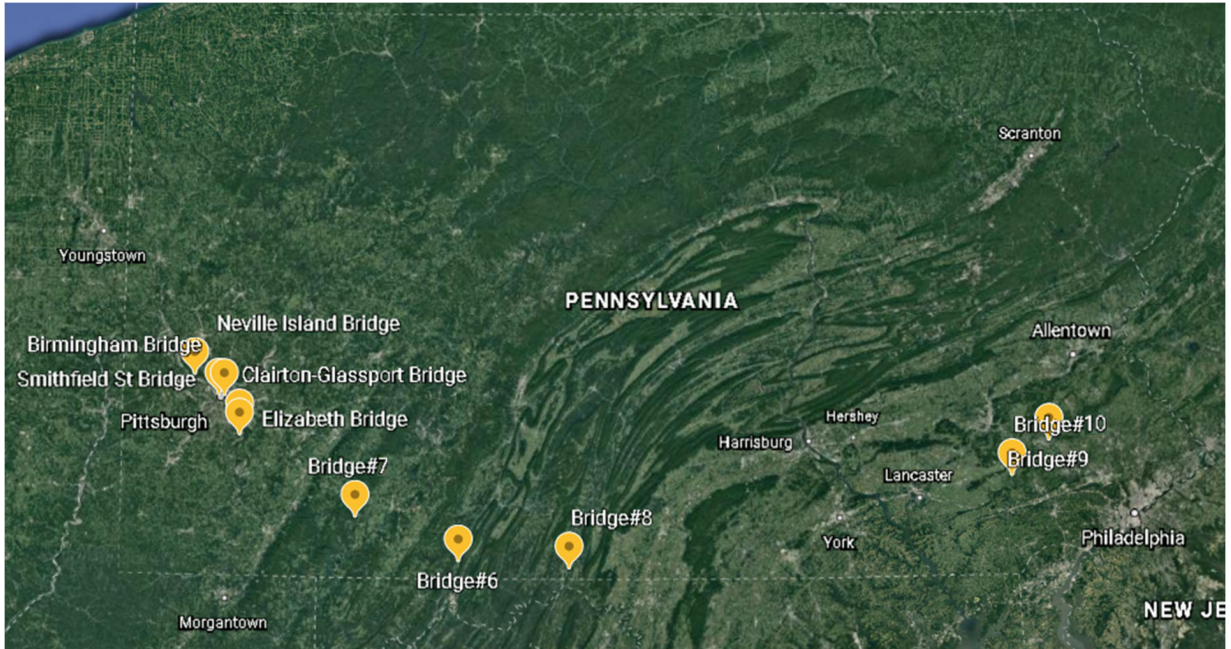


**Fig. 1.1** – Pennsylvania map and location of the bridges under the P2BIP program.





Fig. 3.2 – The Neville Island bridge. Source: <https://www.penndot.gov/RegionalOffices/district-11/PublicMeetings/Documents/SR0079%20A61%20Detour%20Slides%201-21-2020.pdf>

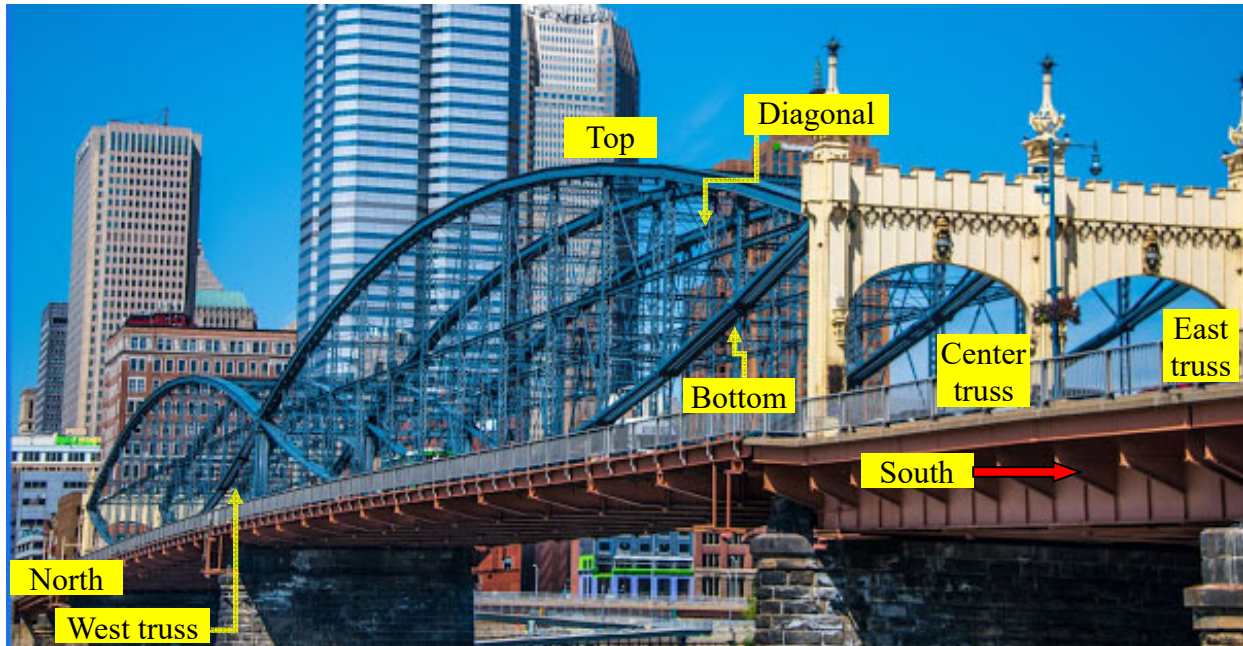


Fig. 3.3 – Photos of the Birmingham Bridge.

Figures adapted from: (a)

<https://www.flickr.com/photos/jag9889/10148146816> ; (b)

<http://pghbridges.com/pittsburghE/0587-4476/birmingham.htm>



**Fig. 3.4** – The Smithfield bridge with directions and nomenclature. Span 3 is in the far end (North side).



**Fig. 3.5** – Photo of the Clairton-Glassport Bridge



**Fig. 3.6** – Photo of the Cooks Mill Bridge.



**Fig. 3.7** – Photos of the 55-3014-0050-0509 bridge (Somerset Bridge). Figure adapted from PennDOT bridge inspection 2014. Upstream view.



**Fig. 3.8** – Photo of the single span ID 29-2004-0040-0000 bridge over little Tonoloway Creek in Fulton County.

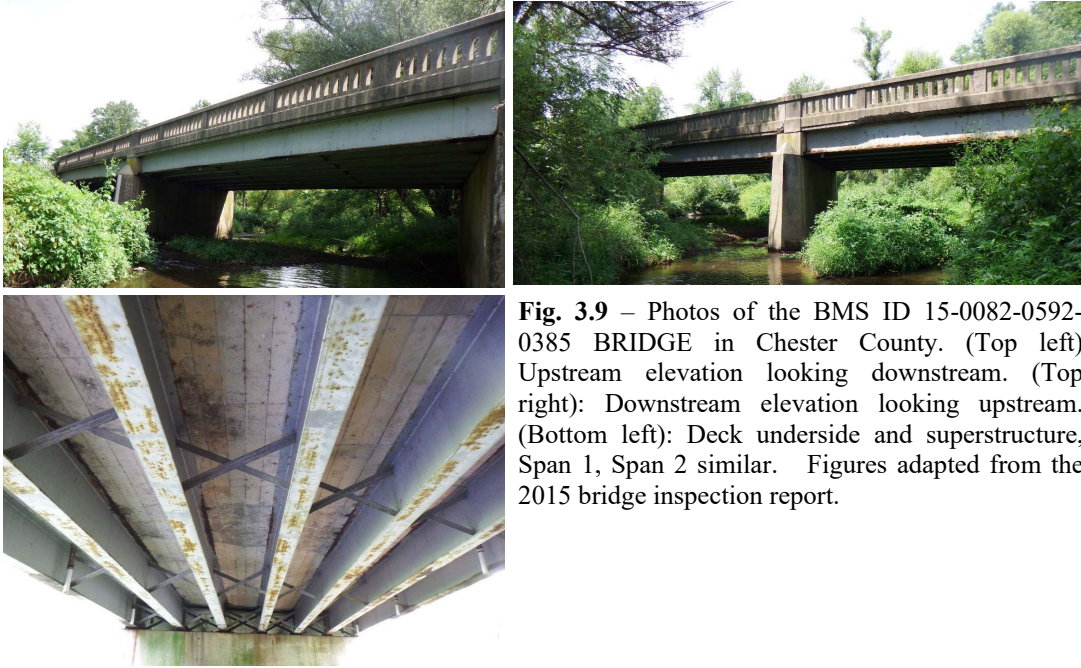


**Fig. 3.9** – Photos of the BMS ID 15-0082-0592-0385 BRIDGE in Chester County. (Top left) Upstream elevation looking downstream. (Top right): Downstream elevation looking upstream. (Bottom left): Deck underside and superstructure, Span 1, Span 2 similar. Figures adapted from the 2015 bridge inspection report.



**Fig. 3.10** – Photos of the BMS ID 46-4031-0314-1676 in the Montgomery County. (Figures adapted from a 2015 bridge inspection report).

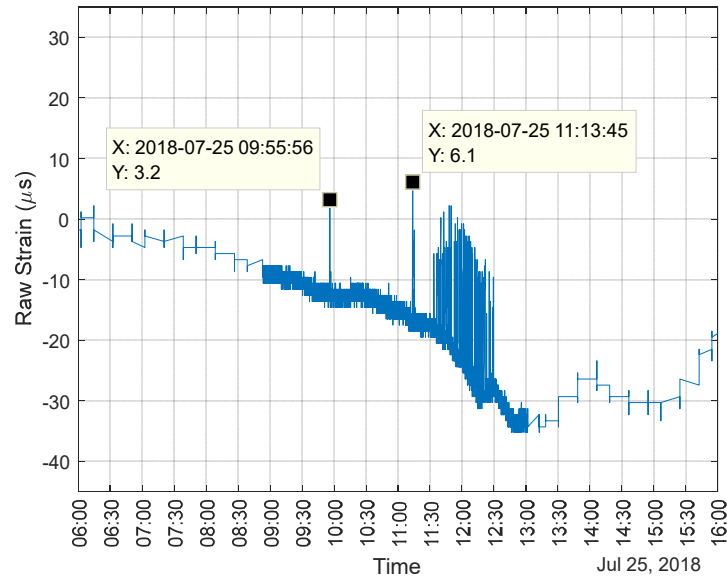


**Fig. 4.1** – Example of raw strain downloaded from the Vendor repository and associated with a strain gage.

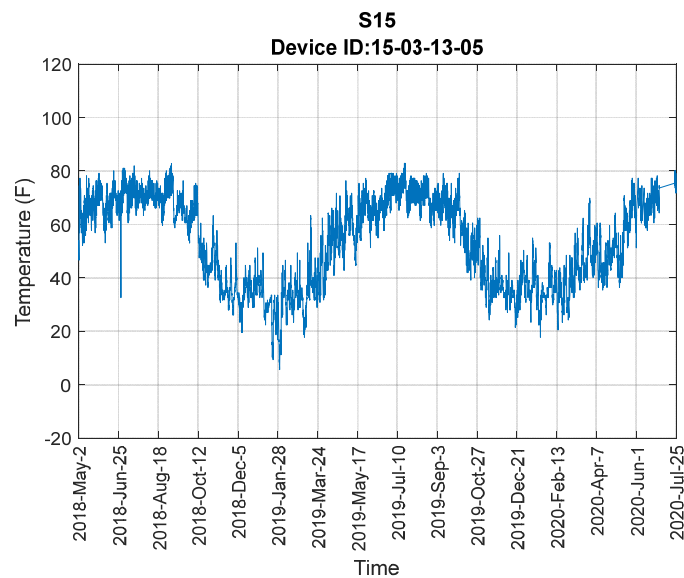


**Fig. 4.2** – Example of the raw temperature downloaded from the Vendor repository. The temperature gage shown here belong to two strain gages installed in the Somerset Bridge. Plots like these may show anomalous spikes, likely due to electromagnetic interference, extreme hot or cold temperature (see second week of January 2018). Last but not least may confirm the termination of a given sensor.

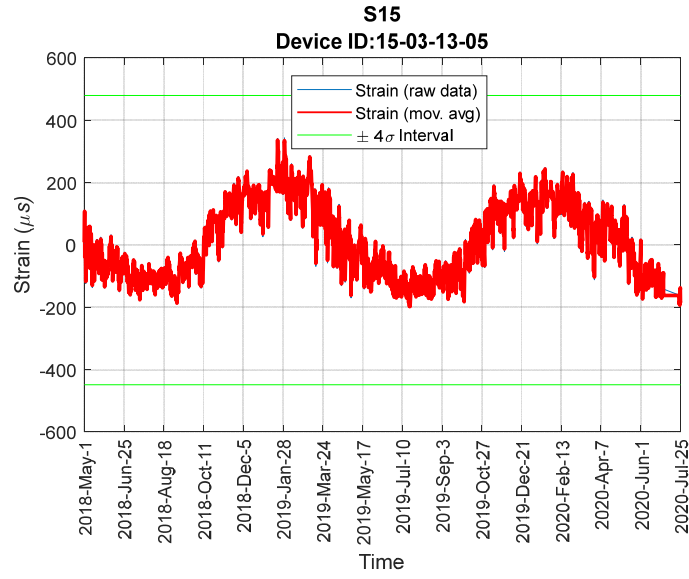


**Fig. 4.3** – Example of the raw strain overlapped to the corresponding 15-minutes average. The data are from the same gages shown in Fig. 2.3, i.e. from the Somerset Bridge.

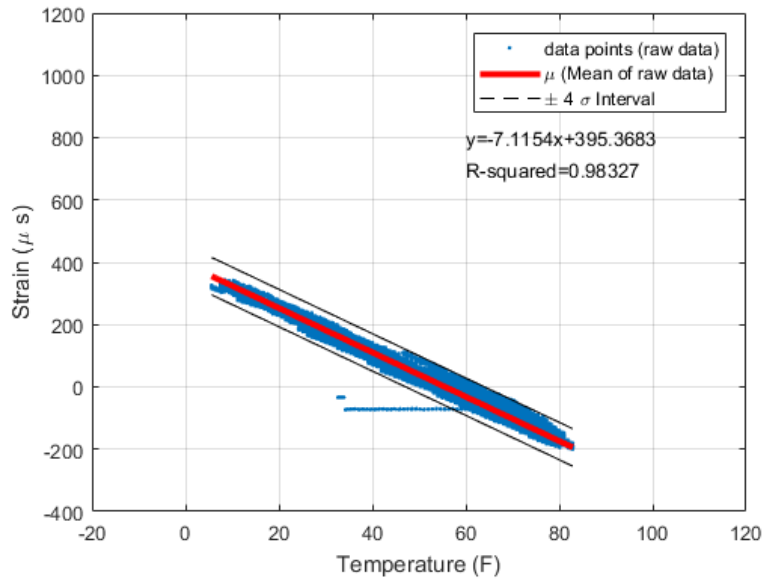


**Fig. 4.4** – Example of the raw strain vs raw temperature. For plots like these, the equation of the linear regression and the corresponding  $R^2$  value are computed for further analysis.

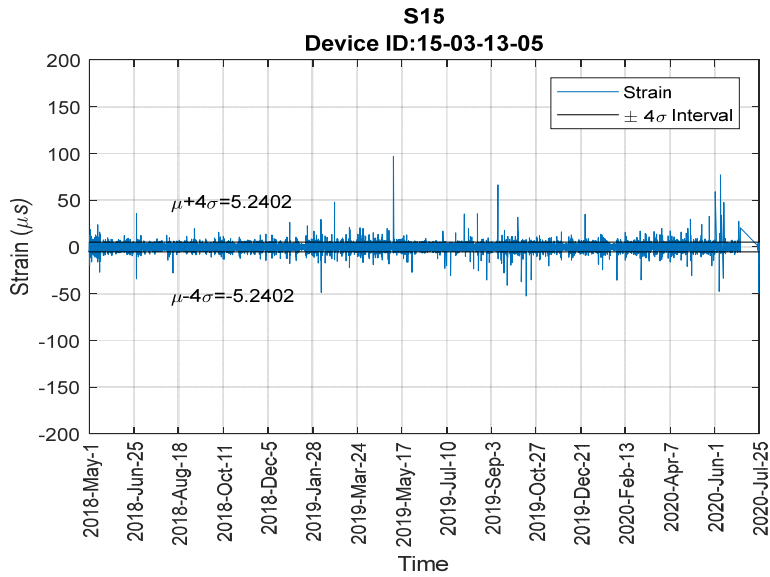


**Fig. 4.5** – True strain computed for the time interval 11:30 – 12:30 of the graph of Fig. 4.2.

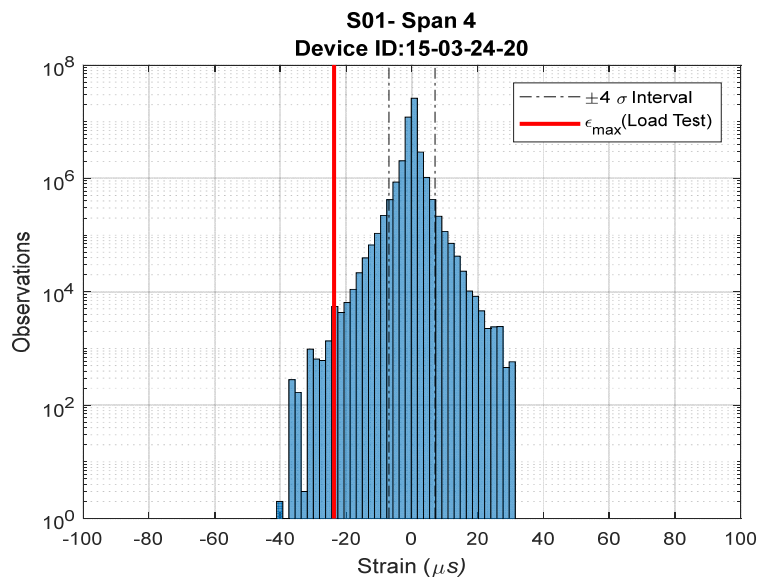


**Fig. 4.6** – Example of counting the number of occurrences by computing how many times a certain strain was observed. The vertical red line represents the maximum value recorded by the given strain sensor during the truck load test. The dashed vertical lines bound the  $\pm 4\sigma$  interval. The strain in question was measured from one of the strain gages mounted on the Smithfield Bridge and the monitoring period in question spanned for 12 months, from 08/01/2019 to 07/31/2020.

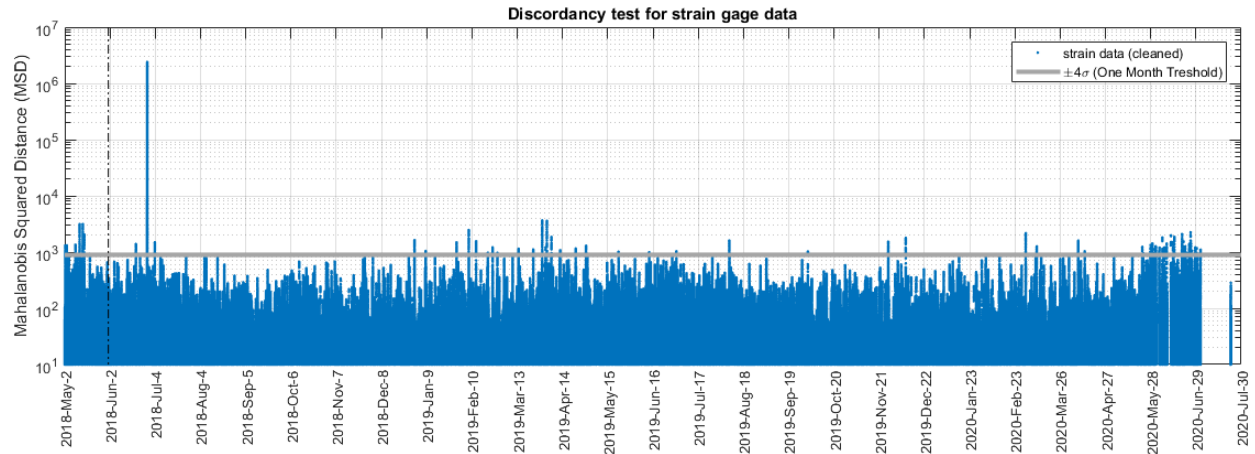


**Fig. 4.7** – Example of outlier analysis applied to true strain data collected from the 30 gages of the Somerset Bridge.

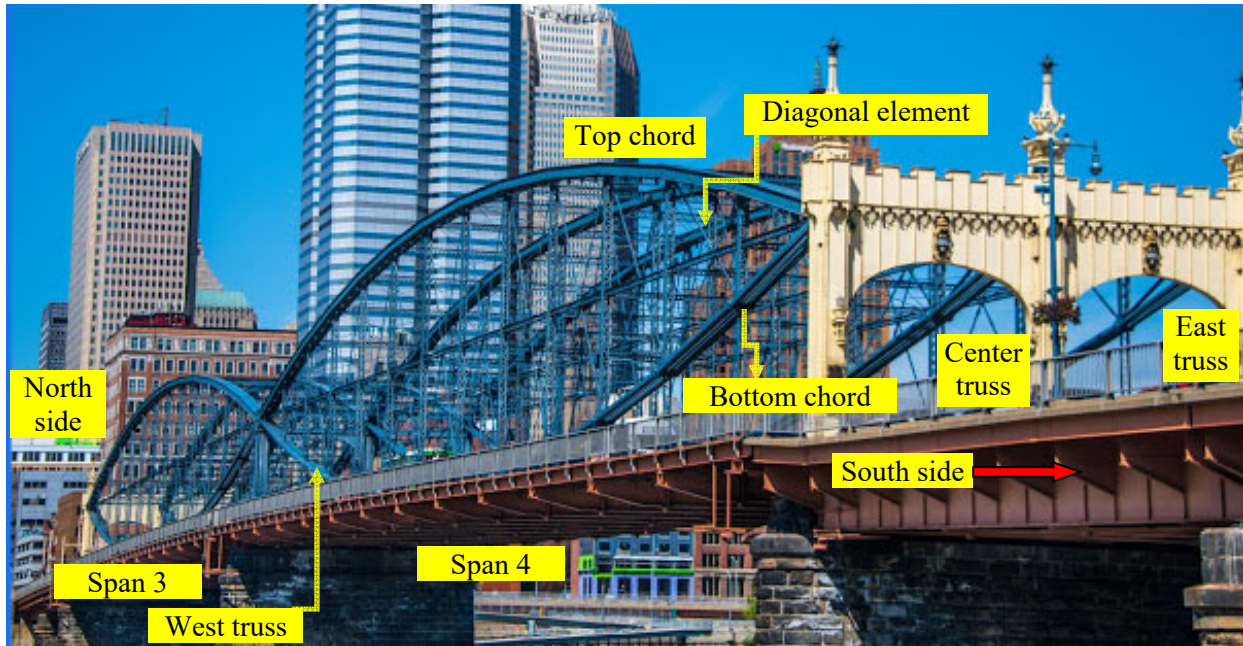
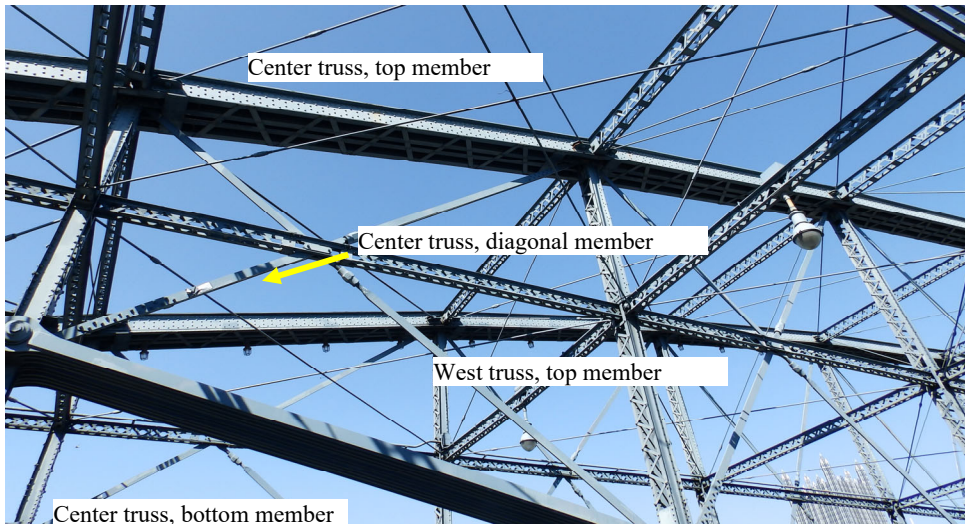
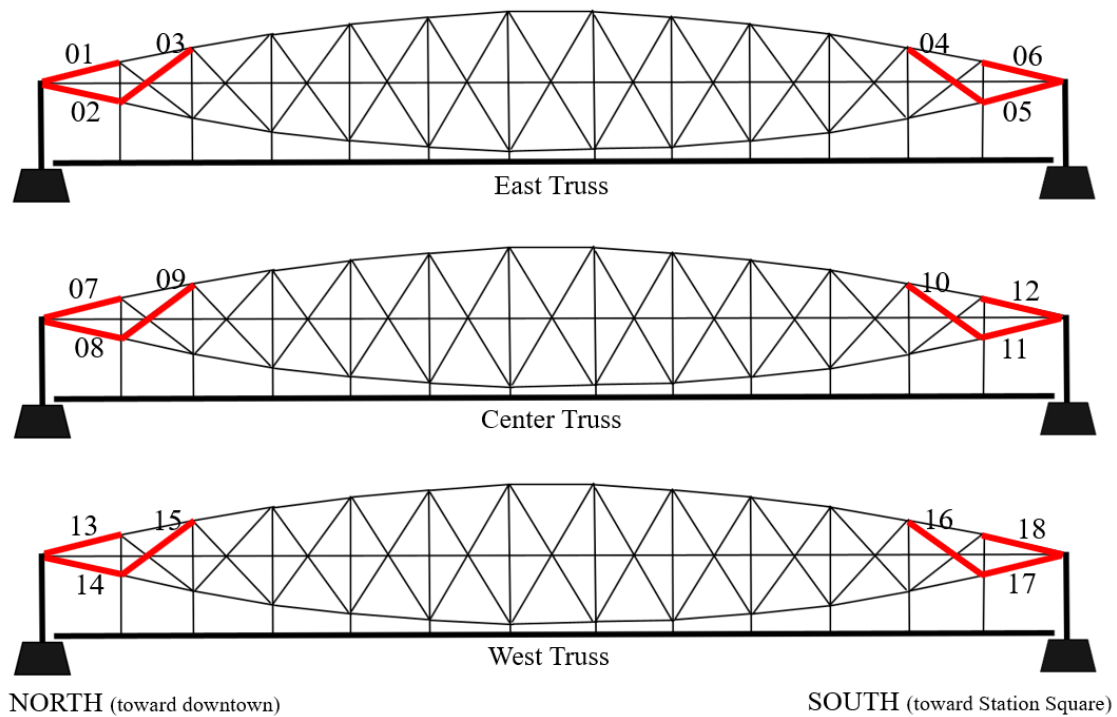


Fig. 5.1 – The Smithfield bridge with directions and nomenclature.



**Fig. 5.2** – Close-up view of the center truss, with the top, diagonal, and bottom member. The west truss and some strain gages are also visible. Photos by Piervincenzo Rizzo.



**Fig. 5.3** – Drawings of the East, Center and West trusses. The members instrumented with a wireless strain gage are labeled according to the gage number.

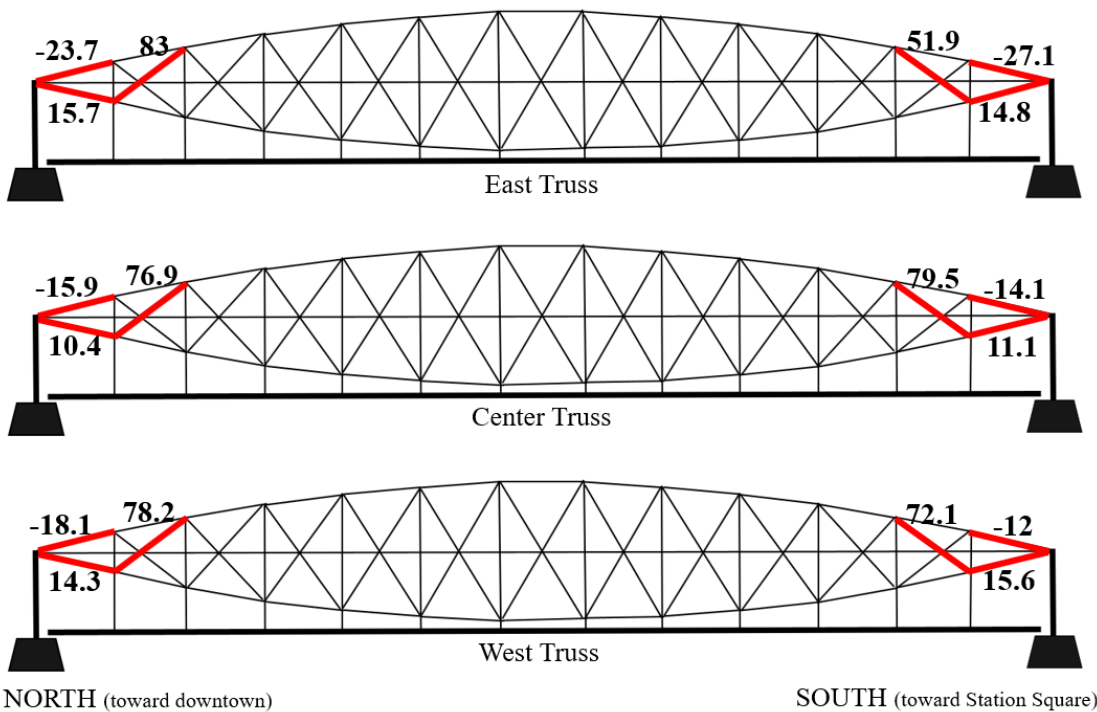


**Fig. 5.4** – Maximum strain increase during the truck test recorded at each of the instrumented members. Note that the sensors on the East truss face west, whereas the gages on the Center and West truss face east. The values are expressed in microstrains.

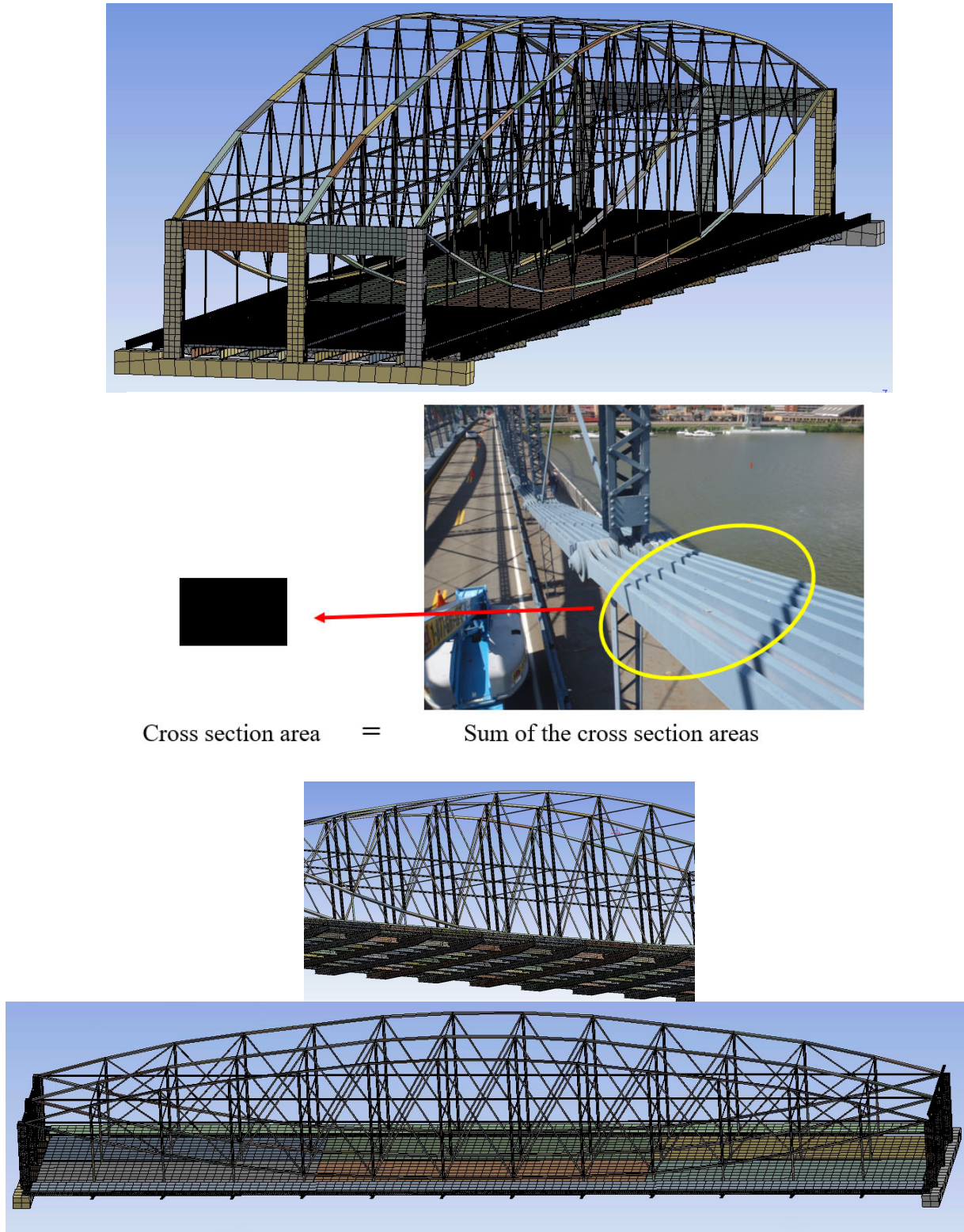
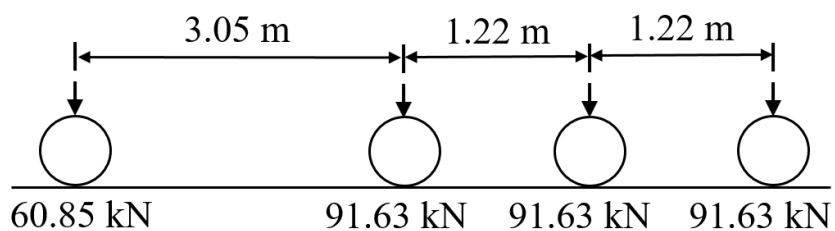
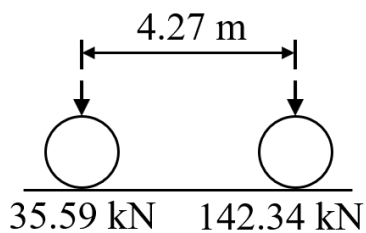


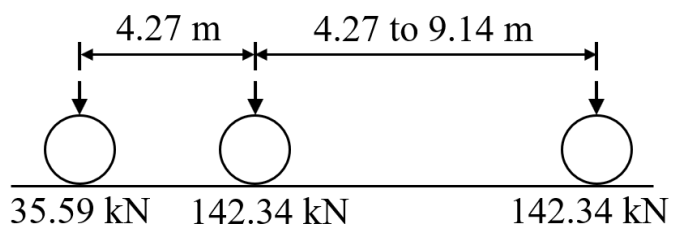
Fig. 5.5 – Finite element model of the Smithfield Street Bridge.



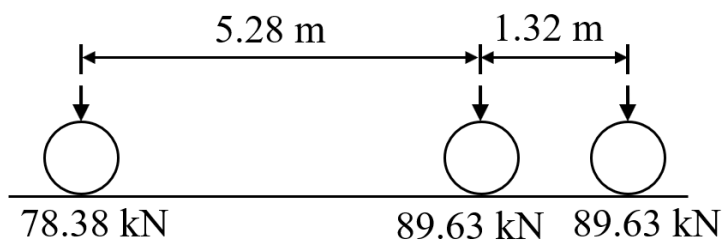
ML-80 Truck



H20 Truck



HS20 Truck



Truck used by the Vendor

**Fig. 5.6** – Schematics of the AASHTO trucks and of the truck used by the Vendor for the test on the bridge.

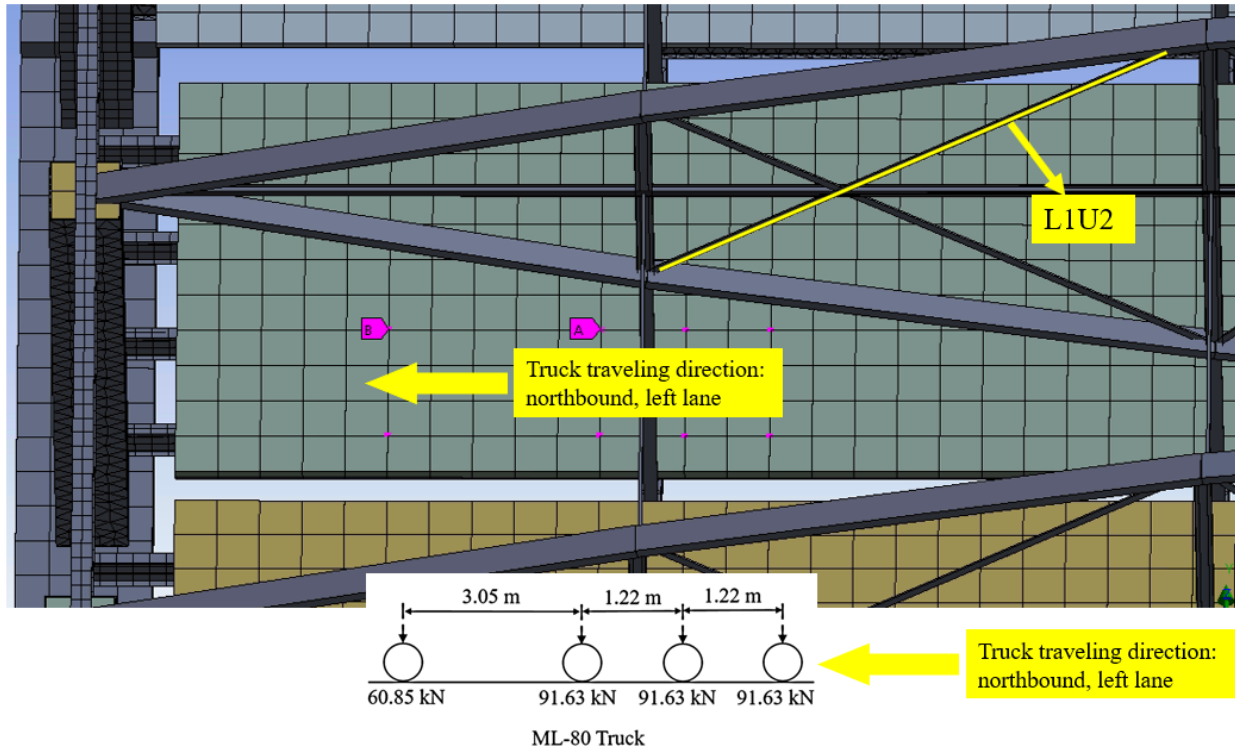
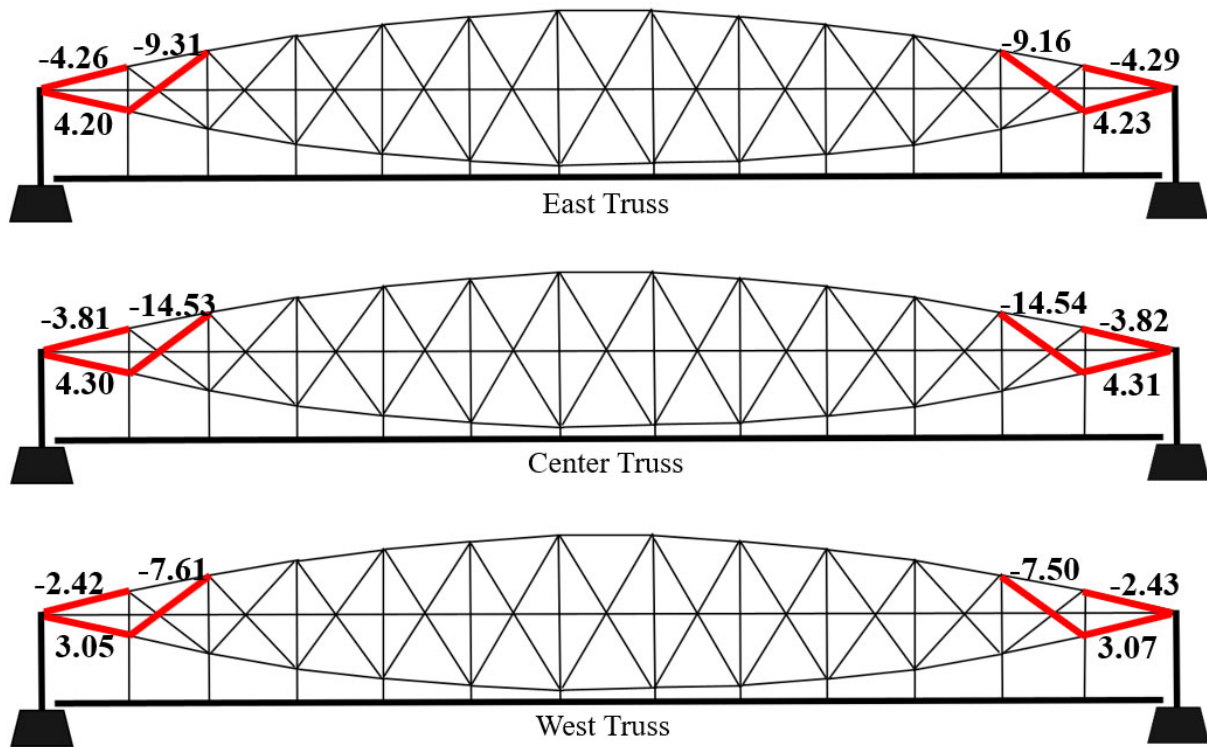


**Fig. 5.7** – Numerical setup relative to the analysis of the ML-80 AASHTO truck. The pink dots locate the position of the truck wheels.



NORTH (toward downtown)

SOUTH (toward Station Square)

Fig. 5.8 – Numerical strains due to a simulated symmetric load. The values are expressed in microstrains.

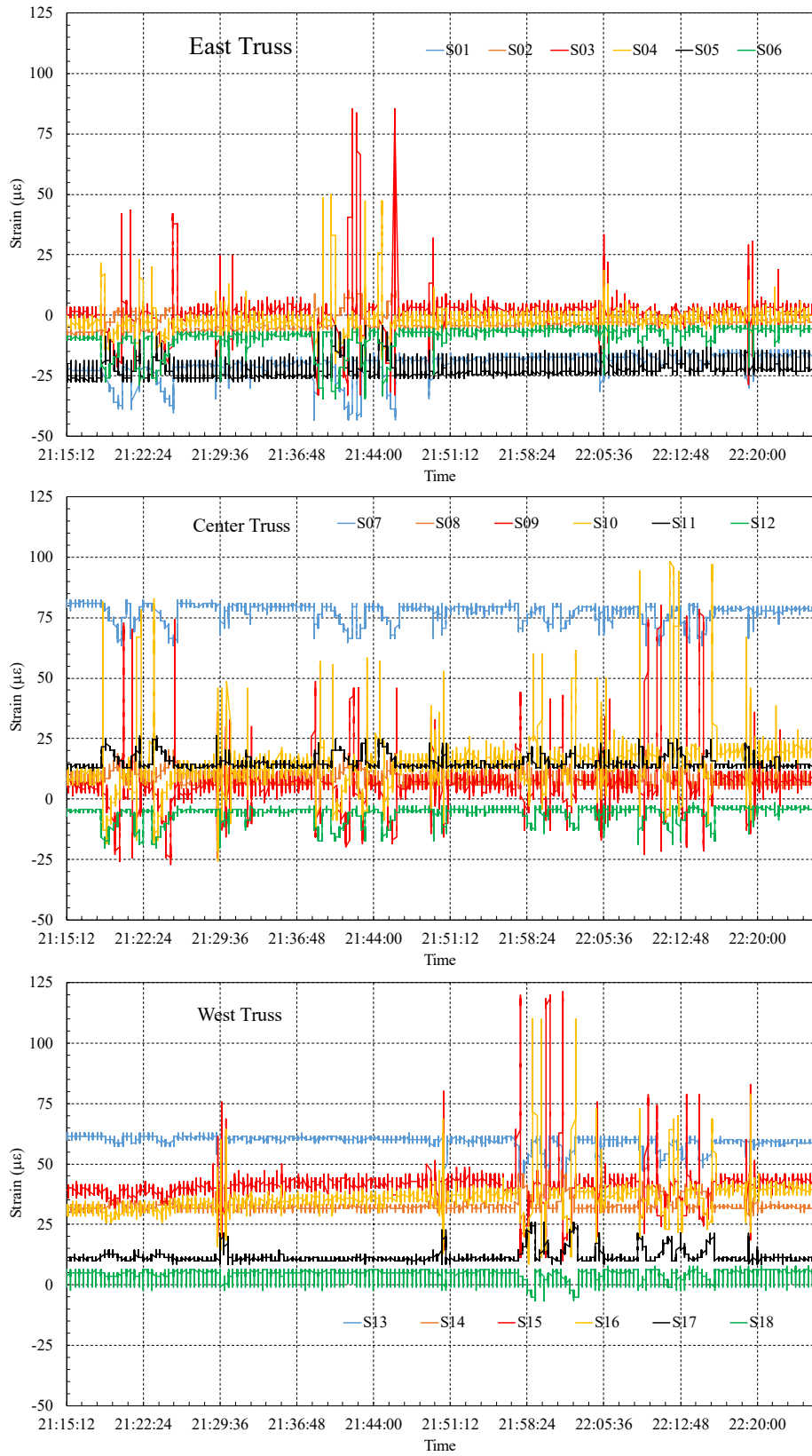
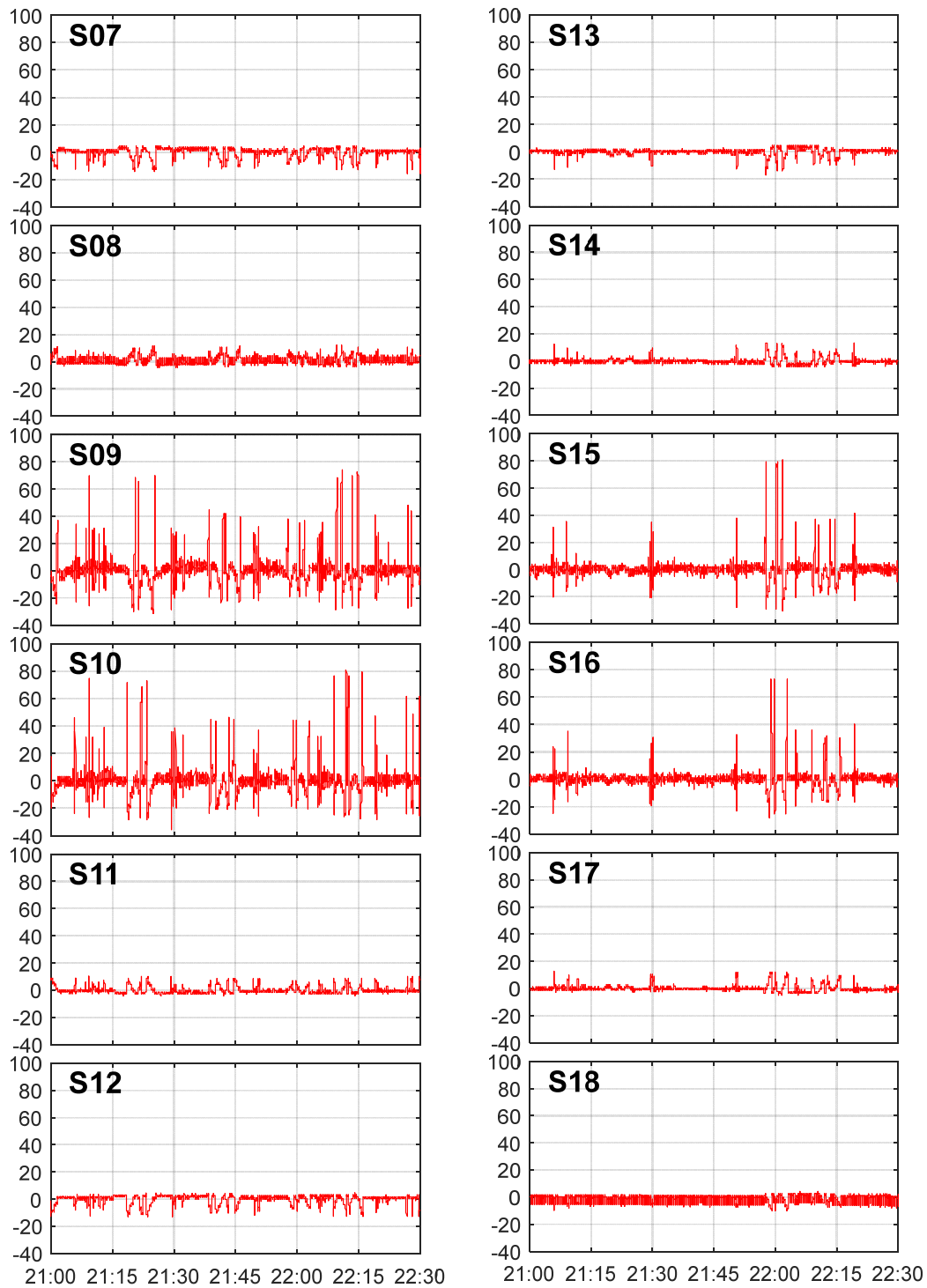
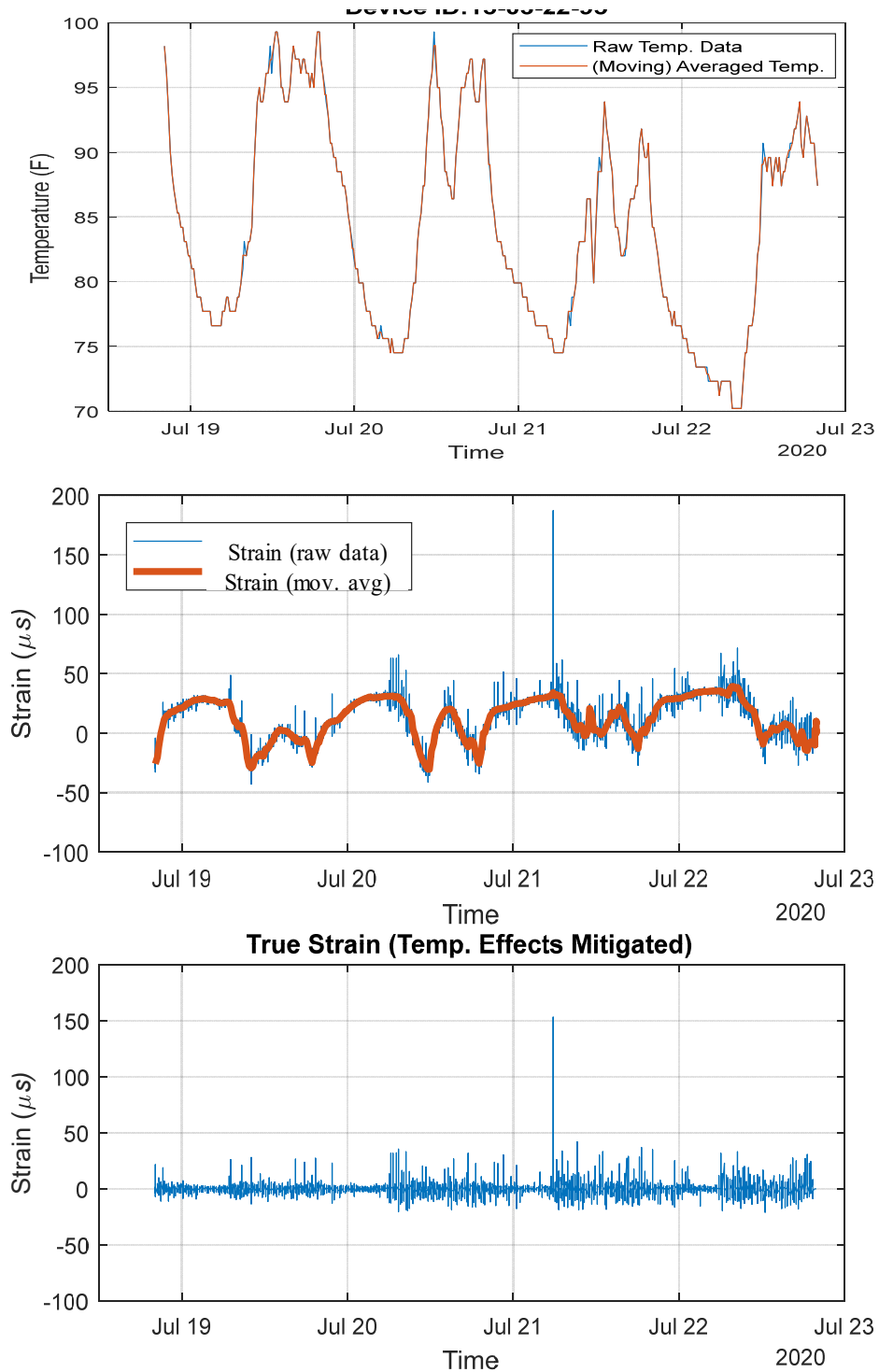


Fig. 5.9 – Strain measured during the truck test performed by Vendor.



**Fig. 5.10** – True strains from gages S07 – S18 extracted from the raw strains stored during the controlled load truck test. (The values on the vertical axes indicate strains and are expressed in microstrains)



**Fig. 5.11** – (a) Top. Raw and 15-minutes moving average of the temperature data. (b) Center. Raw and 15-minutes moving average of the strain data. (c) Bottom. Live load strain.

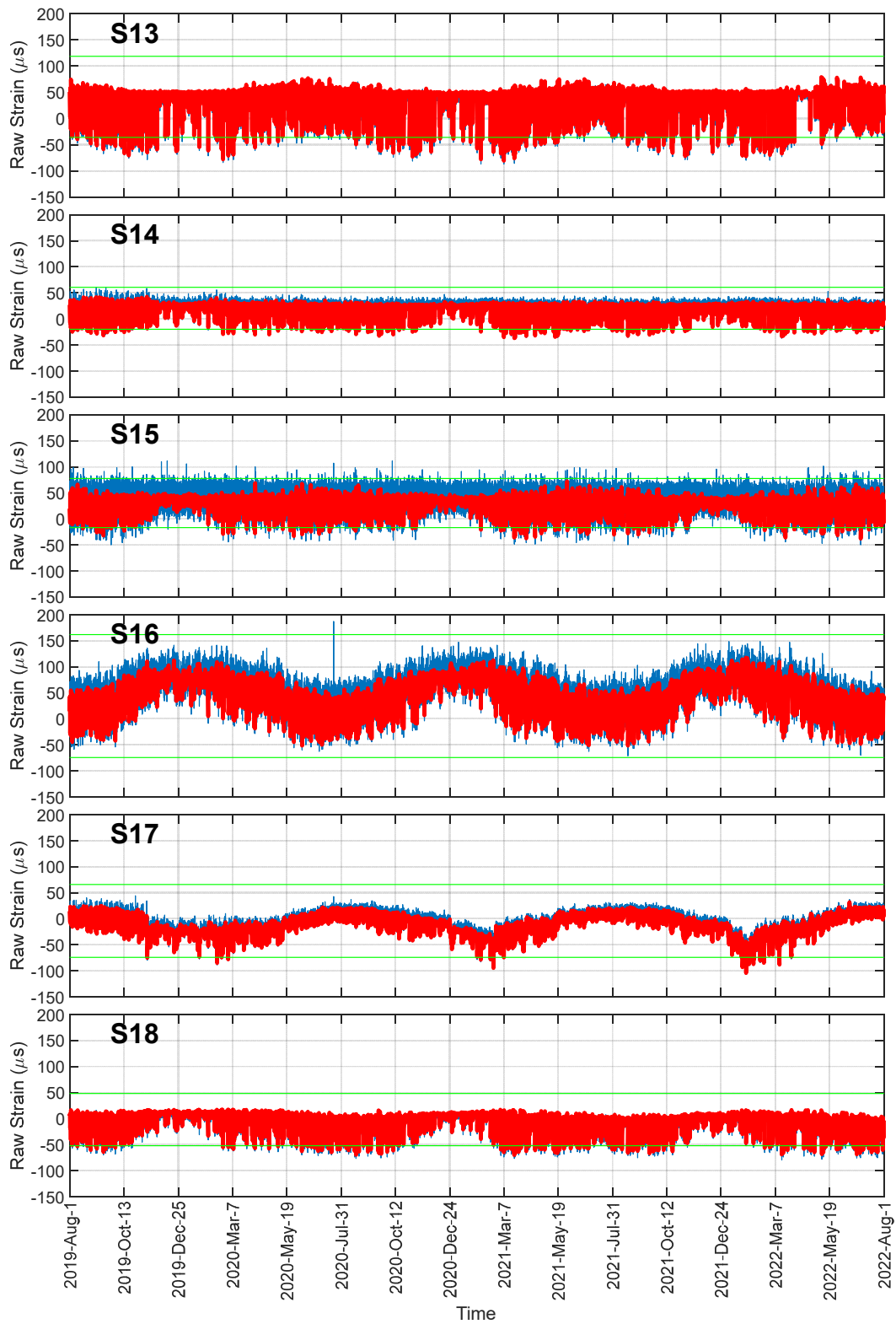


Fig. 5.12 – Raw strain and corresponding moving average recorded by each sensor over the 12 month period.

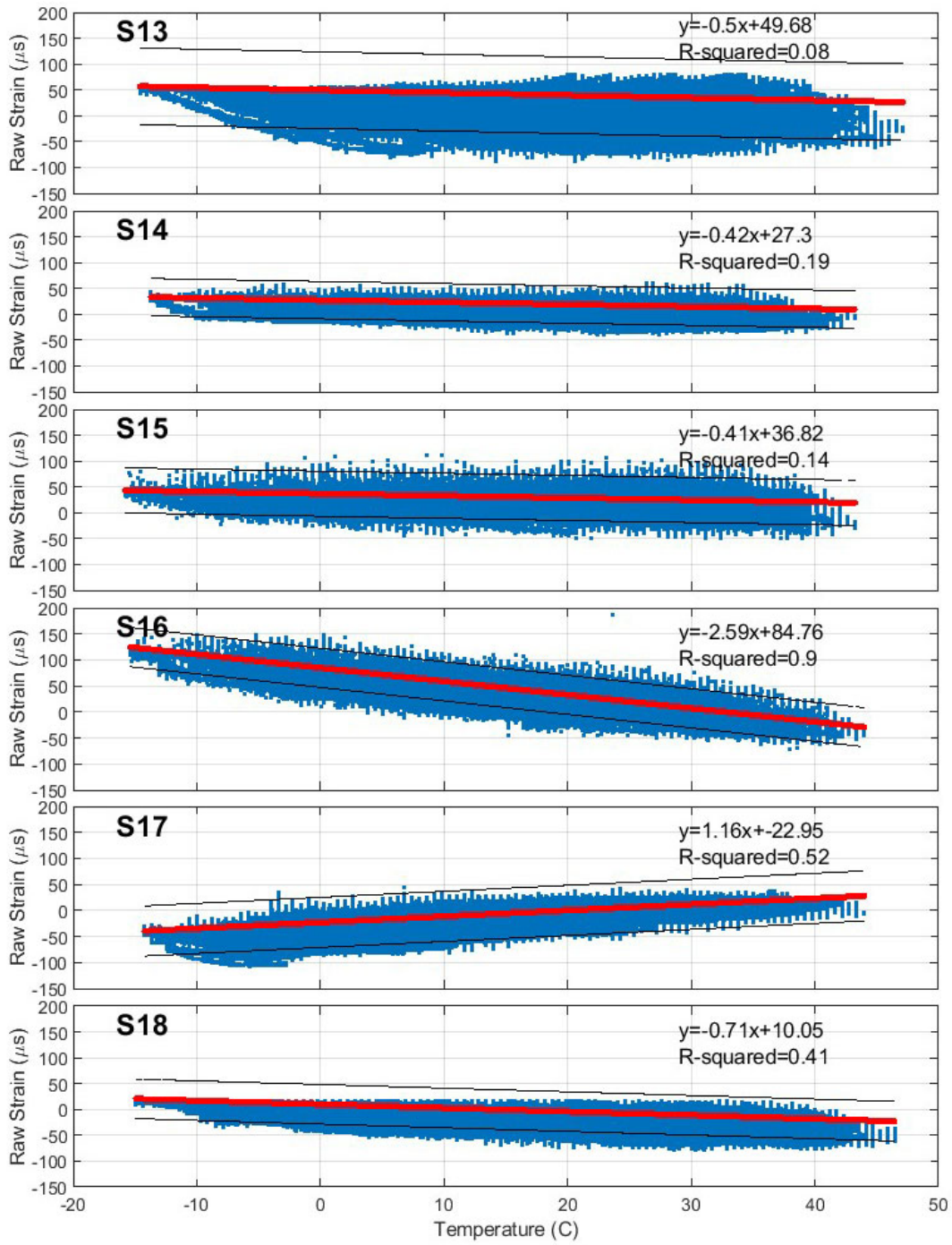
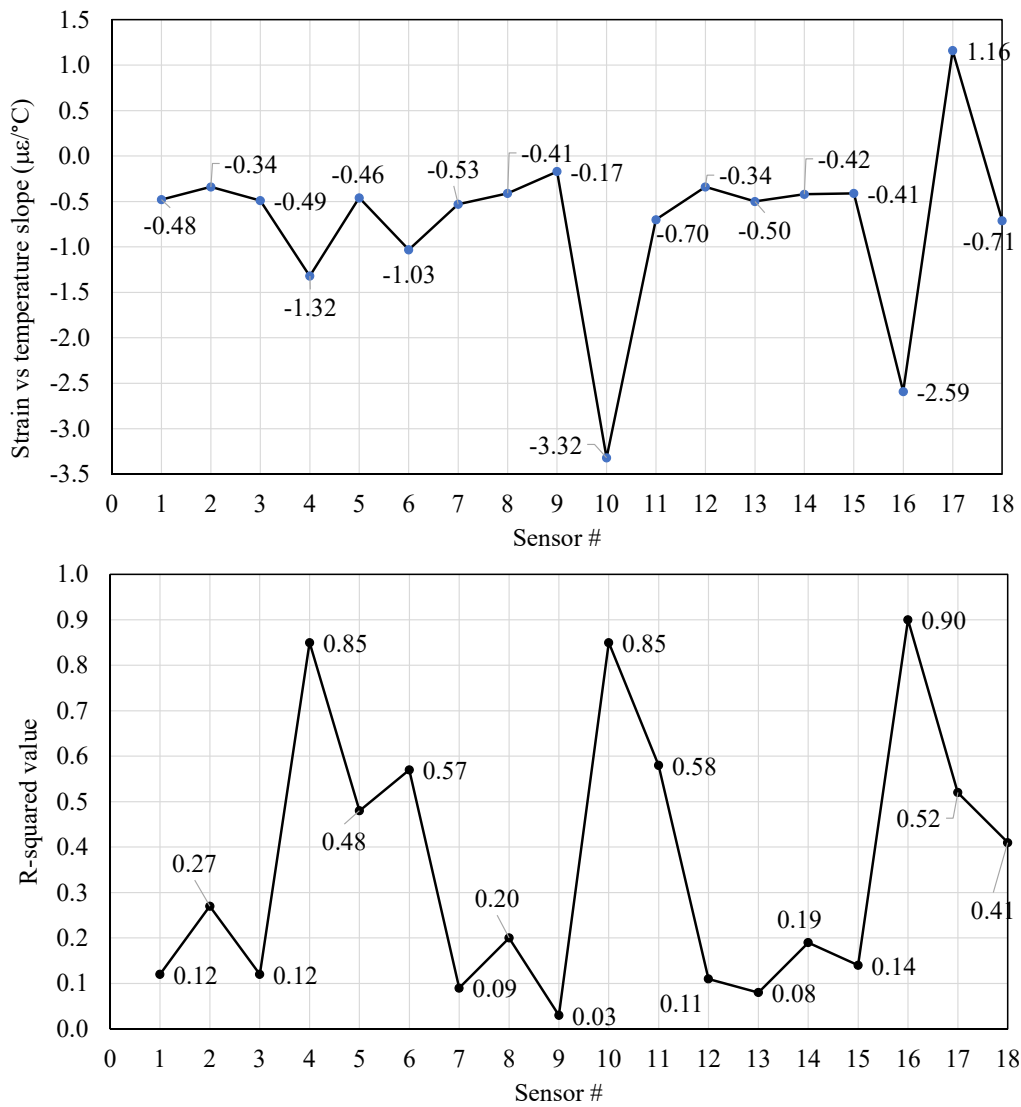


Fig. 5.13 – Raw strain vs raw temperature for all the strain gages.



**Fig. 5.14** – Analysis of the strain gages bonded to the truss. (a) Slope of linear interpolation of the strain vs temperature graphs. The values are expressed in  $\mu\epsilon/^\circ\text{F}$ . (b) Residual  $R^2$  of the linear interpolation strain vs temperature.



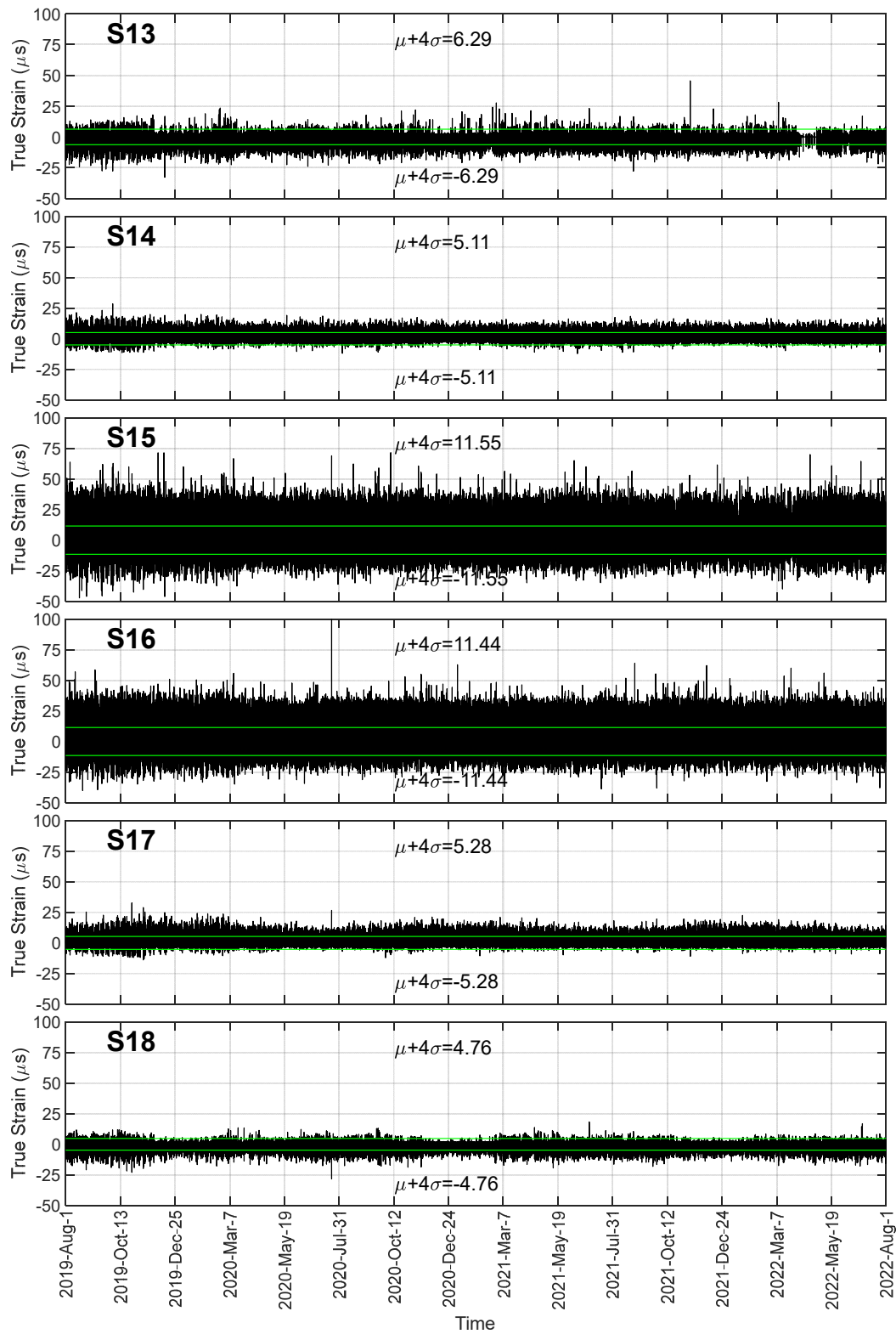


Fig. 5.16 – Live load strain for computed for all 18 strain gages. The  $4\sigma$  interval is overlapped.

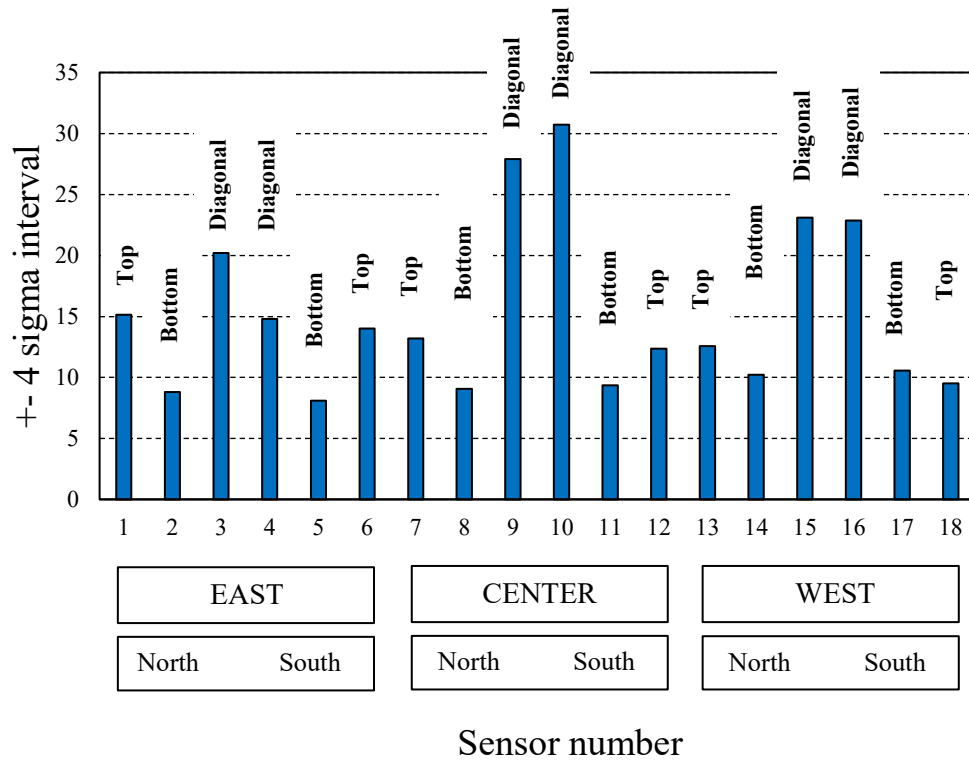


Fig. 5.17 – Value of the  $4\sigma$  interval in  $\mu\epsilon$  calculated for each strain gages on the truss.

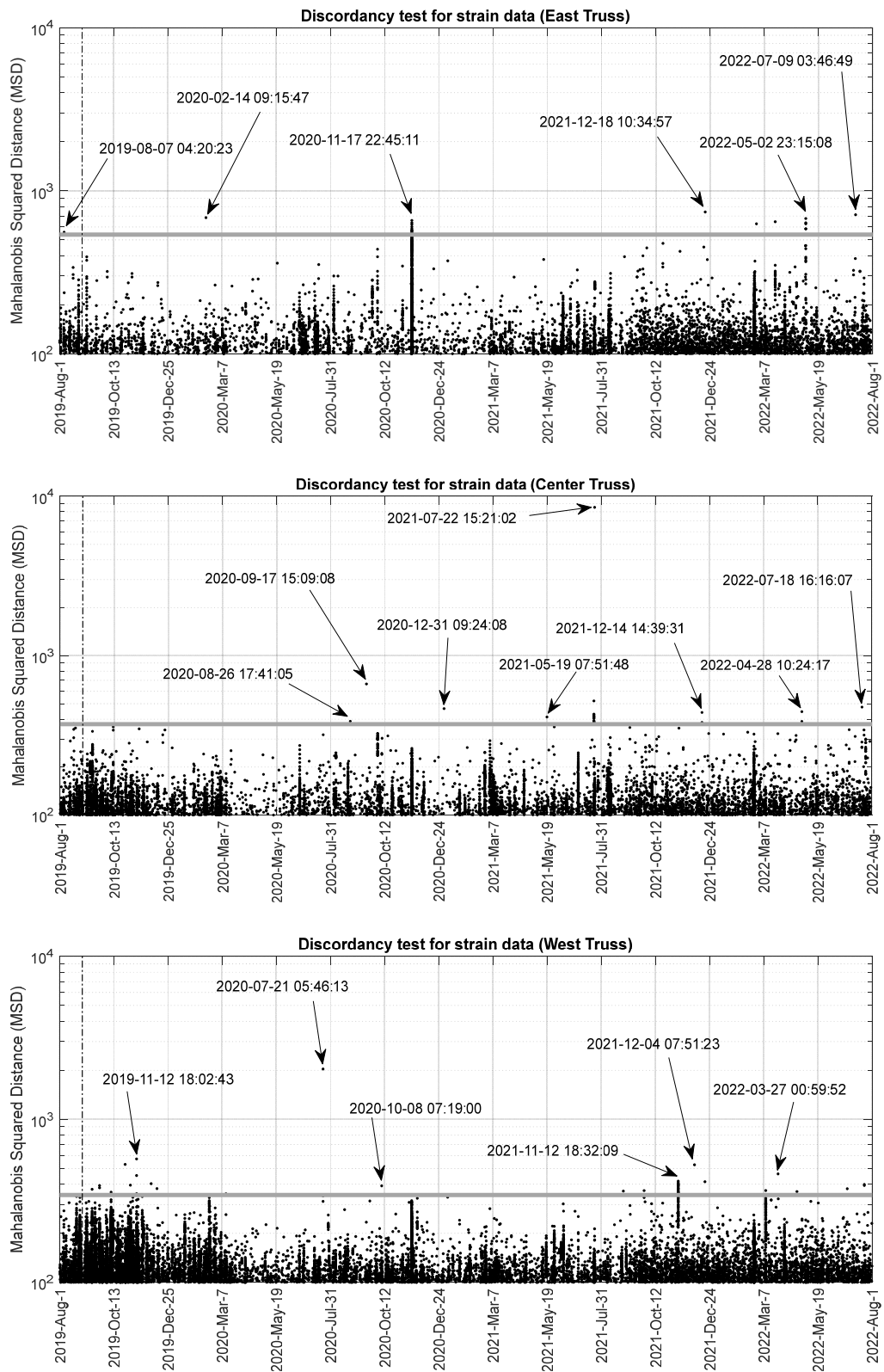
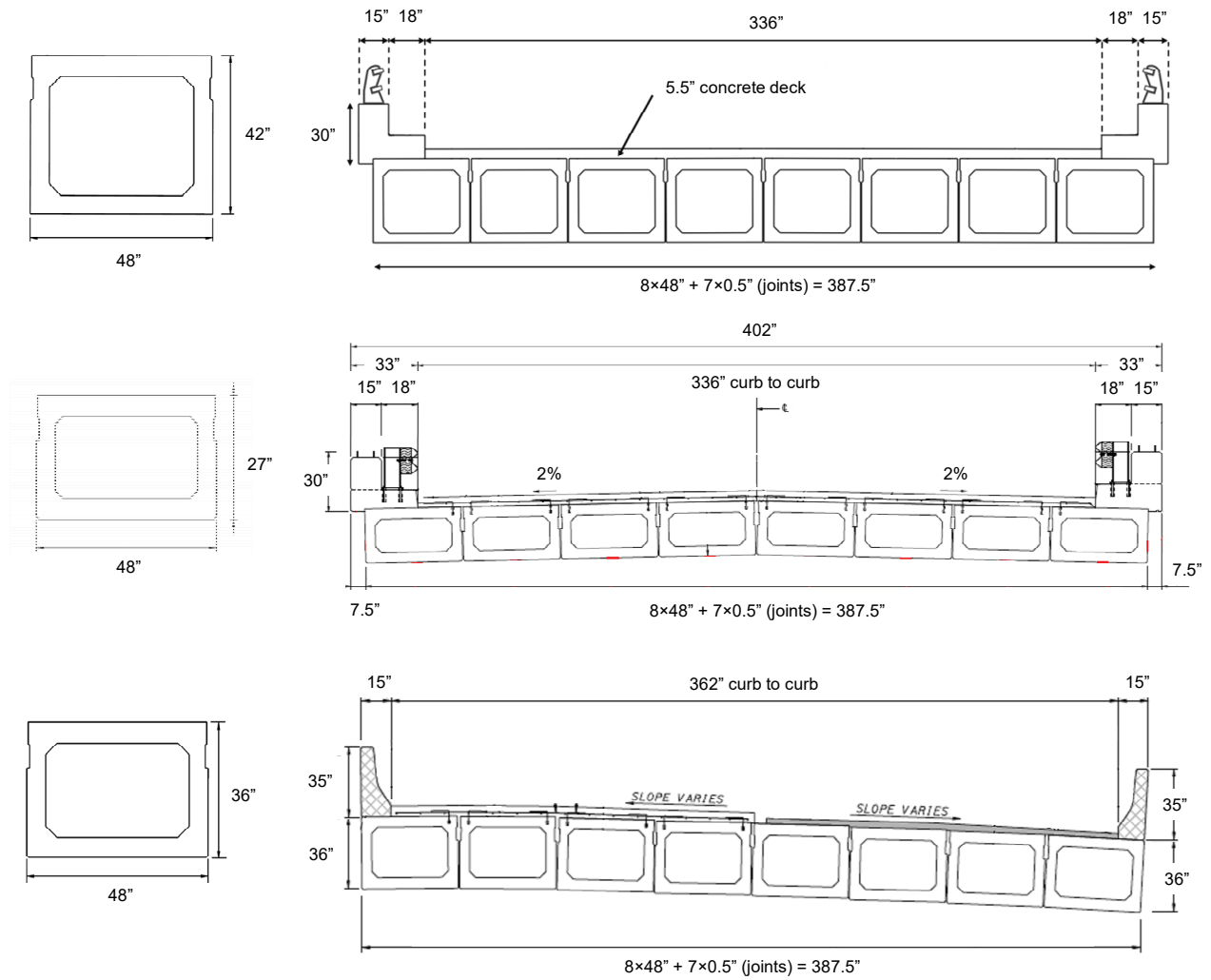


Fig. 5.18 – Mahalanobis squared distance applied to the strain gage data on the individual trusses.



**Fig. 6.1.** Photos of the three bridges considered in this study. (a) Upstream view of the BMS 55-3014-0050-0509 bridge, for convenience referred here as the Somerset bridge. (b) Cooks Mill Bridge (BMS ID 05-3001-0080-0000). (c) Single span ID 29-2004-0040-0000 bridge over little Tonoloway Creek in Fulton County



**Fig. 6.2.** Cross section of the (a) Somerset Bridge, (b) Cooks Mill Bridge, and (c) of the Tonolaway Creek Bridge. Units expressed in inches following the shop drawings provided to the authors.

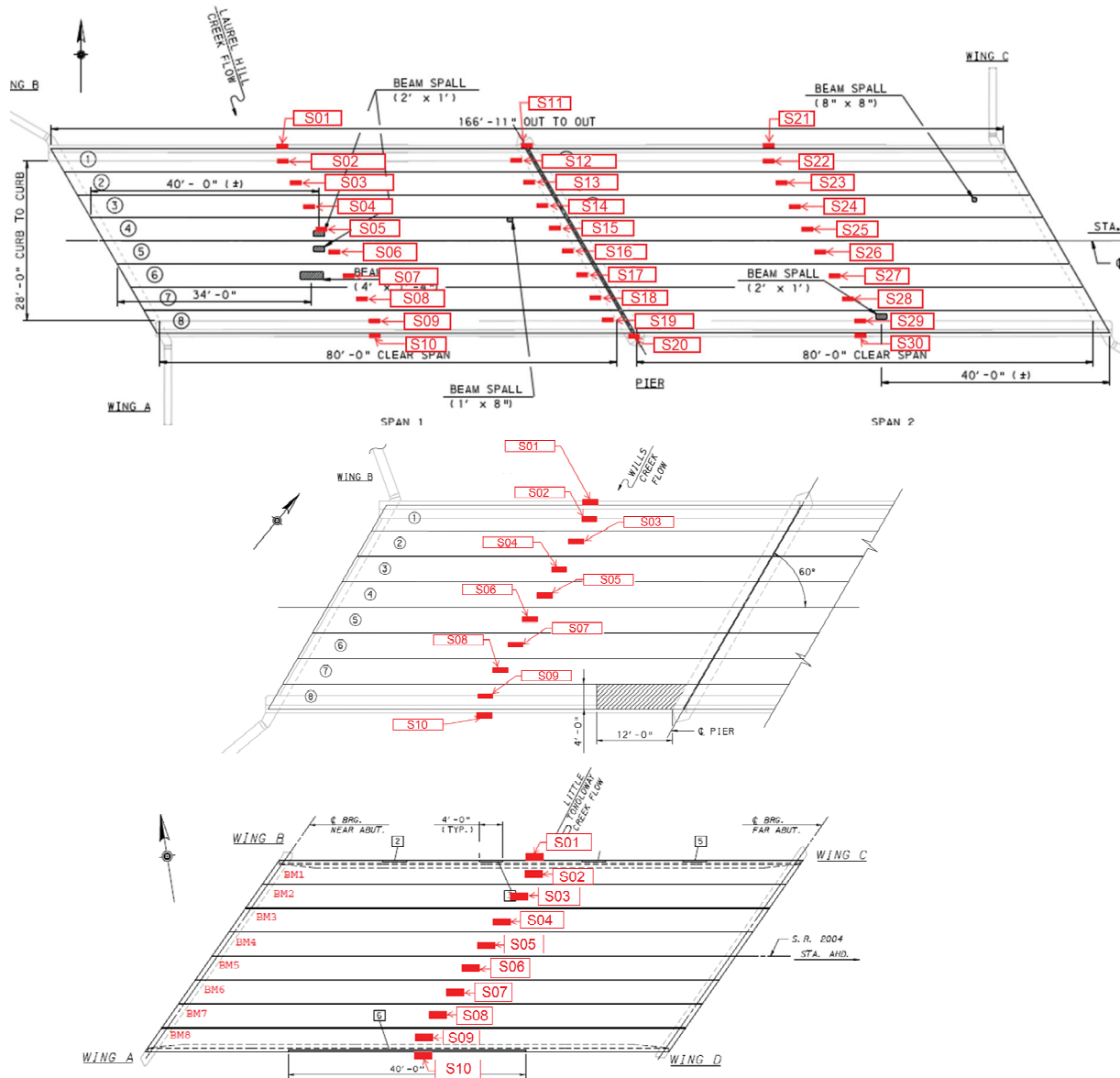


**Fig. 6.3.** Schematics of the location of the strain sensors at the (a) Somerset Bridge, (b) Cooks Mill Bridge, and (c) of the Tonolaway Creek Bridge. The box beams have a skew angle of 30°.

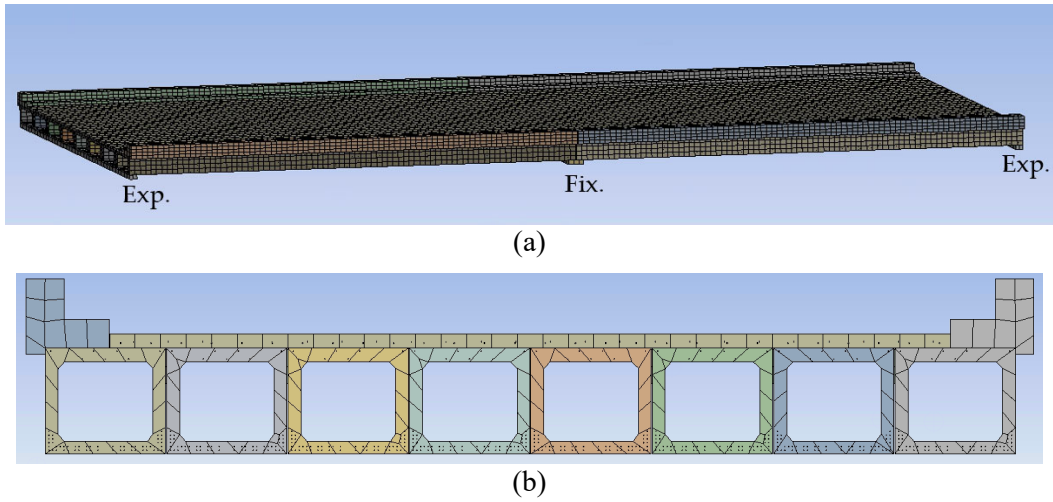


**Fig. 6.4.** Somerset Bridge. Snapshots from the high-fidelity finite element model (a) overall look; (b) cross section.

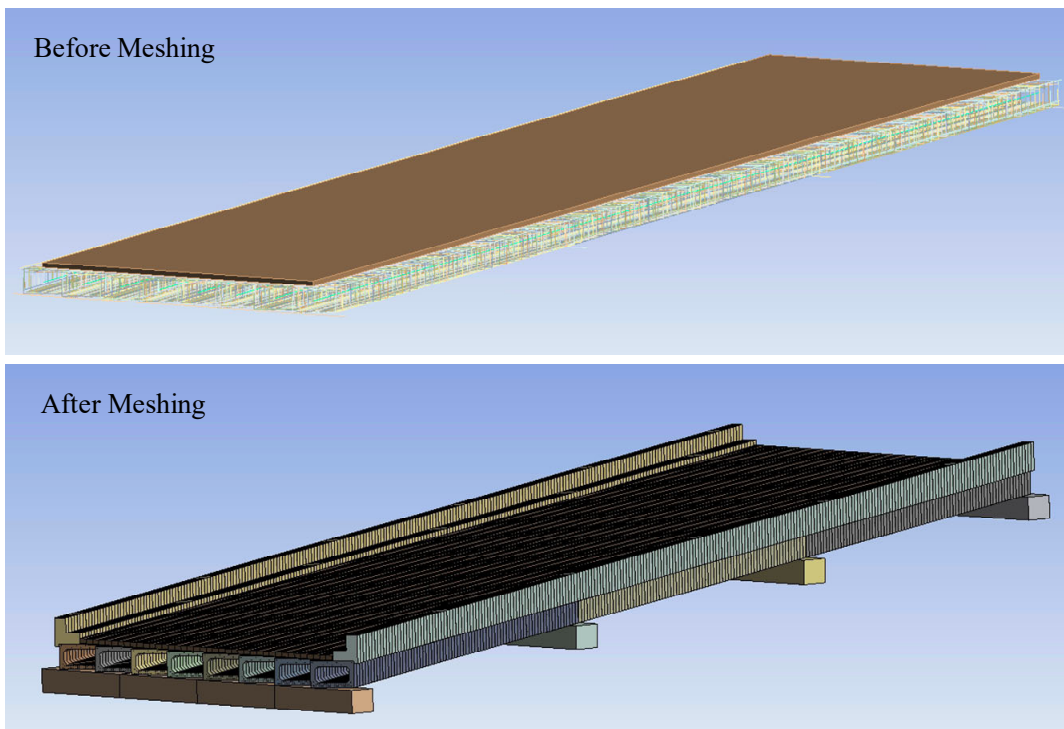


**Figure 6.5** – Cooks Mill Bridge. Snapshots of the low-fidelity model.

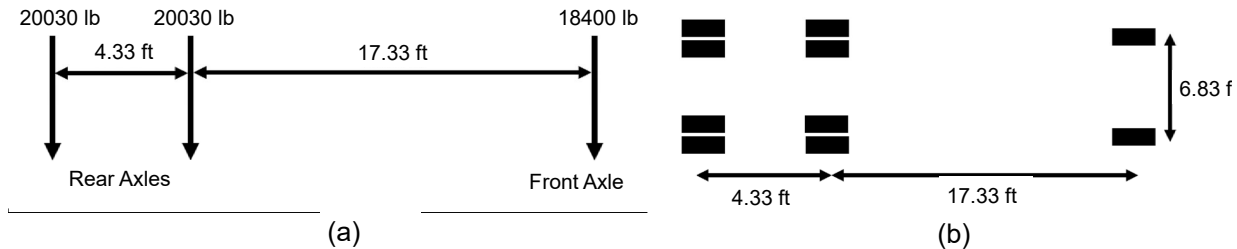


**Fig. 6.6.** Details of the configuration and dimension of the test truck (a) Side view; (b) Top view.

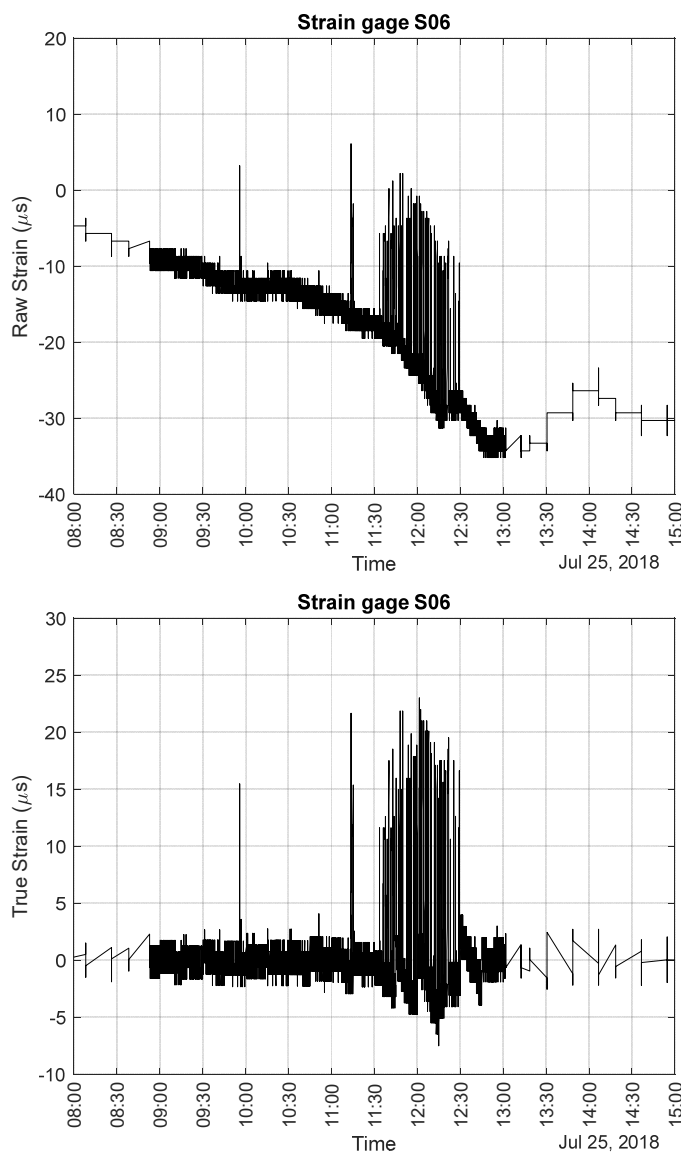


**Fig. 6.7.** Truck load test of the Cooks Mill Bridge. (a) Raw strains and (b) corresponding true strains measured by gage 06.

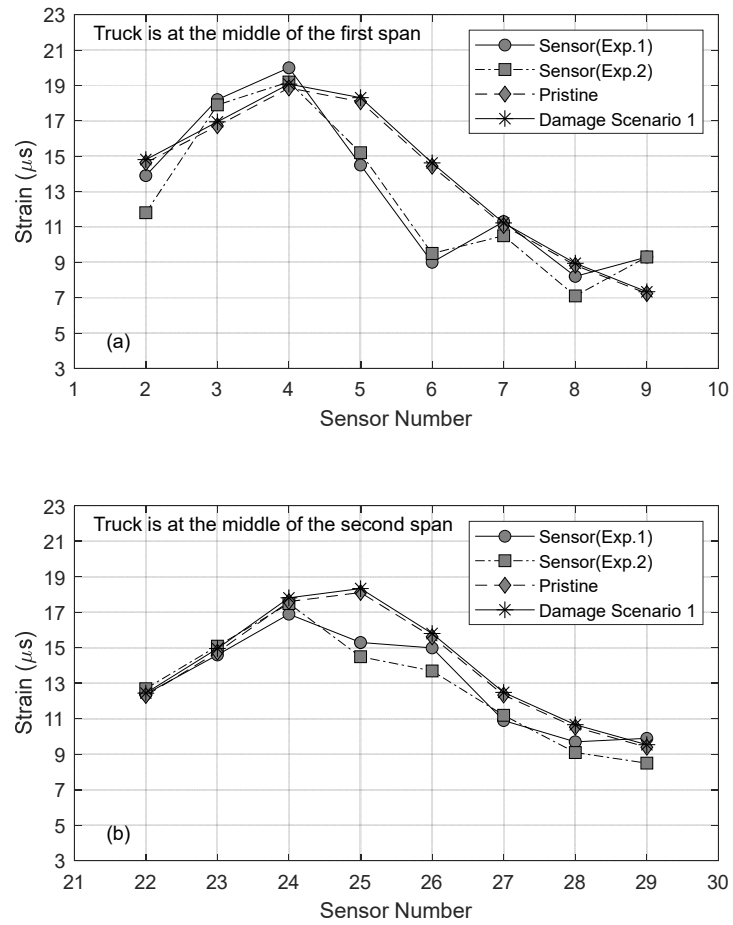


**Fig. 6.8** – Somerset Bridge. Predicted and numerical (under pristine and damage scenario 1) strains when the truck was 1.52 m (5 ft.) away from the north parapet.

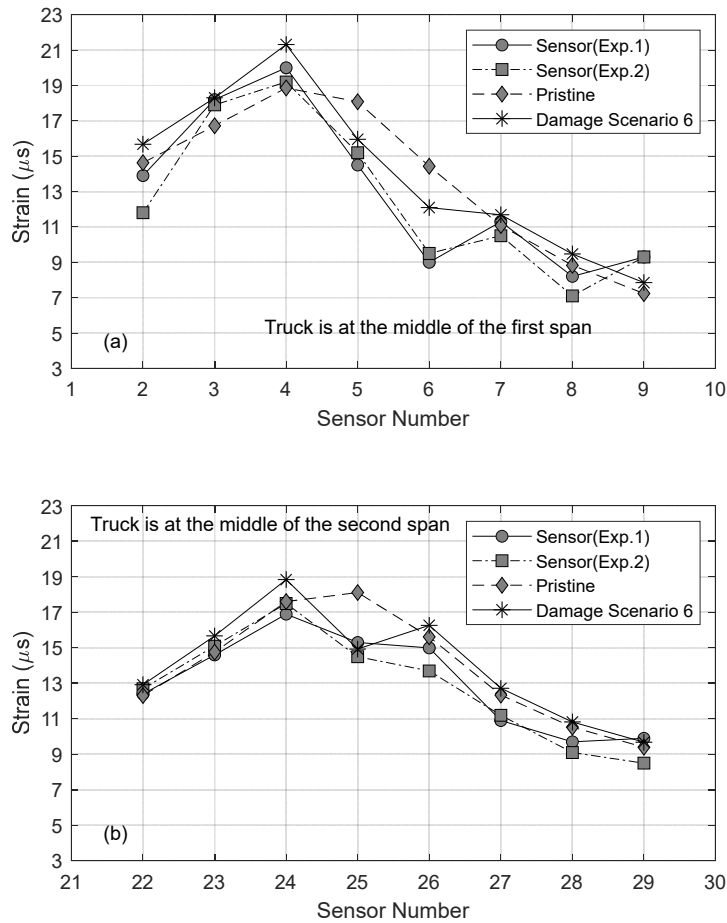


**Fig. 6.9** – Somerset Bridge. Predicted and numerical (under pristine and damage scenario 6) strains when the truck was 1.52 m (5 ft.) away from the north parapet.

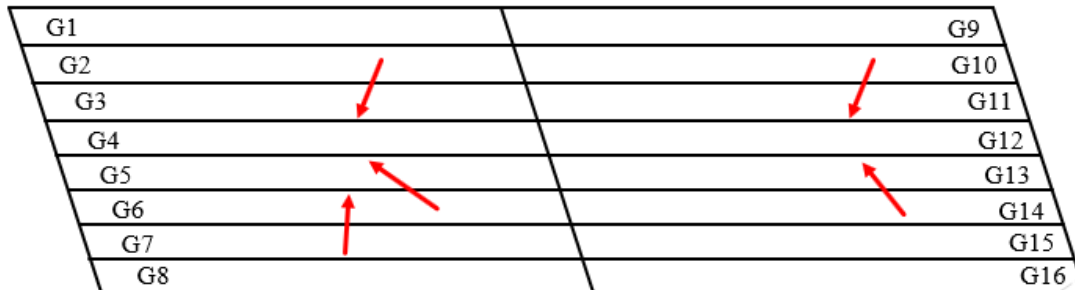


**Fig. 6.10** – The shear keys at the Somerset Bridge that their contacts with the adjacent beams were changed to “No separation”

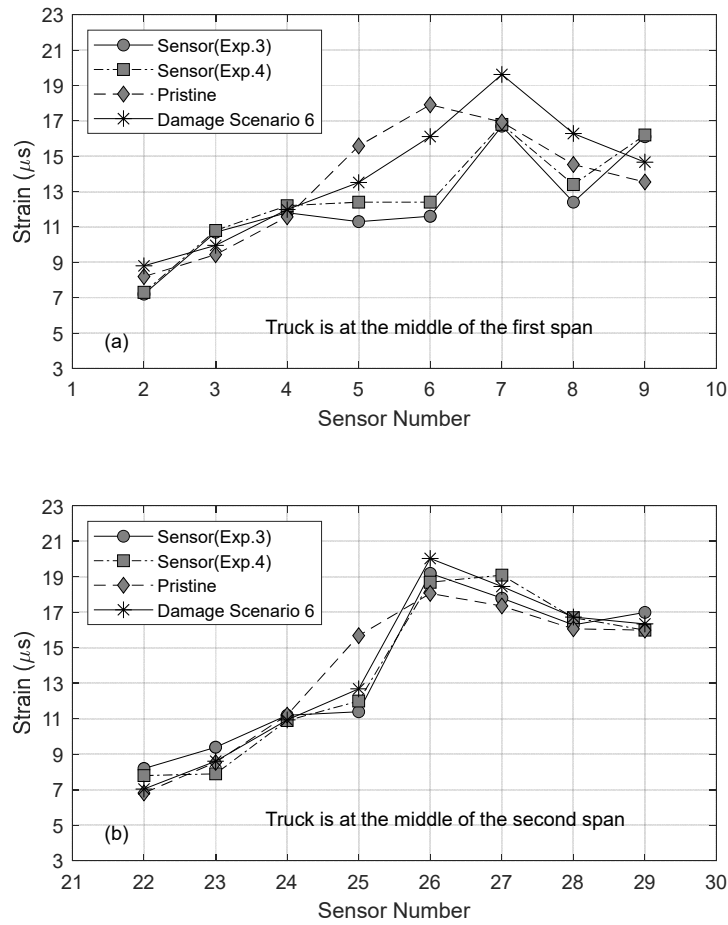


**Fig. 6.11** – Somerset Bridge. Predicted and numerical (under pristine and damage scenario 6) strains when the truck was 4.57 m (15 ft.) away from the north parapet.

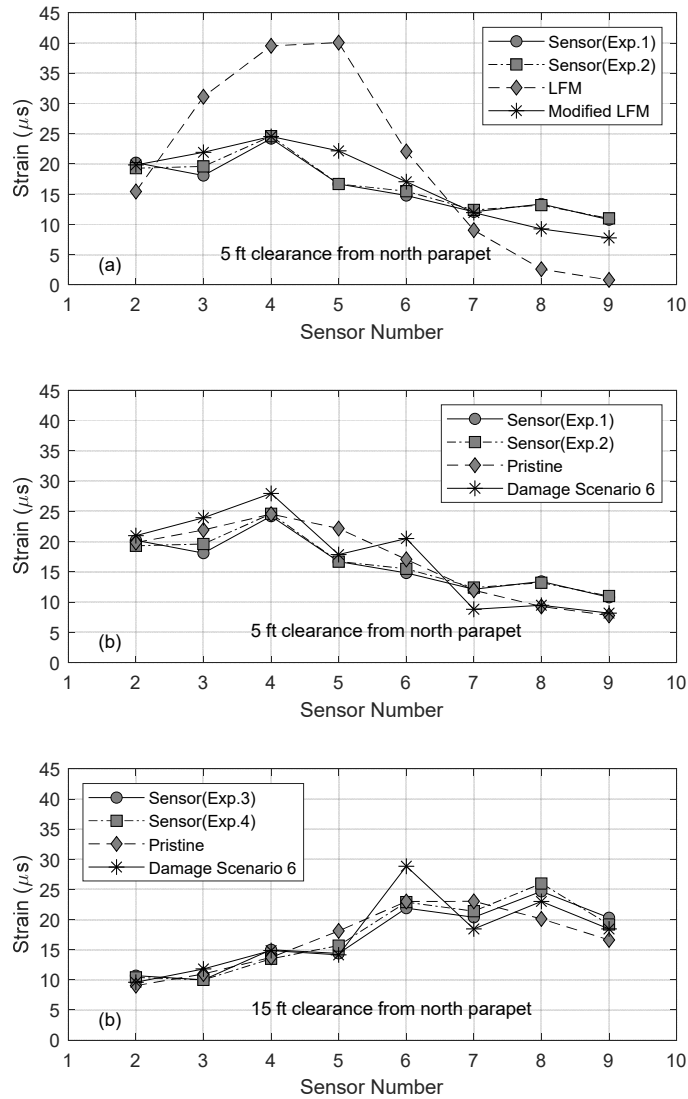


**Fig. 6.12** – Cooks Mill Bridge analysis. Comparison of the experimental and numerical data. (a) Use of low-fidelity finite element models with the truck 1.52 m (5 ft.) away from the north parapet. (b) Same load scenario as in (a) but using EFEM. (c) Same as (b) but the truck at truck 4.57 m (15 ft.) away from the north parapet.



**Fig. 6.13** – (a) The shear keys that their contacts with the adjacent beams were changed to “No separation”

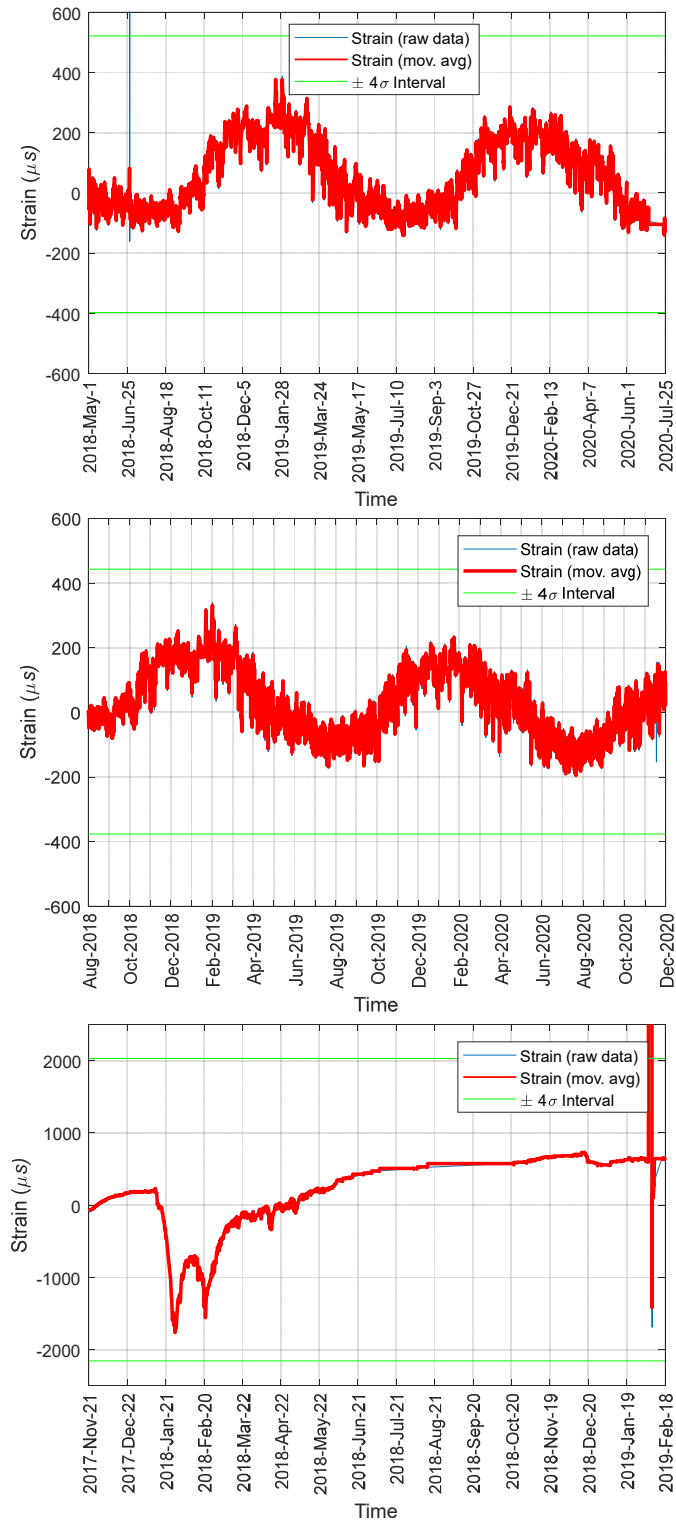


**Fig. 6.14.** Raw strain and corresponding 15-minutes average recorded by sensor 05 mounted on the (a) Somerset Bridge, (b) Cooks Mill Bridge, and (c) Tonolaway Bridge.

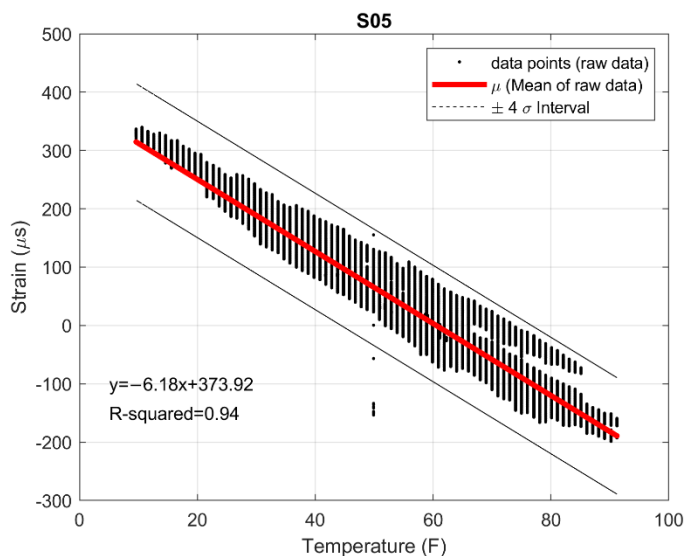


Fig. 6.15. Cooks Mill Bridge. Raw strain vs raw temperature measured by gage 05.

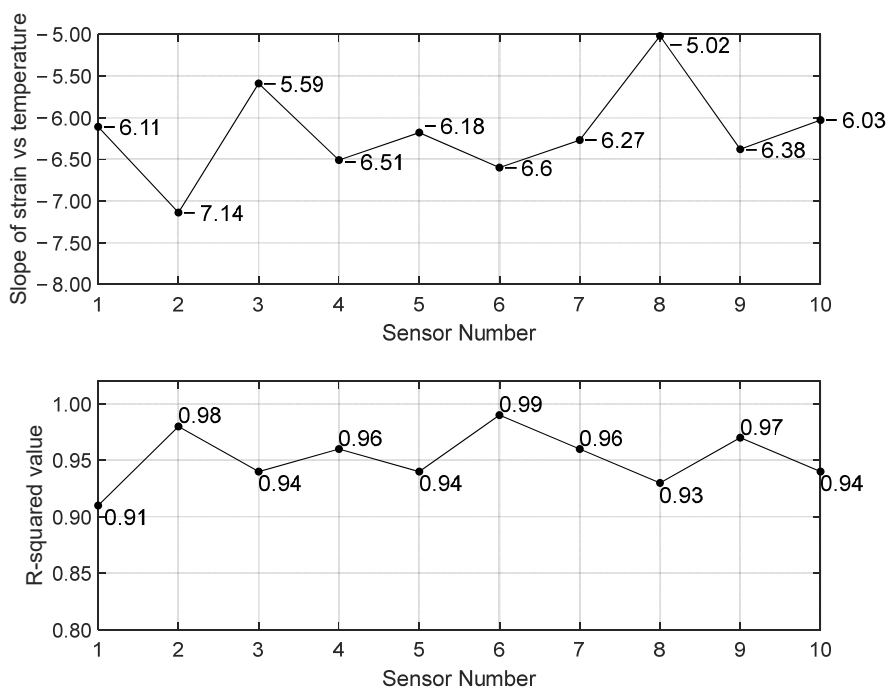
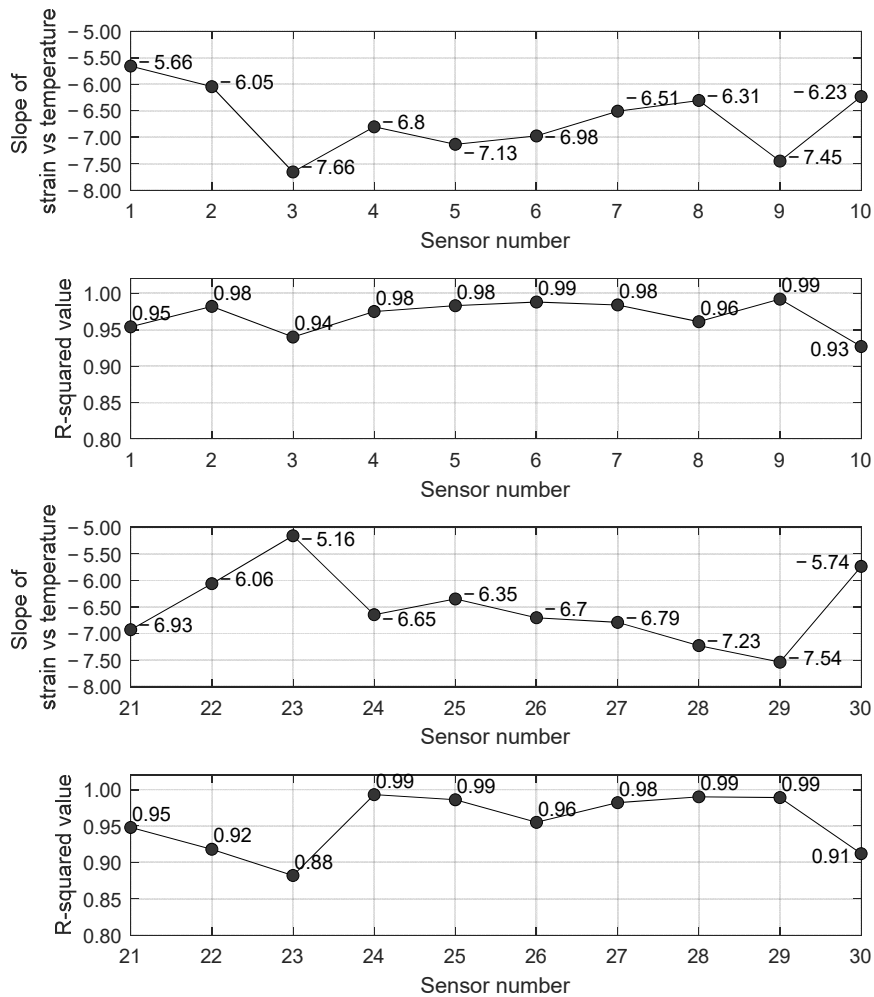
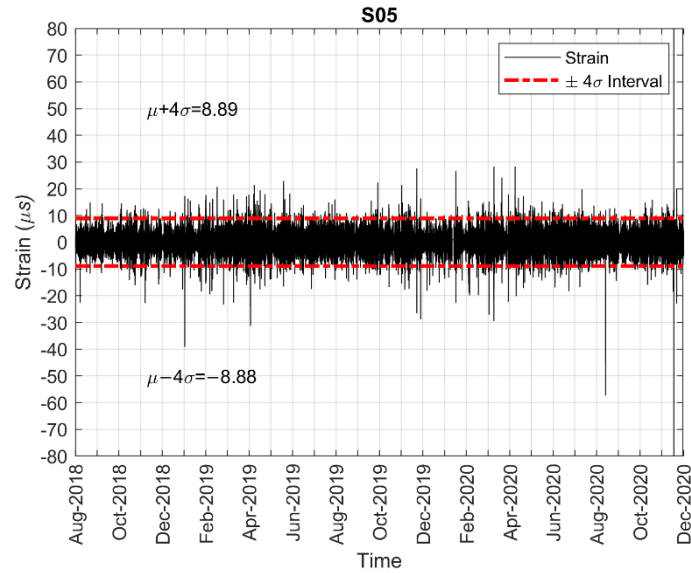


Fig. 6.16. Cooks Mill Bridge. Slope of linear regression of the strain vs temperature graphs (the values are expressed in  $\mu\epsilon/^\circ F$ ) and Residual  $R^2$  of the linear interpolation strain vs temperature. S01-S10 were bolted to the first span and S21-S30 were bolted to the second span.



**Fig. 6.17.** Somerset Bridge. Slope of linear regression of the strain vs temperature graphs (the values are expressed in  $\mu\epsilon/^\circ\text{F}$ ) and Residual  $R^2$  of the linear interpolation strain vs temperature. S01-S10 were bolted to the first span and S21-S30 were bolted to the second span.



**Fig. 6.18. Cooks Mill Bridge.** True strain calculated as the difference between the raw strain and the moving averaged strain.

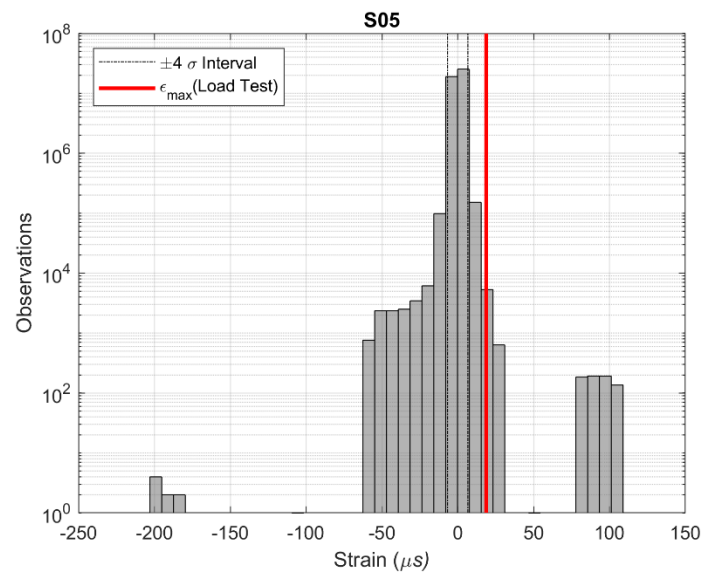


**Fig. 6.19. Cooks Mill Bridge.** Histogram chart relative to the true cleaned strain of gage S05.

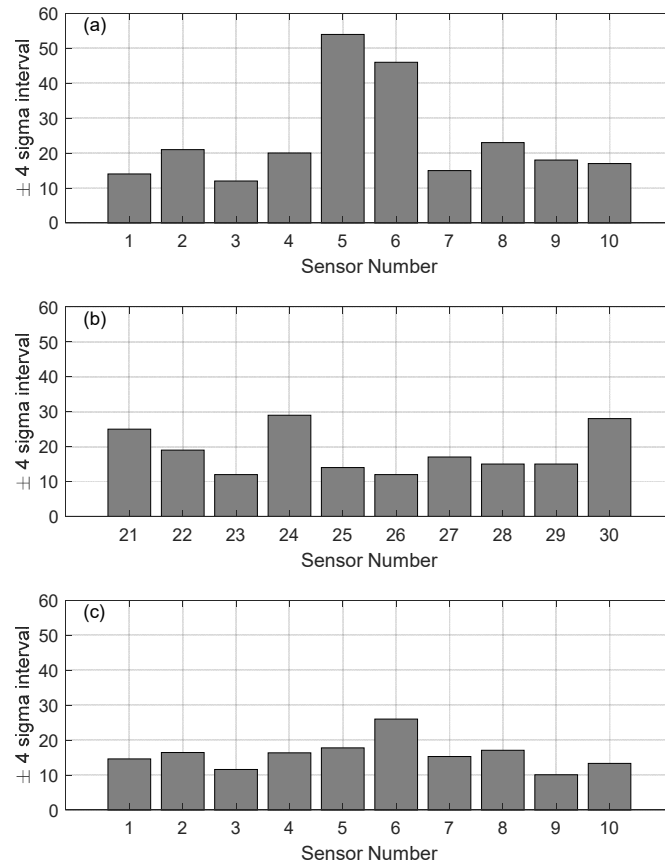


**Fig. 6.20.** Values of the  $\pm 4$  standard deviation range of the true clean strain calculated for (a, b) - the Somerset Bridge and (c) - the Cooks Mill Bridge.

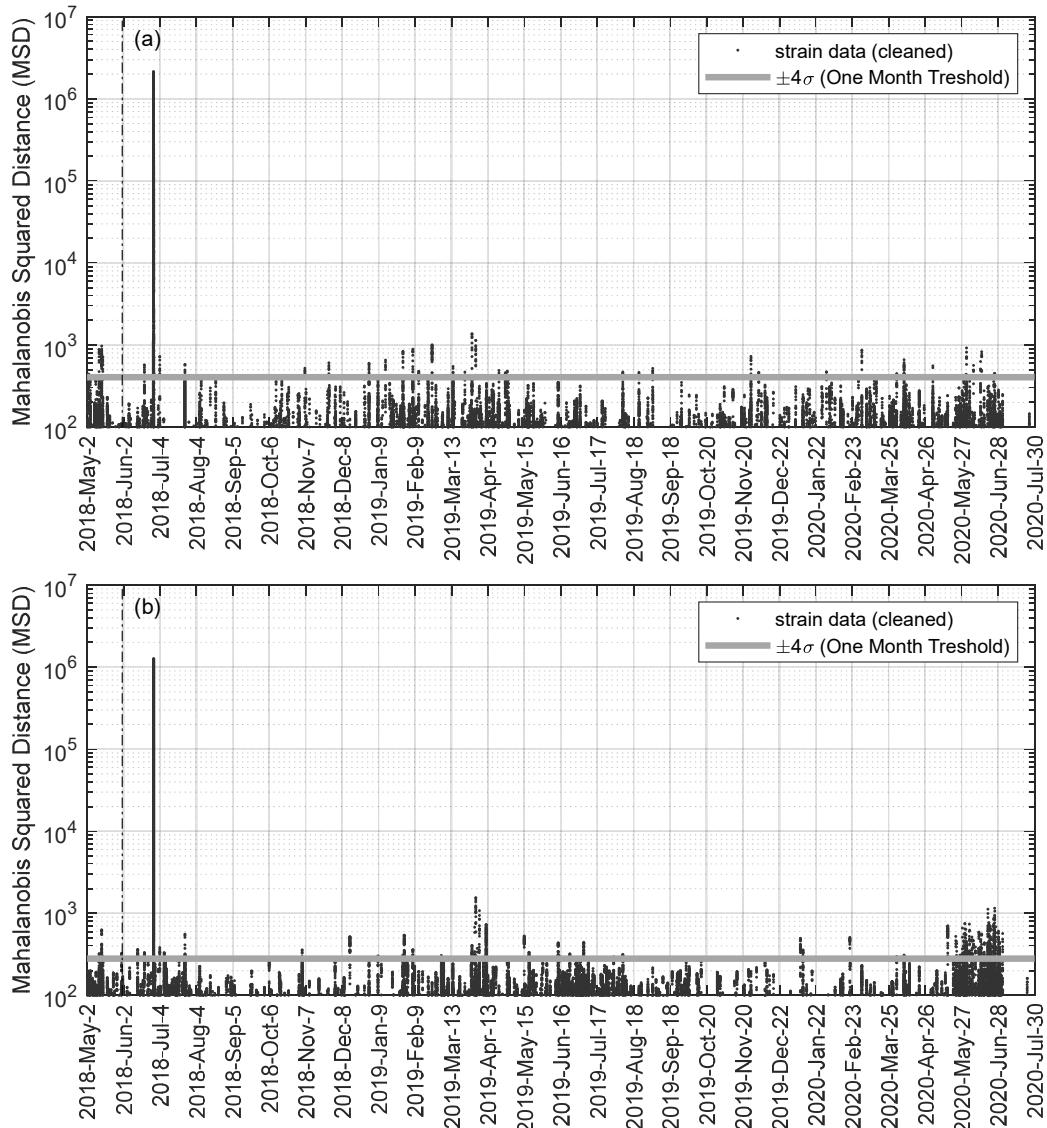
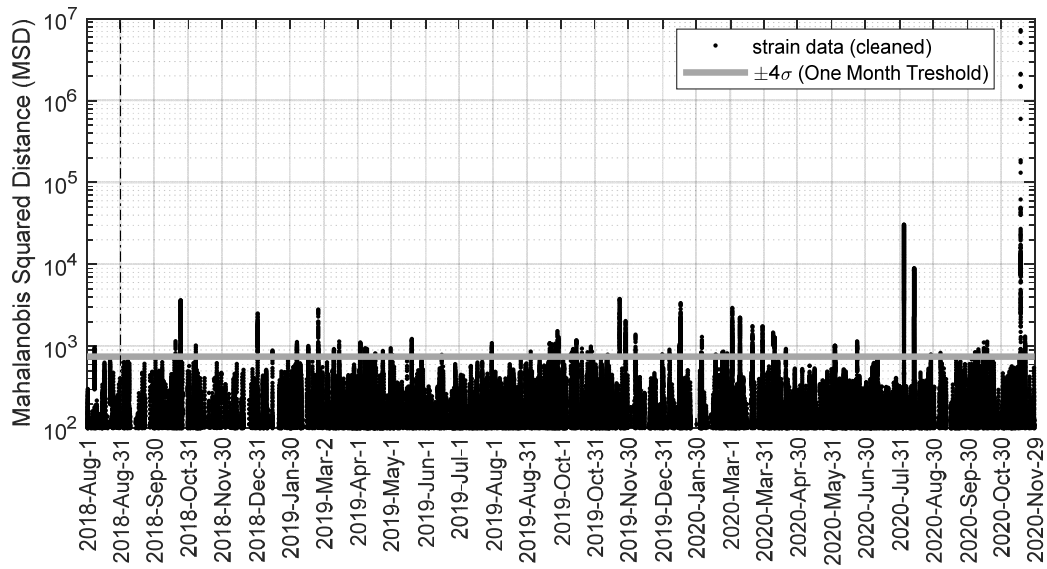
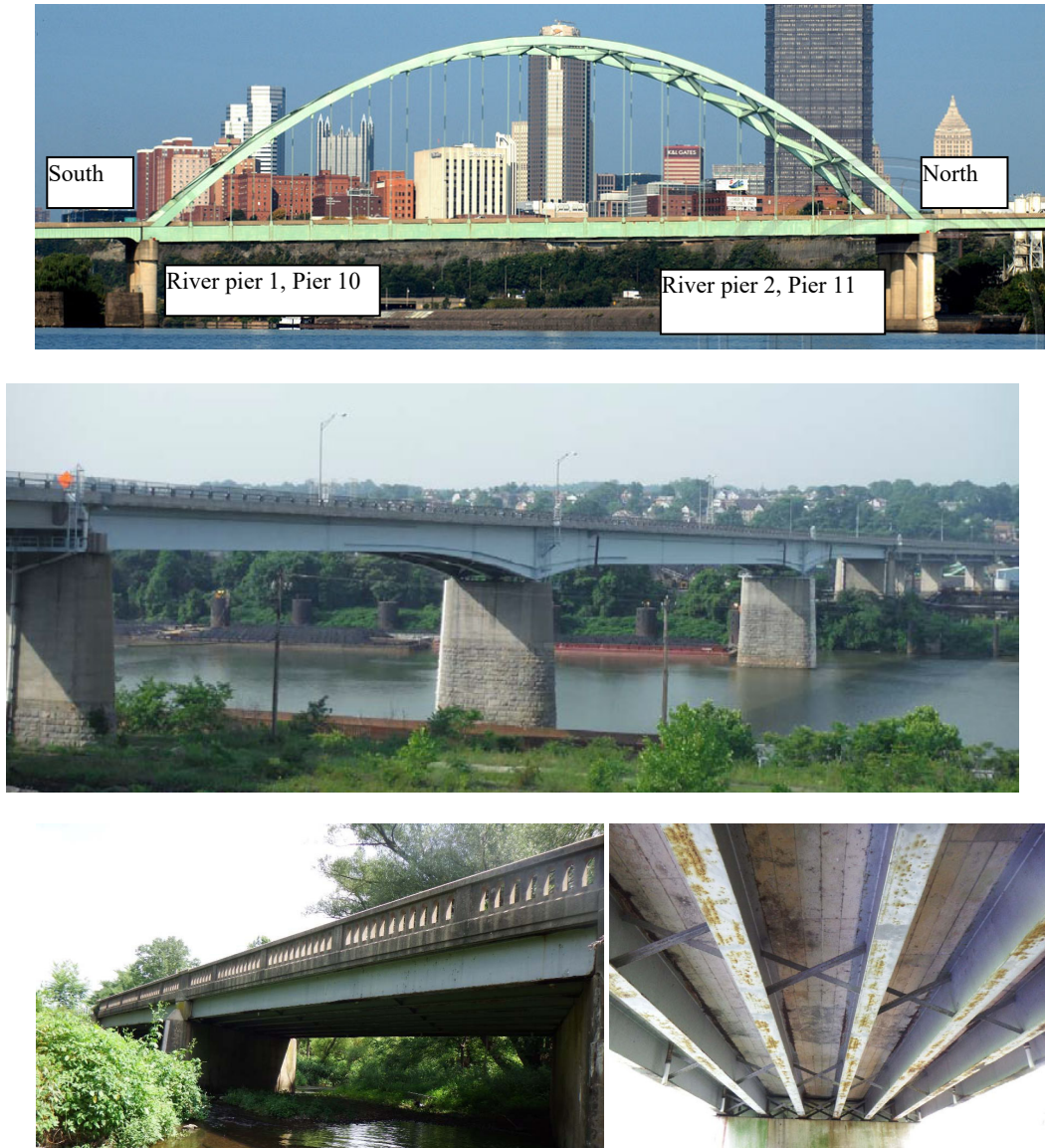


Fig. 6.21- Mahalanobis squared distance applied to the live strains from gages (a)-1 to 10 and (b)- 21 to 30.



**Fig. 6.22** - Mahalanobis squared distance applied to the live strains from all ten strain gages on the Cooks Mill bridge.



**Figure 7.1.** Photos of the (a) Birmingham Bridge. (Figures adapted from <https://www.flickr.com/photos/jag9889/10148146816>) (b) Glassport-Clairton Bridge. (c) Chester Bridge. (Upstream elevation looking downstream and deck underside and superstructure. Figure adapted from the 2015 bridge inspection report).

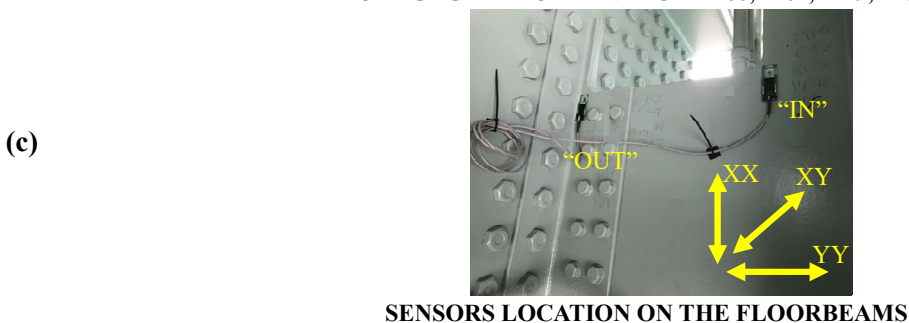
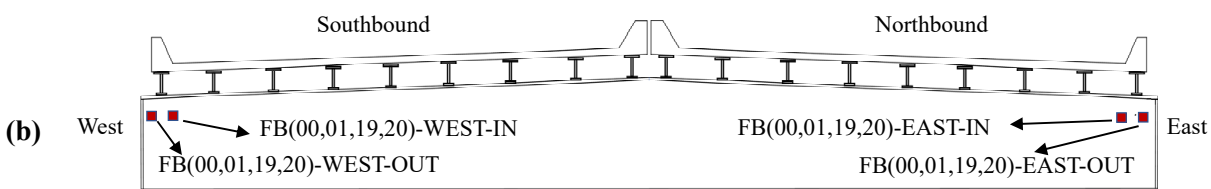
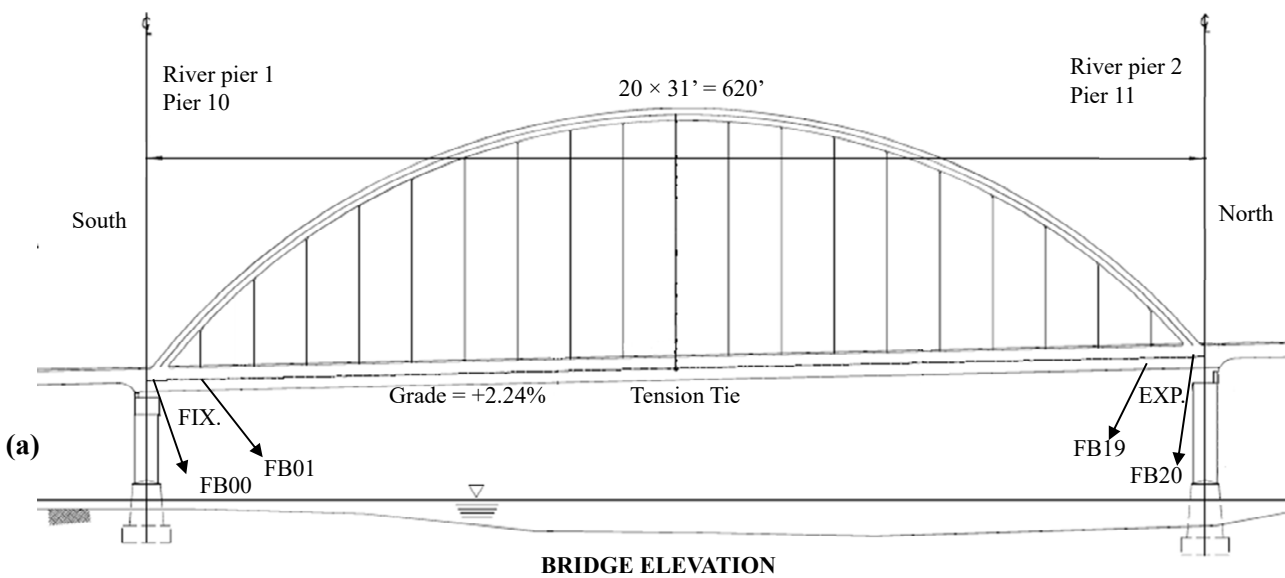


**Fig. 7.2** – Instrumentation plan of the Birmingham Bridge.

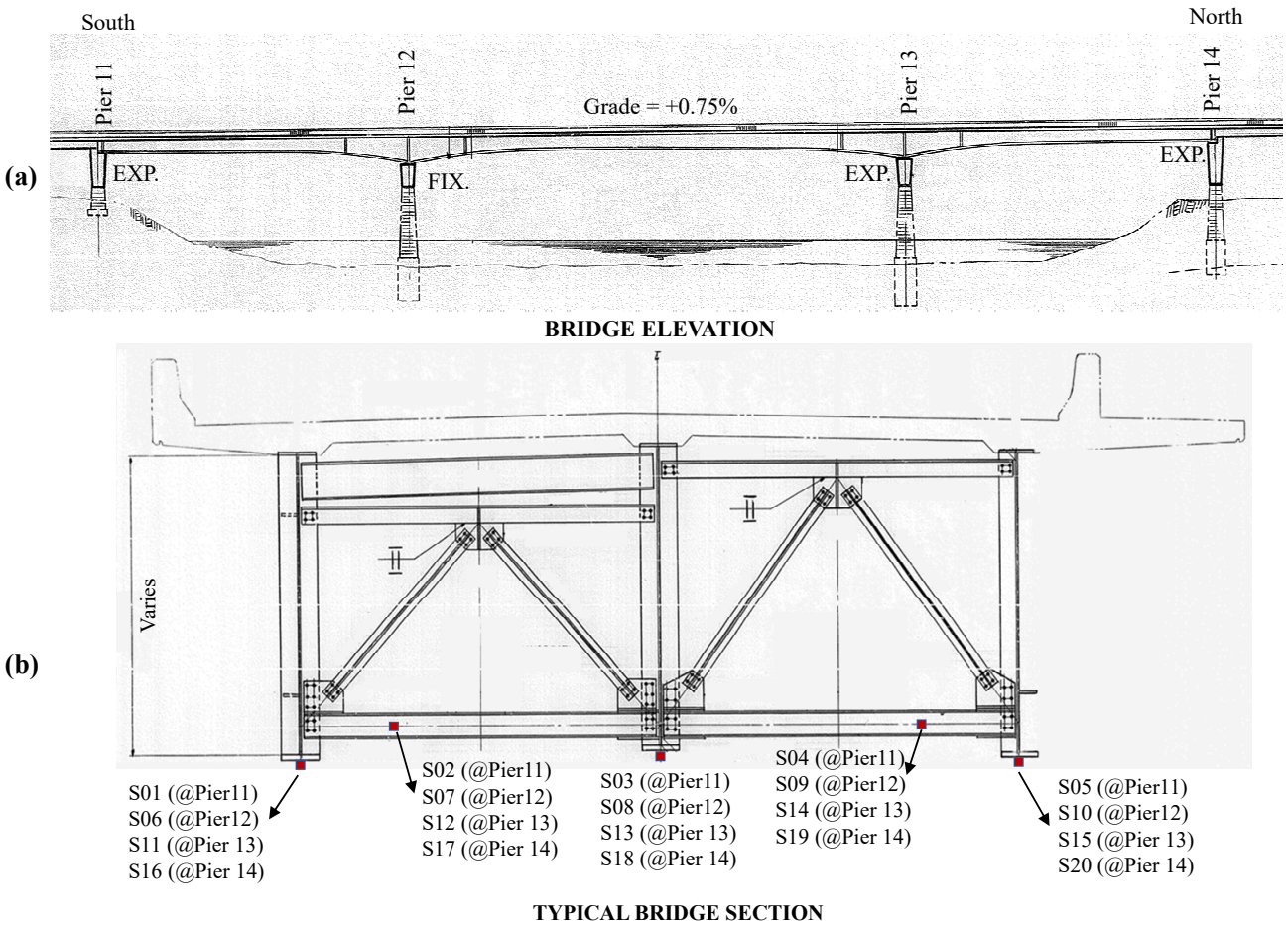


Fig. 7.3 – Instrumentation plan of the Clairton Bridge.

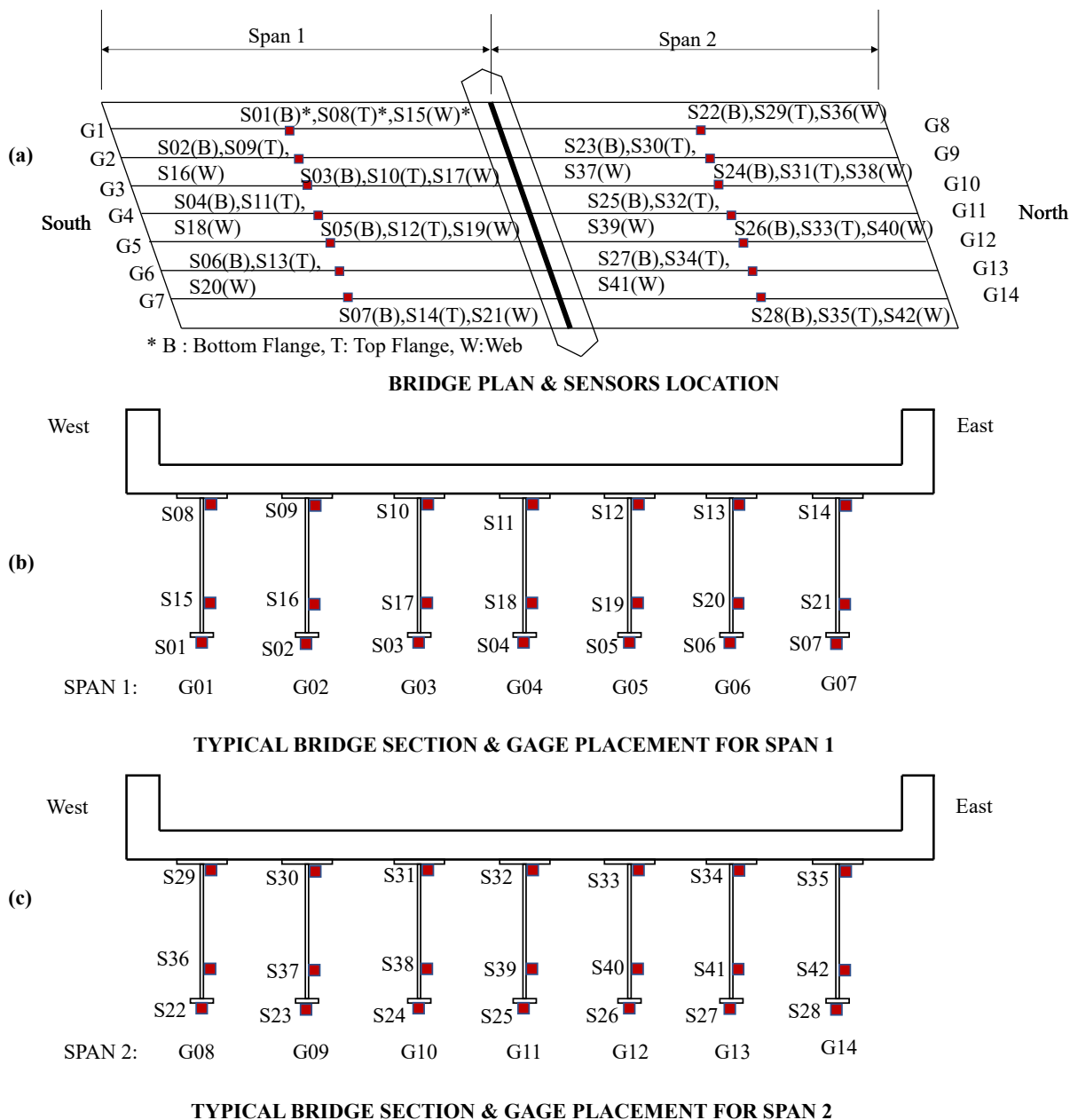


Fig. 7.4 – Instrumentation plan and meaning of the Chester Bridge.

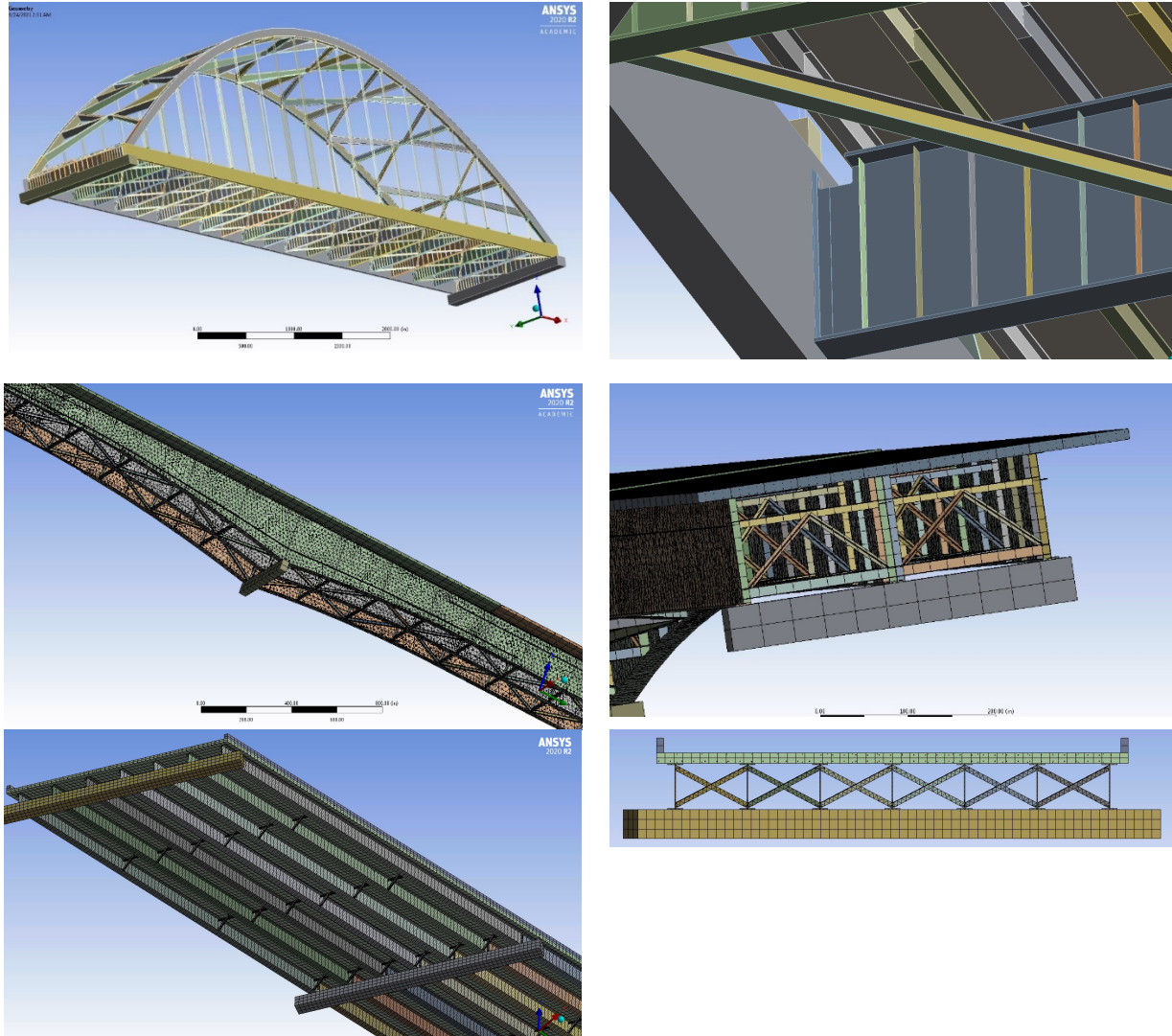


Fig. 7.5 – Snapshots of the digital replicas of the three bridges considered in this study

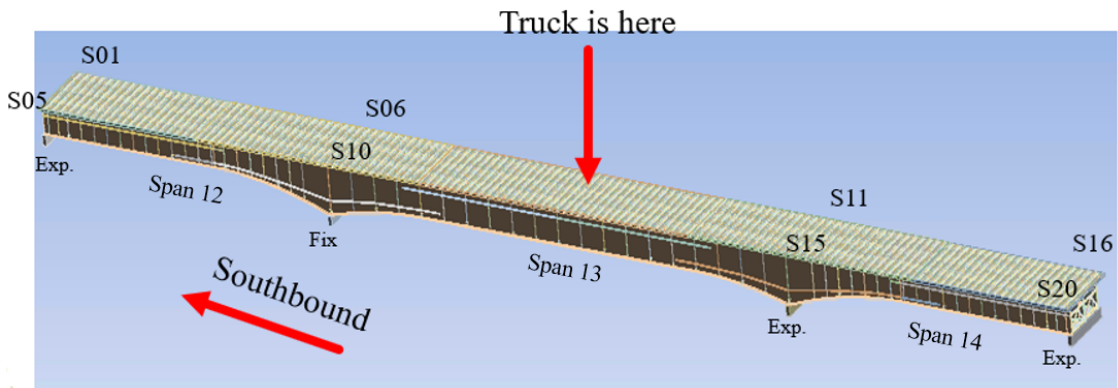
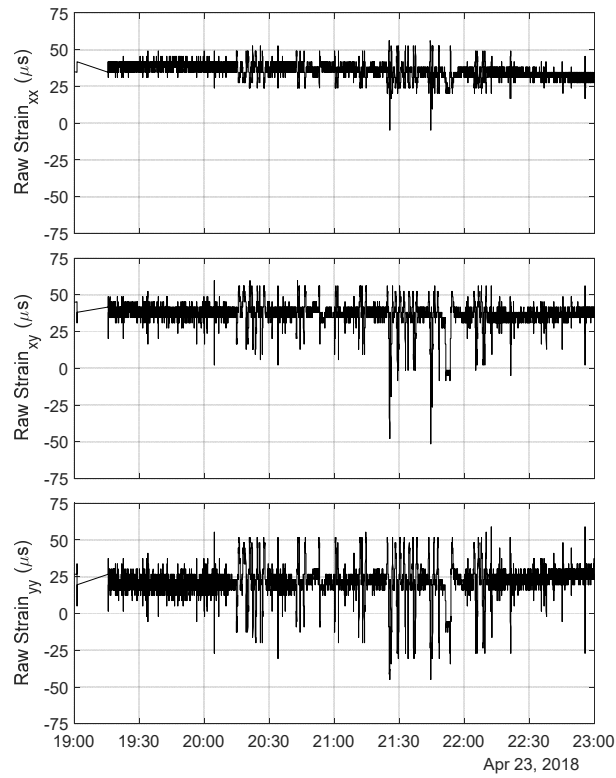
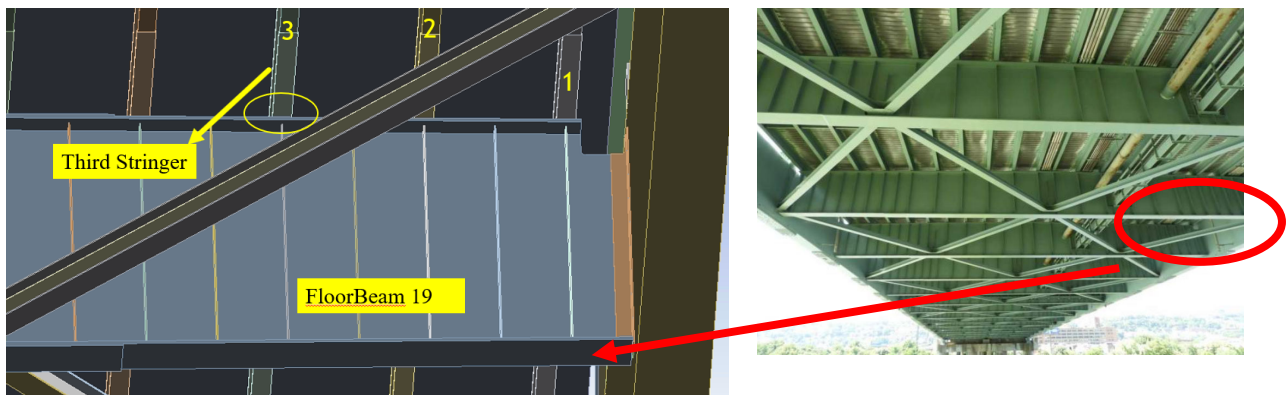


Fig. 7.6 – Clairton Bridge analysis. Load Case 2: A truck load was applied in the middle of Span 13 in South bound direction



**Figure 7.7.** Representative result of the truck load test on the Birmingham Bridge. Values recorded by gage FB01-WEST-IN



**Fig. 7.8** – The changed contacts of the third stringers for damage scenario 3.

Under “pristine” conditions the three stringers from the East and West parapets are expandable and the remaining are fixed. These fixed stringers transfer the load to the floorbeam.

Under damage scenario 3: the third stringer contributes to the load transfer to the FB and it is applied closer to the tie girder.



Fig. 7.9 – Load transfer mechanism between stringer 3 and FB19 under pristine and damage scenario 3.

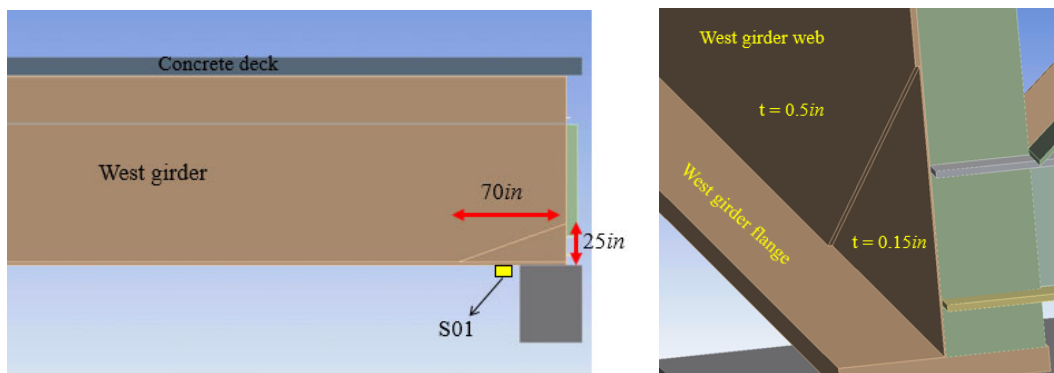


Fig. 7.10 – Clairton Bridge modeling. Damage scenario 5: side view and 3D view from the end of the West girder.

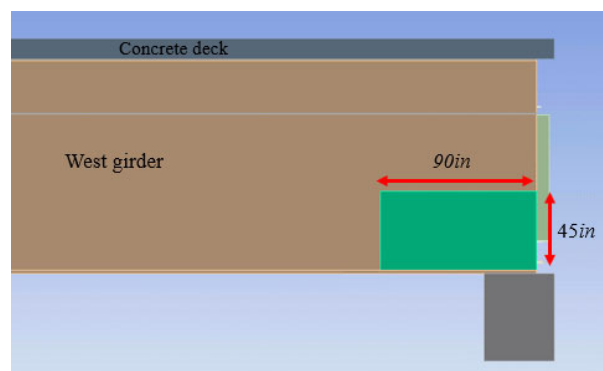
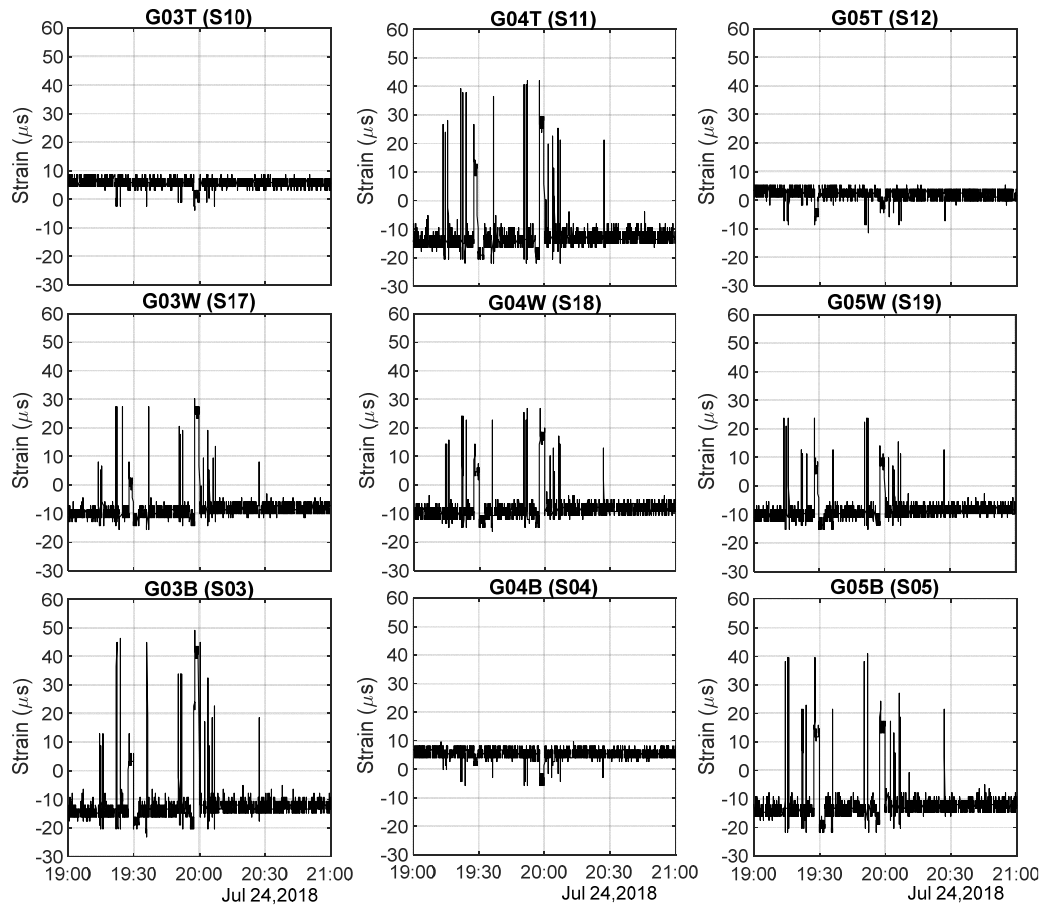
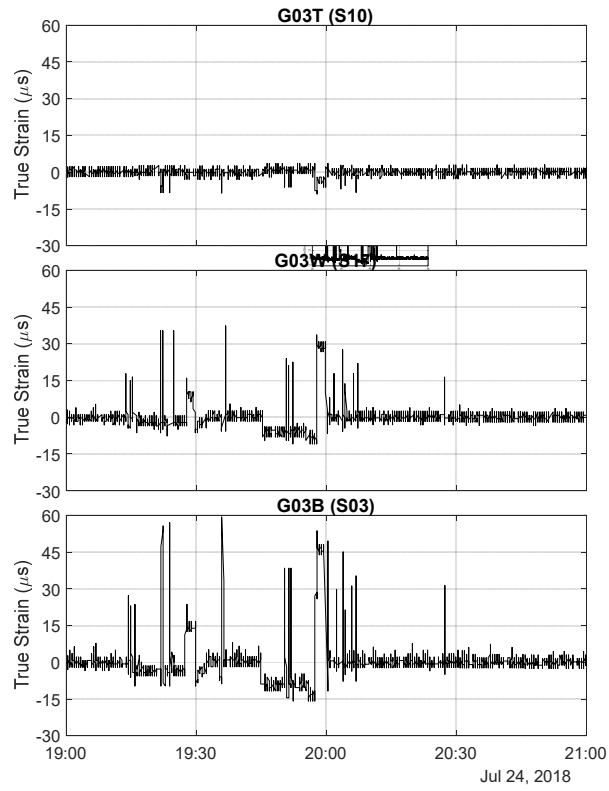


Fig. 7.11 – The added rectangular plate to the location of the fifth damage scenario.



**Figure 7.12.** Chester Bridge truck testing. Raw strains recorded by the sensors bonded to girder 3 (left column), girder 4 (middle column), and girder 5 (right column). From top to bottom the sensors were those bonded to the top flange, web, and the bottom flange.



**Figure 7.13.** Representative result of the truck load test on the Chester Bridge. True strains.

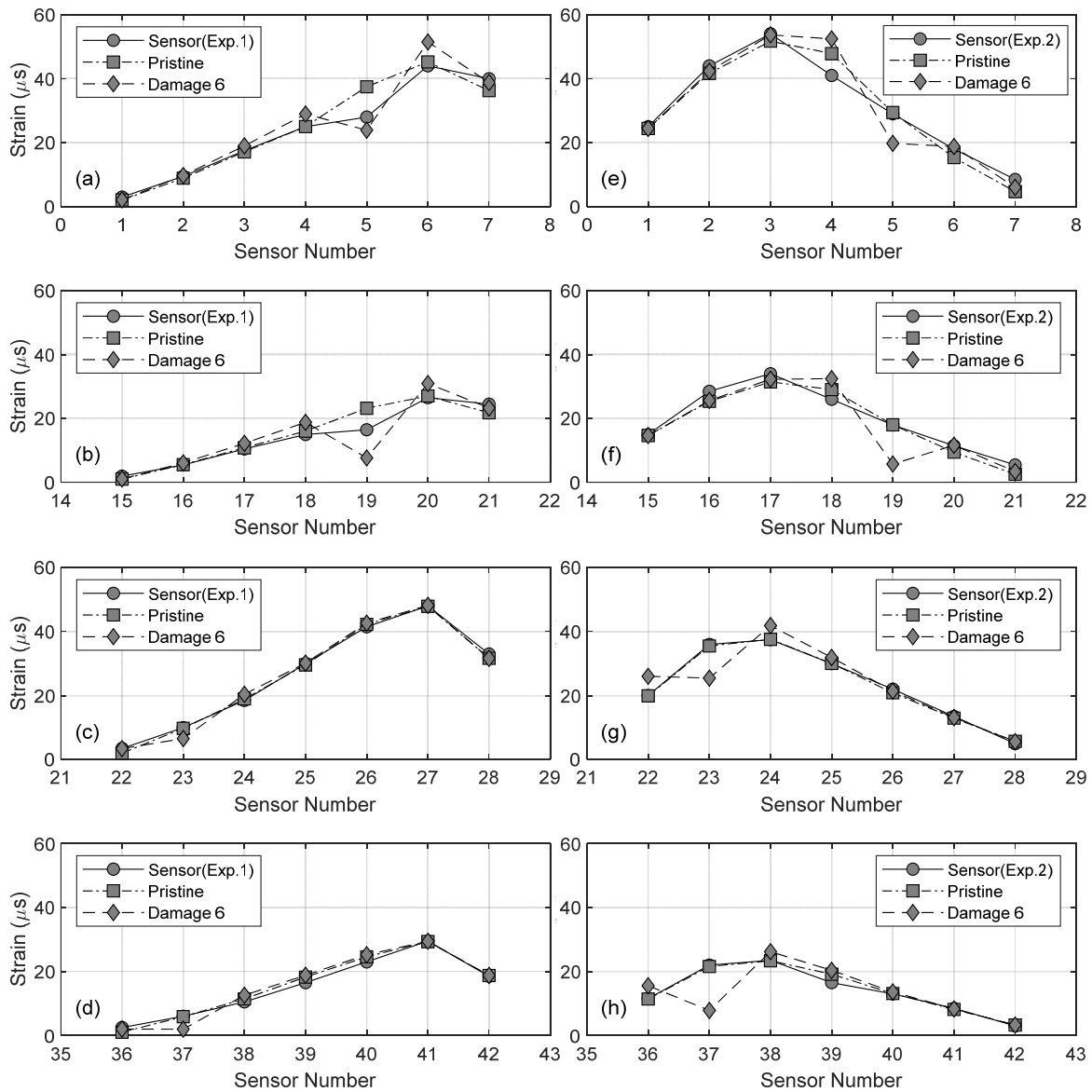


**Fig. 7.14** – The predicted strains at certain locations of the bridge for the sixth damage scenario. (a) to (d) refer to Experiment 1, and (e) to (h) to Experiment 2. In Exp. 1 and 2, the truck travelled over the bridge northbound and southbound, respectively. For (a), (b), (e), and (f), the truck is at the middle of the first span and for (c), (d), (g) and (h) is at the middle of the second span. The field data were extracted from the graphs published by the Company executing the test in the report provided to the authors by the project sponsor.

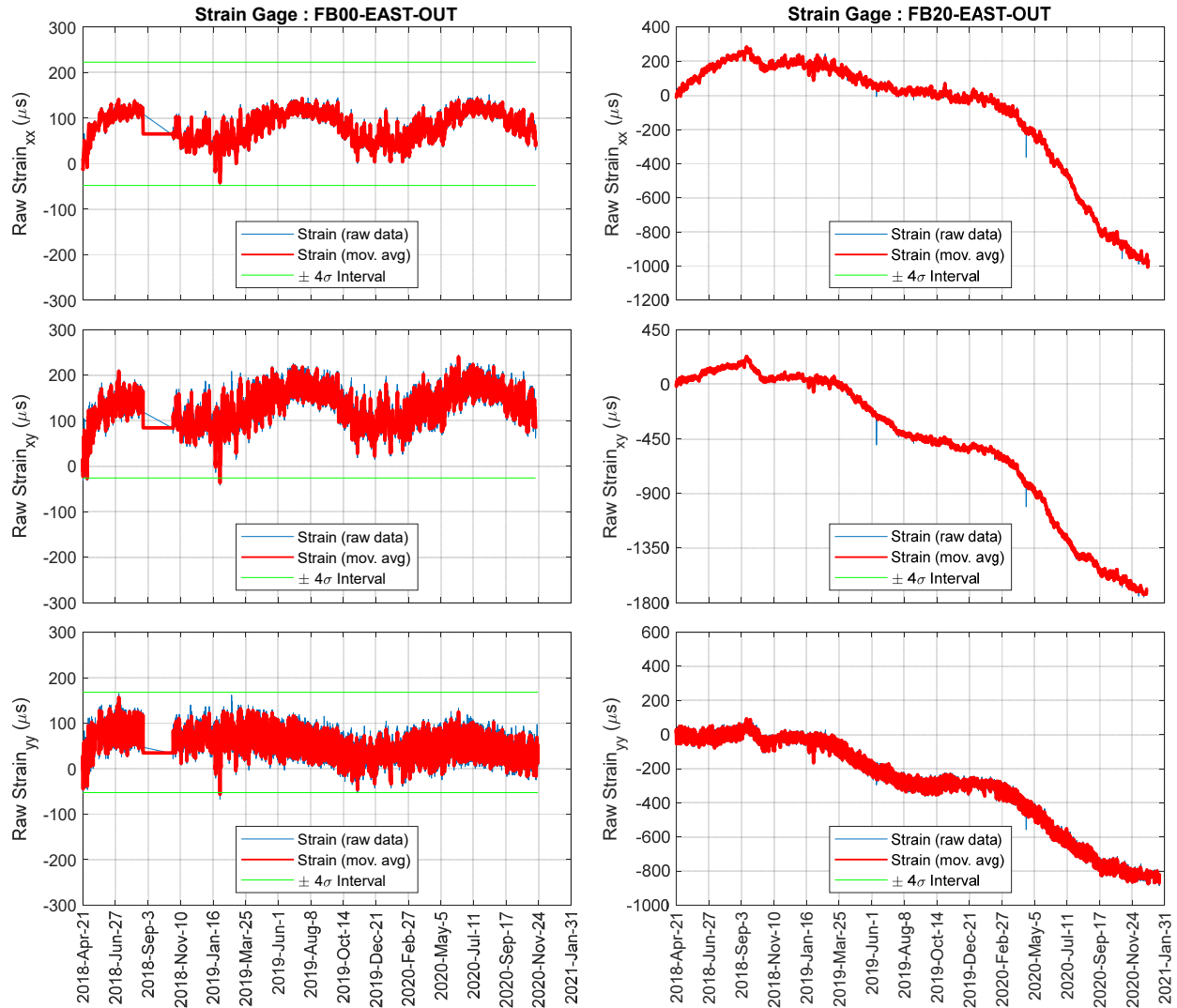


Fig. 7.15– Raw and moving averaged strain recorded through January 31<sup>st</sup> 2021, Birmingham Bridge.

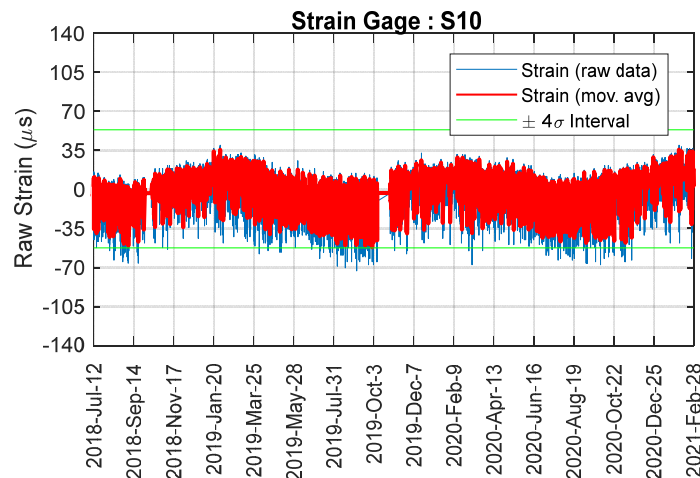
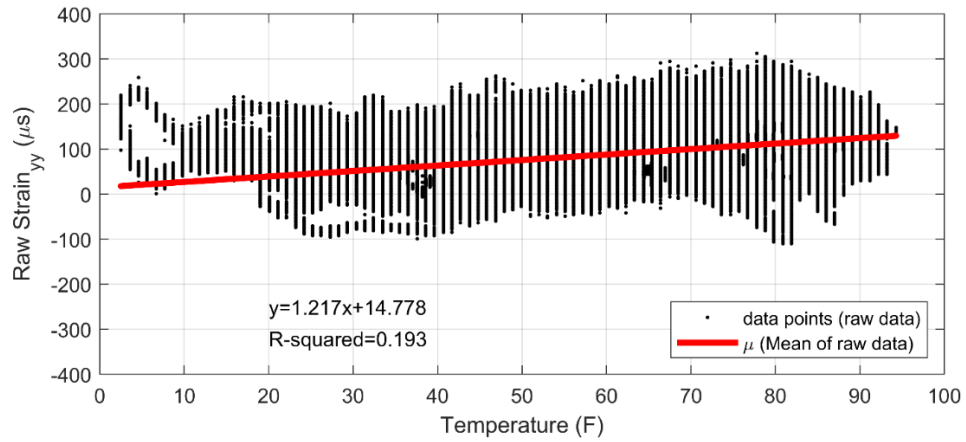
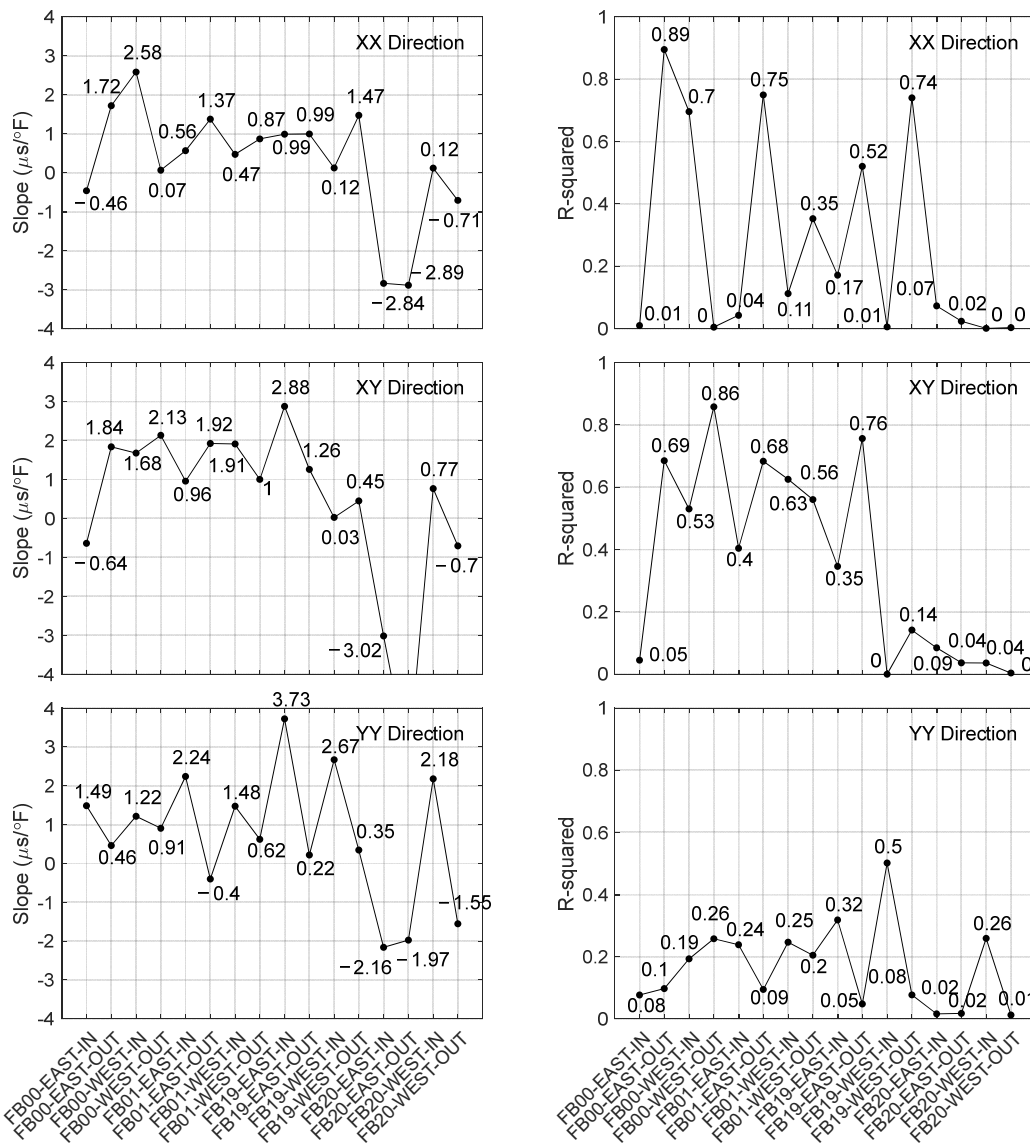


Fig. 7.16 – Raw and moving averaged strain recorded through February 28<sup>th</sup> 2021, Clairton Bridge.



**Fig. 7.17** – Birmingham Bridge. Raw strain vs raw temperature recorded by gage FB00-WEST-IN along the yy direction. The period observation lasted until January 31<sup>st</sup> 2021



**Figure 7.18.** Birmingham Bridge. Slope of linear regression of the strain vs temperature graphs (the values are expressed in  $\mu\epsilon/^\circ\text{F}$ ) and residual  $R^2$  of the linear interpolation strain vs temperature.

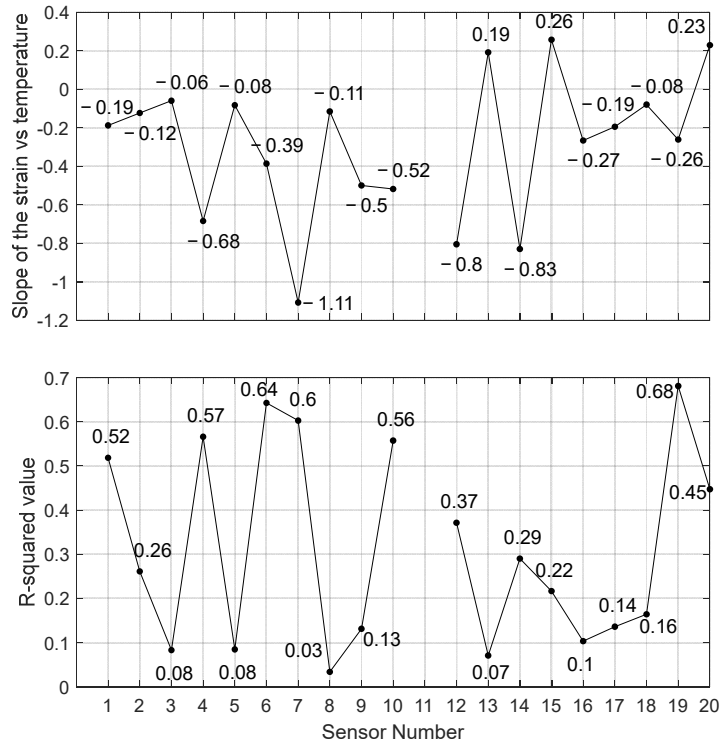


**Figure 7.19** – Clairton Bridge. Slope of linear regression of the strain vs temperature graphs (the values are expressed in  $\mu\epsilon/^\circ\text{F}$ ) and residual  $R^2$  of the linear strain vs temperature.

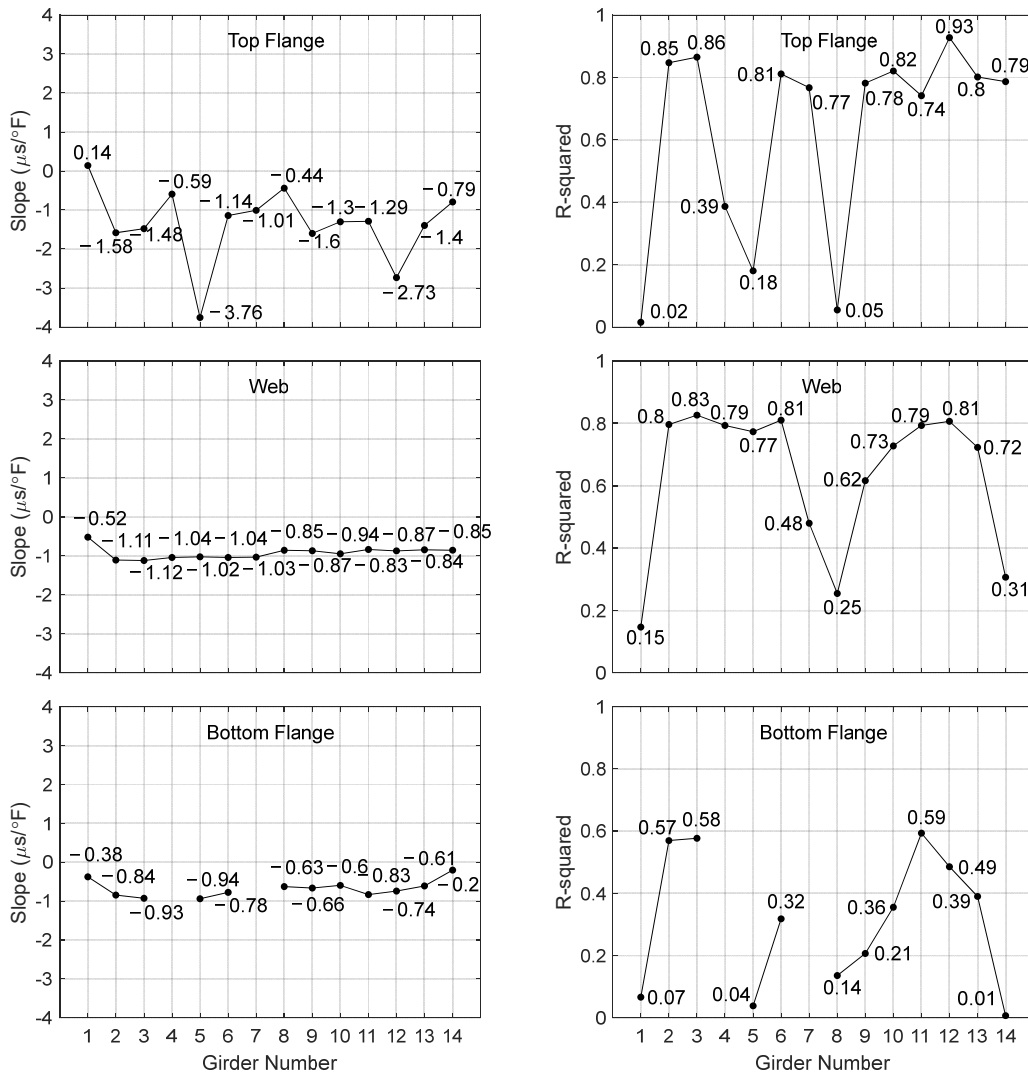


**Fig. 7.20** – (a) Slope of linear interpolation of the strain vs temperature graphs. The values are expressed in  $\mu\epsilon/^\circ\text{F}$ . (b) Residual  $R^2$  of the linear interpolation strain vs temperature.

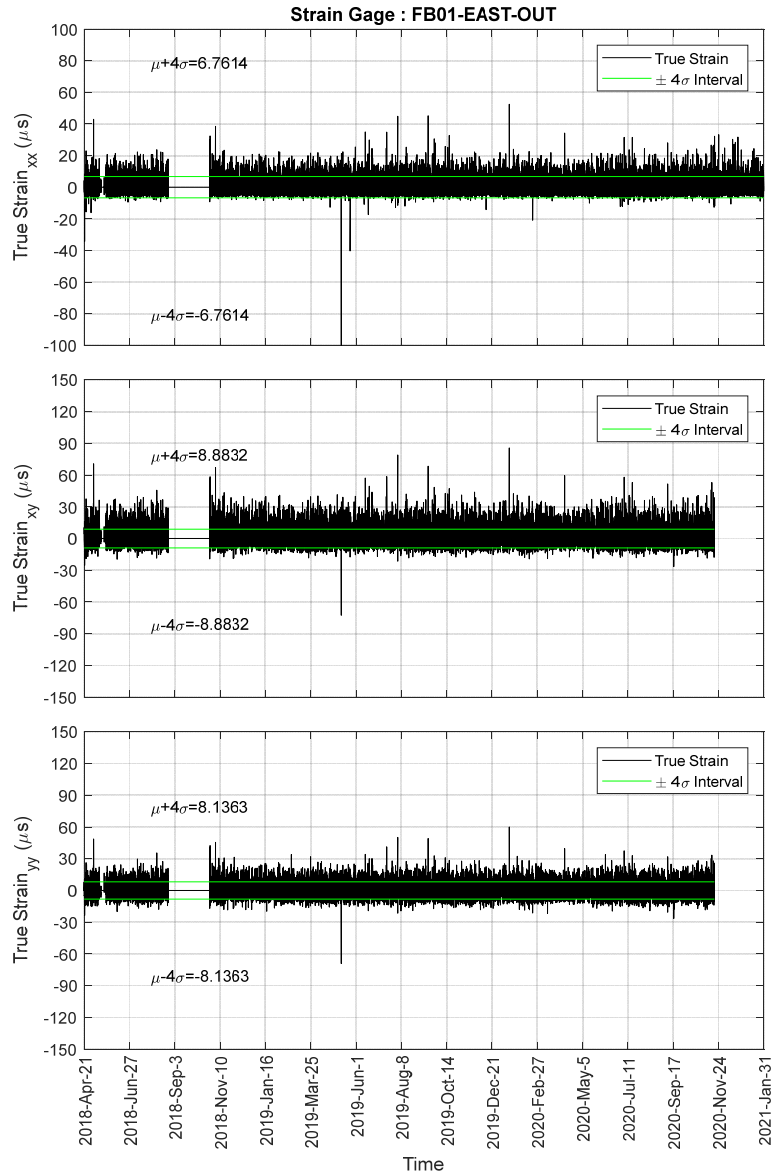


**Fig. 7.21** Brimingham Bridge. Time – histories of the calculated true strains from the rosette FB01-EAST-OUT.

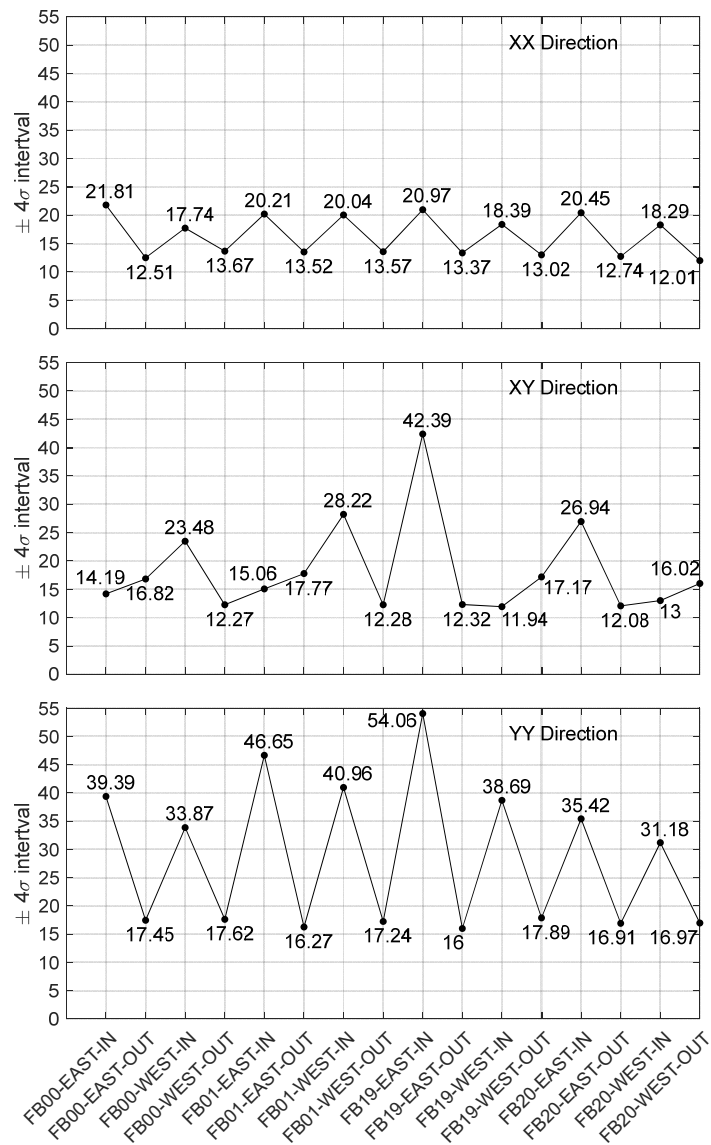
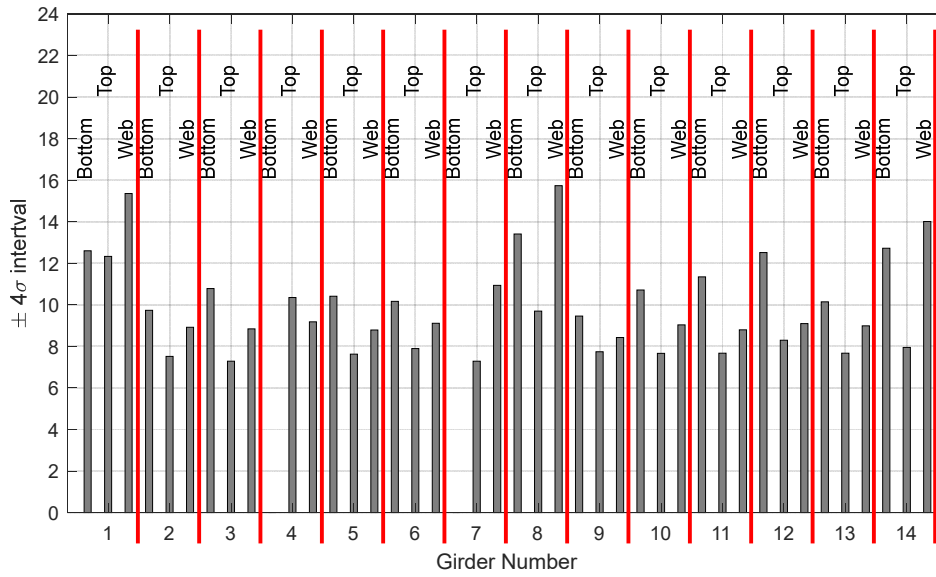
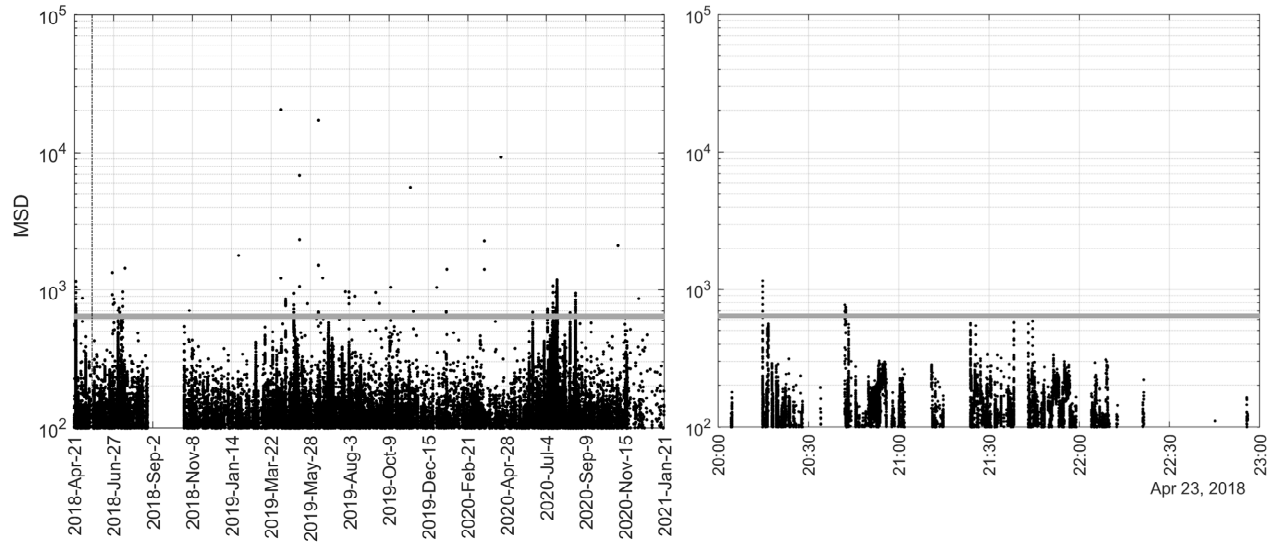


Fig. 7.22– Birmingham Bridge.  $4\pm\sigma$  interval associated with the cleansed true strains.



**Fig. 7.23** – Value of the  $\pm 4\sigma$  interval in  $\mu\epsilon$  calculated for each strain gages. Chester Bridge.



**Fig. 7.24** – Outlier Analysis: XX-direction strains. Mahalanobis Squared Distance calculated during the whole monitoring period and during the truck test.

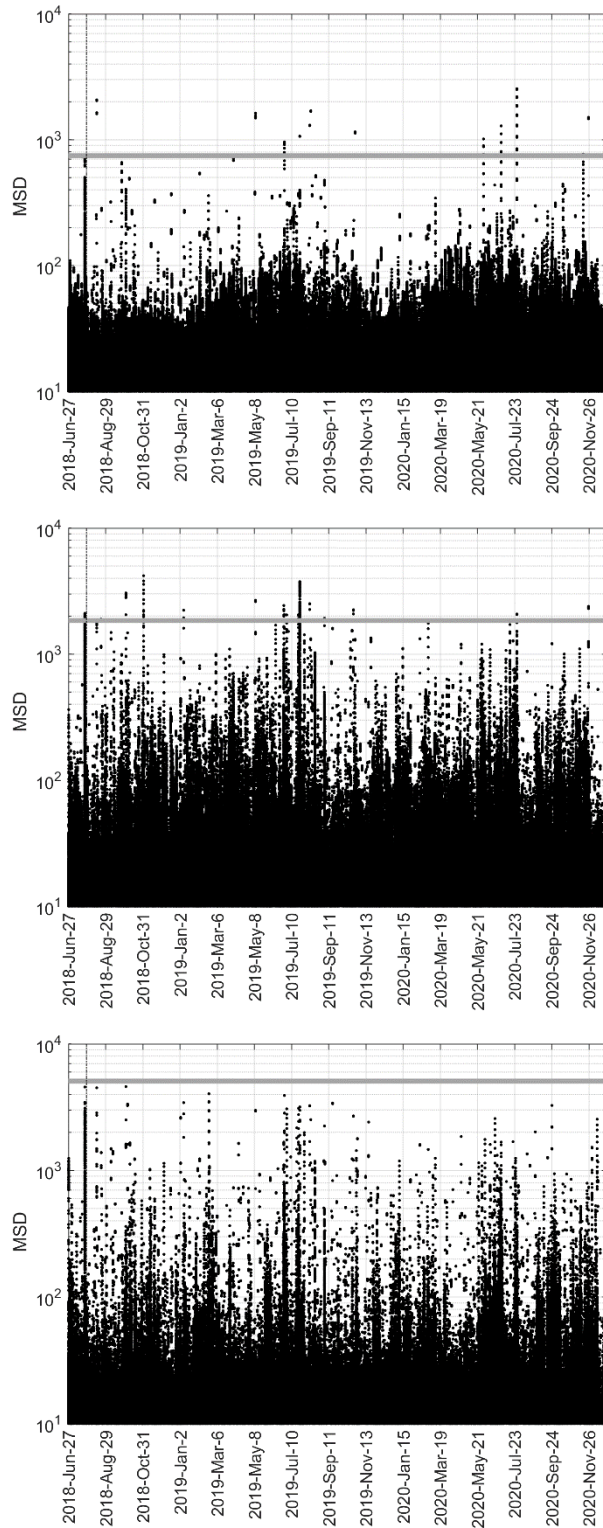


**Fig. 7.25** – Mahalanobis squared distance applied to the whole monitoring period. Top row: top flange. Middle row: web. Bottom row: Bottom flange. The threshold was computed by considering the data from the first month of operation without the truck test.

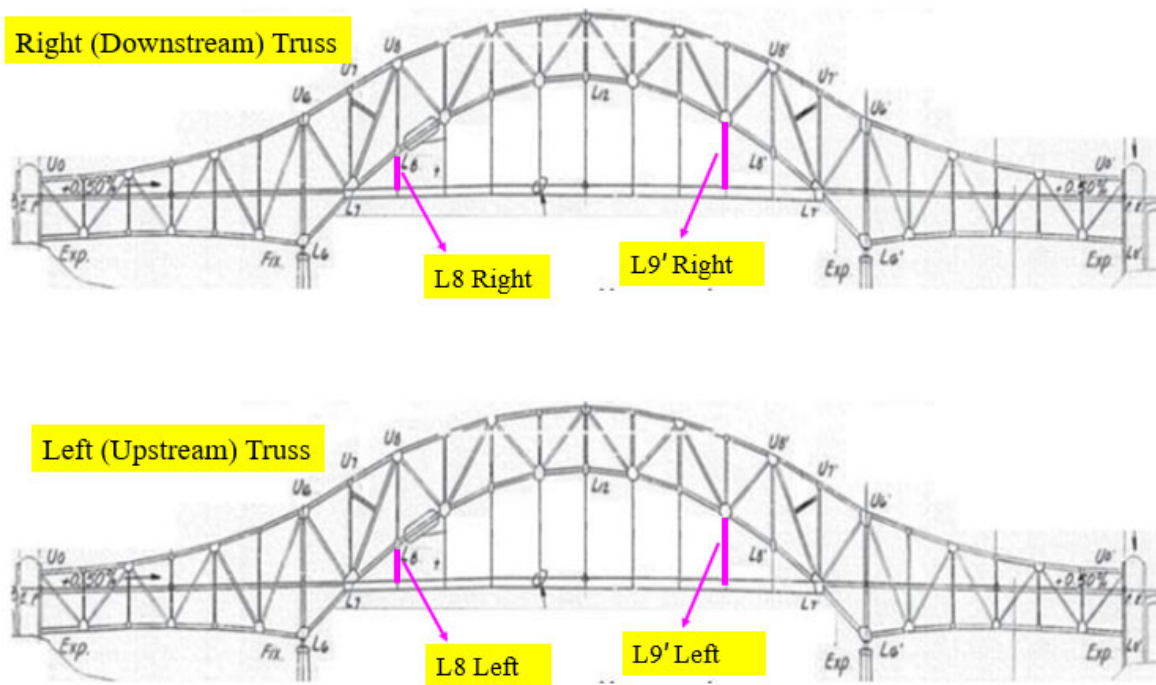


Fig. 8.1 – Cable gauges used for data comparison.

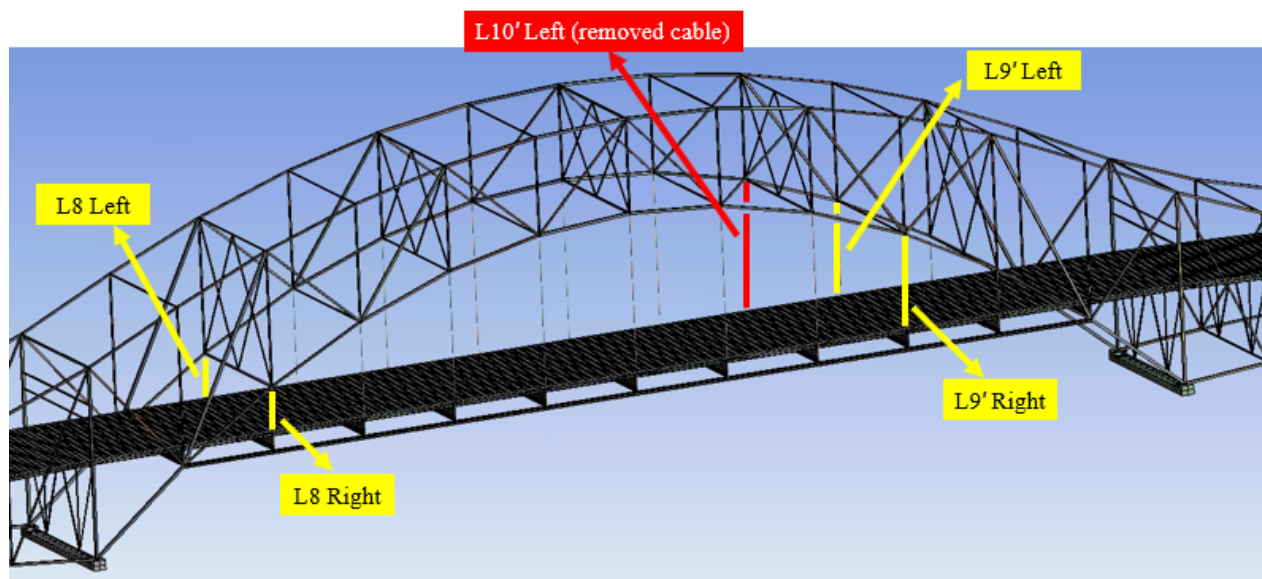


Fig. 8.2 – The location of the removed cable for damage scenario 3.

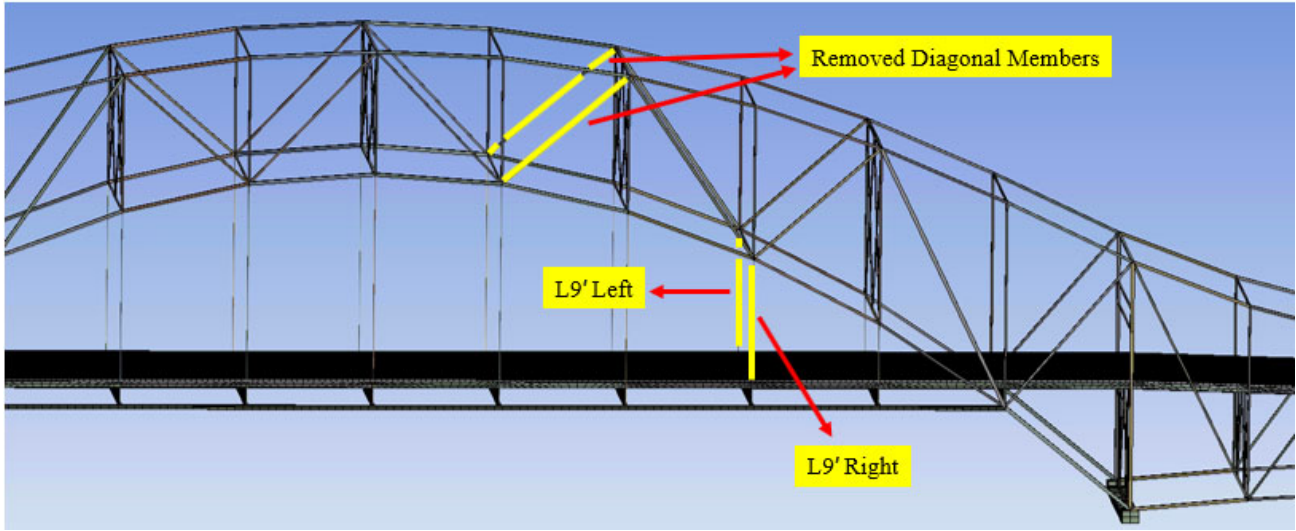


Fig. 8.3 – The location of the removed diagonal members for damage scenario 4.

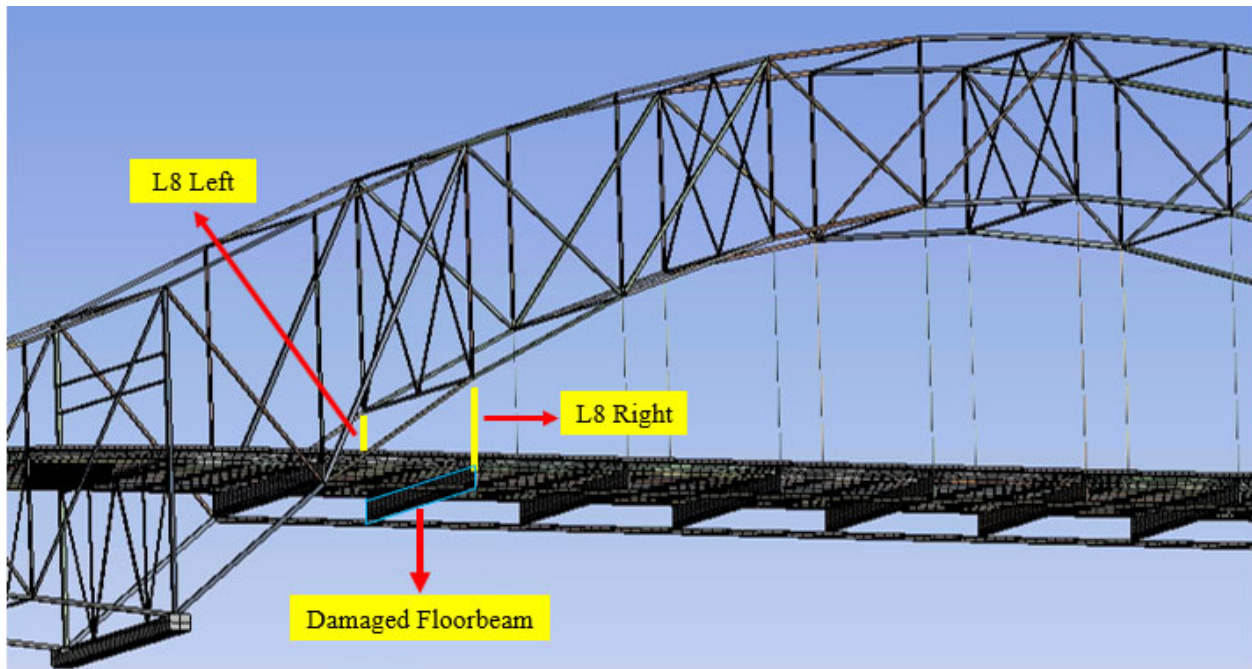


Fig. 8.4 – The location of the damaged floorbeam in damage scenario 5.

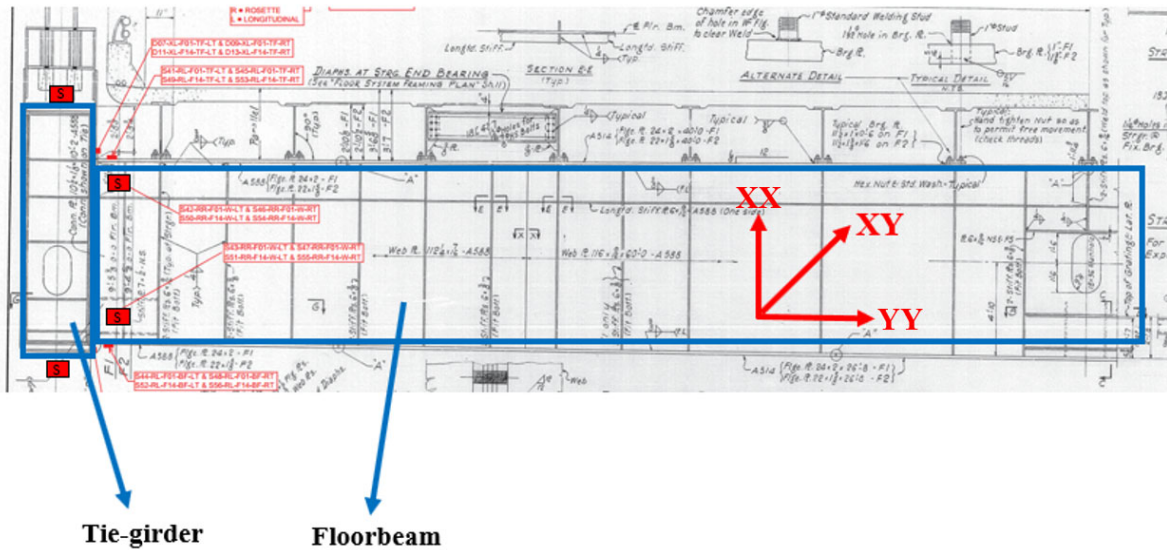
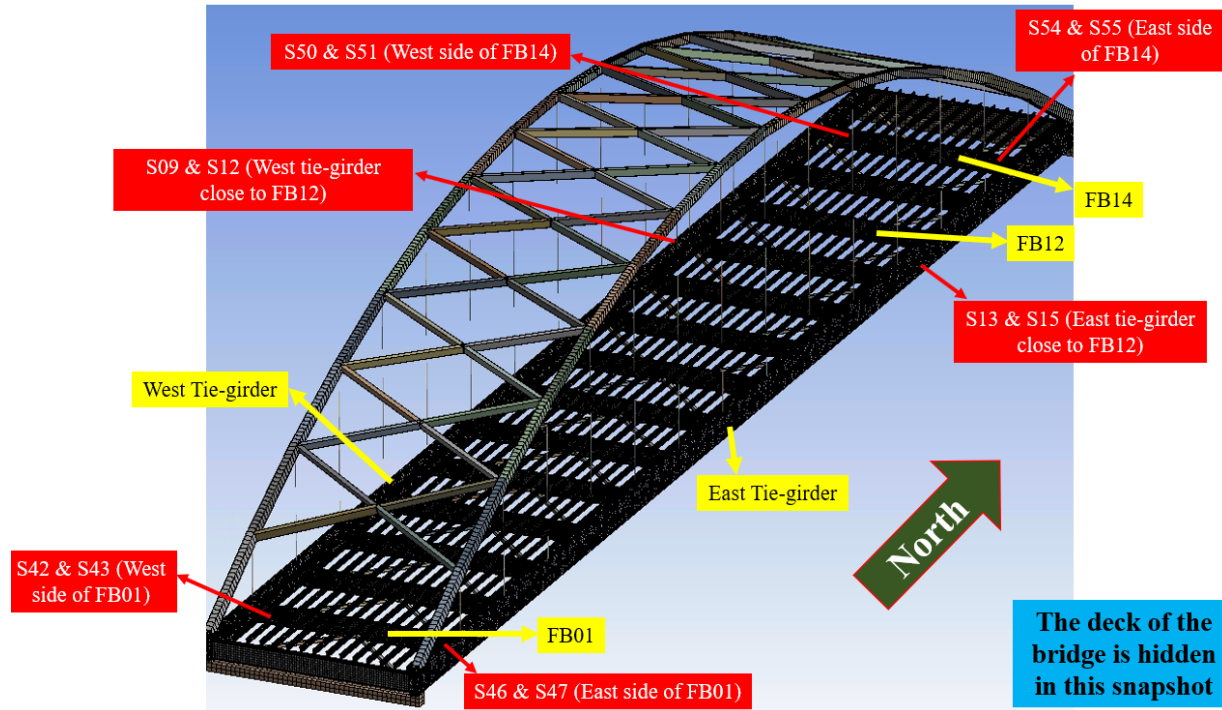


Fig. 9.1 – Location of the structural members and some of the installed sensors on the bridge The letter S means strain gage, the letters RR indicates resistance strain gage, FB means floorbeam, W indicates web, LT stands for left truss, and TP for top.

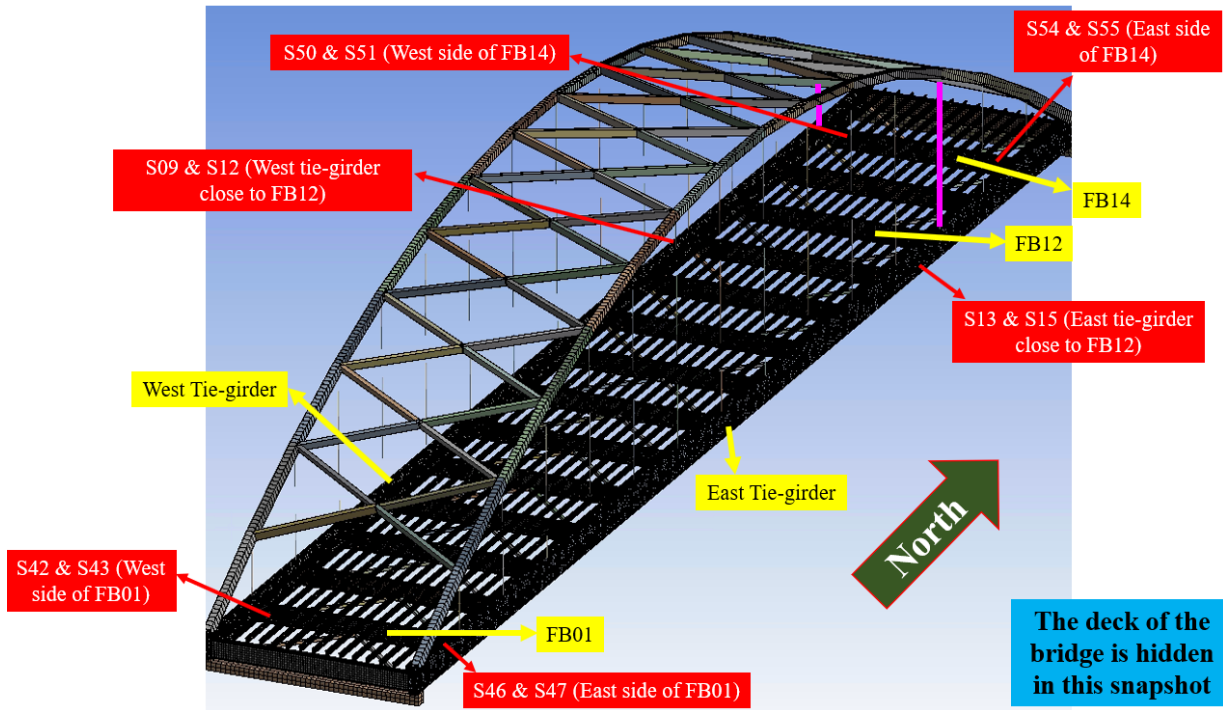


Fig. 9.2 – Removed cables from the East and West arches of the bridge (highlighted in pink).

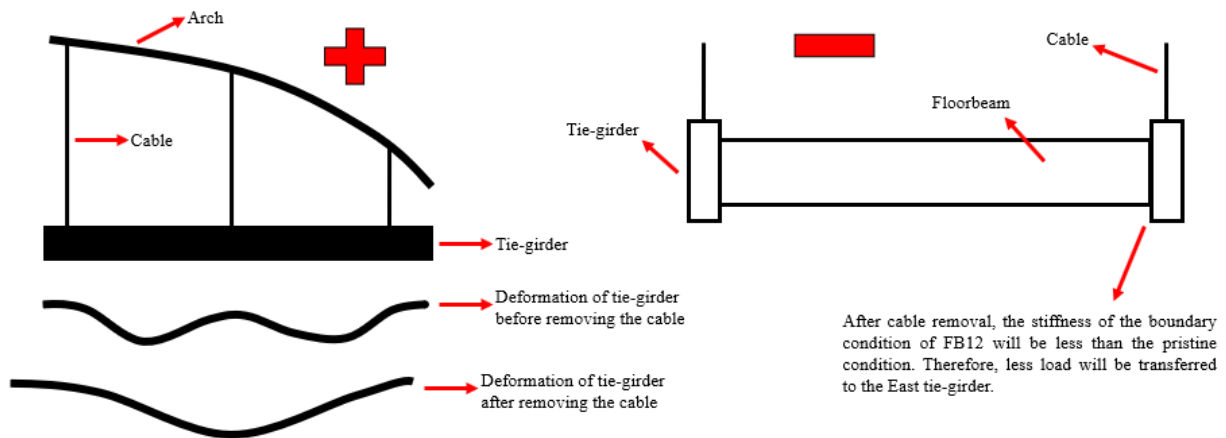


Fig. 9.3 – The factors affecting the predicted strain values under damage scenario 3 condition.

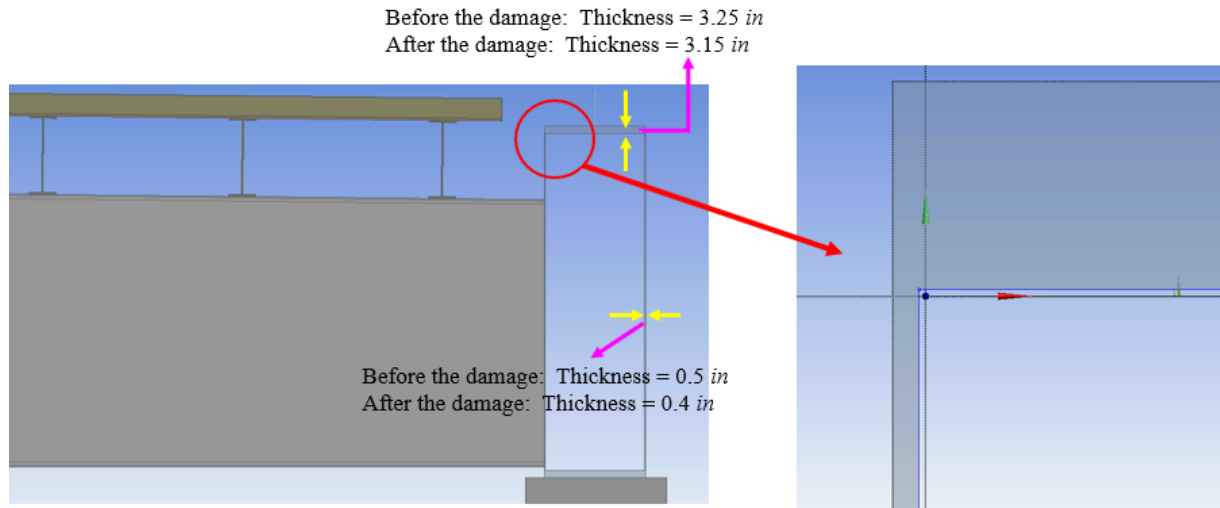
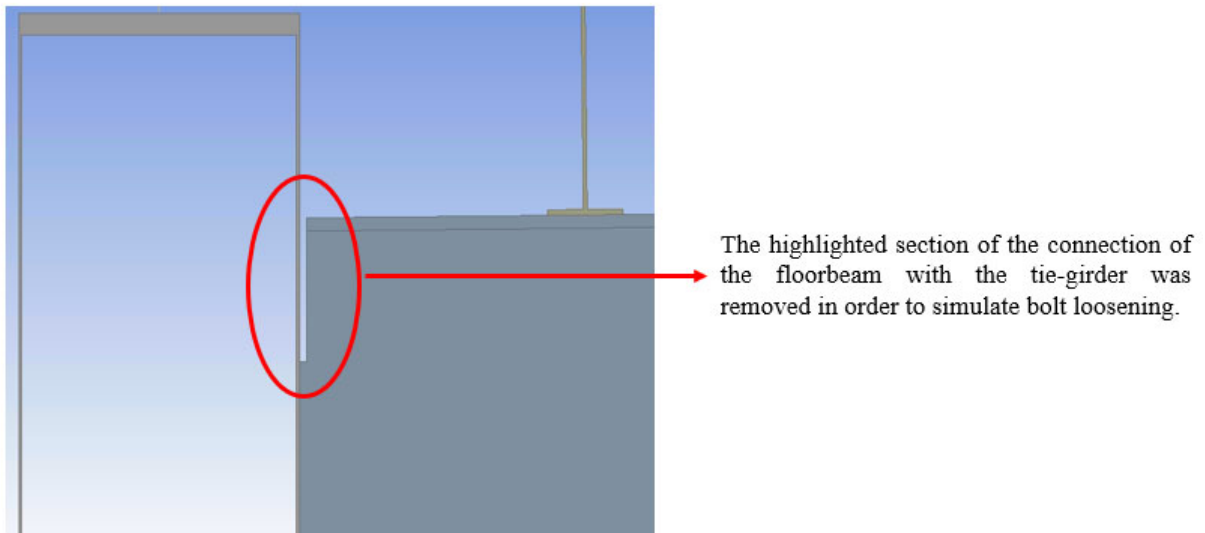


Fig. 9.4 – Simulation of the 0.1 in corrosion in the East tie-girder



After simulating the corrosion, the stiffness of the boundary condition of floorbeams will be less than the pristine condition. Therefore, less load will be transferred to the East tie-girder.

Fig. 9.5 – The justification of the predicted strains under damage scenario 4 condition.



**Fig. 9.6** – Scheme of the damage scenario 5.

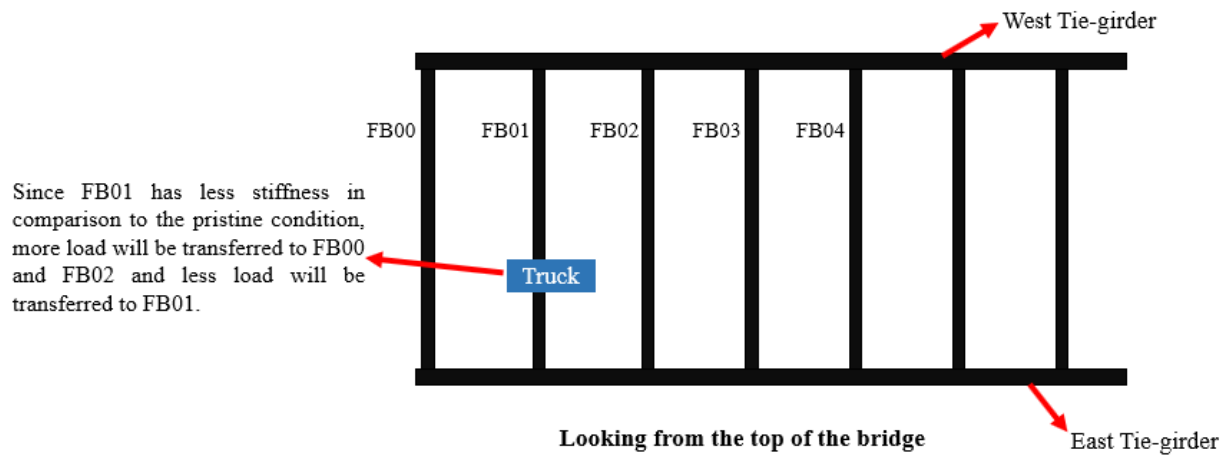


**Fig. 9.7** – The justification of the predicted strains under damage scenario 6.

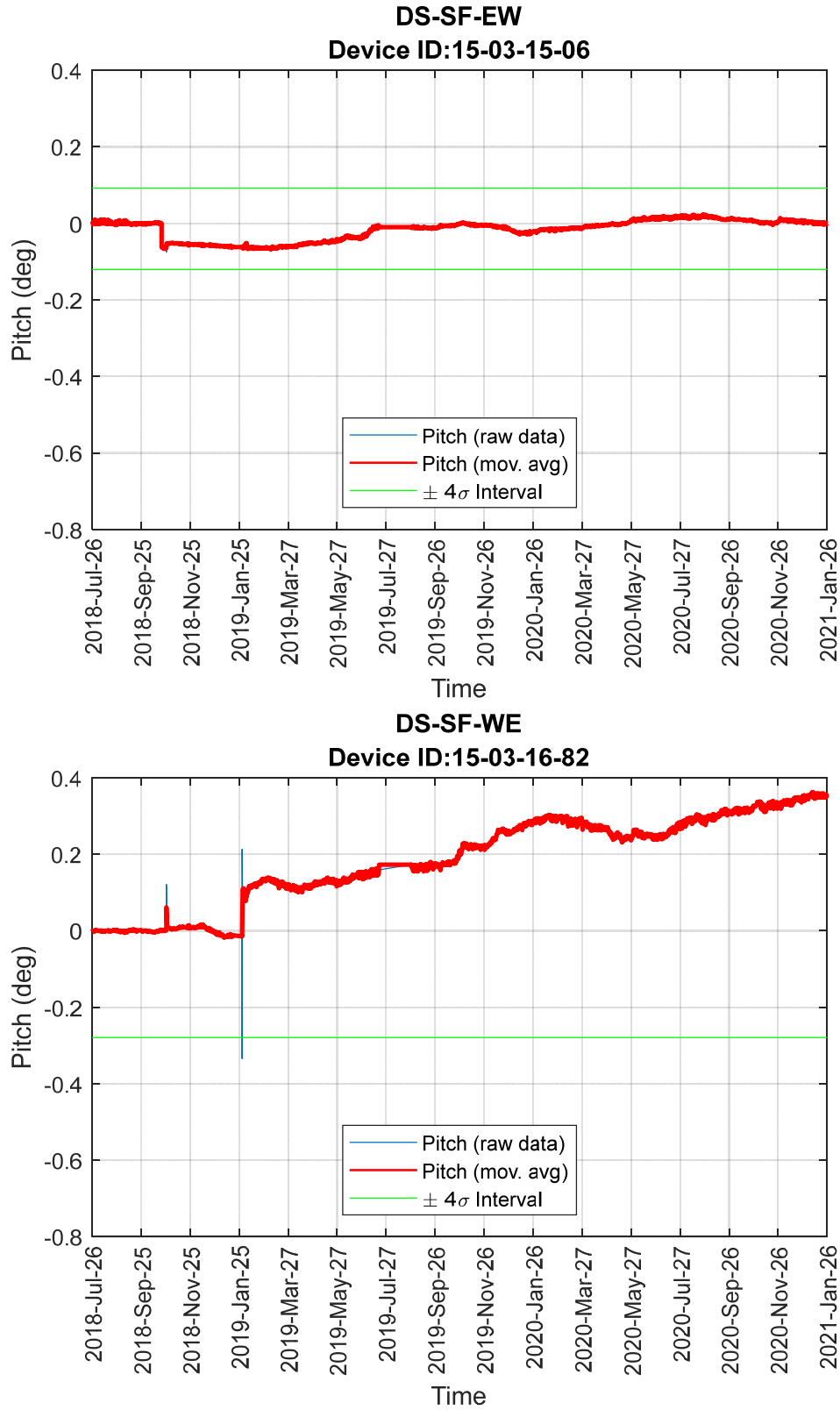


Fig. 10.1 – PITCH. Raw values and corresponding moving average associated with all 8 inclinometers.

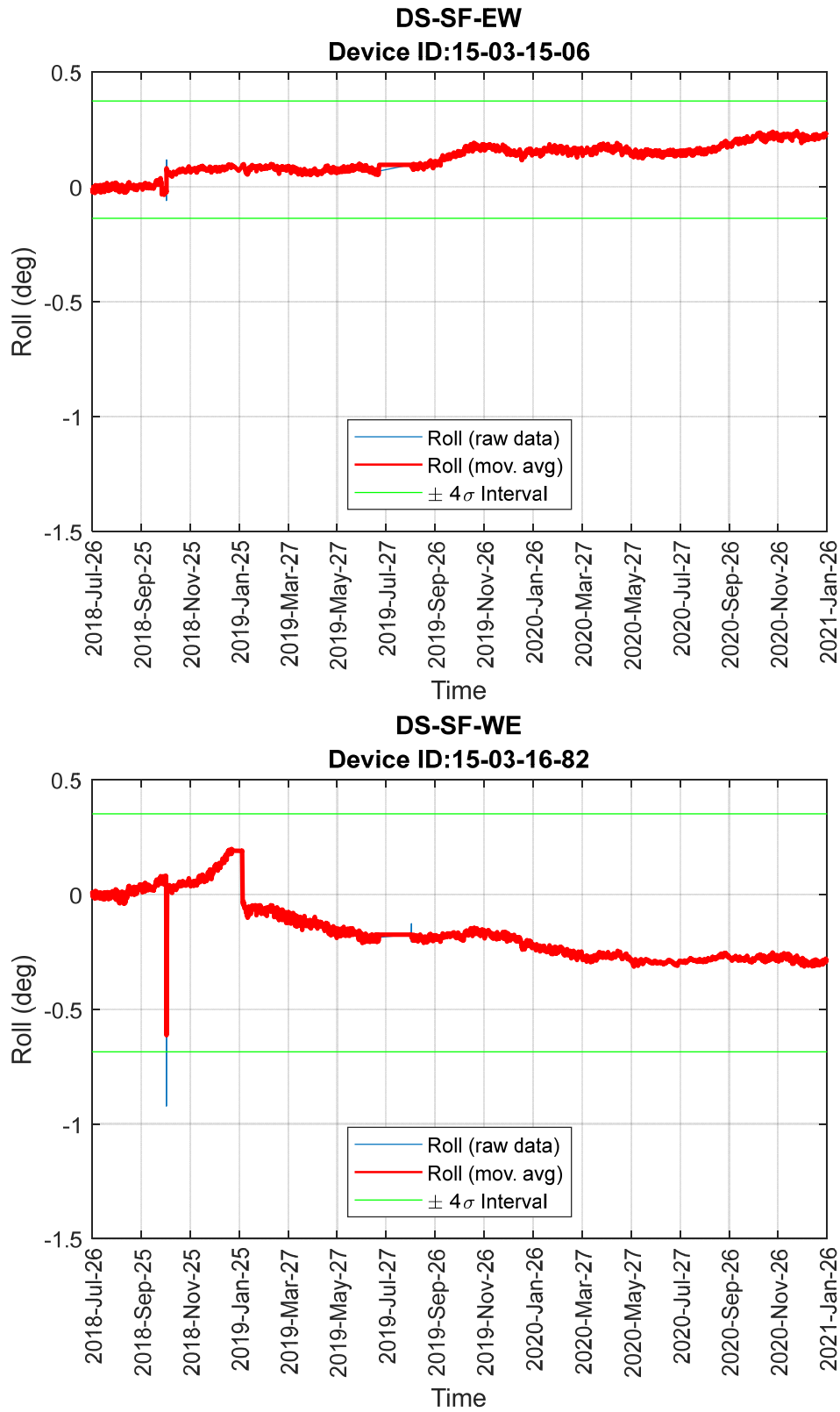


Fig. 10.2 – ROLL. Raw values and corresponding moving average associated with all 8 inclinometers.

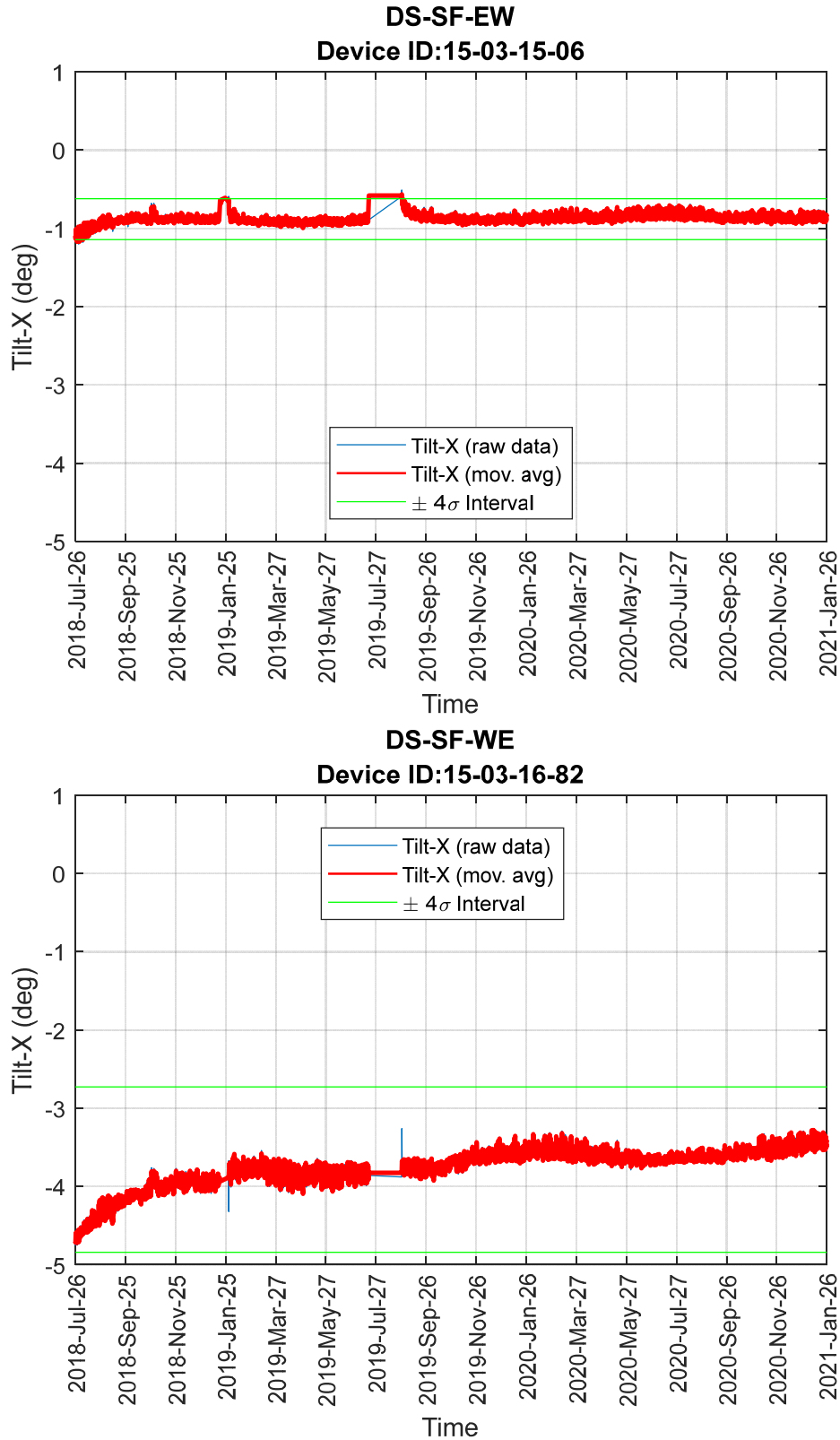


Fig. 10.3 – TILT X. Raw values and corresponding moving average associated with all 8 inclinometers.

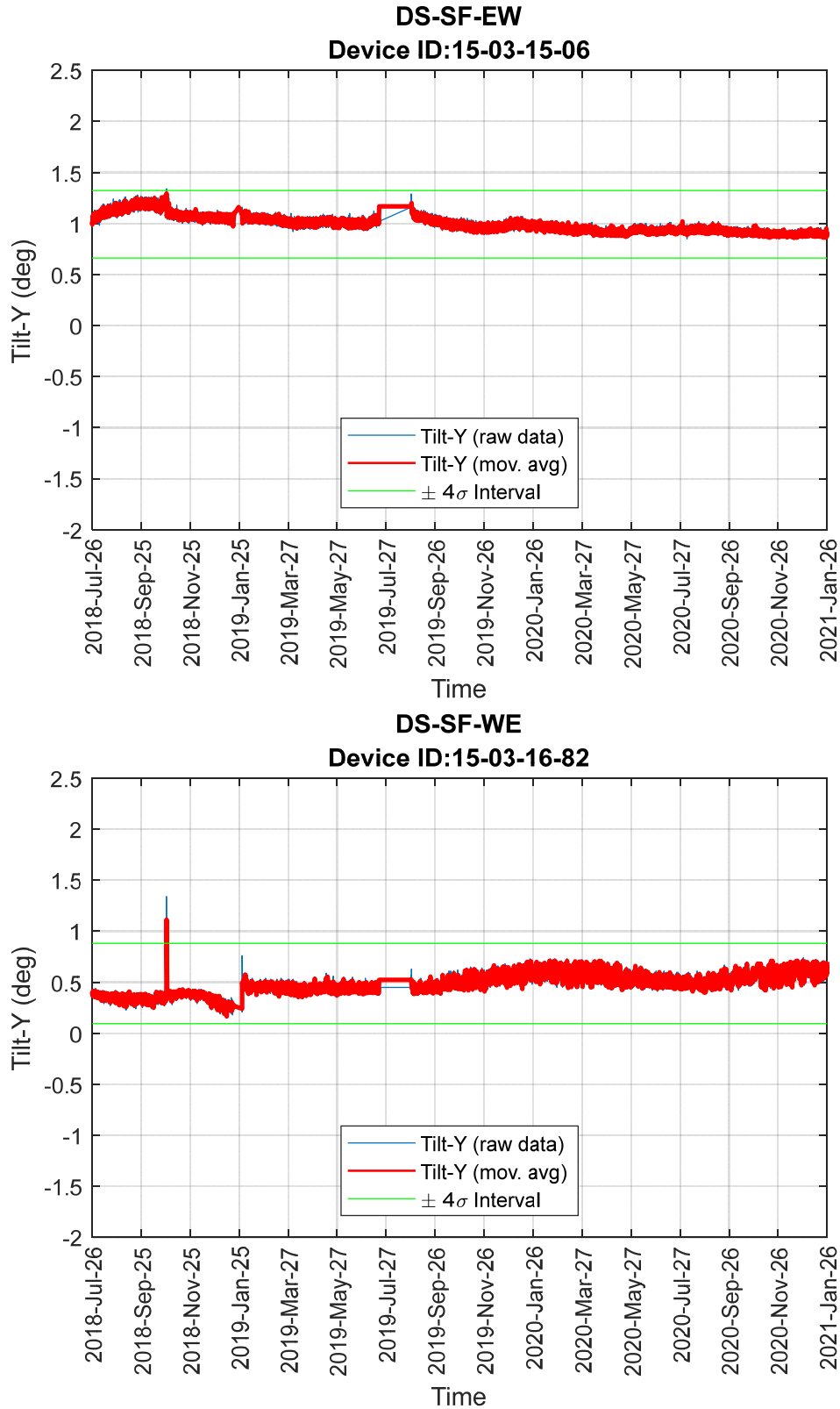


Fig. 10.4 – TILT Y. Raw values and corresponding moving average associated with all 8 inclinometers.

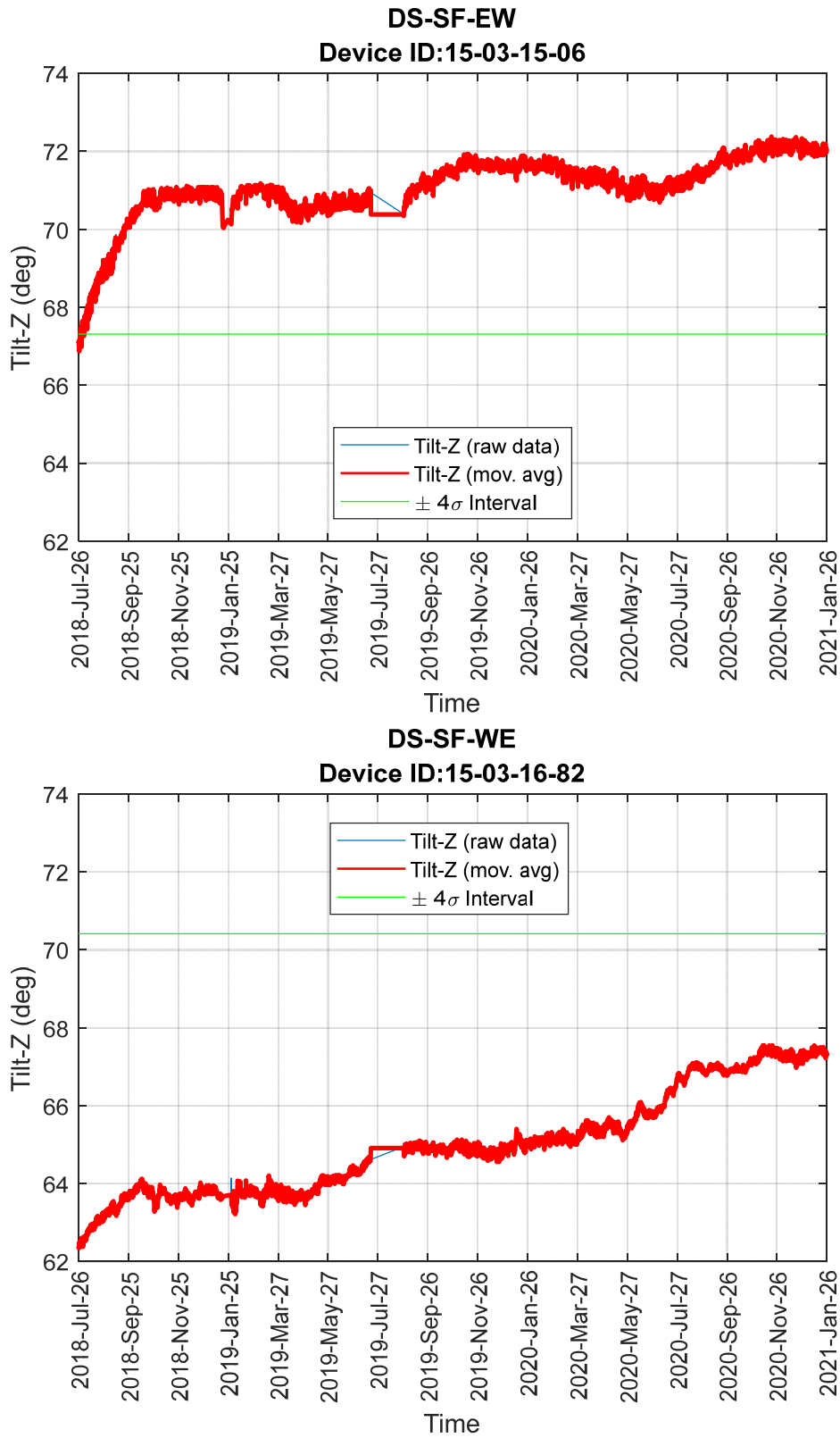
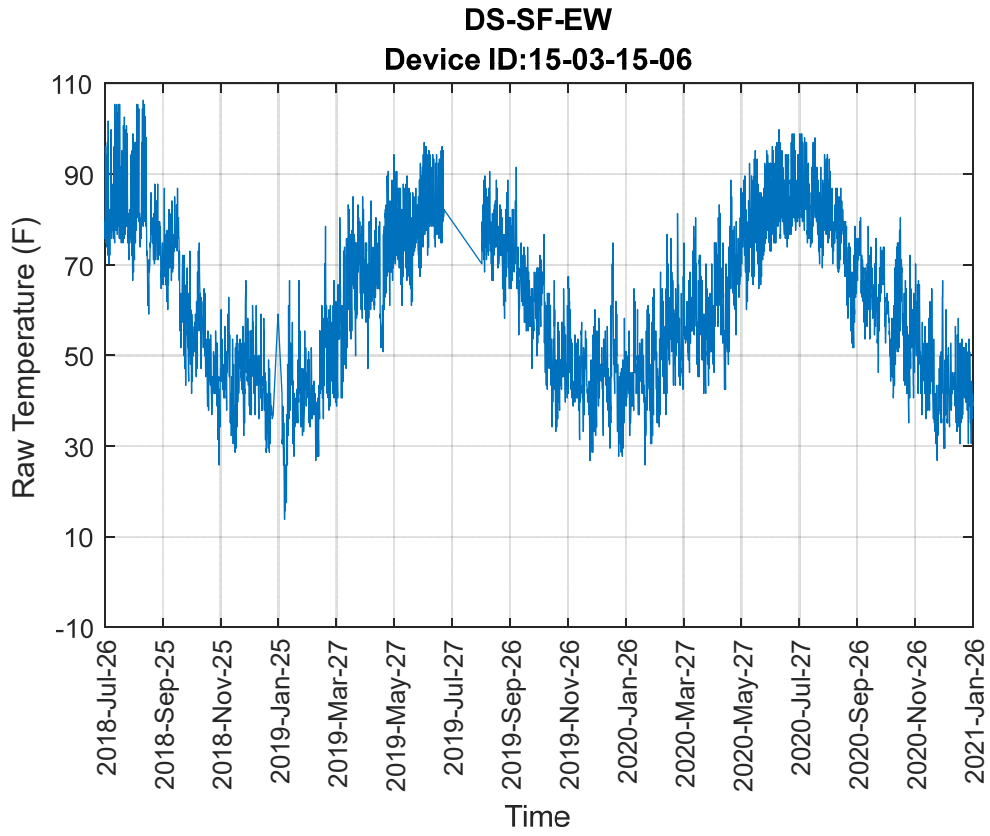
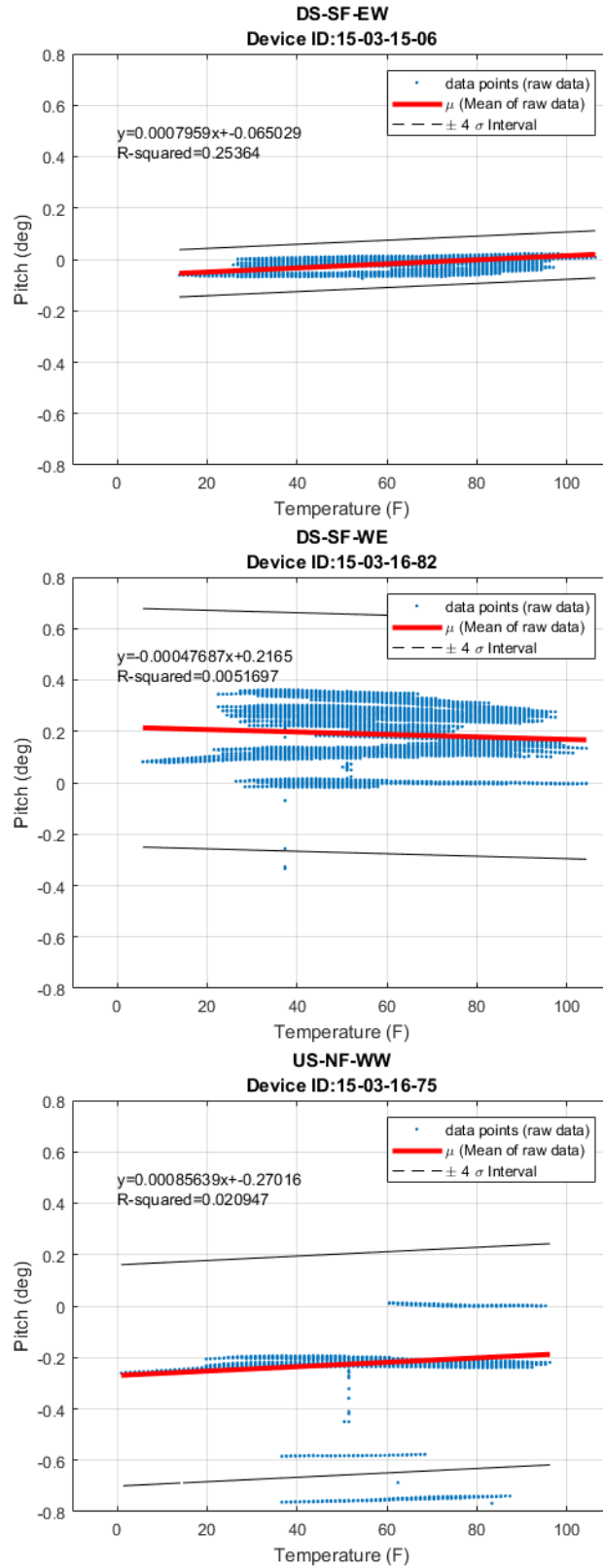


Fig. 10.5 – TILT Z. Raw values and corresponding moving average associated with all 8 inclinometers.



**Fig. 10.6** – Raw temperature from the 42 strain gages.



**Fig. 10.7** – PITCH. Raw pitch vs temperature.

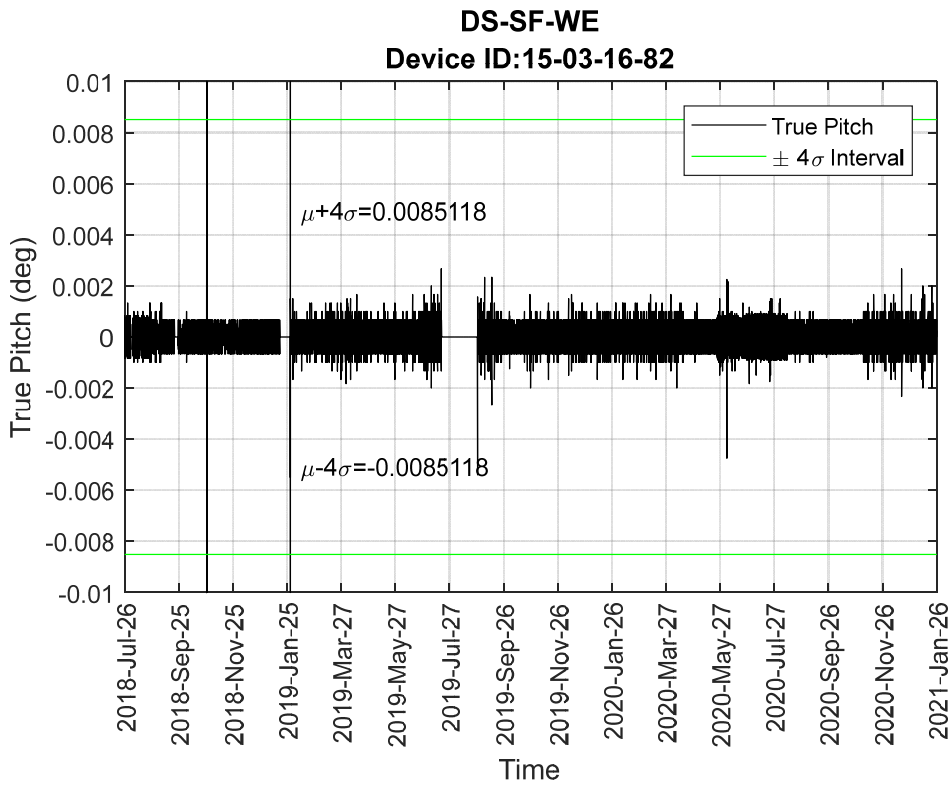
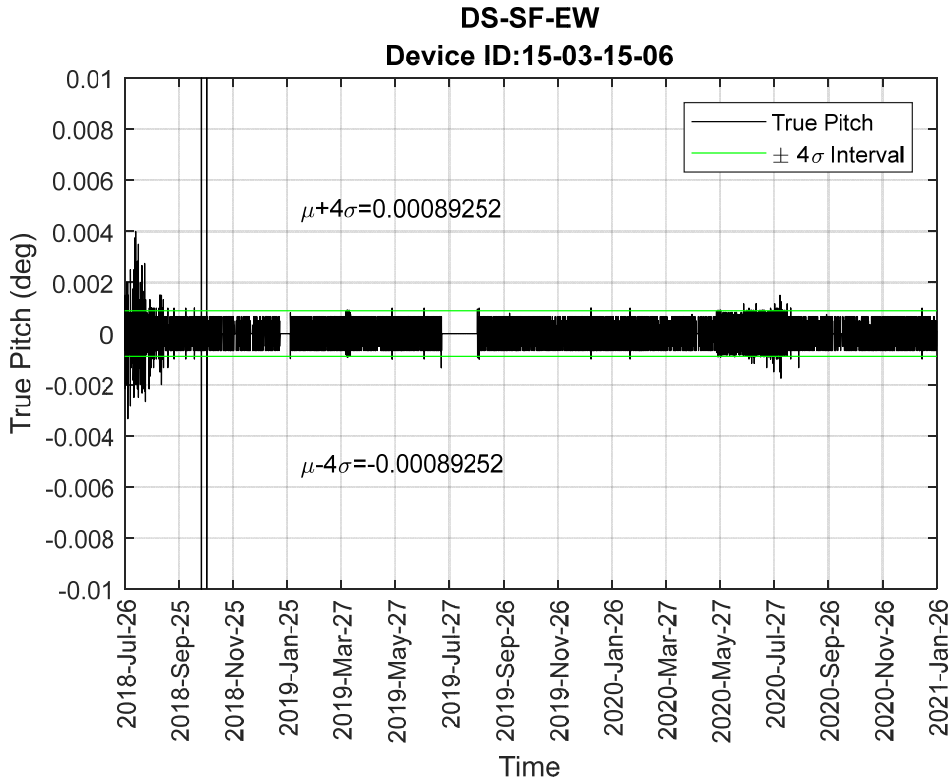


**Fig. 10.8** – PITCH. True pitch during the monitoring period.

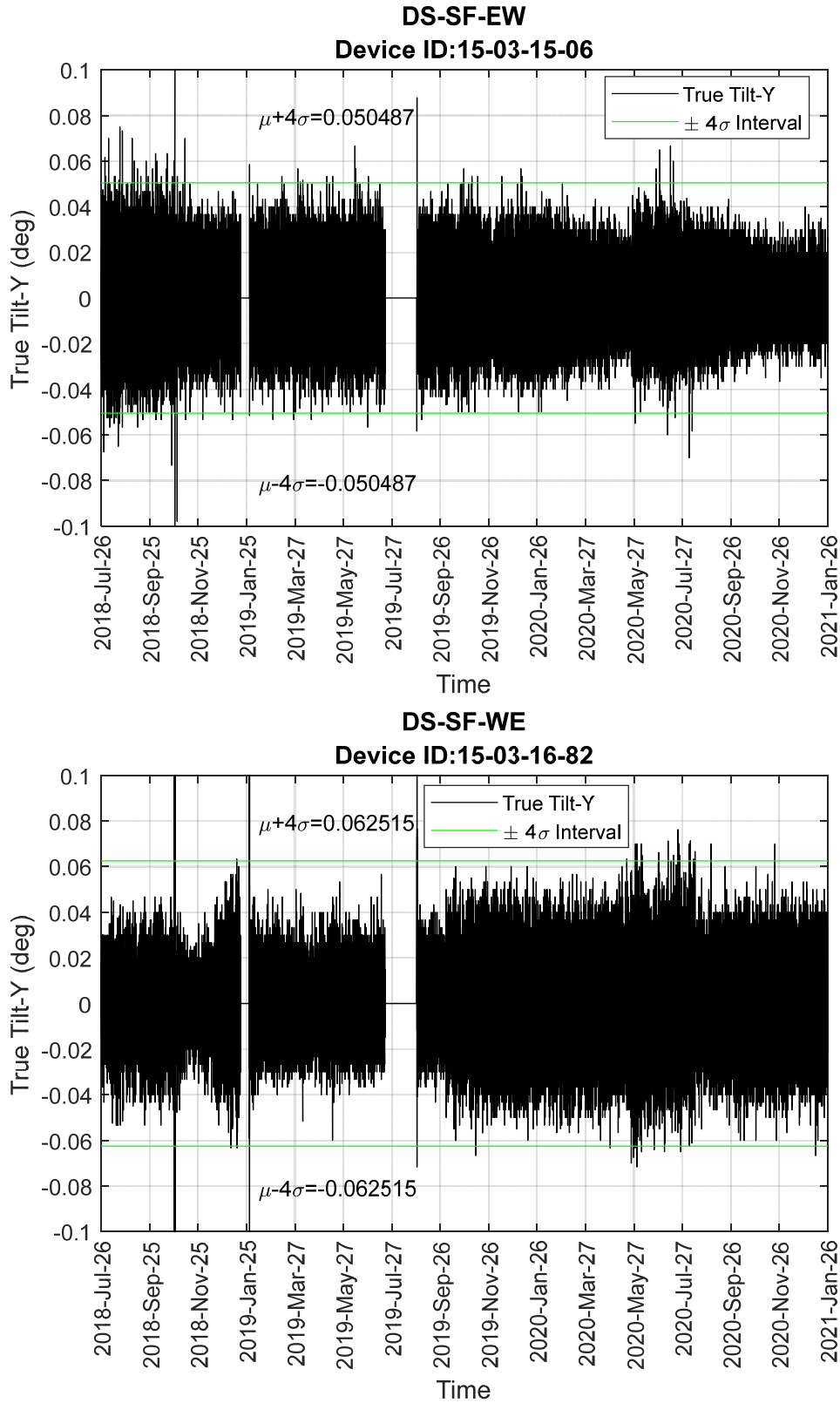


Fig. 10.9 – TILT-Y. True tilt-Y during the monitoring period.

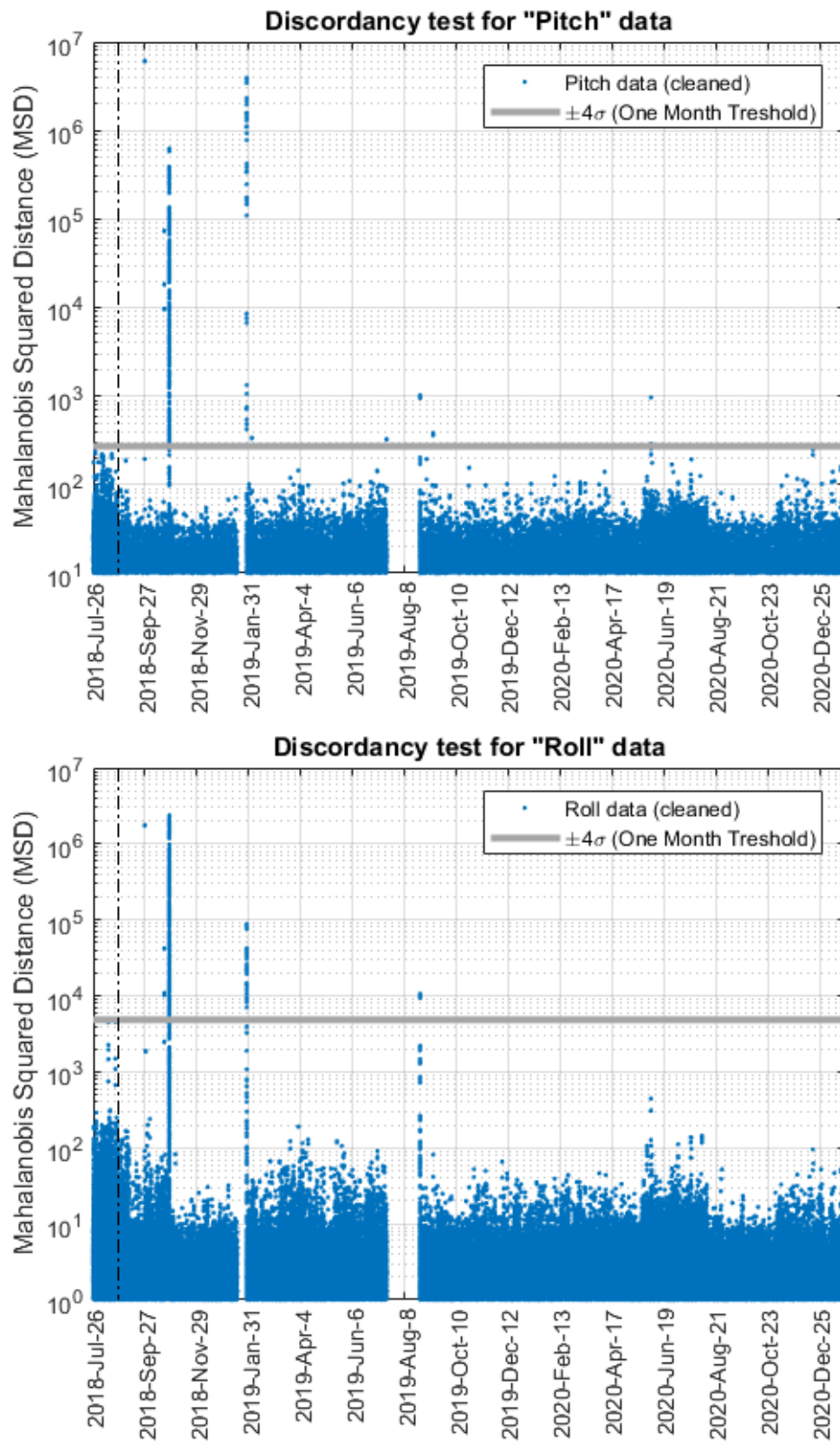


Fig. 10.10 – Mahalanobis squared distance applied to the pitch and the roll data.

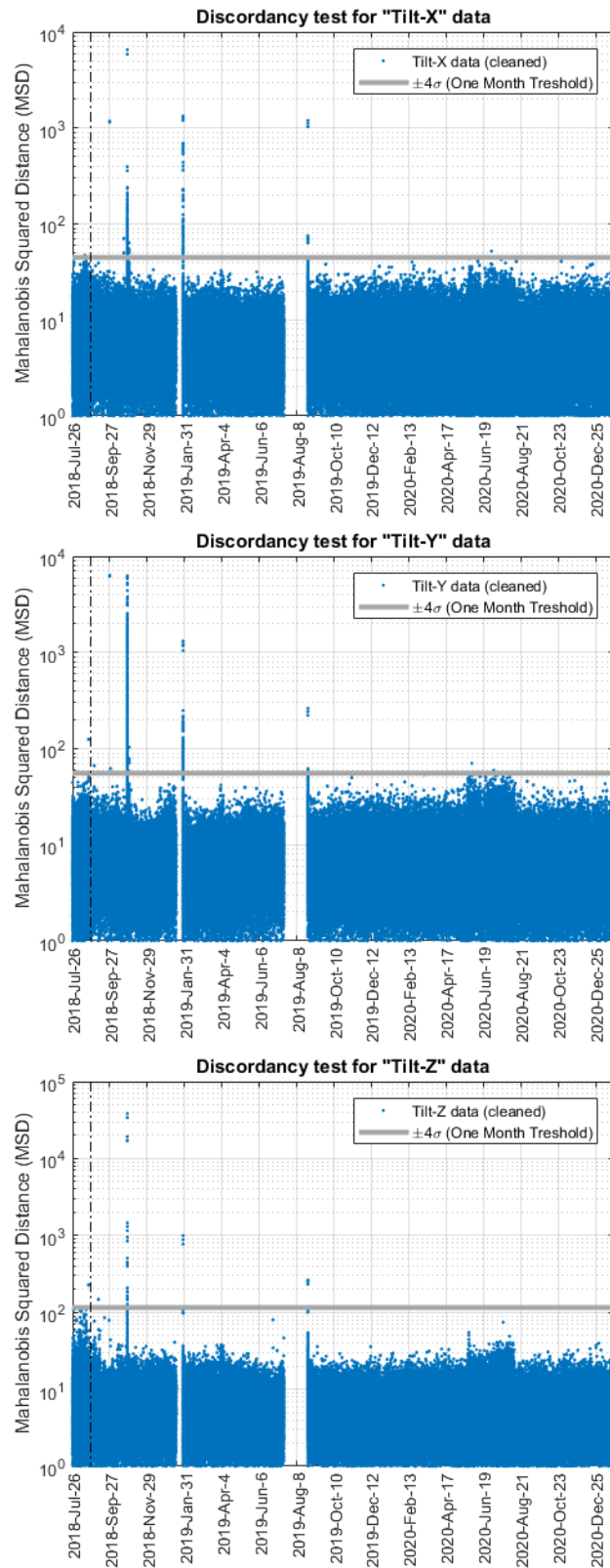
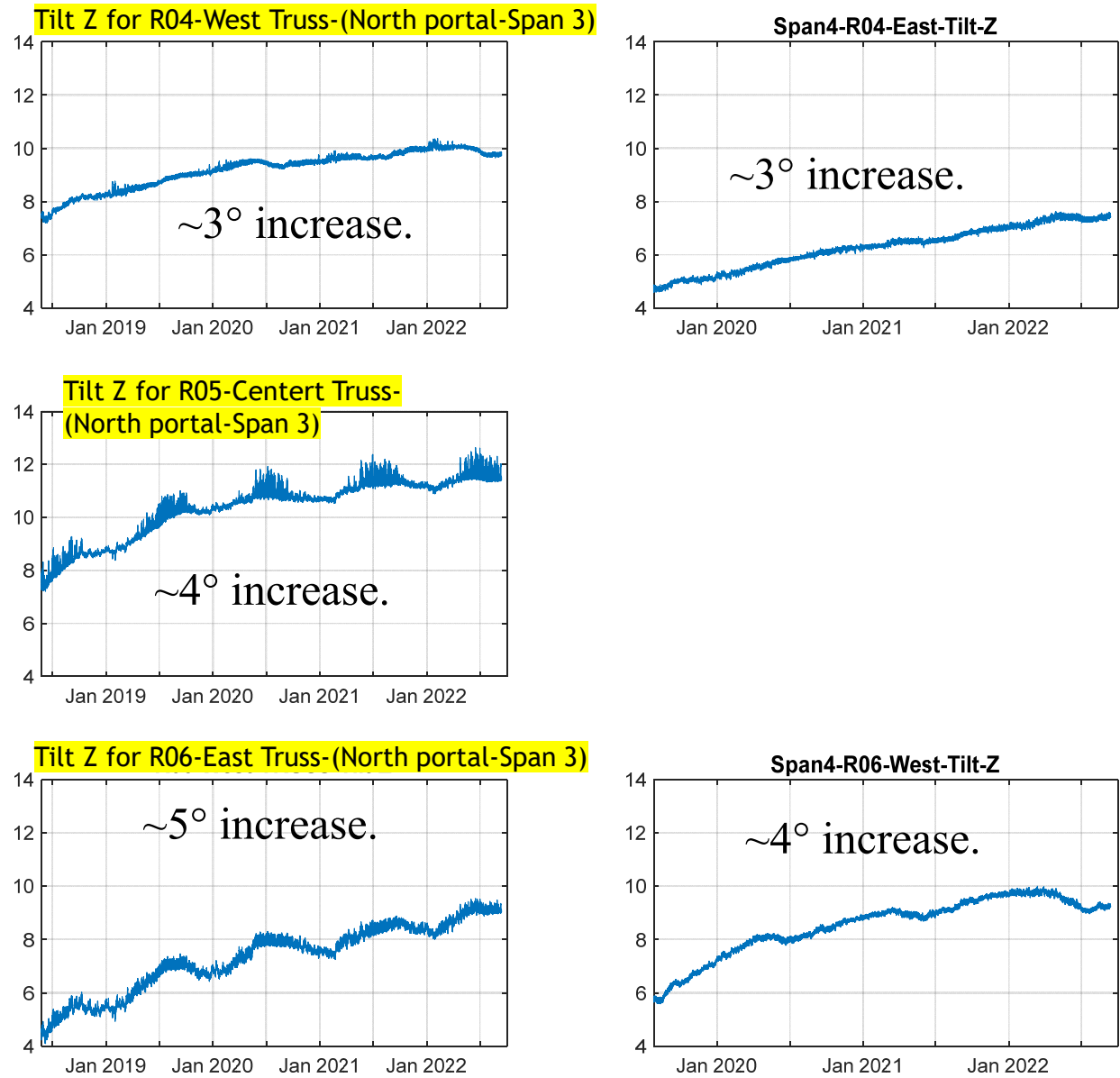
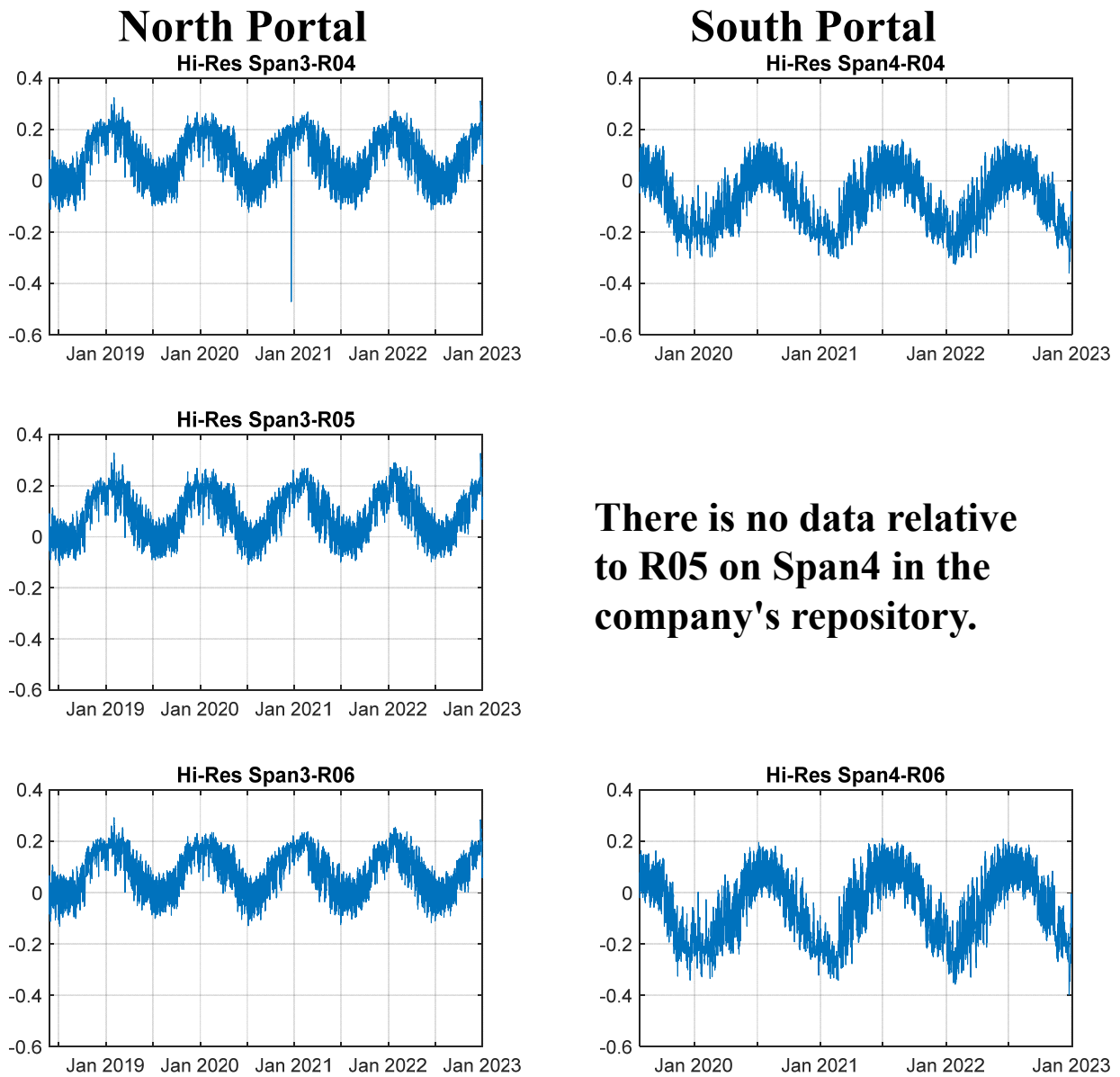


Fig. 10.11 – Mahalanobis squared distance applied to the Tilt data.



**Fig. 11.1** – Readings from the low-resolution tiltmeters installed on the Smithfield Street Bridge. The plots on the left column refer to the gages installed on the north portal of Span 3 (closer to downtown). The plots on the right column refer to the gages installed on the south portal of Span 4 (closer to Southside / Station square).



**Fig. 11.2** – Readings from the hi-res tiltmeters installed on the Smithfield Street Bridge. The plots on the left column refer to the gages installed on the north portal of Span 3 (closer to downtown). The plots on the right column refer to the gages installed on the south portal of Span 4 (closer to Southside / Station square).

## TABLES

<b>Table 1.1 - Bridges under the PennDOT pilot bridge instrumentation program (P2BIP) and typology.</b>			
<b>No.</b>	<b>BMS ID</b>	<b>Name or Location</b>	<b>Bridge Type</b>
1	02-0051-0110-0000	<b>Elizabeth Bridge,</b> Allegheny Co.	Steel Thru-Truss (Deck supported by wire rope hangers)
2	02-0079-0650-0000	<b>Neville Island Bridge,</b> Allegheny Co.	Steel Plate Girders + Steel Arch Truss (751 ft, 229 m) (Deck supported by suspender cables)
3	02-2085-0010-0586	<b>Birmingham Bridge,</b> Allegheny Co.	Steel Plate Girders + Steel Tied-Arch (620 ft, 189 m) (Deck supported by suspender cables)
4	02-3027-0020-0000	<b>Smithfield Bridge,</b> Allegheny Co.	Steel Built-up Girder + Steel Lenticular Through Truss
5	02-2038-0010-0140	<b>Clairton-Glassport Bridge,</b> Allegheny Co.	Steel Girder + Prestressed Concrete I Beams
6	05-3001-0080-0000	<b>Cooks Mill Bridge,</b> Bedford Co. – Londonderry Twsh	Pretensioned Adjacent Concrete Box Beams (194 ft, 59 m)
7	55-3014-0050-0509	Somerset Co.	Pretensioned Adjacent Concrete Box Beams (167 ft, 51 m)
8	29-2004-0040-0000	Fulton Co.	Pretensioned Adjacent Concrete Box Beams (88.6 ft, 27 m)
9	15-0082-0592-0385	<b>Wyebrooke Bridge,</b> Chester Co.	Rolled Steel I-Beams
10	46-4031-0314-1676	<b>Sanatoga Bridge,</b> Montgomery Co.	Closed Spandrel Stone Masonry Arch

**Table 2.1** – Bridges in the United States instrumented with sensing systems prior to 2011 according to Table 1.1 of Xu and Xia (2011).

#	Name	Location	Type	Reference	Sensor Type	Sensors details (whenever available)
1	<b>Golden Gate</b>	San Francisco, CA	Suspension	Pakzad et al. (2008, 2009, 2010); Chang and Pakzad 2013	1, 4, 16	64 wireless nodes: each node consisted of four channel accelerometers.
2	<b>Fred Hartman</b>	Houston Ship Channel, TX	Cable-stayed	Zhu and Jones (2005, 2010); Pure Technologies (2020); Texas Department of Transportation (2020)	1,2,3,4,5	576 acoustic sensors (SoundPrint® system)
3	<b>Sunshine Skyway</b>	Tampa Bay, FL	Cable-stayed	Agdas et al. (2015); Schenewerk et al. (2006); Mehrabi and Farhangdoust (2018).	2,3,5,7,9	Five GPS
4	<b>Quincy Bayview</b>	West Quincy (MO) – Quincy (IL)	Cable-stayed	Dong et al. (2010); Talebinejad et al. (2011);	9, 18	
5	<b>Commodore Barry</b>	Chester (PA) – Logan Twn (NJ)	Truss	Kulcu et al. (2000); Pines and Atkan (2002); Catbas et al. (2008).	1,2,3,4,5,8,12,19,21,22	
6	<b>Ironton-Russell<sup>1</sup></b>	Ironton (OH) – Russell (KY)	Truss		2,3	
7	<b>New Benicia Martinez</b>	San Francisco, CA	Box	Land et al. (2003)	2,3,4,9,12,14	16- gauge stainless steel piano-wire
8	<b>Saint Anthony Falls I-35W</b>	Minnesota, MN	Box	French et al. (2012, 2014); Hedeegard et al. (2013, 2017a, 2017b); Dalia et al. (2018); Gaebler et al. (2018); Inaudi et al. (2009).	2,3,4,9,11,24	500 sensors: 198 vibrating-wire strain gauges, 24 resistive strain gauges, and 12 fiber-optic strain gauges; 246 thermistors; 26 accelerometers; 12 linear potentiometers.
9	<b>North Halawa Valley</b>	Oahu, HI	Box	Robertson (2005).	2,3,5,12	200 instruments at seven different locations: vibrating wire strain gages, electrical resistance strain gages (ERSGs), thermocouples, span extensometers, tendon load cells, base-line deflection systems, tiltmeters, and automated datalogger.

**Note:** The numbers on the “Sensor Type” column refer to: (1) – anemometer; (2) – temperature sensor; (3) – strain gauge; (4) – accelerometer; (5) – displacement transducer; (6) – velocimeter; (7) – global positioning system; (8) – weigh-in-motion sensor; (9) – corrosion sensor; (10) – elasto-magnetic sensor; (11) – optic fibre sensor; (12) – tiltmeter; (13) – level sensing station; (14) – dynamometer; (15) – total station; (16) – seismometer; (17) – fatigue meter; (18) – cable tension force; (19) – joint meter; (20) – laser displacement sensor; (21) – meteorological station; (22) – video camera; (23) – jacking pressure sensor; (24) – potentiometer; (25) – water-level sensor

<sup>1</sup> The original cantilever Ironton–Russell Bridge cited in Xu and Xia (2011) closed in 2016. It was replaced by a new white cable-stayed bridge has two lanes of traffic without a dedicated sidewalk (as the old one). The new bridge was opened on November 23, 2016. It is unclear whether or not the new bridge is under surveillance by an active SHM system.

**Table 2.2** – Bridges in the United States instrumented with sensing systems prior/after 2011 and not included in Table 2.1.

#	Bridge Name	Location	Type	References	Instrumentation (and details whenever available)	Wireless (Y/N) F.E. Analysis (Y/N)
1	<b>Manhattan Bridge</b>	New York, NY	Suspension	Babanajad et al. (2020); Betti et al. (2014, 2016); Feng and Feng 2017; Luo et al. 2018; Feng 2019.	For one cable: acoustic emission sensors; two accelerometers; one weather station; temperature/relative humidity sensors; three fiber optic strain gages; two multiplexed strain sensors; deformation sensors; linear polarization resistance sensors; corrosion sensor; crack gages. For two panels: fiber-optic strain gauges; 8 temperature/humidity sensors, 4 LPR sensors, 4 Corrosion Instrument bimetallic (BM) sensors, and 2 CMAS sensors. For rail joint study: 14 strain gages to capture flexural response, 16 strain gages to measure shear response (8 rosette sensors), 6 temperature sensors, 4 crack gages, and 20 accelerometers.	Wireless parametric sensor interface
2	<b>Throgs Neck Bridge</b>	New York, NY	Suspension	Mahmoud et al. 2006; Guo and Chen (2011); Guo et al. (2012);	Strain gages; linear motion sensors; 5 uniaxial accelerometers; thermocouple wires.	No Yes: 3D model
3	<b>Vincent Thomas Bridge</b>	Los Angeles, CA	Suspension	Yun et al. 2008; Torbol et al. (2013); He et al. 2008	Accelerometers.	Yes: DuraMote Yes: 3D model
4	<b>Bear Mountain Bridge, a.k.a. Purple Heart Veterans Memorial Bridge</b>	Fort Montgomery, NY	Suspension	Dong et al. 2010	Acoustic sensors: SoundPrint® system	
5	<b>Waldo–Hancock Bridge (now demolished)</b>	Verona, ME	Suspension	Dong et al. 2010	Acoustic sensors: SoundPrint® system	
6	<b>Bronx-Whitestone</b>	New York, NY	Suspension	Dong et al. 2010	Acoustic sensors: SoundPrint® system	
7	<b>Mackinac Bridge</b>	Connect the Upper and Lower Peninsulas of Michigan	Suspension	Aono et al. 2019; Faridazar 2019		Yes No
8	<b>Alfred Zampa Memorial (New Carquinez)</b>	Vallejo, CA	Suspension	Nagarajaiah and Erazo 2016; Zhang et al. 2017; Hong et al. 2011; Kurata et al. 2013; Swartz et al. 2005; Conte et al. 2008, He et al. 2009; Zhang et al. (2017)	For system identification prior to inauguration: 34 uniaxial and 10 triaxial force-balanced accelerometers. For permanent wired seismic monitoring: 76 force balance tri-axial accelerometers on the suspension bridge, 27 sensors on the approach, and 1 anemometer.	Yes: Narada wireless sensor platform. No.

					Accelerometers; anemometer; strain gages; thermistors; humidity sensors;	
9	<b>Bill Emerson Memorial Bridge</b>	Connecting MO Route 74 with IL Route 146 across the Mississippi River.	Cable-stayed	Hartnagel et al. 2006; Chen et al. 2007	84 accelerometers; weather station.	No Yes: 3D, SAP2000
10	<b>U.S. Grant Bridge</b>	Portsmouth (OH) over the Ohio river	Cable-stayed	Helmicki and Hunt (2013); Norouzi et al. 2014	Accelerometers; strand meters; strain gages; tiltmeters.	No No
11	<b>Charles W. Cullen Bridge aka Indian River Inlet Bridge</b>	Indian River Inlet, Sussex County, Delaware	Cable-stayed	Shenton et al. 2013, 2017; Al-Khateeb et al. 2019; Wu et al. 2019; Natalicchio (2018)	Fiber optics consisting of: 70 strain sensors; 44 accelerometers; 9 tiltmeters; 3 displacement sensors. Non-fiber-optics based sensors: 2 anemometers; 16 chloride sensors.	No Yes: 3D STAAD.Pro
12	<b>Varina-Enon Bridge</b>	Hopewell, Virginia	Cable-stayed	Maguire 2013, Maguire et al. 2018	77 total strain gages, LVDT, crack sensors, and temperature sensors	No. No.
13	<b>Northbound US 41 over Ohio River</b>	Henderson Co., KY	Truss	Peiris et al. 2018	LVDTs; triaxial accelerometers;	No. No.
14	<b>Albert Gallatin Memorial</b>	Point Marion, PA	Truss	GEOKON 2020; CANARY 2020	Inclinometers; vibrating wire piezometers;	No. No.
15	<b>Government Bridge or Arsenal Bridge</b>	Rock Island, IL to Davenport, IA.	Truss	Dong et al. (2010); Li et al. (2016)	One optical sensing interrogator, one optical channel switch extension, 36 s optical train sensors, 21 optical temperature Sensors, 10 optical accelerometers, one fiber optic tiltmeter. Conventional AE sensors, weather station, and corrosion sensors.	No. No.
16	<b>World War I Memorial Bridge</b>	Portsmouth (NH) to Kittery (ME) over the Piscataqua River	Truss	Shahsavari et al. (2019, 2020); Chen et al. 2018	Twelve accelerometers, uniaxial strain gauges, 11 strain rosettes, and tiltmeters.	No. Yes: 3D with SAP2000
17	<b>New Hope-Lambertville Toll-Supported Bridge</b>	New Hope (PA) to Lambertville (NJ)	Truss	GEOKON (2020)	Wire strain gauges; tiltmeters	No. No.
18	<b>Riverton–Belvidere Toll-Supported Bridge</b>	Riverton (PA) to Belvidere (NJ)	Truss	GEOKON (2020); Chang et al. (2011)	Wire strain gauges; tiltmeters Eight wireless sensor nodes measuring vertical and transverse accelerations	Yes. No.
19	<b>Burlington-Bristol Bridge</b>	Bristol (PA) to Burlington (NJ)	Truss	De Roeck et al. 2011; Campbell Scientific, 2020	45 accelerometers (30 piezoelectric and 15 capacitive); electrical resistance strain gages; vibrating-wire strain gages, vehicle-speed sensors; road-surface temperature sensors	No. Yes: 3D with SAP2000 and Strand7
20	<b>Chulitna River Bridge</b>	Trapper Creek, AL	Steel plate girder	Xiao et al. 2017	8 optical rosette strain sensors; 24 optical strain sensors; 15 optical strain sensors; 5 accelerometers; 4 displacement sensors	No. No.
21	<b>Bridge 1-813, I-495 over the Christina River</b>	Wilmington, DE	Steel plate girder	GEOKON, 2020; McNeil et al. 2019	Tiltmeters	No. No.
22	<b>I-64 over US 60</b>	Franklin Co., KY	Steel plate girder	Harik and Peiris, 2013; Peiris et al. 2018	1 accelerometers; 11 strain gauges; infrared sensors; 1 ultrasonic height sensor	No. No.

23	<b>I -24 over Tennessee River</b>	Marshall Co., KY	Steel arch and plate girder	Peiris et al. 2018	Nine LVDTs; 11 temperature sensors; 8 tiltmeters.	No. No.
24	<b>I-39 Wisconsin River</b>	Wausau, WI	Steel plate girder	Mahmoud et al. 2005; Liu et al. 2009; Orcesi and Frangopol 2011	Twenty-four ERSGs; 2 LVDTs	No. No.
25	<b>P-0962 bridge</b>	Dallas County, MO	Steel girder	Fonda and Watkins 2004; Watkins et al. 2007	EFPI strain sensors; ERSGs	No. Yes: 3D with ABAQUS
26	<b>County Highway Bridge,<sup>2</sup></b>	Town of Spruce, WI	Steel girder	Walker and Hughes (2005)		
27	<b>C-846 Bridge</b>	Salt Lake City, UT	Steel girder	Halling and Petty 2001; Nichols 2017; Nichols et al. 2018	Bi-axial and tri-axial accelerometers; 25 thermocouples	No. No.
28	<b>Interstate 91 (I-91) northbound. Meriden Bridge</b>	Meriden, CT	Steel girder	Christenson and Motaref (2016); Jin et al. (2015, 2016); Xiao et al. 2020; Lobo-Aguillar et al. (2019)	Eighteen foil strain gages; 4 piezoelectric strain sensors, 8 piezoelectric accelerometers, 4 capacitance accelerometers (with additional temperature sensing capability); 4 resistance temperature detectors	No. Yes: 3D with SAP2000
29	<b>US 30 Highway (Iowa)</b>		Steel girder	Seo et al. (2013); Lu et al. 2010; Wipf et al. 2007a, 2007b;	Forty FBG fiber optics strain sensors	No. No.
30	<b>Balsam Road Bridge,<sup>4</sup></b>	Marathon Co., WI	Steel stringer	Walker and Hughes (2005)	Sonar for scour monitoring	No. No.
31	<b>Wisconsin Highway 35 Bridge,<sup>4</sup></b>	Tank Creek, WI		Walker and Hughes (2005)	Sonar for scour monitoring	No. No.
32	<b>Crum Creek Viaduct (Rail bridge)</b>	Swarthmore, PA	Steel girder	IIS, 2020; GEOKON, 2020	Vibrating wire gages	No. No.
33	<b>Telegraph Road</b>	Monroe, MI	Slab-on-girder highway bridge	Hou et al. 2020a, 2020b; O'Connor et al. 2016	Accelerometers; strain gauges; and thermometers	No. No.
34	<b>Carroll Lee Cropper</b>	Boone County, KY	Continuous steel arch-shaped truss	Peiris et al. (2018);	Vibrating wire microcrack meters	No. No.
35	<b>Huey P Long bridge</b>	Bridge City, LA	Cantilevered steel through-truss	Weinmann 2015; Kleinhans 2009	769 static and 50 dynamic sensors: strain gages; tiltmeters	No. No.
36	<b>Tacony-Palmyra Bridge</b>	Tacony (PA); Palmyra (NJ)	Steel tied arch and double-leaf bascule	Yarnold et al. 2012b; Yarnold and Moon (2015)	Vibrating wire strain gages; crack meters	No. No.
37	<b>Streicker Bridge (Pedestrian bridge)</b>	Princeton, NJ	Steel arch and reinforced, post-tensioned	Glisic (2018); Napolitano et al. 2019; SMARTEC 2017b;	Discrete FBG long-gauge sensors; distributed Brillouin Time Domain Analysis sensors; FBG-based strain sensors; sensing	No. No.

<sup>2</sup> Note that the bridges monitored for scour detection are discussed in Ch. 5 of this report

			concrete.		sheets	
38	<b>Fremont Bridge</b>	Portland, OR	Steel-tied arch	Campbell Scientific 2020b	Eight dataloggers, 64 strain and surface temperatures sensors.	No. No.
39	<b>Neville Island</b>	Pittsburgh, PA	Steel-tied arch	Connor et al. (2005); Kwon and Frangopol (2010)	Accelerometers, LVDTs; Uniaxial ERSG.	No. No.
40	<b>Birmingham Bridge</b>	Pittsburgh, PA	Bowstring arch	Kwon and Frangopol (2010); Connor and Fisher 2001; Liang and Chen (2014); Connor et al. 2004, 2005	Accelerometers, LVDTs; Uniaxial ERSG.	No. No.
41	<b>Cedar Avenue Bridge</b>	Burnsville, MN	Tied arch	Schultz et al. (2014)	Sixteen acoustic emission sensors.	No. No.
42	<b>New Mexico I-10 Bridge</b>	Las Cruces, NM	Steel deck arch	SMARTTEC 2020	Seventy-two fiber optics strain gages	No. No.
43	<b>Columbia River I-5 Bridge</b>	Portland, OR	Steel vertical-lift, "Parker type" through-truss	Campbell Scientific 2020c	Tiltmeters, and laser position sensors	No. No.
44	<b>NBI# 00000003231620</b>	Potsdam, N.Y. (Carrying Wright Road over Trout Brook)	Reinforced concrete slab	Whelan et al. 2009;	Twelve dual-axis MEMS accelerometers; 11 strain transducers	Yes: 20 nodes No.
45	<b>New Nibley Bridge</b>	UT	Precast deck T-girders	Alder et al. (2018); Pace et al (2019)	strain gages, thermocouples, accelerometers; geophones velocity transducers	No. No.
46	<b>New Trammel Creek</b>	Allen County, KY	Integral abutment	Peiris et al. 2018; Zhu et al. 2015	pressure transducers, temperature gauges, and tiltmeters	No. No.
47	<b>Lambert Road Bridge</b>	Sacramento, CA	Integral abutment	Barr et al. (2012); Foust 2014; Foust et al. 2014	16 Hitec strain gauges, 4 Geokon vibrating-wire strain gauges, 4 Mark Sercel velocity transducers (geophones), 3 Geokon tiltmeters, and 44 Omega thermocouples.	No. No.
48	<b>I-65 elevated expressway</b>	Jefferson Co., KY	PC I-girder bridge	Peiris et al. 2018	LVDTs	No. No.
49	<b>Powder Mill Pond, a.k.a. Vernon Avenue Bridge</b>	Barre, MA	3 Span Steel Girder	Kaspar 2018; Ahlborn et al. (2010); Santini Bell et al. 2010; Sanayei et al. (2012)	One hundred strain gauges, 36 girder thermistors, 30 concrete thermistors, 16 bi-axial tiltmeters, and 16 accelerometers	No. Yes: 3D with SAP2000
50	<b>Rio Puerco bridge</b>	Albuquerque, NM	Precast, prestressed I-beam girders.	SMARTTEC 2017	Sixty-four fiber optics (SOFO) to measure prestress; 6 thermocouples.	No. No.
51	<b>San Ysidro Bridge</b>		Precast, prestressed I-beam girders.	Barr et al. (2006);	Strain gages	No. No.
52	<b>Horsetail Falls bridge</b>	Multnomah County, OR	Pre-stressed concrete	Soltesz 2002, Kachlakev and McCurry 2000, Kachlakev et al. 2001	Twenty-eight Bragg grating strain gages	No. No.

53	<b>Sylvan Bridge</b>	Oregon (ODOT Bridge No. 02285)	Pre-stressed concrete	Soltesz 2002, Kachlakev and McCurry 2000, Kachlakev et al. 2001	Fourteen fiber optics strain gages	No. No.
54	<b>Kishwaukee River Bridge</b>	Winnebago County, Illinois	Pre-stressed concrete box girder	Intelligent Instrument System, Inc. (2020)	Strain gages, accelerometers, clip gages and LVDT gages	No. Yes.
55	<b>Watson Wash bridge</b>	Mojave Desert, CA	RC T-girder bridge	Lee 2005; Lee et al. (2007)	Accelerometers	No. No.
56	<b>Kings Stormwater Channel bridge</b>	Riverside County, CA	Concrete-filled carbon/epoxy tubes girder	Guan et al. 2006;	Sixty-three 63 single-axis 0-200 Hz accelerometers, 20 strain gages, 4 linear potentiometers, 1 temperature sensor, and 1 pantilt-zoom camera.	No. No.
57	<b>Penncoyd Viaduct</b>	Philadelphia, PA		Furkan et al. (2020)	Displacement string potentiometers sensors	Yes. No.
58	<b>Sunrise Boulevard Bascule Bridge</b>	Fort Lauderdale, FL	Bascule Bridge	Catbas et al. (2010, 2012); Catbas and Malekzadeh (2016)	Dynamic strain gages	No. No.

<b>Table 3.1 – Planned performance of the SHM system.</b>				
<b>No.</b>	<b>Bridge Name</b>	<b>Condition to be Assessed</b>	<b>Min. flaw Detection size, trigger notification, change in value</b>	<b>Number of Gauges</b>
<b>1</b>	<b>Elizabeth</b>	Monitoring major structures for broken wires, redistribution of loads, and notification of barge collisions and other impacts	1 mil ± 2 ksi 0.1g acceleration	98
<b>2</b>	<b>Neville Island</b>	Monitoring major structures for out-of-plane bending, crack length, and notification of barge collisions and other impacts	1 mil ± 2 ksi 0.1g acceleration	76
<b>3</b>	<b>Birmingham</b>	Monitoring major structures for unique issues, such as out-of-plane bending, cracking and longitudinal movement	1 mil ± 2 ksi	40
<b>4</b>	<b>Smithfield Street</b>	Monitor bridges for racking, capacity, and the potential for notification of barge collisions and other impacts	1/16" movement 0.1g acceleration	39
<b>5</b>	<b>Clairton-Glassport</b>	Monitor bridges with the potential for notification of barge collisions and other impacts	1/16" movement 0.1g acceleration	56
<b>6</b>	<b>Cooks Mill</b>	Evaluate the performance of rehabilitation/retrofit strategies such as making decks composite with prestressed box beams	+ 200 psi	10
<b>7</b>	<b>Somerset Co.</b>	Evaluate the performance of rehabilitation/retrofit strategies such as making decks composite with prestressed box beams	+ 200 psi	30
<b>8</b>	<b>Fulton Co.</b>	Evaluate the performance of rehabilitation/retrofit strategies such as making decks composite with prestressed box beams	+ 200 psi	10
<b>9</b>	<b>Wyebrooke</b>	Performance of non-composite steel beams	1 mil ± 2 ksi	42
<b>10</b>	<b>Sanatoga</b>	Stone masonry arch ring or wall movement (1/2 threshold in Pub 238) and scour	1/16" movement	12

<b>No.</b>	<b>Name or Location</b>	<b>Expected Duration</b>	<b>Actual Duration</b>
1	<b>Elizabeth Bridge</b>	2 months	6 months
2	<b>Neville Island Bridge</b>	2 months	2 years and 5 months
3	<b>Birmingham Bridge</b>	2 months	4 years
4	<b>Smithfield Street Bridge</b>	3 years	3 years and 6 months (still active)
5	<b>Clairton-Glassport Bridge</b>	3 years	4 years and 6 months (still active)
6	<b>Cooks Mill Bridge</b>	2 years	3 years and 9 months
7	<b>Somerset Co.</b>	2 weeks	2 years
8	<b>Fulton Co.</b>	2 weeks	1 year and 3 months
9	<b>Wyebrooke Bridge</b>	6 months	3 years and 7 months
10	<b>Sanatoga Bridge</b>	3 years	3 years and 7 months

<b>No.</b>	<b>Bridge Name</b>	<b>Minimum number of Gauges</b>	<b>Effective number of Gauges</b>
<b>1</b>	<b>Elizabeth Bridge</b>	98	85
<b>2</b>	<b>Neville Island Bridge</b>	76	98
<b>3</b>	<b>Birmingham Bridge</b>	40	52
<b>4</b>	<b>Smithfield Bridge</b>	39	46
<b>5</b>	<b>Clairton-Glassport Bridge</b>	56	56
<b>6</b>	<b>Cooks Mill Bridge</b>	10	10
<b>7</b>	<b>Somerset Co.</b>	30	30
<b>8</b>	<b>Fulton Co.</b>	10	10
<b>9</b>	<b>Wyebrooke Bridge</b>	42	42
<b>10</b>	<b>Sanatoga Bridge</b>	12	8

**Table 5.1** – Total cross-section area of each element of the three trusses.

	<b>Truss</b>	<b>Area (m<sup>2</sup>)</b>	<b>Area (in<sup>2</sup>)</b>
<b>Top chord</b>	East	0.04927	76.37
<b>Top chord</b>	Center	0.08323	129.0
<b>Top chord</b>	West	0.08323	129.0
<b>Bottom chord</b>	East	0.04943	77.63
<b>Bottom chord</b>	Center	0.07321	113.5
<b>Bottom chord</b>	West	0.06548	101.5

**Table 5.2** – Position of the rear axle of the truck from Pier 3 and corresponding strain on the diagonal member. The distances are expressed in m. (in.). Forces are expressed in kN (kip)

	Distance of rear axle from north portal	Axial Force at member L <sub>1</sub> U <sub>2</sub>	Axial Strain at member L <sub>1</sub> U <sub>2</sub> (μ $\epsilon$ )
Position 1	15.24 (600)	39.26 (8.83)	58.84
Position 2	13.97 (550)	53.93 (12.12)	80.83
Position 3	12.70 (500)	65.89 (14.81)	98.75
Position 4	11.43 (450)	73.69 (16.57)	110.40
<b>Position 5</b>	<b>10.16 (400)</b>	<b>76.15 (17.12)</b>	<b>114.10</b>
Position 6	8.89 (350)	72.67 (16.34)	108.90
Position 7	7.62 (300)	63.77 (14.34)	95.57

**Table 5.3** – Position of the rear axle of the truck from Pier 4 and corresponding strain on the diagonal member. The distances are expressed in m. (in.). Forces are expressed in kN (kip).

	Distance of rear axle from south portal	Axial Force at member L' <sub>1</sub> U' <sub>2</sub>	Axial Strain at member L' <sub>1</sub> U' <sub>2</sub> (μ $\epsilon$ )
Position 1	1.27 (50)	37.88 (8.85)	56.77
Position 2	2.54 (100)	52.20 (11.74)	78.23
Position 3	3.81 (150)	64.36 (14.47)	96.46
Position 4	5.08 (200)	72.84 (16.38)	109.17
<b>Position 5</b>	<b>6.35 (250)</b>	<b>76.27 (17.15)</b>	<b>114.31</b>
Position 6	7.62 (300)	73.80 (16.59)	110.61
Position 7	8.89 (350)	65.58 (14.74)	98.28

**Table 5.4** – Numerical maximum strain at the two control diagonal members of the Span 4 center truss as a result of the presence of a single truck. Values expressed in  $\mu\epsilon$ .

Truss member	Truck Type			
	Company Truck	ML-80	H20	HS20
Member $L_1U_2$	80.89	114.1	62.28	98.95
Member $L'_1U'_2$	80.92	114.3	62.33	99.05

**Table 5.5** – Predicted numerical response of the bridge element close to the south portal of Span 4 under the action of two simulated extreme load events. Values expressed in  $\mu\epsilon$ . The colored cells cluster the top chords, the bottom chords, and the diagonal members.

	Sensor No.	30% heavier truck + 2 in snow	2 test trucks in opposite directions
East Truss	S04	57.57	29.29
	S05	25.83	14.38
	S06	-26.21	-14.58
Center Truss	S10	49.15	133
	S11	16.5	22.16
	S12	-14.53	-19.5
West Truss	S16	-7.94	26.61
	S17	4.38	9.88
	S18	-3.47	-7.78

**Table 6.1** – Properties of the concrete and steel components used in the finite element models.

<b>CONCRETE</b>	Beams	5000 psi
	Deck	4000 psi
	Parapets	3500 psi
<b>STEEL</b>	Stirrups	Grade 40 steel
	Rebars (deck)	Grade 60 steel
	Strands (for prestressing)	Grade 250 steel

**Table 6.2a – Damage Scenarios simulated in the study presented in this paper. (Somerset Bridge)**

<b>Damage scenario</b>	<b>Description</b>
1	The cross-section area of all strands in concrete beams was reduced by 20%.
2	The modulus of elasticity of beam' concrete was reduced by 10%.
3	The modulus of elasticity of concrete for G4 (S5), G7 (S8), and G11 (S24) was reduced by 50%.
4	A few cracks in G3, G4, G8, G13, and G14 were modeled. The crack width is 0.2 in and its depth is 2 in.
5	The contact type of the G4, G5, and G12 with the deck was changed from “Bounded” to “No Separation” (Loss of composite behavior). . In ANSYS software, “Bounded” contact type between two objects means that the objects are perfectly bounded to each other and they cannot slide or be separated. “No separation” contact type between two components means that the objects can slide along the contact surface but they cannot be separated.
6	The contact type of the G4, G5, and G12 with the deck was changed from “Bounded” to “No Separation” (Loss of composite behavior). Also, the contact of the mentioned beams with adjacent shear keys was changed to “No separation”.

**Table 6.2b – Damage Scenarios simulated in the study presented in this paper. (Cooks Mill Bridge)**

<b>Damage scenario</b>	<b>Description</b>
1	10% reduction of the modulus of elasticity of the boxes' concrete while the stiffness of the deck and parapets was left unchanged.
2	Severe localized stiffness loss: 40% lower modulus of elasticity of one box.
3	Steel corrosion was simulated under damage scenario by reducing the cross-section area of all the strands by 20%.
4	Localized cracks in G2 and G5 were modeled under damage scenario 4. The crack width and depth were 0.2 in and 2 in, respectively. Three cracks were introduced at the bottom surface of some concrete beams.
5	Damage Scenario 5 consisted of modifying the contact type of girders G4 and G6 with the deck. Such contact was changed from “Bounded” to “No Separation”, which means loss of composite behavior
6	Damage scenario 5 with modified adjacent shear keys connections, which were changed to “No separation”.

**Table 6.2c – Damage Scenarios simulated in the study presented in this paper. (Tonoloway Bridge)**

<b>Damage scenario</b>	<b>Description</b>
1	The modulus of elasticity of beams' concrete was reduced by 10%.
2	The modulus of elasticity of concrete for G3 (S4) and G6 (S7) was reduced by 50%.
3	The cross-section area of all strands in concrete beams was reduced by 20%.
4	Cracks in G2 and G5 were modeled. The crack width is 0.2 in and its depth is 2 in.
5	The contact type of the G4 and G5 with the deck was changed from “Bounded” to “No Separation” (Loss of composite behavior).
6	The contact type of the G4 and G5 with the deck was changed from “Bounded” to “No Separation” (Loss of composite behavior). Also, the contact of the mentioned beams with adjacent shear keys was changed to “No separation”.

**Table 7.1** – Properties of the concrete and steel components used in the finite element models.

<b>CONCRETE</b>	Deck or Slab	4000 psi
<b>STEEL</b>	Cables (only for Birmingham Bridge)	Grade 250 steel
	Other Steel Components (Beams, girders, etc.)	Grade 60 steel

**Table 7.2a** – Damage scenarios simulated for the Birmingham Bridge.

<b>Damage scenario</b>	<b>Description</b>
<b>1</b>	The modulus of elasticity of steel was reduced by 5%.
<b>2</b>	The modulus of elasticity of concrete was reduced by 10%.
<b>3</b>	The contact of the stringers (the third counting from the curbs) with FB01 and FB19 changed from expandable to fixed (locked).
<b>4</b>	Simultaneous absence of one of the inner cables above FB01 and FB19
<b>5</b>	Two diaphragms that are approximately under the front axle of the truck were removed.
<b>6</b>	Bolt Loosening at the connection of FB01 to the West tie girder (the tie girder that is in the right-hand side of the south bound)

**Table 7.2b** – Damage scenarios simulated for the Clairton Bridge.

<b>Damage scenario</b>	<b>Description</b>
<b>1</b>	The modulus of elasticity of steel was reduced by 5%.
<b>2</b>	The modulus of elasticity of the concrete deck was reduced by 15%.
<b>3</b>	Removed diaphragms and diagonal bracing members from the middle of the span 12 (west side) and span 13 (east side).
<b>4</b>	The modulus of elasticity of the middle girder was reduced by 10%.
<b>5</b>	Beam end severe corrosion is modeled.
<b>6</b>	Repair Scenario 1: A rectangular plate was added to the location of the previous damage scenario to repair the modeled corrosion.

**Table 7.2c** – Damage scenarios simulated for the Chester Bridge

<b>Damage scenario</b>	<b>Description</b>
<b>1</b>	0.1 inches corrosion at the bottom flange of each girder.
<b>2</b>	0.06 in corrosion at the web of each girder.
<b>3</b>	The modulus of elasticity of girders' steel was reduced by 5%.
<b>4</b>	Damage Scenario 4: The modulus of elasticity of steel for girder 3 (G3) and girder 12 (G12) was reduced by 10%.
<b>5</b>	Seven diaphragms (steel bracing) were removed.
<b>6</b>	The contact of the Girder 5 (G5) and Girder 9 (G9) with the deck was changed from "Bounded" to "No separation". (Loss of composite behavior)

**Table 7.3a** – Birmingham Bridge. The predicted strains at certain locations of the bridge for the third damage scenario. The measured data refers to the north bound crossing of the truck along the bike lane. (Two crossings were completed).

Sensor No.	Strain in <b>XX</b> direction ( $\mu\epsilon$ )					Strain in <b>YY</b> direction ( $\mu\epsilon$ )				
	Measured		Predicted			Measured		Predicted		
	Truck crossings		Pristine	Damage 3	Diff. (%)	Test 1	Test 5	Pristine	Damage 3	Diff. (%)
FB01-East-IN	-73.40	-57.50	-62.72	-61.10	-2.6%	-81.40	-71.10	-76.61	-88.29	15.2%
FB01-East-Out	16.20	19.30	14.08	14.24	1.1%	14.70	18.40	19.22	20.43	6.3%
FB19-East-IN	-50.40	-49.50	-60.91	-61.92	1.7%	-79.40	-77.50	-72.67	-76.09	4.7%
FB19-East-Out	15.60	18.30	15.19	15.04	-1.0%	12.30*	11.90*	20.53	19.95	-2.8%

**Table 7.3b** – Birmingham Bridge. The predicted strains at certain locations of the bridge for the third damage scenario. The measured data refers to the south bound crossing of the truck along the right lane. (Two crossings were completed).

Sensor No.	Strain in <b>XX</b> direction ( $\mu\epsilon$ )					Strain in <b>YY</b> direction ( $\mu\epsilon$ )				
	Measured		Predicted			Measured		Predicted		
	Truck crossings		Pristine	Damage 3	Diff. (%)	Test 11	Test 15	Pristine	Damage 3	Diff. (%)
FB01-West-IN	-16.10	-16.20*	-20.34	-20.01	-1.6%	-32.00*	-29.10*	-17.15	-27.03	58%
FB01-West-Out	19.00	19.00	14.34	14.03	-2.2%	19.70	20.10	23.49	22.56	-4.0%
FB19-West-IN	-15.40*	-14.90*	-19.83	-18.42	-7.1%	-34.50*	-31.10*	-21.80	-35.06	61%
FB19-West-Out	17.90	18.40	15.74	15.47	-1.7%	22.00	28.00	24.56	24.14	-1.7%

**Table 7.4** – Clairton Bridge. The predicted strains at certain locations of the bridge under damage scenario 5 and Load Case 2.

Sensor No.	Predicted ( $\mu\epsilon$ )		Diff. (%)
	Pristine	Damage 5	
S01	4.88	3.36	-31.1%
S03	4.70	4.72	0.4%
S05	4.86	4.88	0.4%
S06	-16.42	-16.42	0.0%
S08	-12.65	-12.65	0.0%
S10	-7.60	-7.59	-0.1%
S11	-13.60	-13.61	0.0%
S13	-11.33	-11.33	0.0%
S15	-8.34	-8.34	0.0%
S16	2.79	2.79	0.0%
S18	2.36	2.36	0.0%
S20	2.71	2.70	-0.4%

**Table 7.5** – Chester Bridge. Predicted strains at certain locations under damage scenario 4. (Test 5)

<b>Truck is at the middle of the <i>first</i> span</b>				
Sensor No.	Measured Strain ( $\mu\epsilon$ )	Predicted Strain ( $\mu\epsilon$ )		Diff. (%)
		Pristine	Damage 4	
1	3.00	2.09	2.17	3.8%
2	9.50	8.91	9.11	2.2%
3	17.50	17.12	17.51	2.3%
4	25.00	25.04	25.58	2.2%
5	28.00	37.47	37.56	0.2%
6	44.00	45.23	45.25	0.0%
7	40.00	36.28	36.31	0.1%
15	2.00	1.08	1.13	4.6%
16	5.50	5.59	5.73	2.5%
17	10.50	10.87	11.09	2.0%
18	15.00	16.08	16.37	1.8%
19	16.50	23.20	23.24	0.2%
20	26.50	27.04	27.05	0.0%
21	24.50	21.81	21.80	0.0%

<b>Truck is at the middle of the <i>second</i> span</b>				
Sensor No.	Measured Strain ( $\mu\epsilon$ )	Predicted Strain ( $\mu\epsilon$ )		Diff. (%)
		Pristine	Damage 4	
22	3.50	2.02	2.01	-0.5%
23	10.00	9.78	9.89	1.1%
24	18.50	18.98	19.30	1.7%
25	30.00	29.62	30.24	2.1%
26	41.50	42.26	43.61	3.2%
27	48.00	47.93	48.91	2.0%
28	33.00	31.65	32.04	1.2%
36	2.50	1.03	1.03	0.0%
37	6.00	5.88	5.93	0.9%
38	10.50	11.44	11.62	1.6%
39	16.50	18.25	18.66	2.2%
40	23.00	24.58	25.46	3.6%
41	29.50	29.36	29.98	2.1%
42	18.50	18.74	18.94	1.1%

**Table 7.6 – Chester Bridge. Predicted strains at certain locations under damage scenario 5. (Test 5)**

<b><i>Truck is at the middle of the first span</i></b>				
Sensor No.	Measured Strain ( $\mu\epsilon$ )	Predicted Strain ( $\mu\epsilon$ )		Diff. (%)
		Pristine	Damage 5	
1	3.00	2.09	1.97	-5.7%
2	9.50	8.91	8.83	-0.9%
3	17.50	17.12	17.13	0.1%
4	25.00	25.04	25.39	1.4%
5	28.00	37.47	37.94	1.3%
6	44.00	45.23	45.44	0.5%
7	40.00	36.28	35.96	-0.9%
15	2.00	1.08	1.02	-5.6%
16	5.50	5.59	5.55	-0.7%
17	10.50	10.87	10.92	0.5%
18	15.00	16.08	16.33	1.6%
19	16.50	23.20	23.50	1.3%
20	26.50	27.04	27.27	0.9%
21	24.50	21.81	21.52	-1.3%

<b><i>Truck is at the middle of the second span</i></b>				
Sensor No.	Measured Strain ( $\mu\epsilon$ )	Predicted Strain ( $\mu\epsilon$ )		Diff. (%)
		Pristine	Damage 5	
22	3.50	2.02	1.93	-4.5%
23	10.00	9.78	9.69	-0.9%
24	18.50	18.98	19.03	0.3%
25	30.00	29.62	29.74	0.4%
26	41.50	42.26	42.67	1.0%
27	48.00	47.93	48.04	0.2%
28	33.00	31.65	31.54	-0.3%
36	2.50	1.03	0.97	-5.8%
37	6.00	5.88	5.81	-1.2%
38	10.50	11.44	11.48	0.4%
39	16.50	18.25	18.33	0.4%
40	23.00	24.58	24.91	1.3%
41	29.50	29.36	29.50	0.5%
42	18.50	18.74	18.66	-0.4%

**Table 8.1** - The experimental and numerical tension (axial) forces (kips) at specific locations of the bridge for damage scenario 1. The “Diff.” column quantifies the difference between the numerical tension forces under pristine and damaged conditions.

Cable Gauge	Measured Tension (kips)	Predicted Tension (kips) - (FE Model)		
		Pristine	Damage Scenario 1	Diff. (%)
L8 Right	26.90	24.55	24.40	-0.6%
L8 Left	30.50	25.72	25.55	-0.7%
L9' Right	27.90	20.37	20.21	-0.8%
L9' Left	24.10	20.58	20.41	-0.8%

**Table 8.2** - The experimental and numerical tension (axial) forces (kips) at specific locations of the bridge for damage scenario 2.

Cable Gauge	Measured Tension (kips)	Predicted Tension (kips) - (FE Model)		
		Pristine	Damage Scenario 2	Diff. (%)
L8 Right	26.90	24.55	25.03	2.0%
L8 Left	30.50	25.72	26.27	2.1%
L9' Right	27.90	20.37	20.89	2.6%
L9' Left	24.10	20.58	21.10	2.5%

**Table 8.3** - The experimental and numerical tension (axial) forces (kips) at specific locations of the bridge for damage scenario 3.

Cable Gauge	Measured Tension (kips)	Predicted Tension (kips) - (FE Model)		
		Pristine	Damage Scenario 3	Diff. (%)
L8 Right	26.90	24.55	24.55	0.0%
L8 Left	30.50	25.72	25.73	0.0%
L9' Right	27.90	20.37	20.59	1.1%
L9' Left	24.10	20.58	22.55	9.6%

**Table 8.4** - The experimental and numerical tension (axial) forces (kips) at specific locations of the bridge for damage scenario 4.

Cable Gauge	Measured Tension (kips)	Predicted Tension (kips) - (FE Model)		
		Pristine	Damage Scenario 4	Diff. (%)
L8 Right	26.90	24.55	24.55	0.0%
L8 Left	30.50	25.72	25.72	0.0%
L9' Right	27.90	20.37	20.37	0.0%
L9' Left	24.10	20.58	20.58	0.0%

**Table 8.5** - The experimental and numerical tension (axial) forces (kips) at specific locations of the bridge for damage scenario 5.

Cable Gauge	Measured Tension (kips)	Predicted Tension (kips) - (FE Model)		
		Pristine	Damage Scenario 5	Diff. (%)
L8 Right	26.90	24.55	24.08	-1.9%
L8 Left	30.50	25.72	25.22	-1.9%
L9' Right	27.90	20.37	20.37	0.0%
L9' Left	24.10	20.58	20.58	0.0%

**Table 9.1** - The experimental and numerical strains ( $\mu\epsilon$ ) at specific locations of the bridge for damage scenario 1 (Tests 5 and 6)

Installed sensors on FB01					
Sensor No.	Measured		Predicted (FE Model)		
	Test 5 (xy)	Test 6 (xy)	Pristine	Damage Scenario 1	Diff. (%)
S46	-16.80	-15.70	-17.96	-18.87	5.1%
S47	-13.90	-12.50	-13.72	-14.44	5.2%
Installed sensors on the tie-girder close to FB12					
Sensor No.	Measured		Predicted (FE Model)		
	Test 5	Test 6	Pristine	Damage Scenario 1	Diff. (%)
S13	-23.00	-23.60	-22.15	-23.33	5.3%
S15	25.60	27.80	26.92	28.37	5.4%
Installed sensors on FB14					
Sensor No.	Measured		Predicted (FE Model)		
	Test 5 (xy)	Test 6 (xy)	Pristine	Damage Scenario 1	Diff. (%)
S54	23.30	28.40	17.27	18.13	5.0%
S55	16.80	13.00	13.48	14.14	4.9%

**Table 9.2** - The experimental and numerical strains ( $\mu\epsilon$ ) at specific locations of the bridge for damage scenario 1 (Tests 9 and 10)

Installed sensors on FB01					
Sensor No.	Measured		Predicted (FE Model)		
	Test 9 (xy)	Test 10 (xy)	Pristine	Damage Scenario 1	Diff. (%)
S42	28.20	23.70	27.99	29.35	4.9%
S43	19.90	20.20	22.70	23.88	5.2%
Installed sensors on the tie-girder close to FB12					
Sensor No.	Measured		Predicted (FE Model)		
	Test 9	Test 10	Pristine	Damage Scenario 1	Diff. (%)
S09	-26.90	-25.60	-26.08	-27.40	5.1%
S12	30.40	30.50	32.02	33.57	4.8%
Installed sensors on FB14					
Sensor No.	Measured		Predicted (FE Model)		
	Test 9 (xy)	Test 10 (xy)	Pristine	Damage Scenario 1	Diff. (%)
S50	-18.40	-19.00	-19.47	-20.51	5.3%
S51	-21.30	-20.60	-16.06	-16.87	5.0%

**Table 9.3** - The experimental and numerical strains ( $\mu\epsilon$ ) at specific locations of the bridge for damage scenario 2 (Tests 5 and 6)

Installed sensors on FB01					
Sensor No.	Measured		Predicted (FE Model)		
	Test 5 (xy)	Test 6 (xy)	Pristine	Damage Scenario 2	Diff. (%)
S46	-16.80	-15.70	-17.96	-18.12	0.9%
S47	-13.90	-12.50	-13.72	-13.83	0.8%
Installed sensors on the tie-girder close to FB12					
Sensor No.	Measured		Predicted (FE Model)		
	Test 5	Test 6	Pristine	Damage Scenario 2	Diff. (%)
S13	-23.00	-23.60	-22.15	-22.34	0.9%
S15	25.60	27.80	26.92	27.19	1.0%
Installed sensors on FB14					
Sensor No.	Measured		Predicted (FE Model)		
	Test 5 (xy)	Test 6 (xy)	Pristine	Damage Scenario 2	Diff. (%)
S54	23.30	28.40	17.27	17.43	0.9%
S55	16.80	13.00	13.48	13.59	0.8%

**Table 9.4** - The experimental and numerical strains ( $\mu\epsilon$ ) at specific locations of the bridge for damage scenario 2 (Tests 9 and 10)

Installed sensors on FB01					
Sensor No.	Measured		Predicted (FE Model)		
	Test 9 (xy)	Test 10 (xy)	Pristine	Damage Scenario 2	Diff. (%)
S42	28.20	23.70	27.99	28.25	0.9%
S43	19.90	20.20	22.70	22.94	1.1%
Installed sensors on the tie-girder close to FB12					
Sensor No.	Measured		Predicted (FE Model)		
	Test 9	Test 10	Pristine	Damage Scenario 2	Diff. (%)
S09	-26.90	-25.60	-26.08	-26.30	0.8%
S12	30.40	30.50	32.02	32.34	1.0%
Installed sensors on FB14					
Sensor No.	Measured		Predicted (FE Model)		
	Test 9 (xy)	Test 10 (xy)	Pristine	Damage Scenario 2	Diff. (%)
S50	-18.40	-19.00	-19.47	-19.68	1.1%
S51	-21.30	-20.60	-16.06	-16.26	1.2%

**Table 9.5** - The experimental and numerical strains ( $\mu\epsilon$ ) at specific locations of the bridge for damage scenario 3 (Tests 5 and 6)

Installed sensors on FB01					
Sensor No.	Measured		Predicted (FE Model)		
	Test 5 (xy)	Test 6 (xy)	Pristine	Damage Scenario 3	Diff. (%)
S46	-16.80	-15.70	-17.96	-17.96	0.0%
S47	-13.90	-12.50	-13.72	-13.74	0.1%
Installed sensors on the tie-girder close to FB12					
Sensor No.	Measured		Predicted (FE Model)		
	Test 5	Test 6	Pristine	Damage Scenario 3	Diff. (%)
S13	-23.00	-23.60	-22.15	-23.13	4.4%
S15	25.60	27.80	26.92	28.02	4.1%
Installed sensors on FB14					
Sensor No.	Measured		Predicted (FE Model)		
	Test 5 (xy)	Test 6 (xy)	Pristine	Damage Scenario 3	Diff. (%)
S54	23.30	28.40	17.27	17.28	0.0%
S55	16.80	13.00	13.48	13.50	0.1%

**Table 9.6** - The experimental and numerical strains ( $\mu\epsilon$ ) at specific locations of the bridge for damage scenario 3 (Tests 9 and 10)

Installed sensors on FB01					
Sensor No.	Measured		Predicted (FE Model)		
	Test 9 (xy)	Test 10 (xy)	Pristine	Damage Scenario 3	Diff. (%)
S42	28.20	23.70	27.99	28.00	0.0%
S43	19.90	20.20	22.70	22.70	0.0%
Installed sensors on the tie-girder close to FB12					
Sensor No.	Measured		Predicted (FE Model)		
	Test 9	Test 10	Pristine	Damage Scenario 3	Diff. (%)
S09	-26.90	-25.60	-26.08	-26.10	0.1%
S12	30.40	30.50	32.02	32.05	0.1%
Installed sensors on FB14					
Sensor No.	Measured		Predicted (FE Model)		
	Test 9 (xy)	Test 10 (xy)	Pristine	Damage Scenario 3	Diff. (%)
S50	-18.40	-19.00	-19.47	-19.39	-0.4%
S51	-21.30	-20.60	-16.06	-15.95	-0.7%

**Table 9.7** - The experimental and numerical strains ( $\mu\epsilon$ ) at specific locations of the bridge for damage scenario 4 (Tests 5 and 6)

Installed sensors on FB01					
Sensor No.	Measured		Predicted (FE Model)		
	Test 5 (xy)	Test 6 (xy)	Pristine	Damage Scenario 4	Diff. (%)
S46	-16.80	-15.70	-17.96	-16.57	-7.7%
S47	-13.90	-12.50	-13.72	-13.55	-2.2%
Installed sensors on the tie-girder close to FB12					
Sensor No.	Measured		Predicted (FE Model)		
	Test 5	Test 6	Pristine	Damage Scenario 4	Diff. (%)
S13	-23.00	-23.60	-22.15	-22.65	2.3%
S15	25.60	27.80	26.92	28.16	4.6%
Installed sensors on FB14					
Sensor No.	Measured		Predicted (FE Model)		
	Test 5 (xy)	Test 6 (xy)	Pristine	Damage Scenario 4	Diff. (%)
S54	23.30	28.40	17.27	17.09	-2.0%
S55	16.80	13.00	13.48	12.61	-6.5%

**Table 9.8** - The experimental and numerical strains ( $\mu\epsilon$ ) at specific locations of the bridge for damage scenario 4 (Tests 9 and 10)

Installed sensors on FB01					
Sensor No.	Measured		Predicted (FE Model)		
	Test 9 (xy)	Test 10 (xy)	Pristine	Damage Scenario 4	Diff. (%)
S42	28.20	23.70	27.99	28.34	1.3%
S43	19.90	20.20	22.70	24.03	5.9%
Installed sensors on the tie-girder close to FB12					
Sensor No.	Measured		Predicted (FE Model)		
	Test 9	Test 10	Pristine	Damage Scenario 4	Diff. (%)
S09	-26.90	-25.60	-26.08	-26.27	0.7%
S12	30.40	30.50	32.02	32.41	1.2%
Installed sensors on FB14					
Sensor No.	Measured		Predicted (FE Model)		
	Test 9 (xy)	Test 10 (xy)	Pristine	Damage Scenario 4	Diff. (%)
S50	-18.40	-19.00	-19.47	-19.63	0.8%
S51	-21.30	-20.60	-16.06	-16.30	1.5%

**Table 9.9** - The experimental and numerical strains ( $\mu\epsilon$ ) at specific locations of the bridge for damage scenario 5 (Tests 5 and 6)

Installed sensors on FB01					
Sensor No.	Measured		Predicted (FE Model)		
	Test 5 (xy)	Test 6 (xy)	Pristine	Damage Scenario 5	Diff. (%)
S46	-16.80	-15.70	-17.96	-20.83	16.0%
S47	-13.90	-12.50	-13.72	-13.79	0.5%
Installed sensors on the tie-girder close to FB12					
Sensor No.	Measured		Predicted (FE Model)		
	Test 5	Test 6	Pristine	Damage Scenario 5	Diff. (%)
S13	-23.00	-23.60	-22.15	-22.07	-0.4%
S15	25.60	27.80	26.92	26.56	-1.3%
Installed sensors on FB14					
Sensor No.	Measured		Predicted (FE Model)		
	Test 5 (xy)	Test 6 (xy)	Pristine	Damage Scenario 5	Diff. (%)
S54	23.30	28.40	17.27	17.29	0.1%
S55	16.80	13.00	13.48	13.47	-0.1%

**Table 9.10** - The experimental and numerical strains ( $\mu\epsilon$ ) at specific locations of the bridge for damage scenario 5 (Tests 9 and 10)

Installed sensors on FB01					
Sensor No.	Measured		Predicted (FE Model)		
	Test 9 (xy)	Test 10 (xy)	Pristine	Damage Scenario 5	Diff. (%)
S42	28.20	23.70	27.99	8.14	-70.9%
S43	19.90	20.20	22.70	16.96	-25.3%
Installed sensors on the tie-girder close to FB12					
Sensor No.	Measured		Predicted (FE Model)		
	Test 9	Test 10	Pristine	Damage Scenario 5	Diff. (%)
S09	-26.90	-25.60	-26.08	-26.23	0.6%
S12	30.40	30.50	32.02	32.30	0.9%
Installed sensors on FB14					
Sensor No.	Measured		Predicted (FE Model)		
	Test 9 (xy)	Test 10 (xy)	Pristine	Damage Scenario 5	Diff. (%)
S50	-18.40	-19.00	-19.47	-19.48	0.0%
S51	-21.30	-20.60	-16.06	-16.06	0.0%

**Table 9.11** - The experimental and numerical strains ( $\mu\epsilon$ ) at specific locations of the bridge for damage scenario 6 (Tests 5 and 6)

Installed sensors on FB01					
Sensor No.	Measured		Predicted (FE Model)		
	Test 5 (xy)	Test 6 (xy)	Pristine	Damage Scenario 6	Diff. (%)
S46	-16.80	-15.70	-17.96	-17.29	-3.7%
S47	-13.90	-12.50	-13.72	-13.06	-4.8%
Installed sensors on the tie-girder close to FB12					
Sensor No.	Measured		Predicted (FE Model)		
	Test 5	Test 6	Pristine	Damage Scenario 6	Diff. (%)
S13	-23.00	-23.60	-22.15	-22.15	0.0%
S15	25.60	27.80	26.92	26.92	0.0%
Installed sensors on FB14					
Sensor No.	Measured		Predicted (FE Model)		
	Test 5 (xy)	Test 6 (xy)	Pristine	Damage Scenario 6	Diff. (%)
S54	23.30	28.40	17.27	17.28	0.1%
S55	16.80	13.00	13.48	13.48	0.0%

**Table 9.12** - The experimental and numerical strains ( $\mu\epsilon$ ) at specific locations of the bridge for damage scenario 6 (Tests 9 and 10)

Installed sensors on FB01					
Sensor No.	Measured		Predicted (FE Model)		
	Test 9 (xy)	Test 10 (xy)	Pristine	Damage Scenario 6	Diff. (%)
S42	28.20	23.70	27.99	26.87	-4.0%
S43	19.90	20.20	22.70	21.98	-3.2%
Installed sensors on the tie-girder close to FB12					
Sensor No.	Measured		Predicted (FE Model)		
	Test 9	Test 10	Pristine	Damage Scenario 6	Diff. (%)
S09	-26.90	-25.60	-26.08	-26.08	0.0%
S12	30.40	30.50	32.02	32.03	0.0%
Installed sensors on FB14					
Sensor No.	Measured		Predicted (FE Model)		
	Test 9 (xy)	Test 10 (xy)	Pristine	Damage Scenario 6	Diff. (%)
S50	-18.40	-19.00	-19.47	-19.46	0.0%
S51	-21.30	-20.60	-16.06	-16.05	-0.1%

**Table 10.1** – Data analysis of the raw data as a function of the corresponding raw temperature

Sensor	Quantity	Slope	Intercept	R <sup>2</sup>
DS-SF-EE	Pitch	0.00037	-0.03193	0.013402
	Roll	0.003636	-0.28376	0.174425
	Tilt-X	-0.01078	-2.3819	0.051375
	Tilt-Y	0.003601	1.145619	0.00046
	Tilt-Z	-0.03251	67.02197	0.041008
DS-SF-EW	Pitch	0.000796	-0.06503	0.253637
	Roll	-0.00101	0.182524	0.07072
	Tilt-X	0.000599	-0.92062	0.024006
	Tilt-Y	0.000238	0.977343	0.002362
	Tilt-Z	-0.02421	72.53201	0.198369
DS-SF-WE	Pitch	-0.00048	0.2165	0.00517
	Roll	-0.00157	-0.06969	0.045223
	Tilt-X	-0.00326	-3.58103	0.047199
	Tilt-Y	-0.00198	0.611224	0.124233
	Tilt-Z	0.004647	64.72145	0.003657
DS-SF-WW	Pitch	3.71E-05	0.101372	0.000155
	Roll	0.00026	-0.12266	0.002267
	Tilt-X	-0.00329	0.47095	0.088227
	Tilt-Y	-0.00219	1.524651	0.229143
	Tilt-Z	-0.00202	67.18642	0.000816
US-NF-EE	Pitch	0.000131	-0.01488	0.003544
	Roll	-0.00315	0.03689	0.158179
	Tilt-X	0.000638	-1.01774	0.016229
	Tilt-Y	0.002484	0.46896	0.126982
	Tilt-Z	-0.00124	65.76478	0.000389
US-NF-EW	Pitch	-0.00031	0.092835	0.016659
	Roll	-0.00113	-0.01985	0.086691
	Tilt-X	0.000445	-1.91379	0.002449
	Tilt-Y	-0.00132	-0.55343	0.120906
	Tilt-Z	0.00337	67.55027	0.004667
US-NF-WE	Pitch	-0.00014	0.099114	0.00274
	Roll	-0.00155	0.076577	0.333307
	Tilt-X	-0.00372	-2.05688	0.201669
	Tilt-Y	-0.00813	-0.86621	0.923956
	Tilt-Z	-0.00886	65.661	0.079108
US-NF-WW	Pitch	0.000856	-0.27016	0.020947
	Roll	-0.0012	-0.04715	0.013732
	Tilt-X	0.000755	-0.76765	0.011164
	Tilt-Y	-0.0032	0.987877	0.047965
	Tilt-Z	-0.00417	66.92424	0.012388

**Table 11.1** – Details about which and when some sensors failed

Strain Gage			
Bridge Name	No. Used	No. Active	Date Stopped (No of Sensors)
Elizabeth Bridge	40	0	Jan-2018(1), Mar-2018(1), Apr-2018(7), May-2018(30), June-2019(1)
Neville Island Bridge	63	0	Dec-2018(5), Jan-2019(11), Feb-2019(11), Mar-2019(2), Apr-2019(2), Jun-2019(1), Sep-2019(1), Oct-2019(1), Dec-2019(1), Jan-2020(4), Feb-2020(17), Jul-2020(3), Aug-2020(2), Sep-2020(1), Oct-2020(1)
Clairton-Glassport Bridge	20	2	Oct-2019(1), Apr-2021(1), Dec-2021(2), Jan-2022(3), Apr-2022(1), Jun-2022(1), Aug-2022(2), Sep-2022(5), Oct-2022(2)
Birmingham Bridge	16	0	Jan-2020(1), May-2022(15)
Smithfield St. Bridge	30	30	-
Cooks Mills Bridge	10	0	Apr-2021(3), Mar-2022(7)
Wyebrooke Bridge	42	0	Aug-2019(1), Oct-2019(1), Jul-2020(1), Oct-2021(2), Nov-2021(7), Dec-2021(5), Feb-2022(2), Jan-2022(10), Mar-2022(13)
Fulton Co.	10	0	Feb-2019(10)
Sanatoga Bridge			
Somerset Bridge	30	0	Jul-2020(28), Aug-2019(1), Jul-2019(1)
Displacement Gage			
Bridge Name	No. Used	No. Active	Date Stopped (No of Sensors)
Elizabeth Bridge	7	0	Jan-2018(1), Mar-2018(4), Apr-2018(2),
Neville Island Bridge	22	0	Jan-2019(1), Jan-2021(2), Feb-2021(10), Mar-2021(9)
Clairton-Glassport Bridge	24	24	-
Birmingham Bridge	18	0	Nov-2020(2), May-2022(16)
Smithfield St. Bridge	5	1	Aug-2018(1), May-2022(3)
Cooks Mills Bridge			
Wyebrooke Bridge			
Fulton Co.			
Sanatoga Bridge			
Somerset Bridge			

Rotation Gage			
Bridge Name	No. Used	No. Active	Date Stopped (No of Sensors)
Elizabeth Bridge	16	0	Feb-2018(1), Mar-2018(6), Apr-2018(3), May-2018(2), Oct-2020(4)
Neville Island Bridge	6	0	Jan-2021(1), Feb-2021(2), Mar-2021(3)
Clairton-Glassport Bridge	4	4	-
Birmingham Bridge	18	0	May-2018(2), Jul-2019(1), Mar-2021(1), Feb-2022(1), May-2022(13)
Smithfield St. Bridge	6	6	-
Cooks Mills Bridge			
Wyebrooke Bridge			
Fulton Co.			
Sanatoga Bridge	8	0	Jan-2019(1),Feb-2022(7)
Somerset Bridge			
Cable Gage			
Bridge Name	No. Used	No. Active	Date Stopped (No of Sensors)
Elizabeth Bridge	16	0	May-2018(16)
Neville Island Bridge			
Clairton-Glassport Bridge			
Birmingham Bridge			
Smithfield St. Bridge			
Cooks Mills Bridge			
Wyebrooke Bridge			
Fulton Co.			
Sanatoga Bridge			
Somerset Bridge			

Accelerometer			
Bridge Name	No. Used	No. Active	Date Stopped (No of Sensors)
Elizabeth Bridge	4	0	Jan-2018(1), Feb-2018(1), May-2018(1), Sep-2020(1)
Neville Island Bridge	7	0	Mar-2019(1), Jan-2020(2), Dec-2020(1), Feb-2021(3)
Clairton-Glassport Bridge	4	2	Jul-2019(1), Nov-2020(1)
Birmingham Bridge			
Smithfield St. Bridge	2	0	Jan-2019(1), Dec-2019(1)
Cooks Mills Bridge			
Wyebrooke Bridge			
Fulton Co.			
Sanatoga Bridge			
Somerset Bridge			

Camera			
Bridge Name	No. Used	No. Active	Date Stopped (No of Sensors)
Elizabeth Bridge	2	0	Feb-2022(1), Jan-2023(1)
Neville Island Bridge	2	0	Apr-2022(1), May-2021(1)
Clairton-Glassport Bridge	6	2	Apr-2022(3), May-2022(1)
Birmingham Bridge			
Smithfield St. Bridge	3	1	May-2022(2)
Cooks Mills Bridge			
Wyebrooke Bridge			
Fulton Co.			
Sanatoga Bridge			
Somerset Bridge			

<b>Table 13.1 – Summary of the bridge ratings according to inspections reports dated not later than 2020.</b>			
<b>No.</b>	<b>BMS ID</b>	<b>Name or Location</b>	<b>Rating: deck/superstructure/substructure</b>
1	02-0051-0110-0000	Elizabeth Bridge	4 / 4 / 5
2	02-0079-0650-0000	Neville Island Bridge	5 / 5 / 5
3	02-2085-0010-0586	Birmingham Bridge	7 / 6 / 6
4	02-3027-0020-0000	Smithfield St. Bridge	5 / 5 / 5
5	02-2038-0010-0140	Clairton-Glassport Bridge	6 / 5 / 6
6	05-3001-0080-0000	Cooks Mill Bridge	7 / 6 / 5
7	55-3014-0050-0509	Somerset Co.	7 / 4 / 6
8	29-2004-0040-0000	Fulton Co.	7 / 5 / 7
9	15-0082-0592-0385	Wyebrooke Bridge	5 / 5 / 4
10	46-4031-0314-1676	Sanatoga Bridge <sup>3</sup>	- / 4 / 4

<sup>3</sup> For this bridge there is no rating for the deck. Quoting the April 2019 bridge inspection, “A deck is not provided for the stone masonry arch structure.”